UNIVERSITY OF OKLAHOMA

GRADUATE COLLEGE

A MULTISCALE INVESTIGATION OF THE 26–27 APRIL 2011 TORNADO OUTBREAK

A DISSERTATION

SUBMITTED TO THE GRADUATE FACULTY

in partial fulfillment of the requirements for the

Degree of

DOCTOR OF PHILOSOPHY

By

MANDA BETH CHASTEEN
Norman, Oklahoma
2021

A MULTISCALE INVESTIGATION OF THE
26–27 APRIL 2011 TORNADO OUTBREAK

A DISSERTATION APPROVED FOR THE
SCHOOL OF METEOROLOGY

BY THE COMMITTEE CONSISTING OF

Dr. Steven Koch, Co-Chair

Dr. Cameron Homeyer, Co-Chair

Dr. Howard Bluestein

Dr. Adam Clark

Dr. Alan Shapiro

Dr. Nusrat Yussouf

Dr. Nikola Petrov

To the person who truly believed that I could accomplish anything,
gave me his curiosity, creativity, unconventionality, and independence,
and always made sure that I knew just how proud of me he was.

To my dad.

Thomas Alan Chasteen
June 28, 1946 – July 17, 2020

YOU MAKE ME PROUD
of YOU

LOVE DAD

Acknowledgments

The completion of this doctoral degree and my overall perseverance and success as a student in meteorology would not have been possible without the continued support, encouragement, guidance, and opportunities that I was afforded by numerous people during my time at both the University of Oklahoma and the University of Illinois. Although it is easy to lose perspective of how much you have grown as a person and a scientist, I can confidently say that the childhood version of Manda—who was incredibly fascinated by weather, but spent most of her days riding four wheelers through corn fields and shamelessly beating middle-aged men on a trap-shooting league with her dad—would be absolutely stunned by who I am today. All that I have experienced and accomplished seemed entirely out of reach and beyond the wildest dreams of a kid growing up outside a 600-person town in southern Illinois, and I cannot even begin to properly express the gratitude to all of the people who have guided me down this path and believed in me every step of the way.

First and foremost, I am indebted to my advisor, Dr. Steven Koch, who truly went above and beyond as a dedicated mentor with an incredible breadth of knowledge and experience that he eagerly shared with me, all while providing me with the freedom to think creatively and forge my own path. Although the journey was not always smooth and was frankly downright arduous at times, Steve knew when to teach me and when to challenge me to expand my knowledge and skillset as an independent researcher, and I have grown considerably as an analyst and scientist under his direction. Additionally, I am immensely grateful to Dr. Glen Romine for generously hosting me as a visitor at the National Center for Atmospheric Research's Mesoscale and Microscale Meteorology Laboratory (NCAR/MMM) in Boulder, Colorado, for the last 2.5 years of my Ph.D. and for patiently waiting for me to graduate so that he could ultimately hire me as a postdoc. Glen provided me with guidance, feedback, support, and numerous resources throughout my degree (including the generation of the ensemble forecasts described in this dissertation), and I am incredibly thankful for all the doors that he has opened for me.

I am grateful to Dr. Cameron Homeyer for providing his support, encouragement, and advice as the co-chair of my doctoral committee. I also want to thank Drs. Howie Bluestein, Alan Shapiro, Nusrat Yussouf, Adam Clark, and Nikola Petrov for their feedback and service as members of my doctoral committee. Additionally, I extend my gratitude to numerous members of the meteorological community who graciously provided invaluable guidance and feedback throughout the course of this project, including Drs. Lance Bosart, Jimmy Correia, Chris Davis, Tom Galarneau, Tony Lyza, Erik Rasmussen, Rich Rotunno, Chris Snyder, Ryan Sobash, Stan Trier, and Morris Weisman. Additionally, I give special thanks to Drs. Erik Rasmussen and Michael Coniglio for giving me the unique opportunity to participate in multiple field campaigns during my doctoral program.

I absolutely would not have reached the finish line without the support, encouragement, and distractions provided by all the wonderful people in my life. I am appreciative of my family for always believing in me and providing encouragement and financial support on my quest to becoming a Weather Doctor. I am especially grateful for the friends who have stuck by my side throughout graduate school and supported me during my time in Norman and beyond, including Dan Phoenix, Zach Wienhoff, Ethan Collins, Hristo Chipilski, Ryan Lagerquist, and Elizabeth Smith. I am extremely thankful for all the truly amazing friends that I have made since moving to Boulder, without whom I would not have gotten through the roughest final two years of my degree while dealing with the pandemic, loss of my dad, and other hardships. I am particularly grateful for all the shenanigans and memories made with my main COVID crew, including Sam Lillo, Bo Huang, Ryan Sobash, Austin Coleman, and Blake Allen. There is truly no better group to visit Boulder's classiest basement establishments with or to accidentally stay up until sunrise with you while drowning in the Devils River. I am also incredibly grateful to my amazing roommates, Sean Constantine and Kelsey Barton, for their moral support, encouragement, life advice, entertainment, and a seemingly endless supply of bathroom closet liquor. Finally, I am thankful for my favorite cat-loving hiking partner, Shima Shams, and all the other amazingly supportive and welcoming NCAR visitors whom I met or reunited with when I first came to Boulder in Summer 2019.

Financial support for this work was provided by NOAA/National Severe Storms Laboratory VORTEX-SE funding, the NCAR Advanced Study Program (ASP) Graduate Visitor Fellowship, and the NCAR/MMM Visitor Program. The analyses and simulations presented in this dissertation were conducted using both the OU Supercomputing Center for Education and Research (OSCER) Schooner and NCAR Computational and Information Systems Laboratory (CISL) Cheyenne supercomputers. I gratefully acknowledge Kiel Ortega for supplying the MYRORSS radar composites, Dr. David Dowell and Eric James for granting access to the Experimental HRRR forecasts, Dr. Maria Molina for providing guidance and assistance with running HYSPLIT, Dr. Stan Trier for producing the derived sounding kinematic profiles, Dr. Pat Skinner for supplying code to compute various WRF diagnostics, and Cameron Nixon for providing code to generate the spatial hodograph maps.

Table of Contents

List of Tables

List of Figures

Abstract

One of the most prolific tornado outbreaks ever documented occurred on 26–27 April 2011 and comprised three successive episodes of tornadic convection that primarily impacted the southeastern United States, including two quasi-linear convective systems (hereafter QLCS1 and QLCS2) that preceded the notorious outbreak of long-track, violent tornadoes spawned by numerous supercells over the warm sector during the afternoon and evening of 27 April. The ~36-h period encompassing these three convective episodes was part of a longer multiday outbreak that occurred ahead of a highly amplified and slowly moving upper-level trough as three embedded shortwaves supported destabilization and episodic convective development over the south-central U.S.

This research employs a combination of observational datasets, operational models, and convection-permitting WRF-ARW simulations to provide a multiscale investigation of the 26–27 April 2011 tornado outbreak. Particular attention is given to 1) identifying the mesoscale processes that contributed to the initiation, organization, and morphological evolution of each of the three convective episodes; 2) evaluating how the environmental conditions evolved throughout the outbreak to support three successive convective episodes with differing severities and modalities; and 3) assessing how the environment was altered by latent processes occurring within the first two convective episodes and how these upscale environmental modifications influenced the overall severity and evolution of this multiepisode outbreak.

Herein we demonstrate that the second shortwave in the sequence moved into the southern Great Plains (SGP) prior to the formation of QLCS1 on the evening of 26 April, while the third and most predominant shortwave—which was attended by an exceptionally strong upper-level jet streak, deep tropopause fold, and Pacific cold front that evolved into a cold front aloft (CFA) as it moved downslope over Texas and ultimately acquired the character of a dryline at the surface—supported both the development of QLCS2 and the

afternoon supercell outbreak that subsequently unfolded over the Southeast. The development of QLCS1 was immediately followed by unbalanced upper-level jetogenesis, rapid amplification of the large-scale flow pattern, considerable intensification of the low-level jet (LLJ) and vertical wind shear over the warm sector, and secondary surface cyclogenesis over the Midwest. The dramatic flow modifications stemming from this system contributed to both its rapid upscale growth and exceptional severity and persisted throughout the remainder of the outbreak. QLCS2 produced additional modifications to the mesoscale environment over the Southeast by promoting the downstream formation of a pronounced upper-level jet streak, altering the midlevel jet structure, furthering the development of a highly ageostrophic LLJ, and reinforcing a convectively generated thermal boundary that behaved as an effective warm front. Finally, the prolific afternoon supercell outbreak commenced as the third shortwave moved into the Lower Mississippi Valley and convection erupted primarily—but not exclusively—along two bands that were associated with the dryline and preceding CFA. The upscale flow modifications collectively produced by both antecedent QLCSs contributed to the notably favorable shear profiles present over the warm sector at the beginning of the supercell outbreak. Although the thermodynamic environment over the Southeast was also influenced by outflow from the two QLCSs, rapid destabilization occurred throughout the morning in response to surface heating, strong differential advection, and mesoscale lifting by prefrontal disturbances that were triggered ahead of the CFA. *Ultimately, the unique overlap of anomalously large buoyancy, highly favorable vertical shear profiles, and the mesoscale organization of numerous supercells that remained largely discrete for several hours as they traversed the warm sector enabled this final and most devastating tornadic episode.*

Chapter 1

Introduction

1.1 Overview of the 26–27 April 2011 tornado outbreak

One of the most prolific tornado outbreaks ever documented impacted the United States between 25–28 April 2011 (Knupp et al., 2014; Fuhrmann et al., 2014). During this extended outbreak, multiple consecutive episodes of convection yielded 343 confirmed tornadoes (Fig. 1) that caused 321 fatalities and more than $11 billion in damages (NOAA, 2011, 2017). The most destructive portion of this outbreak occurred in the Southeast

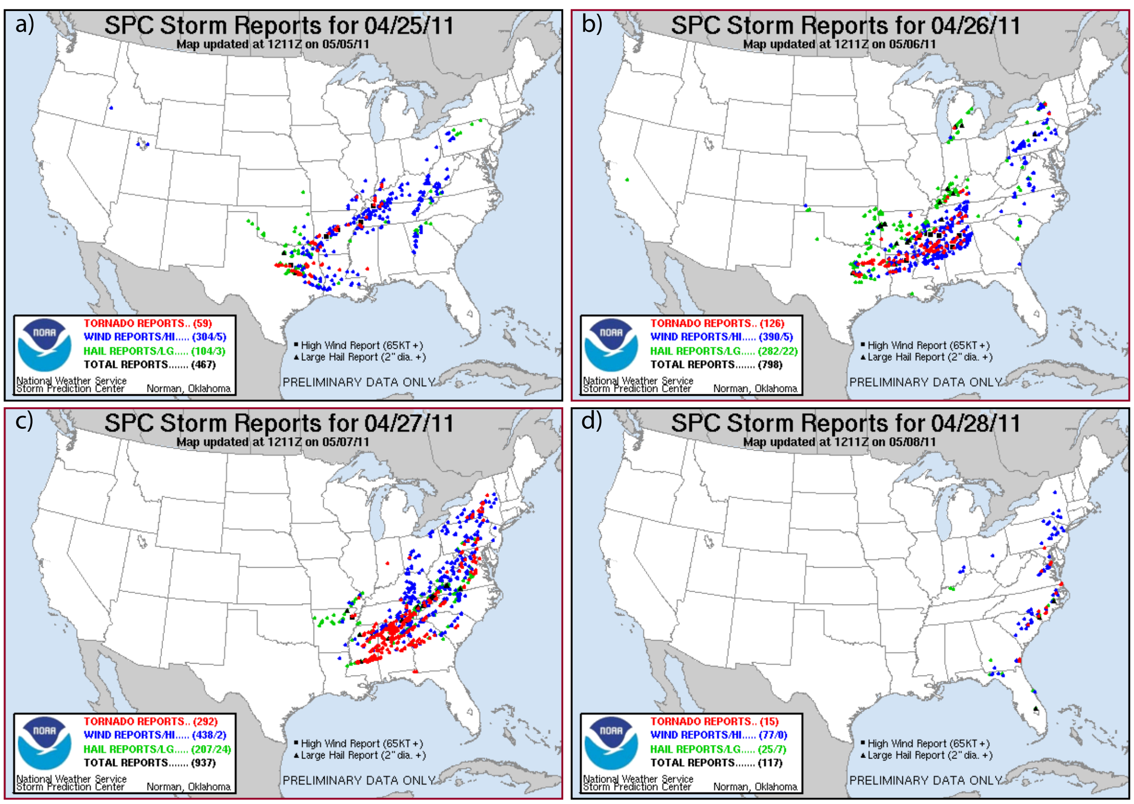

Figure 1: *Preliminary SPC storm reports for the extended outbreak spanning (a) 1200 UTC 25 April – 1159 UTC 26 April, (b) 1200 UTC 26 April – 1159 UTC 27 April, (c) 1200 UTC 27 April – 1159 UTC 28 April, and (d) 1200 UTC 28 April – 1159 UTC 29 April 2011. The panels outlined in red denote the periods of primary emphasis in this study.*

on 27 April, during which three separate convective episodes collectively produced 199 tornadoes and 316 fatalities over a 24-h period (Fig. 2; Knupp et al., 2014). The pinnacle of this event—the afternoon supercell outbreak—was preceded by two quasi-linear convective systems (QLCSs), the first of which (hereafter QLCS1) developed during the evening of 26 April and impacted the Southeast overnight and during the early morning (Figs. 3a-f). QLCS1 was exceptionally severe and alone produced over 100 tornadoes—several of which were long-track and/or rated up to EF3 intensity on the enhanced Fujita (EF) scale. A second weakly tornadic QLCS (hereafter QLCS2) subsequently developed in the wake of QLCS1 and moved through the Southeast during the late morning (Figs. 3e-h). Shortly thereafter, numerous supercells erupted within the warm sector (i.e., away from any discernible surface boundaries) and spawned multiple long-track, violent tornadoes (11 EF4 and 4 EF5) throughout the afternoon and evening (Figs. 2 and 3h-l). *The ~36-h period that began with the formation of QLCS1 on the evening of 26 April and extended through the supercell outbreak that commenced during the afternoon of 27 April will be the primary focus of this dissertation.*

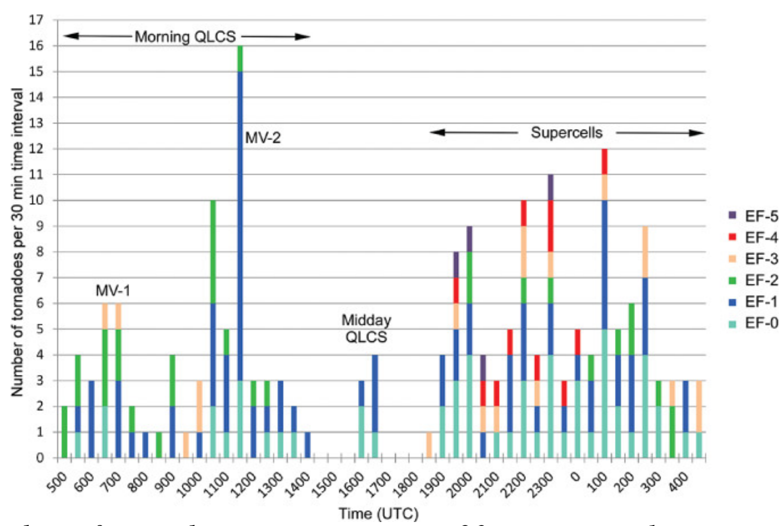

Figure 2: *Number of tornadogenesis events per 30-min interval spanning 0500 UTC 27 April – 0500 UTC 28 April 2011 from Knupp et al. (2014). The EF-scale rating and parent convective episode ("Morning QLCS" is QLCS1, and "Midday QLCS" is QLCS2) are indicated for each tornado during this period.*

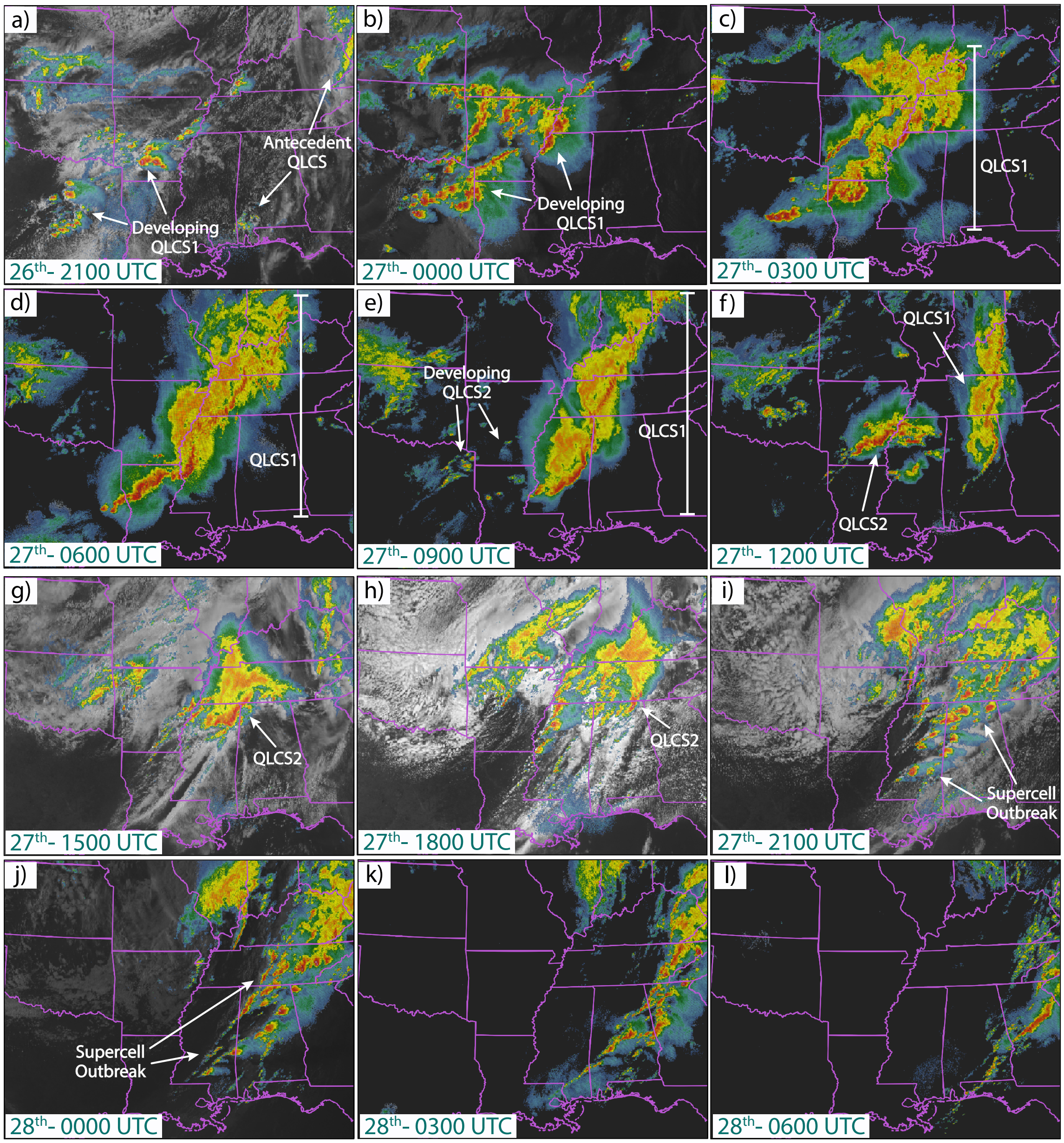

Figure 3: *NEXRAD composite radar reflectivity from the Multi-Year Reanalysis Of Remotely-Sensed Storms (MYRORSS) archive (Ortega et al., 2012) overlaid with GOES-13 visible satellite imagery (when available) every 3 h from 2100 UTC 26 April 2011 to 0600 UTC 28 April 2011.*

Although the potential for a high-impact severe weather event over the Southeast during the afternoon of 27 April was well-anticipated by forecasters and the tornado warning lead times during this event (average of 22 min) were longer than the national average, the mortality rate during this outbreak was notably high and was attributed a combination of sociological and meteorological factors, including the prevalence of strong tornadoes at night and in conditions of poor visibility, the incidence of recurring tornadic systems impacting the same geographic region, and the sheer strength and long-track nature of the tornadoes (Simmons and Sutter, 2012; Chiu et al., 2013; Knupp et al., 2014; Sanders et al., 2020). The remarkable severity of this tornado outbreak and its impacts on the Southeast—particularly the state of Alabama—helped to motivate NOAA's Verification of the Origins of Rotation in Tornadoes EXperiment-Southeast (VORTEX-SE) program (Rasmussen, 2015), through which the research presented herein was supported.

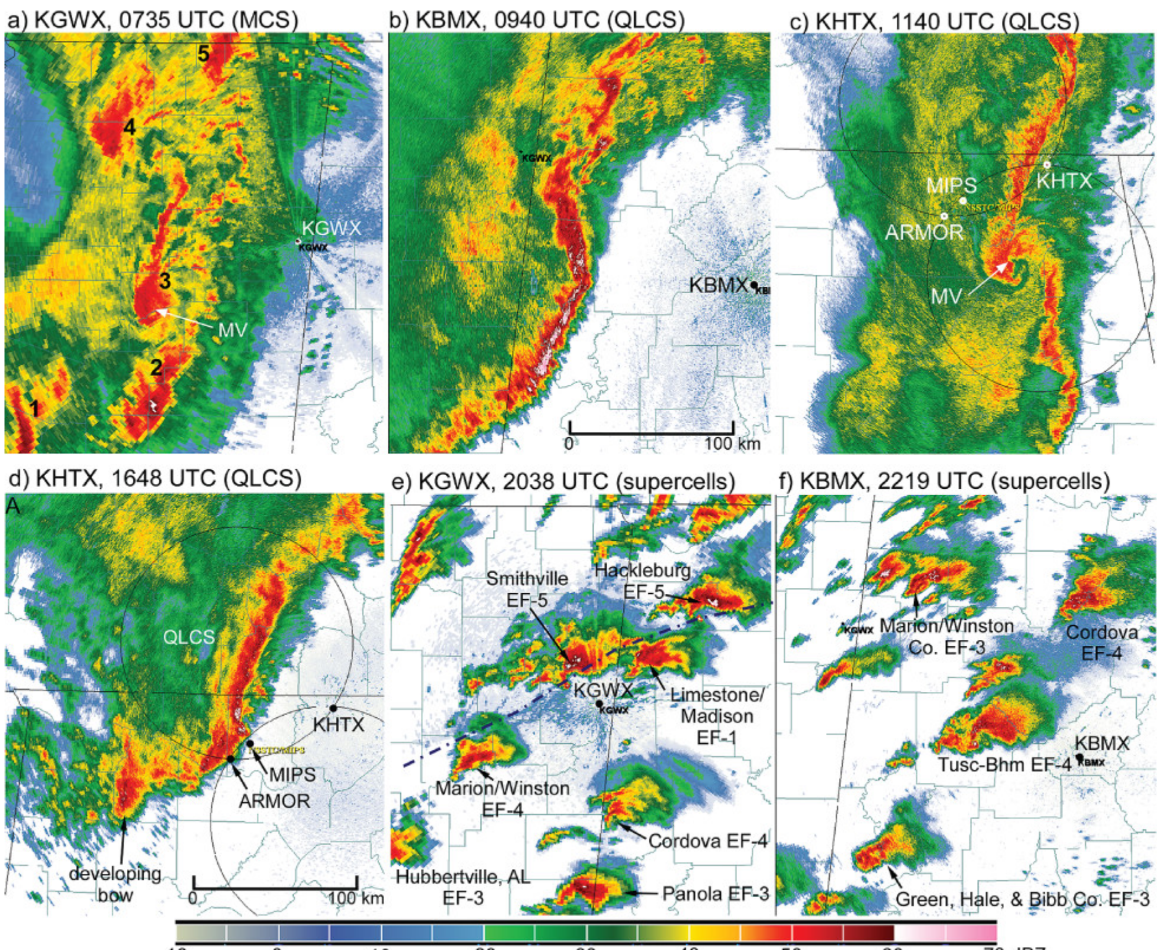

Figure 4: *Observed radar reflectivity of the three tornadic episodes that impacted the Southeast on 27 April 2011 from Knupp et al. (2014). QLCS1 is shown in (a)-(c), QLCS2 is shown in (d), and the supercell outbreak is shown in (e)-(f).*

When this doctoral research began in 2017, few meteorological studies had been conducted on the 26–27 April 2011 outbreak despite its prominence. Except for the publications that have since stemmed from the research contained herein—to date, Chasteen and Koch (2021a) and Chasteen and Koch (2021b)—the most comprehensive overview of this outbreak was provided by Knupp et al. (2014), which focused largely on the unique morphological evolutions and storm-scale structures of the three episodes as they moved through the Southeast (Fig. 4) and the mesoscale environment over northern Mississippi and Alabama. This paper drew attention to several intriguing aspects of the event, including the development of two long-lived meso-β-scale vortices embedded within QLCS1 that were associated with several long-track, significant tornadoes (Figs. 4a,c) and the significance of a thermal boundary produced by the two QLCSs during the subsequent supercell outbreak. Saide et al. (2015) conducted an investigation into the potential influence that aerosols stemming from biomass burning over Central America had on the mesoscale environment during the supercell outbreak. Their findings suggest that radiative effects associated with these aerosols enhanced the background thermodynamic and kinematic profiles by strengthening the capping inversion and increasing the optical thickness of the low-level cloud layer, which in turn promoted lower cloud bases and stronger low-level vertical wind shear within the warm sector. Clark et al. (2013) used ensemble forecasts from this event to evaluate the relationship between the pathlengths of simulated rotating storms (based on swaths of updraft helicity; Kain et al., 2008) and the pathlengths of observed tornadoes. Additionally, Yussouf et al. (2015) evaluated short-term probabilistic forecasts of low-level rotation during the supercell outbreak that were generated through continuously cycled storm-scale ensemble data assimilation with 5-min updates.

Although tornado outbreaks of similar magnitude to the outbreak discussed herein are exceptionally rare, we expect that important features identified in other outbreaks may be present in this case. By many metrics, the most comparable event was the notorious 3–4 April 1974 Super Outbreak (Doswell et al., 2006; Knupp et al., 2014; Fuhrmann et al.,

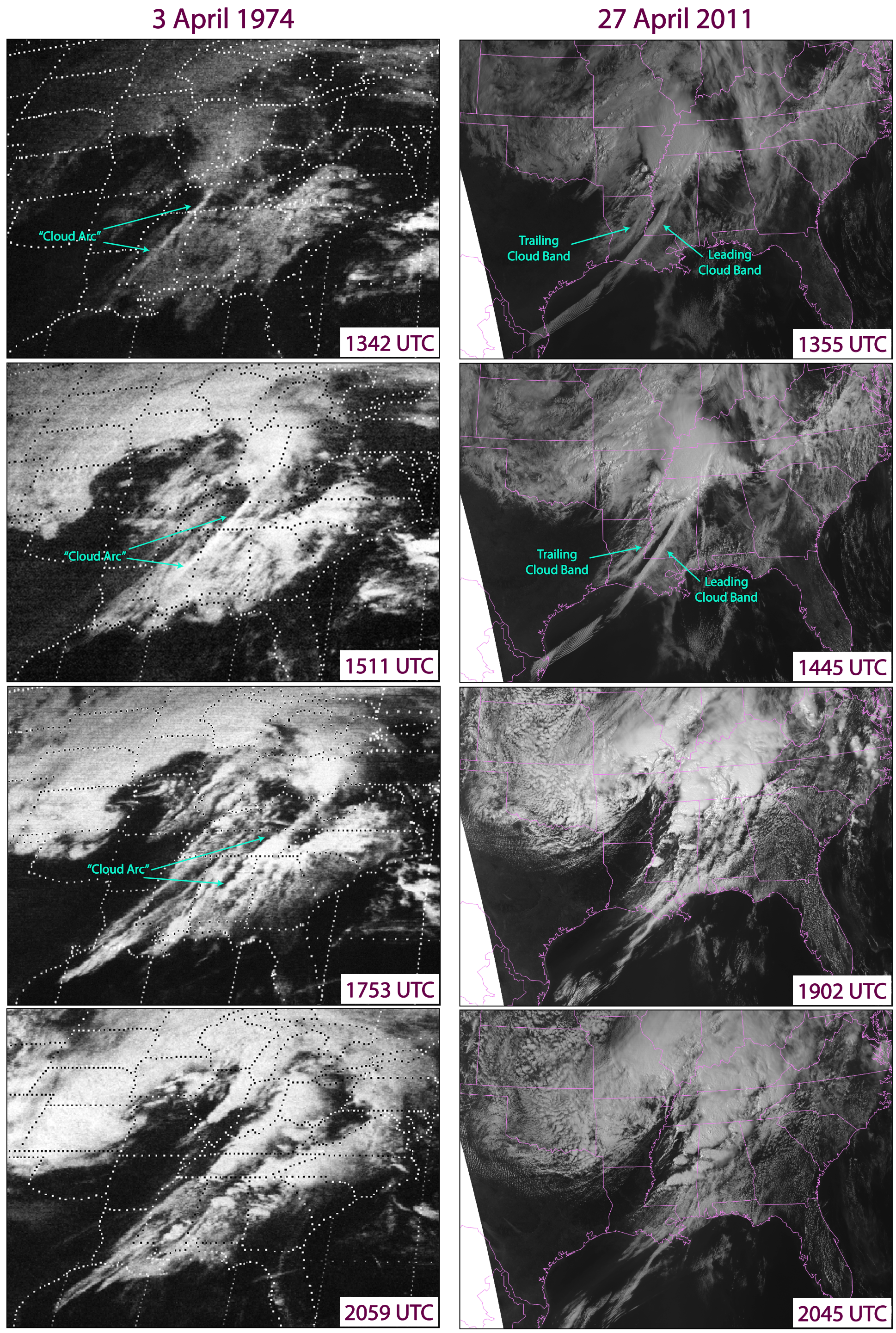

Figure 5: *Visible satellite imagery depicting the warm sector cloud bands during the (left) 3 April 1974 Super Outbreak and (right) 27 April 2011 afternoon supercell outbreak. The 3 April 1974 satellite images were adapted from Fig. 4 of Corfidi et al. (2010), and the cloud arc band described in their paper is annotated.*

2014), during which three systems simultaneously developed and produced nearly 150 tornadoes over the central and southeastern U.S. (Agee et al., 1975; Hoxit and Chappell, 1975; Miller and Sanders, 1980; Locatelli et al., 2002b; Corfidi et al., 2010). The convective organization during the heat of the Super Outbreak on 3 April 1974 was highly analogous to that which occurred during the afternoon of 27 April—namely, convection initiated along multiple coherent bands that were removed from any surface fronts (Fig. 5). As we will uncover throughout this dissertation, many noteworthy features and environmental characteristics that were identified during the 1974 Super Outbreak were indeed present during this outbreak. These include a highly amplified upper-level trough, prominent baroclinic shortwave, strong midlevel and low-level jets, and a surface cyclone that originated in the lee of the Rocky Mountains and was attended by a Pacific cold front, dryline, and cold front aloft (CFA).

The sparsity of publications on the prolific 26–27 April 2011 tornado outbreak and the abundance of perplexities about its severity and evolution provided us with considerable freedom as to which of its numerous facets we wanted to explore. Ultimately, the analyses presented in this dissertation strive to untangle the outbreak by answering the following research questions:

1. *What mesoscale processes contributed to the initiation, organization, and morphological evolution of the three tornadic convective systems that impacted the Southeast on 27 April 2011?* **[Q1]**

2. *How did the environmental characteristics evolve throughout the outbreak to support three successive convective episodes that each exhibited a different severity and modality?* **[Q2]**

3. *How was the environment modified by latent processes occurring within the first two convective systems and how did these upscale environmental modifications contribute to the severity of this prolific multiepisode tornadic outbreak?* **[Q3]**

4. *How are the relevant multiscale processes and upscale feedbacks arising from convection depicted within a convection-permitting ensemble?* **[Q4]**

Owing to the sheer complexity of this multiepisode outbreak and the prominence of scale interactions occurring between the convection and surrounding environment, each of these questions will be addressed progressively throughout the dissertation, which is organized as follows. The remainder of this chapter provides background on tornado outbreaks in the southeastern United States and the established importance of elevated fronts in the formation of organized convection within the warm sector of an extratropical cyclone, which we found to be an essential component of this outbreak. Chapter 2 introduces the operational model and observational datasets used throughout this dissertation. Chapter 3 provides a chronological description of the multiepisode outbreak, with particular attention given to explaining how the synoptic- and subsynoptic-scale environment evolved to support the successive formation of three convective episodes that each exhibited a different morphology and severity. Chapter 4 provides a detailed dynamical investigation into the upscale environmental modifications produced by QLCS1 and QLCS2 and how they contributed to the overall severity and evolution of the outbreak. Chapter 5 evaluates forecasts of the outbreak from two convection-permitting ensembles and employs one of the ensembles to further investigate the influence of latent heat release and upscale feedbacks on the outbreak evolution. Chapter 6 uses a combination of observations and convection-permitting forecasts to detail the evolution of mesoscale disturbances during the outbreak and how they contributed to rapid destabilization of the warm sector and convection initiation during the afternoon supercell outbreak. Finally, the conclusions of this comprehensive multiscale investigation are summarized in Chapter 7.

1.2 General characteristics of tornado outbreaks in the Southeast

Tornadoes within the Southeast are responsible for a disproportionately greater number of fatalities than those in other parts of the country—a statistic that has been acknowledged for several decades and attributed to the complex overlap of numerous physical and societal factors that render this region highly vulnerable (e.g., Sims and Baumann, 1972; Galway and Pearson, 1981; Ashley, 2007; Ashley et al., 2008; Sutter and Simmons, 2010; Strader and Ashley, 2018; Anderson-Frey and Brooks, 2019; Anderson-Frey et al., 2019; Biddle et al., 2020). Several past studies have examined the physical characteristics of tornadic events that occur in the Southeast. These studies primarily emphasized the seasonal and diurnal variability of tornadoes within this region (e.g., Brooks et al., 2003; Trapp et al., 2005; Kis and Straka, 2010; Smith et al., 2012; Thompson et al., 2012; Sherburn and Parker, 2014; Rogers et al., 2017; Anderson-Frey et al., 2019), the synoptic patterns conducive to these events (e.g., Whitney, 1977; Uccellini and Johnson, 1979; Galway and Pearson, 1981; Guyer et al., 2006; Sherburn et al., 2016; Rogers et al., 2017; Kelnosky et al., 2018), and the convective modes responsible for producing the majority of tornadoes (e.g., Trapp et al., 2005; Kis and Straka, 2010; Smith et al., 2012; Thompson et al., 2012; Grams et al., 2012; Ashley et al., 2019). Collectively, these studies determined that tornado outbreaks in the

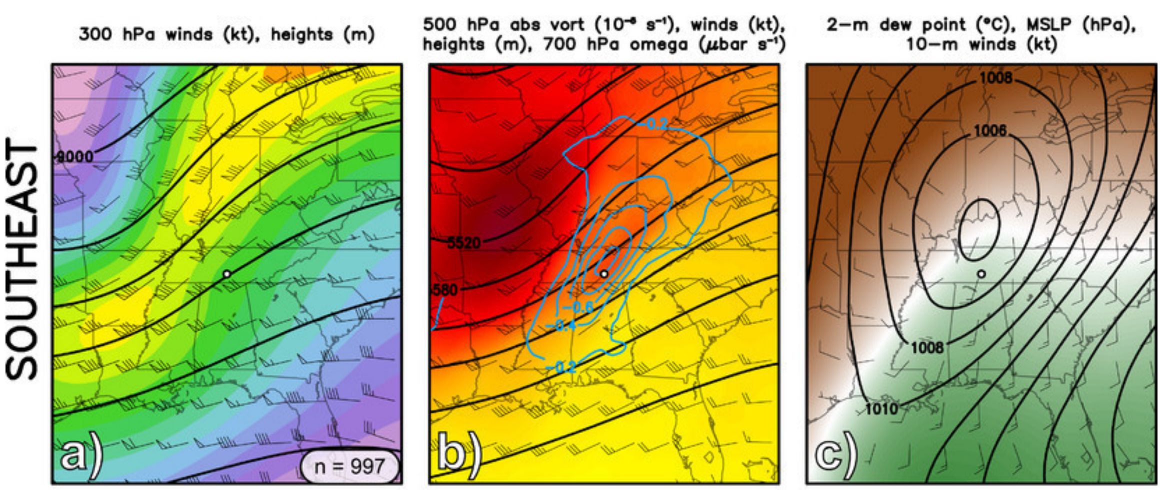

Figure 6: *Environmental composites for severe HSLC events in the Southeast from Sherburn et al. (2016). Shown are (a) 300-hPa winds (shaded; kt), wind barbs (kt), and geopotential heights (black contours,; every 120 m), (b) 500-hPa absolute vorticity (shaded; 10^{-5} s^{-1}), wind barbs (kt), geopotential heights (black contours, every 60 m), and 700-hPa omega (blue contours; μbar s^{-1}), and (c) 2-m dewpoint (shaded; $^\circ C$), mean sea level pressure (black contours, every 2 hPa), and 10-m wind barbs (kt).*

Southeast are typically associated with a highly-amplified synoptic pattern, strong large-scale forcing for ascent, and multiple interacting upper-level jet streaks (e.g., Fig. 6 from Sherburn et al., 2016). Furthermore, tornadoes generally develop within the warm sector of an extratropical cyclone that initially formed in the lee of the Rocky Mountains ahead of a vigorous midlevel shortwave trough (e.g., Galway and Pearson, 1981; Guyer et al., 2006; Sherburn et al., 2016). Guyer et al. (2006) found that most significant tornadoes typically developed on the anticyclonic flank of a midlevel jet streak and in the vicinity of a strong southerly low-level jet (LLJ), which provided warm air advection (WAA), poleward moisture transport, and strong low-level vertical wind shear. Additionally, the convection from which these tornadoes develop often exhibits a highly complex and/or quasi-linear organization (e.g., Smith et al., 2012; Thompson et al., 2012; Ashley et al., 2019) and may initiate within the warm sector away from any discernible surface boundaries due to mesoscale processes that remain elusive (e.g., Koch et al., 1998; Trier et al., 2021), thus posing significant forecasting and warning challenges for meteorologists that ultimately affect how decision-makers, stakeholders, and members of the public prepare for and respond to such events (e.g., Brotzge and Donner, 2013; Ellis et al., 2020).

Most recent attention given to tornadic environments in the Southeast has focused on the high-shear, low-CAPE (HSLC) regimes that are common during the cool and transition seasons and during nocturnal tornado events (e.g, Guyer et al., 2006; Dean and Schneider, 2008; Guyer and Dean, 2010; Kis and Straka, 2010). Sherburn and Parker (2014) classified events as HSLC if they had environments with surface-based CAPE (SBCAPE) ≤ 500 J kg^{-1}, most-unstable CAPE (MUCAPE) ≤ 1000 J kg^{-1}, and 0–6-km bulk wind difference (BWD) ≥ 18 m s^{-1}. Recently, Brown et al. (2021) showed that HSLC environments in the Southeast tend to evolve differently than those with high CAPE during the early-evening transition period, with CAPE values increasing and higher low-level shear and storm-relative helicity (SRH; Davies-Jones, 1984, 1990) values persisting within these environments after sunset.

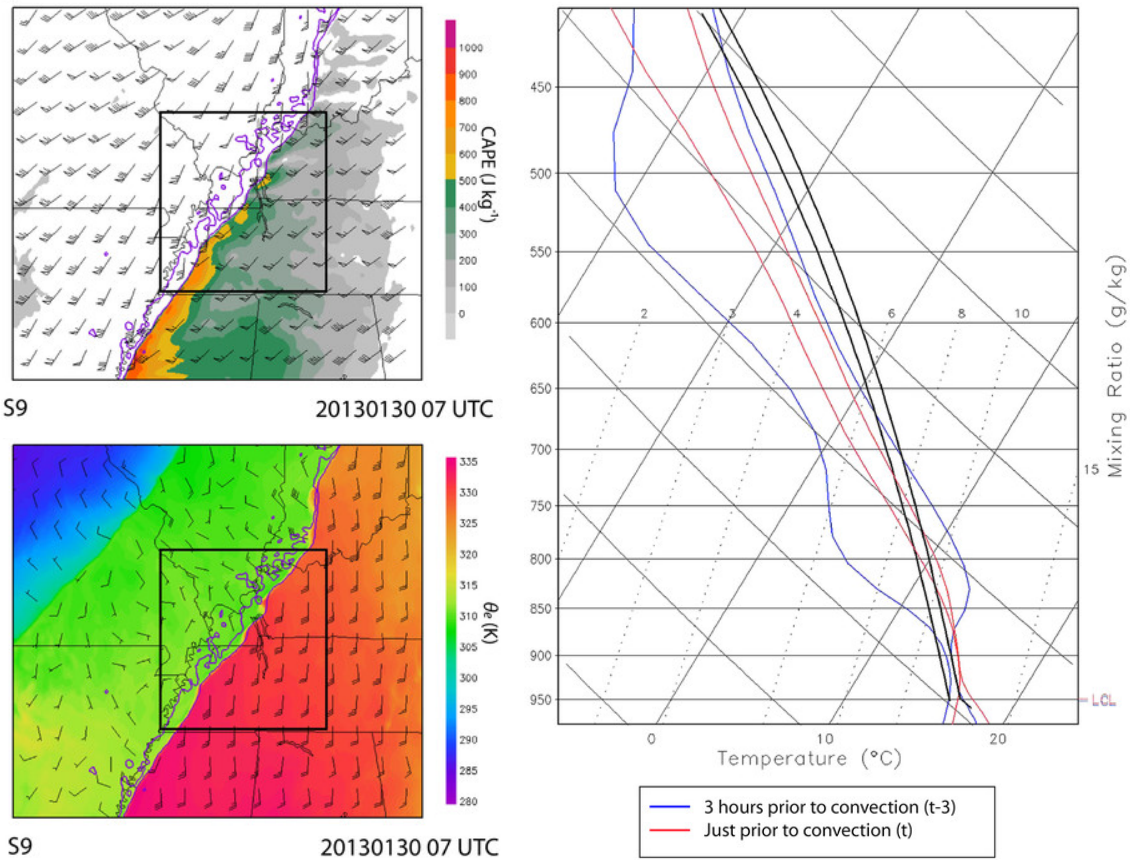

Figure 7: *Simulated depiction of a Southeast HSLC event on 30 January 2013 from King et al. (2017). In the (top left), SBCAPE (shaded; J kg^{-1}), 0–3-km wind shear (barbs; kt), and 40-dBZ reflectivity (purple contours); (bottom left) 10-m equivalent potential temperature (shaded; K), 10-m wind (barbs; kt), and 40-dBZ reflectivity (purple contours); and (right) composite soundings (blue) 3 h prior to convection and (red) just prior to convection. The black box in the left two panels denotes the area over which the composite soundings were constructed. The black lines in the right panel represent the surface-based parcel traces.*

Furthermore, QLCS tornadoes were found to be more prevalent in HSLC environments, whereas supercellular tornadoes generally occurred in higher CAPE environments.

HSLC regimes are notoriously challenging for both operational forecasters and numerical weather prediction (NWP) models—in large part due to the sensitivity of CAPE to the vertical profiles of temperature and moisture (e.g., Dean and Schneider, 2008; Cohen et al., 2015, 2017; Anderson-Frey et al., 2019). Guyer et al. (2006) found that CAPE during HSLC was typically dominated by low-level moisture and that midlevel lapse rates were relatively weak, which would imply that elevated mixed layers (EMLs; Carlson et al., 1983) were generally absent in these environments. Sherburn and Parker (2014) found that the lapse rates between 0–3 km and 700–500 hPa were two of the most skillful parameters for distinguishing between significant severe and nonsevere HSLC events. Expanding upon these findings, Sherburn et al. (2016) determined that the release of potential instability was often present during HSLC severe events and that 750–700-hPa frontogenesis was a skillful forecasting parameter. Furthermore, King et al. (2017) found that HSLC environments tend to exhibit considerable mesoscale heterogeneity and rapidly destabilize on timescales < 3 h (Fig. 7). This destabilization was attributed to both low-level warming and moistening (i.e., low-level increases in equivalent potential temperature; θ_e) and appreciable midlevel cooling, which resulted from the release of potential instability and promoted large CAPE increases over periods of 1–3 h. Sherburn and Parker (2014), Sherburn et al. (2016), and King et al. (2017) postulated that a dry intrusion and/or CFA may have contributed to the development and release of potential instability that promoted rapid destabilization in these environments.

1.3 Background on elevated fronts and warm sector convection

Organized precipitation is known to develop within the warm sector[1] of an extratropical cyclone globally and is often attributed to ascent and destabilization ahead of a tropopause fold (e.g., Griffiths et al., 2000; Antonescu et al., 2013) and/or the release of potential instability created by a dry intrusion (or dry conveyor belt; DCB) that moves ahead of the surface cold front (i.e., a "split front", Fig. 8; Browning and Monk, 1982; Browning, 1986; Browning and Roberts, 1994; Browning, 1997). Tropopause folds typically form within a region of confluent northwesterly flow upstream from a longwave trough in response to upper-level frontogenesis coinciding with along-jet geostrophic cold air advection (CAA; e.g., Danielsen, 1968; Keyser and Shapiro, 1986; Rotunno et al., 1994; Schultz and Doswell, 1999). Strong subsidence develops beneath the upper-level jet axis in this configuration,

[1]Our use of the term "warm sector" refers specifically to the region of warm, moist surface air located ahead of any *surface* fronts.

which also yields a pronounced DCB comprising air that originated near the tropopause and progressively descends into the middle and lower troposphere as the baroclinic wave amplifies (e.g., Danielsen, 1964, 1974; Carlson, 1980; Browning, 1997). The leading edge of the DCB—which becomes a split front if it moves over the warm sector—generally exhibits a strong gradient in θ_e but only a weak gradient in potential temperature (θ; e.g., Browning and Monk, 1982). We note that potential temperature (or virtual potential temperature, θ_v) is directly proportional to density while θ_e is not.

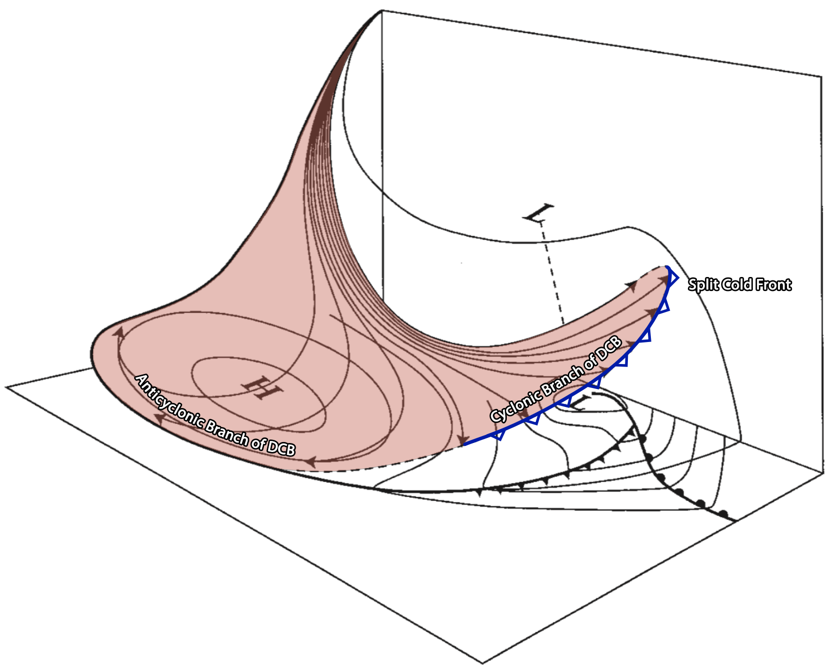

Figure 8: *3D depiction of flow within the dry intrusion of an extratropical cyclone. Arrows are trajectories of air originating from a small region near the tropopause, drawn within a curved isentropic surface. These trajectories come close to the ground in the left part of the diagram but not in the right-hand part, where they remain aloft and overrun the surface fronts. Figure was adapted from Browning (1997) based on the original Danielsen (1964) conceptual model.*

Furthermore, the significance of elevated baroclinic zones in the formation of warm sector convection *east of the Rocky Mountains* has been known for nearly a century (e.g., Holzman, 1936; Lichtblau, 1936; Lloyd, 1942). In addition to the aforementioned phenomena—which are simply attributes of amplifying baroclinic waves—the passage of frontal systems over the Rocky Mountains may yield considerable deviations from the Norwegian cyclone model and the formation of nonclassical features, including the EML, dryline, and CFA (e.g., Schaefer, 1974; Danielsen, 1974; Carlson et al., 1983; Hobbs et al., 1990; Martin et al., 1995; Locatelli et al., 1995; Hobbs et al., 1996; Neiman et al., 1998; Neiman and Wakimoto, 1999; Locatelli et al., 2002a). As a Pacific cold front traverses the Rockies, the postfrontal air mass experiences both adiabatic and diabatic thermodynamic modifications that substantially reduce its baroclinity and potential density within the lower troposphere. Consequently, this modified postfrontal air mass may overrun the relatively stable low-level

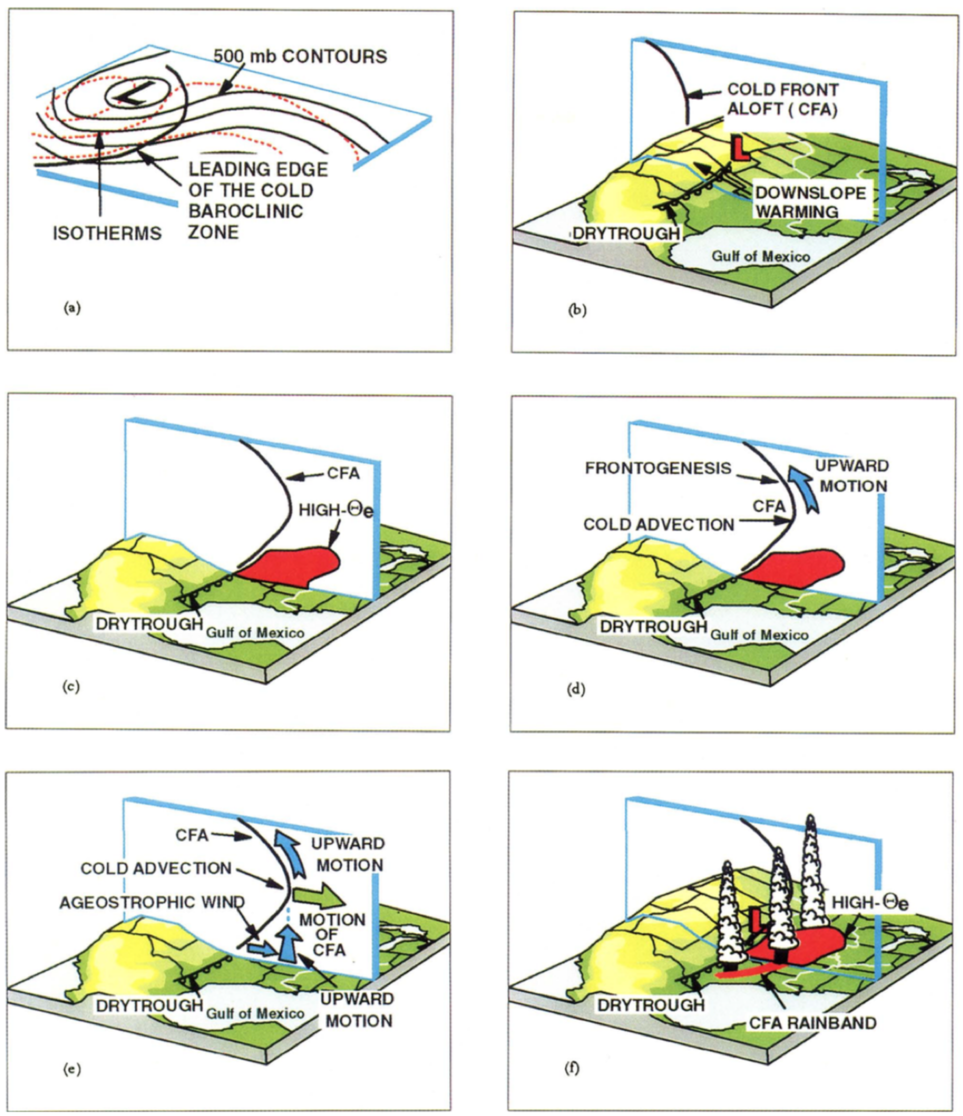

Figure 9: *Schematic from Hobbs et al. (1996) depicting the movement of a cold front aloft across the dryline and the subsequent formation of convective rain band over the warm sector.*

moist layer (or any air masses that exhibit greater potential densities, such as remnant outflow boundaries) after it moves downslope in the lee of the Rockies and merges with a dryline or lee trough. This induces a warm-type occlusion structure, wherein the low-level moist air is overlaid by a layer of elevated CAA associated with the Pacific cold front aloft (i.e., a CFA) that is preceded by an EML plume comprising relatively high potential temperatures (Figs. 9 and 10). One would expect that the nature of these postfrontal modifications and thus the resultant frontal structure have a strong diurnal dependence owing to the magnitude of sensible heating and prevalence of deep planetary boundary layer (PBL) turbulent mixing over elevated terrain during the daytime. This topographically influenced evolution may proceed concurrently with tropopause-level processes such that a prominent tropopause fold, DCB, and CFA all coexist within a maturing baroclinic system east of the Rockies.

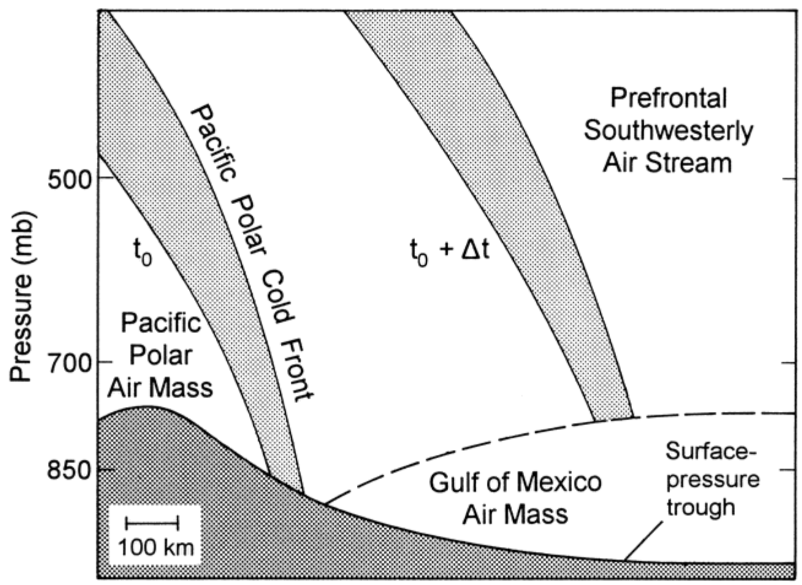

Figure 10: *Schematic from Neiman et al. (1998) showing the decoupling of the Pacific cold front from the surface by the shallow Gulf of Mexico air mass. The Pacific front is shown at two times (t_0 and $t_0 + \Delta t$, where $\Delta t \cong 18$ h) relative to the nearly stationary gulf air mass. The dashed line denotes the top of the shallow gulf air mass, and the intersection of the dashed line with the ground represents the surface position of the dryline.*

Generally, the air behind a PCF becomes considerably dry during its traverse over the Rocky Mountains, and a dryline frequently persists or redevelops at the surface—particularly during the daytime when PBL fluxes are prominent—as elevated CAA progresses over the

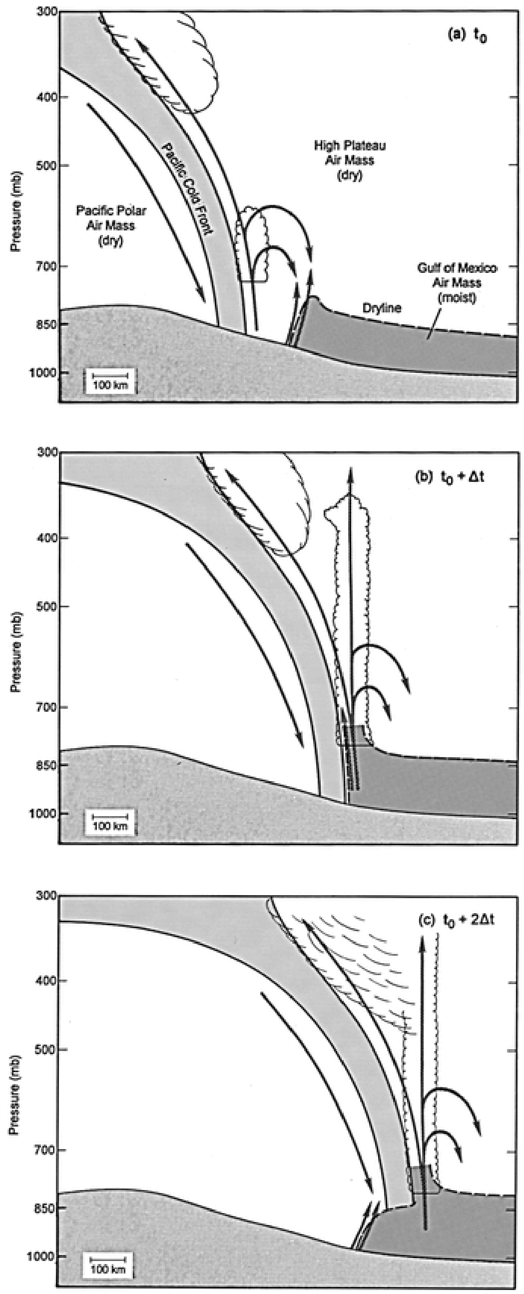

Figure 11: *Schematic from Neiman and Wakimoto (1999) showing of the merger of the Pacific cold front with the dryline, where Δt is ~3 h: (a) distinct separation between the advancing front and dryline, (b) merging of the front with the dryline and phasing of their vertical circulations, and (c) decoupling of the front from the surface by the shallow Gulf of Mexico air mass. The Pacific cold frontal zone and Gulf of Mexico air mass are shaded light and dark, respectively. The dashed lines mark the dryline. The gray-shaded arrows portray the vertical motions associated with the Pacific cold front and dryline.*

warm sector behind a CFA. Although drylines in the United States typically form over the southern Great Plains (SGP) during the daytime in response to confluence and spatial variations in moisture and PBL mixing (e.g., Schaefer, 1974; Hoch and Markowski, 2005), the eastward movement of a dryline into the Mississippi River Valley often occurs during prominent severe weather outbreaks and may be accompanied by a CFA (e.g., Castle et al., 1996; Lee et al., 2006; Maddox et al., 2013; Duell and Van Den Broeke, 2016). Fujita et al. (1970) discussed the significance of elevated CAA occurring ahead of a surface "dry cold front" in promoting destabilization and convection initiation (CI) within the warm sector during the 1965 Palm Sunday tornado outbreak. Additionally, Locatelli et al. (2002b) described the evolution of a dryline and preceding CFA during the prolific 1974 Super Outbreak, the former of which developed in response to the diurnal modification of postfrontal air that had subsided from the upper troposphere within a DCB. In this and other previous studies (e.g., Businger et al., 1991; Locatelli et al., 1995, 1997; Neiman and Wakimoto, 1999), strong low-level convergence and ascent occurring within the moist air mass ahead of the CFA were primarily responsible for CI. This is depicted schematically in Fig. 11, in which a mesoscale corridor of deepened moisture (width < 100 km) develops after the Pacific cold front occludes with the dryline in association with the CFA's ageostrophic frontal circulation (Neiman and Wakimoto, 1999).

Although several studies have clearly established that mass and momentum adjustments within the underlying moist layer accompany the passage of a CFA, papers on CFAs (perhaps paradoxically) typically describe the top of the moist layer as a "pseudosurface" such that the Pacific cold front glides over this layer without considerably disturbing it—at least after the front-dryline merger occurs (e.g., the schematic in Fig. 10 from Neiman et al., 1998). This conceptual framework is in contrast to Fig. 11, which illustrates that the CFA produces distortions to the underlying moist air mass that in turn lead to CI. Although studies have documented the presence of gravity waves within the capping inversion atop the moist layer prior to the merger between a Pacific cold front and dryline (e.g., Koch and McCarthy, 1982;

Neiman and Wakimoto, 1999; Parsons et al., 2000), Locatelli et al. (2002b) is mysteriously the only paper (to the author's knowledge) that entertains the possibility that disturbances produced within the underlying stable layer by the CFA may lead to the generation of gravity waves and/or bores that propagate into the warm sector ahead of the front. This evolution—which occurred during the 1974 Super Outbreak and was thought to be responsible for the formation of a prefrontal squall line—is shown in Fig. 12.

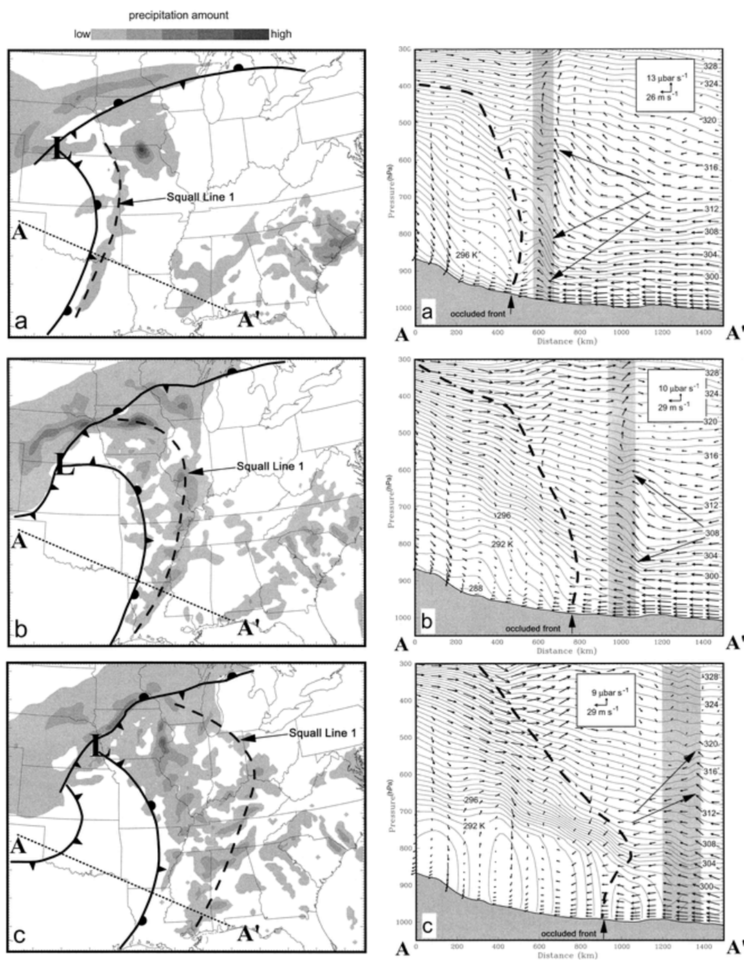

Figure 12: *Figure adapted from Locatelli et al. (2002b) of the 1974 Super Outbreak that depicts (left) precipitation with "Squall Line 1" and frontal positions at (a) 0800 UTC, (b) 1400 UTC, and (c) 1800 UTC 3 Apr 1974, and (right) corresponding vertical cross sections along the line AA' of potential temperature (contours; solid K), winds in the plane of the cross section relative to the motion of Squall Line 1 (see legend), position of the Pacific cold front (dashed line), and the location in the cross section of Squall Line 1 (vertical shaded rectangle). The arrows point to the leading edge of the undular bore identified to be associated with Squall Line 1.*

Chapter 2

Data and methods: Operational models and observations

The operational models and unique observational datasets employed throughout this dissertation are described below. These datasets were used in combination with several conventional observations, including: GOES-13 Advanced Baseline Imager (ABI) observations from the visible, water vapor, and longwave infrared (IR) channels (e.g., Schmit et al., 2017); Next Generation Weather Radar (NEXRAD) WSR-88D radar reflectivity composites obtained from the Multi-Year Reanalysis of Remotely Sensed Storms (MYRORSS) archive (Ortega et al., 2012); hourly surface observations from Automated Weather Observing System (AWOS) sites; hourly and 1-m surface observations from Automated Surface Observing Systems (ASOS) sites; and operational upper-air soundings. Other invaluable datasets that were used to develop our understanding of the environmental characteristics and dynamical processes described in this dissertation but are not explicitly presented include NOAA 915-MHz boundary layer wind profiling radars (Ecklund et al., 1988), upper-air soundings released every ~3 h from several sites over the SGP as part of the ongoing Midlatitude Continental Convective Cloud Experiment (MC3E; Jensen et al., 2016), and 5-min surface observations from the Oklahoma Mesonet (Brock et al., 1995).

2.1 Operational models

2.1.1 RUC analyses and 1-h forecasts

The environmental fields presented throughout Chapters 3 and 4 were primarily derived from the NOAA/NCEP operational Rapid Update Cycle (RUC) data assimilation system and hydrostatic forecast model, which ingests numerous in situ and remotely sensed observations (including radar reflectivity) each hour to provide accurate mesoscale analyses and short-term forecasts over the CONUS (Benjamin et al., 2004a,b, 2010, 2016). The

RUC assimilation system employs a diabatic digital filter initialization technique to reduce the effect of dynamical imbalance that is introduced artificially through the hourly cycling procedure. Most of the environmental analysis presented herein was conducted using a series of 1-h RUC forecasts, as these exhibit greater stability and reduced noise compared to the 0-h analyses (see Fig. 2 of Benjamin et al., 2004b). However, 0-h analyses are displayed for several surface fields to facilitate improved agreement with observations and more accurately depict frontal positions and characteristics.

A summary of the RUC model configuration is contained in Table 2.1. The RUC model has a 13-km horizontal grid spacing and uses a hybrid isentropic-sigma vertical coordinate with 50 levels extending up to ~50 hPa. Convective-scale circulations are not explicitly resolved at this grid scale, and the effects of convection are represented implicitly within the model using the Grell-Devenyi cumulus parameterization (Grell and Devenyi, 2002). An adequate depiction of convective cold pools is therefore highly dependent on the hourly assimilation procedure. For a comprehensive description of the RUC model configuration, we refer the reader to Benjamin et al. (2016).

Table 2.1: *The model configuration and physics parameterizations used in the operational RUC and HRRRx Version 1. The scheme descriptions and references are included in Benjamin et al. (2016).*

Grid Configuration	**RUC**	**HRRRx**
Initial conditions	North American Mesoscale Model (NAM)	Experimental RAP analysis
Lateral boundary conditions	NAM	Experimental RAP forecasts
Horizontal grid spacing	13 km	3 km
Number of grid points	451 × 337	1059 × 1799
Number of vertical levels	50	51
Model top	~50 hPa	10 hPa
Physics parameterizations		
Cumulus	Grell-Devenyi	None
PBL	Burk-Thompson	MYJ
Land surface model	RUC	RUC
Microphysics	Thompson	Thompson
Shortwave radiation	Dudhia	Goddard
Longwave radiation	RRTM	RRTM

2.1.2 Experimental HRRR forecasts

Prior to conducting the ensemble simulations presented in Chapter 5 and owing to limitations of the RUC model (particularly the reliance on parameterized convection and relatively coarse horizontal grid spacing), forecasts from Version 1 of the (then Experimental) WRF-ARW-based High-Resolution Rapid Refresh model (HRRRx; Alexander et al., 2012; Benjamin et al., 2016) were used to examine the character of mesoscale boundaries and disturbances during the outbreak. The HRRRx was run using a convection-permitting horizontal grid spacing of 3 km and a sigma vertical coordinate with 51 levels extending up to 10 hPa (Table 2.1). Initial and boundary conditions were obtained from the Experimental Version 1 of the 13-km Rapid Refresh (RAP) Model (Benjamin et al., 2016), which replaced the operational RUC model in 2012. Similar to the RUC, the RAP model possesses an hourly data assimilation system that ingests a variety of in situ and remotely sensed observations (including radar reflectivity) with the primary objective of providing accurate and frequently updated short-term forecasts. For a comprehensive discussion of the differences between the RUC and RAP models and the HRRR model configuration, the reader is referred to Benjamin et al. (2016).

During April 2011, HRRRx forecasts were initialized hourly in real-time at NOAA's Earth System Research Laboratory (ESRL), and each individual forecast was run for 15 hours (Alexander et al., 2012). The deterministic HRRRx forecasts demonstrated skill in depicting convection during the outbreak discussed herein, with relative peaks in forecast skill during the early morning of the 27th (corresponding to QLCS1) and during the latter portion of the supercell outbreak (Alexander et al., 2012). However, none of the individual forecasts were able to capture the entirety of the outbreak, requiring that multiple forecast runs be used in order to analyze different portions of the event. Unfortunately, this limitation precluded us from fully understanding how disturbances generated upstream during the early morning of 27 April affected conditions over the Southeast during the supercell outbreak. In Chapter 6, we present cursory analyses that were conducted using the 0000 UTC 27 April

2011 initialization of the HRRRx, which provided forecasts through 1500 UTC 27 April (27/1500Z; dates and times are hereafter presented in DD/HHMMZ format).

2.1.3 HYSPLIT trajectories

With hourly data from the RUC analyses, trajectories were computed using the NOAA Air Resources Laboratory's Hybrid Single-Particle Lagrangian Integrated Trajectory (HYSPLIT) model (Stein et al., 2015) to depict the 3D flow evolution and how it influenced the thermodynamic environment over the Southeast during the afternoon supercell outbreak. For four locations over the Southeast (Monroe, LA, Jackson, MS, Meridian, MS, and Montgomery, AL), ensembles comprising 27 trajectory "members" were initialized from several different heights (defined AGL) at 27/1900Z and integrated backward in time for 24 h. For each individual trajectory, several quantities were output at each hour of the model integration, including the 3D position (latitude, longitude, height AGL), pressure, potential temperature, relative humidity, specific humidity, and water vapor mixing ratio. From these fields, we derived additional quantities, such as virtual potential temperature and equivalent potential temperature, along each trajectory. The results from this analysis are presented in Chapter 3.

2.2 Observations

2.2.1 NOAA Profiler Network 404-MHz wind profilers

Hourly-averaged wind observations from the NOAA Profiler Network of wind profiling Doppler radars (e.g., Ralph et al., 1995) were obtained from the NOAA/NCEP Meteorological Assimilation Data Ingest System (MADIS) in order to produce time-height diagrams of horizontal wind speed and derived geostrophic CAA for four locations (Ledbetter, TX, Winnfield, LA, Okolona, MS, and Wolcott, IN), which are presented in Chapters 3 and 4. These wind profilers operate at a frequency of 404.4 MHz and sample radial velocity measurements along three individual beams (Fig. 13; Ralph et al., 1995). The use of two different sampling modes enables wind measurements to be obtained throughout the depth of the troposphere. Specifically, the "low" mode provides radial velocity measurements between 0.5–9.25 km AGL along each of the three beams, and the "high" mode provides radial velocity measurements between 7.5–16.25 km AGL. Two independent observations are obtained within the 7.5–9.25-km AGL layer due to overlap between the low and high modes. From the radial velocity measurements, the horizontal wind components are derived trigonometrically by assuming that the wind field is horizontally homogeneous across the area swept out by three beams. The MADIS files contained the derived 3D wind components at 250-m intervals between 0.5–16.25 km AGL, with two independent observations corresponding to the low and high sampling modes included in the 7.5–9.25 km AGL layer. The wind observations presented at the "valid time" represent temporal averages that were computed over the preceding hour—i.e., the winds shown at 0700 UTC represent averaged sub-hourly observations obtained between 0600–0700 UTC.

The profiler observations were first quality controlled (QC) using MADIS spatial and temporal consistency checks. Following the method described in Trexler and Koch (2000), observations were also removed if they corresponded to low power ($<$ 29 dB) or were collocated with vertical motions exceeding ± 4 m s^{-1}. The low and high mode observations were subsequently blended within the overlap layer using a simple linear weighting scheme where data from both modes existed (see Table 2.2); otherwise, the non-missing observation from either mode was included. Another QC procedure was then used to remove any erroneous observations that differed appreciably from surrounding observations in both space and time. Moreover, highly isolated clusters of wind observations were manually removed from the Okolona (located above 7 km AGL at 27/2000Z) and Winnfield (located above 7 km AGL at 27/2200Z–27/2300Z) sites as they would introduce spurious gradients and undesired complexity to the objectively analyzed fields. We then applied a linear interpolation procedure to replace (in height) up to three adjacent missing observations and

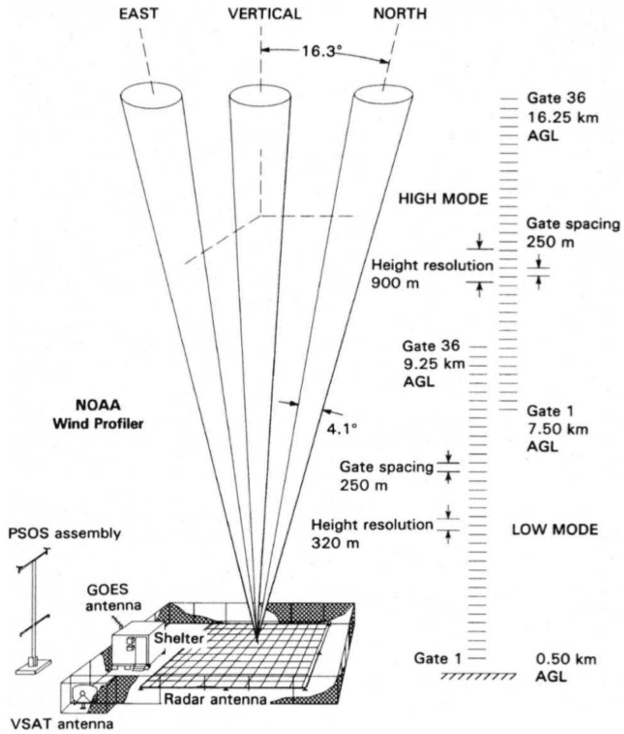

Figure 13: *Depiction of the 404-MHz NOAA wind profler beam configuration and range gate spacing for both low and high sampling modes. From Fig. 2 in Ralph et al. (1995).*

then (in time) one missing observation on either side of a non-missing observation in order to mitigate the effects of small data gaps following the QC procedures. Finally, a two-pass Barnes objective analysis procedure (e.g., Koch et al., 1983; Carr et al., 1995) was employed to produce time-height diagrams of horizontal wind speed for each site. A convergence parameter of $\gamma = 0.4$ was used for the second pass.

In addition to the horizontal wind observations ($\vec{v_r} = u_r\hat{\imath} + v_r\hat{\imath}$), the geostrophic component of the thermal advection profile was retrieved under the assumption of thermal wind balance following the procedure presented in Koch (2001). For each hour and profiler site, the pressure field required to complete this retrieval was obtained from the RUC analyses by interpolating the geopotential height field to isobaric levels for the height values that corresponded to each observation height above MSL. The obtained pressure field was then

Table 2.2: *NOAA wind profiler low and high mode blending weights.*

Height AGL	Low Mode Weight	High Mode Weight
7.25	1.0	0.0
7.5	0.875	0.125
7.75	0.75	0.25
8.0	0.625	0.375
8.25	0.5	0.5
8.5	0.5	0.5
8.75	0.375	0.625
9.0	0.25	0.75
9.25	0.125	0.875
9.5	0.0	1.0

objectively analyzed in the same manner as the observed winds in order to retrieve the horizontal thermal gradient $\nabla_r T$ from the objectively analyzed wind field. Finally, the thermal advection profiles were obtained via the following relation:

$$-\vec{v_r} \cdot \nabla_r T \;=\; -u_r \left(\frac{\partial T}{\partial x}\right)_r - v_r \left(\frac{\partial T}{\partial y}\right)_r . \tag{2.1}$$

Regions where derived CAA overlapped with significant backing of the observed winds (change in wind direction of $\geq 10°$ over the backing layer; regions were evaluated manually using the linearly interpolated wind field) are also displayed on the time-height diagrams.

2.2.2 USArray Transportable Array

The USArray Transportable Array, which is a deployable network of stations that are primarily intended to obtain seismic observations (e.g., Tytell et al., 2016), was set up throughout the Great Plains and much of the Southeast during April 2011 (Fig. 14). The network contains approximately 400 observing stations that have an average spacing of 70 km and each contain barometric pressure sensors that provide surface pressure observations sampled at a frequency of 1 Hz. Thus, this mesoscale network of high-resolution pressure observations provides a unique dataset that can be used in tandem with other observations (e.g., 1-min ASOS data) to understand the character of mesoscale disturbances that moved through the outbreak region. Pressure traces from several USArray sites are presented in Chapter 6 and were low-pass filtered with a cutoff period of 1 minute to remove small-scale turbulent fluctuations.

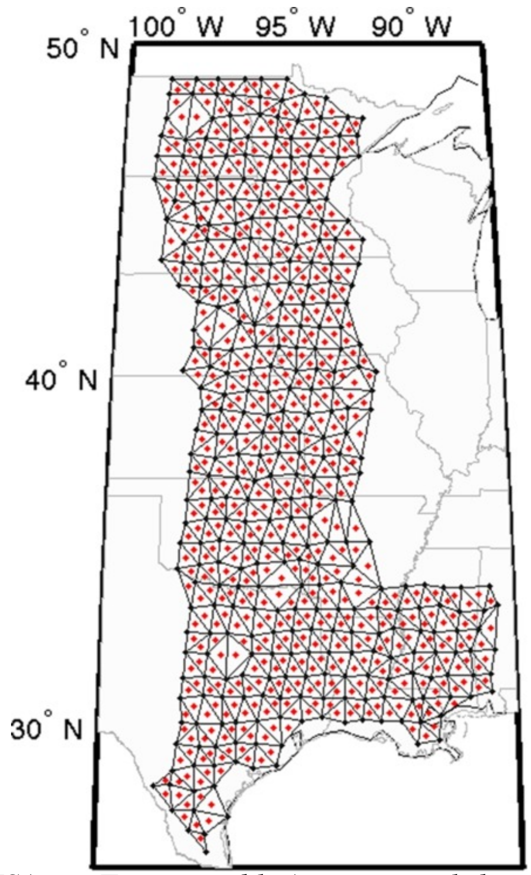

Figure 14: *Map of the USArray Transportable Array network during the outbreak described herein, as presented in de Groot-Hedlin et al. (2014). The gray dots at the vertices of each triangle represent the individual observing stations.*

Chapter 3

Outbreak chronology and environmental evolution

3.1 Introduction

In this chapter, we use observations and a series of RUC analyses and 1-h forecasts to provide a chronological description of this prolific tornado outbreak. We first describe how the synoptic environment evolved throughout this multiday outbreak, which spanned from 25–28 April 2011 in its entirety. We then focus our attention on the three tornadic episodes of interest, beginning with the formation of QLCS1 during the evening of 26 April and extending through the supercell outbreak that commenced over the Southeast on the afternoon of 27 April. Particular attention is given to how these three convective systems developed and evolved within a rapidly changing environment. The contents of this chapter were recently published as Part I of a two-part paper in *Monthly Weather Review* (Chasteen and Koch, 2021a).

3.2 Synopsis of the 25–28 April 2011 extended outbreak

The extended outbreak spanning 25–28 April occurred ahead of a slowly moving, negatively tilted longwave trough that amplified with time over the Rocky Mountains (Fig. 15). During this period, an extensive and anomalously strong upper-level jet streak (hereafter "J_1") with maximum wind speeds ≥ 160 kt slowly progressed equatorward within a region of sustained confluence on the upstream flank of the amplifying trough. J_1 was accompanied by strong baroclinity and was the manifestation of a polar-front and subtropical jet superposition (Christenson and Martin, 2012; Christenson et al., 2017) that resulted from a multiday anticyclonic Rossby wave breaking event over the Pacific Ocean (e.g., Thorncroft et al., 1993; Homeyer and Bowman, 2013). This prolonged wave breaking episode yielded a highly complex tropopause structure (as indicated in Fig. 15 by potential temperature variations on the dynamic tropopause[1], θ_{DT}) and a nonuniform along-jet θ_{DT} gradient (or, analogously, upper-level PV gradient) that supported several shortwave disturbances that were embedded within the broader upper-level jet. The baroclinity accompanying these shortwaves was primarily confined to the middle and upper troposphere—even prior to any modifications that arose during their progression over complex terrain—such that they lacked particularly distinct surface fronts.

The highly amplified nature of the synoptic pattern enabled the upper-level trough base and jet exit region to persist over the south-central United States for multiple consecutive days (Fig. 15). This flow configuration was conducive to development of a lee trough and dryline over the SGP (e.g., Schultz et al., 2007) and the continued replenishment of potential instability through differential advection of low-level warm, moist air originating over the Gulf of Mexico and Caribbean Sea (Molina and Allen, 2019) and an overlying EML plume that was transported off the elevated terrain in the southwestern U.S. and northern Mexico following prolonged subsidence and strong sensible heating (e.g., Carlson et al., 1983). A sequence of upper-level disturbances crossed the Rocky Mountains and supported episodic CI throughout this multiday period, including three predominant shortwave troughs (labeled "SW_1", "SW_2", and "SW_3" in Fig. 15). The first shortwave, SW_1, moved into the SGP on 25 April (Figs. 15a,b) and promoted surface cyclogenesis (hereafter "L_1") along a quasi-stationary front (Figs. 17a,b) and the development of an expansive "antecedent QLCS"—the remnants of which can be seen in Fig. 16a. SW_1 amplified considerably over time, leading to the formation of a "PV hook" structure (e.g., Dickinson et al., 1997; Posselt and Martin, 2004; Novak et al., 2010) over the Upper Midwest by 26/1200Z (Fig. 15c) and the eastward expansion of the longwave trough—an evolution characteristic of cyclonic Rossby wave breaking (Thorncroft et al., 1993). This evolution was accompanied by upper-level ridge amplification over the eastern U.S. and the sustained development (and

[1]The DT is the highest level of the 2-PVU isosurface, where 1 PVU = 10^{-6} K kg^{-1} m^2 s^{-1}. Negative θ_{DT} anomalies are dynamically equivalent to positive isentropic PV anomalies at tropopause level, and vice versa (e.g., Morgan and Nielsen-Gammon, 1998).

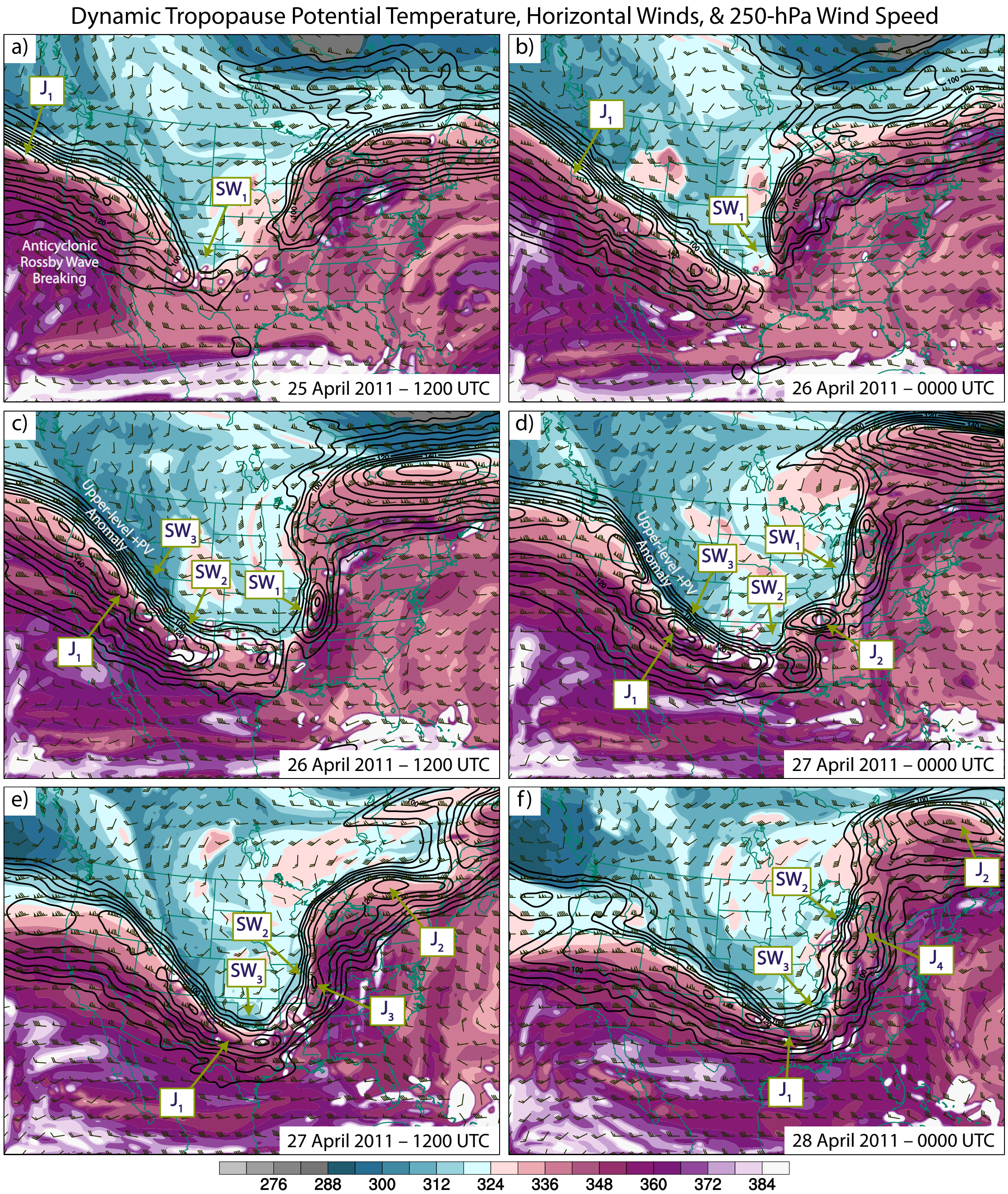

Figure 15: *Potential temperature on the dynamic tropopause (shaded; K), horizontal winds on the dynamic tropopause (barbs; kt), and 250-hPa wind speed (black contours; every 10 kt ≥ 70 kt) from the corresponding RUC 1-h forecast valid at (a) 1200 UTC 25 April, (b) 0000 UTC 26 April, (c) 1200 UTC 26 April, (d) 0000 UTC 27 April, (e) 1200 UTC 27 April, and (f) 0000 UTC 28 April 2011.*

eventual occlusion) of "L_1", which supported a marked poleward expansion of the warm sector and the southward movement of polar air into the SGP by 26/1200Z (Fig. 17c). Note that the antecedent QLCS produced a widespread region of surface outflow that influenced thermodynamic conditions across the warm sector on 26 April (Figs. 17c,d).

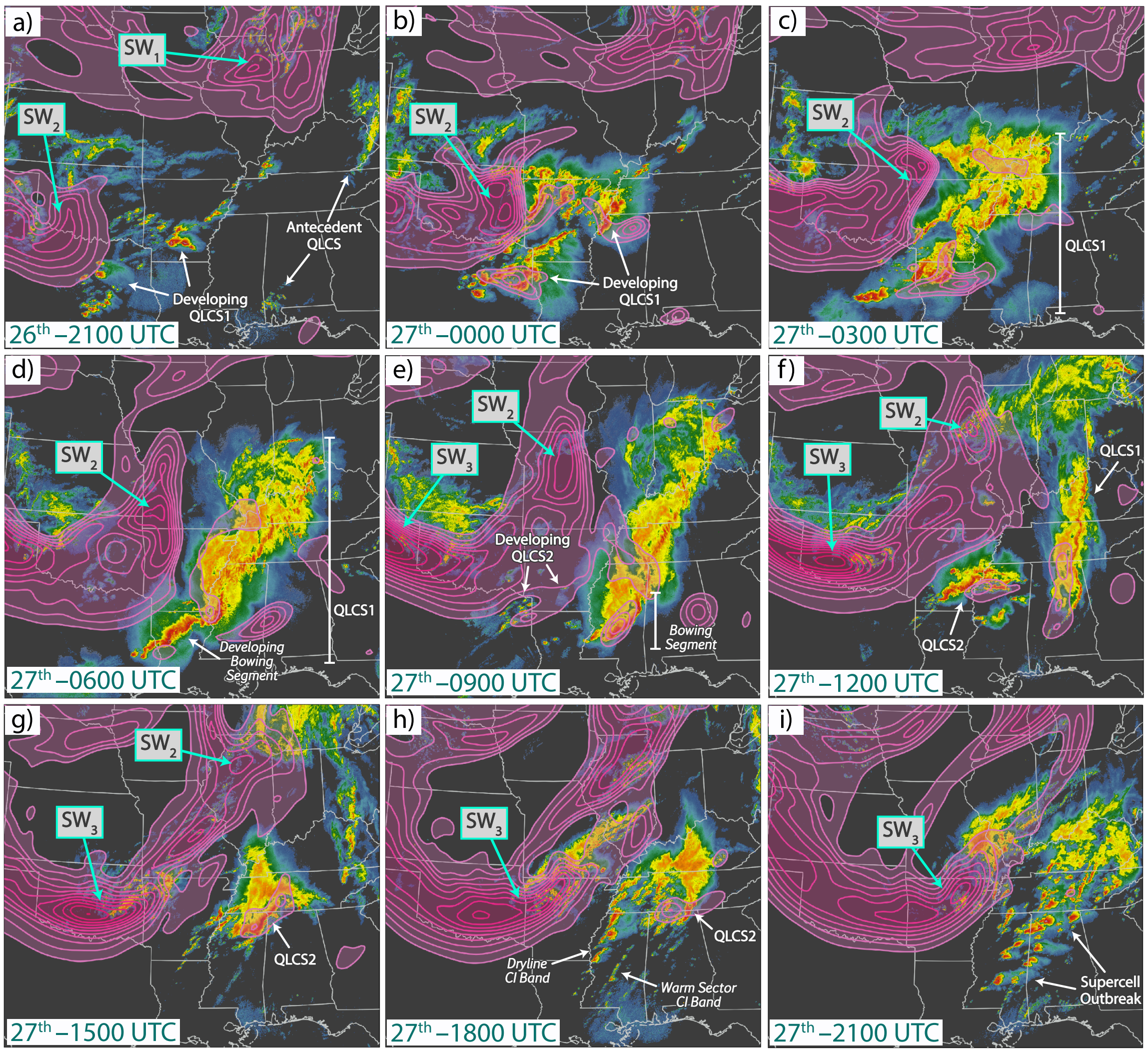

Figure 16: *NEXRAD composite radar reflectivity overlaid with PV averaged in the 400–300-hPa layer (pink contours; every 0.5 PVU ≥ 1 PVU) from the corresponding RUC 1-h forecast valid at (a) 2100 UTC 26 April, (b) 0000 UTC 27 April, (c) 0300 UTC 27 April, (d) 0600 UTC 27 April, (e) 0900 UTC 27 April, (f) 1200 UTC 27 April, (g) 1500 UTC 27 April, (h) 1800 UTC 27 April, and (i) 2100 UTC 27 April 2011.*

The second shortwave, SW_2, moved into the lee of the Rockies during the afternoon on 26 April (Figs. 15c,d). Ahead of this disturbance (and the negative θ_{DT} anomaly accompanying

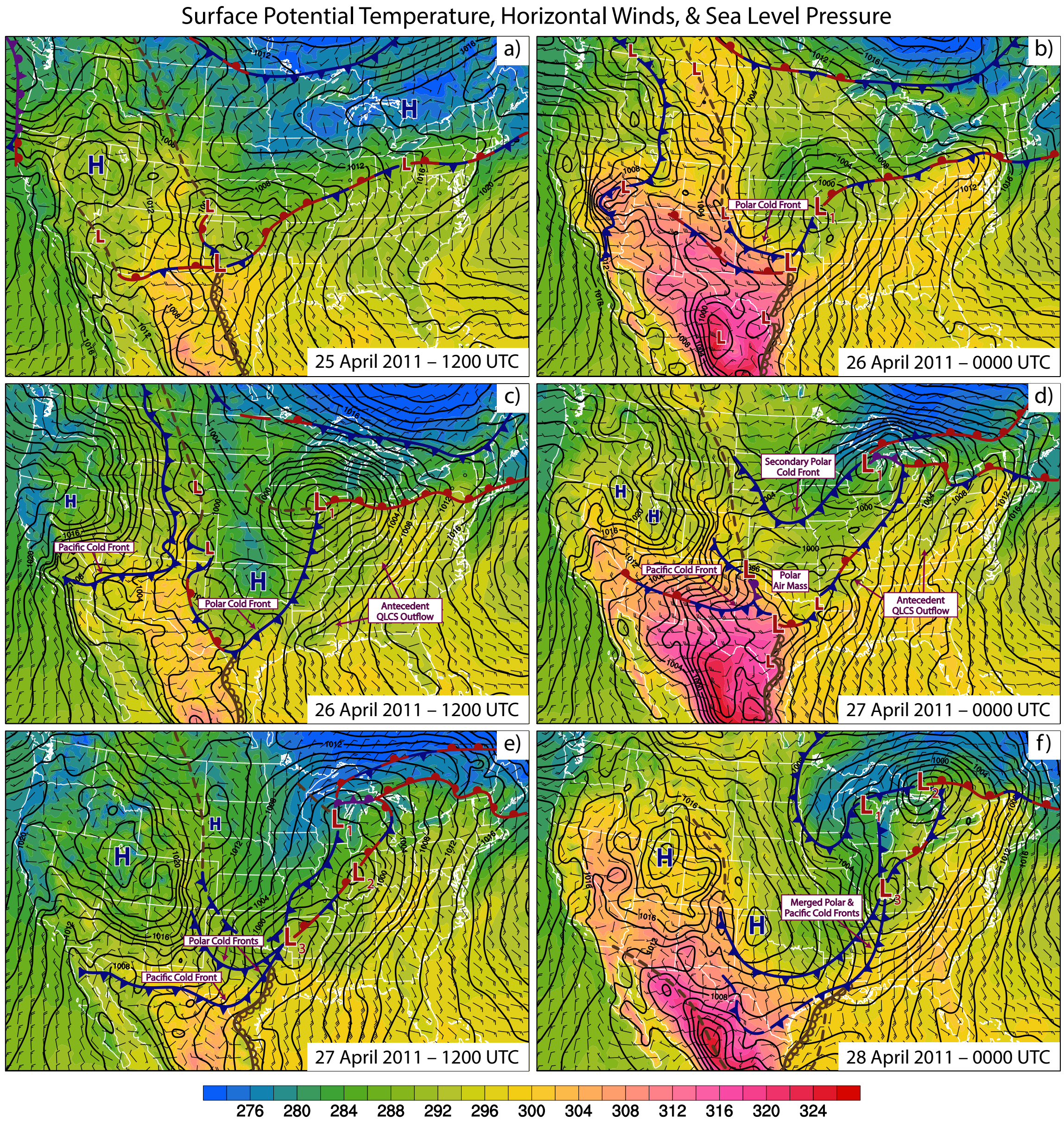

Figure 17: *Surface potential temperature (shaded; K), horizontal winds (barbs; kt), and sea level pressure (black contours; hPa) from the RUC analysis valid at (a) 1200 UTC 25 April, (b) 0000 UTC 26 April, (c) 1200 UTC 26 April, (d) 0000 UTC 27 April, (e) 1200 UTC 27 April, and (f) 0000 UTC 28 April 2011. All synoptic fronts are denoted using conventional notation. Predominant (mesoscale) lows and highs are shown with large (small) "L" and "H", respectively.*

SW_3 that remained upstream), lee troughing and cyclogenesis were restored over the SGP, which led to the reestablishment of low-level southerly flow, northward retreat of the polar air mass that previously advanced into southern Texas, and replenishment of warm, moist air at low levels over the region (Fig. 17d). By 27/0000Z, convection associated with QLCS1 had developed over the south-central U.S. ahead of SW_2 (Fig. 16b) and immediately south of the negative θ_{DT} anomaly that extended over the Midwest with SW_1 (Fig. 15d). This convection quickly grew upscale as it progressed northeastward overnight in tandem with SW_2 (Figs. 16c-f). Concurrent with this evolution, the upper-level ridge appreciably strengthened over the Midwest, which effectively shifted the longwave trough back toward the west and reduced the wavelength of the large-scale flow pattern by 27/1200Z, while two prominent jet streaks (labeled "J_2" and "J_3" in Fig. 15e) had developed downstream from the upper-level trough. At the surface, cyclogenesis had commenced along the quasi-stationary front ahead of SW_2 by 27/1200Z, yielding a subsynoptic-scale low over the Midwest (denoted "L_2" in Figs. 17e,f) and further poleward expansion of the warm sector.

Finally, the primary shortwave, SW_3, which was attended by a deep tropopause fold and supported the development of both QLCS2 and the afternoon supercell outbreak (Figs. 16e-l), had moved into the longwave trough base over the SGP by 27/1200Z (Fig. 15e). This evolution was accompanied by the cessation of upper-level support for pressure falls in the lee of the Rockies, the resultant breakdown of the lee trough over New Mexico and Texas, the unhindered progression of a Pacific cold front into the SGP, and the gradual baroclinic redevelopment of the former lee cyclone into the primary low (hereafter "L_3") as it moved eastward ahead of SW_3 (Figs. 17d,e). Consequently, the polar air that had been restrained over Oklahoma and North Texas was permitted to advance southward behind L_3, yielding a broad region of CAA by 27/1200Z.

By 28/0000Z, the supercell outbreak had been ongoing over the Southeast for ~6 h, and a highly compact negative θ_{DT} anomaly associated with SW_3 had moved into the Lower Mississippi Valley (Fig. 15f). Furthermore, the J_1 exit region extended through the upper-level trough base into eastern Mississippi, while another pronounced jet streak that developed in conjunction with QLCS2 (hereafter "J_4") was situated downstream over the Great Lakes. At the surface, a synoptic-scale region of low pressure was centered over the Midwest beneath the inflection axis of the upper-level trough-ridge pattern, while three embedded subsynoptic-scale perturbations characterized the individual lows (Fig. 17f). By this time, L_3 had moved into southwestern Indiana ahead of SW_3, and a cold front—which demarcated the leading edge of the polar air mass following its merger with the Pacific cold front—extended into southern Louisiana. A dryline that represented the surface position of the diurnally modified Pacific cold front was located off the Texas Gulf Coast farther toward the southwest.

We note the absence of a prominent cold surge east of the Rockies during this multiday period, which would have cut off the warm sector and thus prematurely terminated the outbreak (e.g., Colle and Mass, 1995; Hamill et al., 2005). Largely contributing to its absence was the longevity of the lee trough—shown to span from the SGP into southern Alberta in Fig. 17—that extended as far north as Alaska due to sustained forcing for ascent, cross-barrier flow, and surface pressure falls ahead of the elongated upper-level positive PV anomaly associated with SW_3. This PV anomaly and the resultant lee trough induced a persistent southerly flow component over much of central Canada. As a consequence of this evolution and the warm sector expansion that occurred with the northeastward progression of SW_1 and SW_2, the coldest air over North America remained primarily over eastern Canada—well displaced from the area of tornadic convection—until very late in the outbreak. The absence of a strong cold front was also emphasized by Hamill et al. (2005) as an enabling factor in the longevity of the May 2003 extended tornado outbreak.

3.3 Outbreak chronology

3.3.1 QLCS1

We henceforth focus specifically on the three tornadic episodes that impacted the Southeast on 27 April. The first system—QLCS1—originated from widespread convection that developed in the Ark-La-Tex region during the evening of 26 April (Figs. 16a,b). This convection exhibited a highly complex organization and quickly grew upscale into an expansive QLCS by 27/0300Z (Figs. 16c-f). The NOAA/NWS Storm Prediction Center (SPC) issued a High Risk for this system (SPC Convective Outlook valid from 26/1630Z–27/1200Z is shown in Fig. 18) that paralleled an "effective warm front" (demarcating the northern periphery of the warm sector that recovered behind the antecedent QLCS; Fig. 19a)[2], anticipating a significant threat for severe weather—including large hail, strong tornadoes, and damaging winds—that persisted into the nighttime. Ultimately, QLCS1 produced at least 118 confirmed tornadoes: 5 were rated EF3, 26 had path lengths > 20 km, and 8 had widths > 1 km. However, most of these tornadoes occurred outside of SPC's Moderate and High Risk areas following the upscale growth of convection that initially

[2]This boundary is shown with double ticks to signify the importance of convection on its identity. We use this notation throughout the paper.

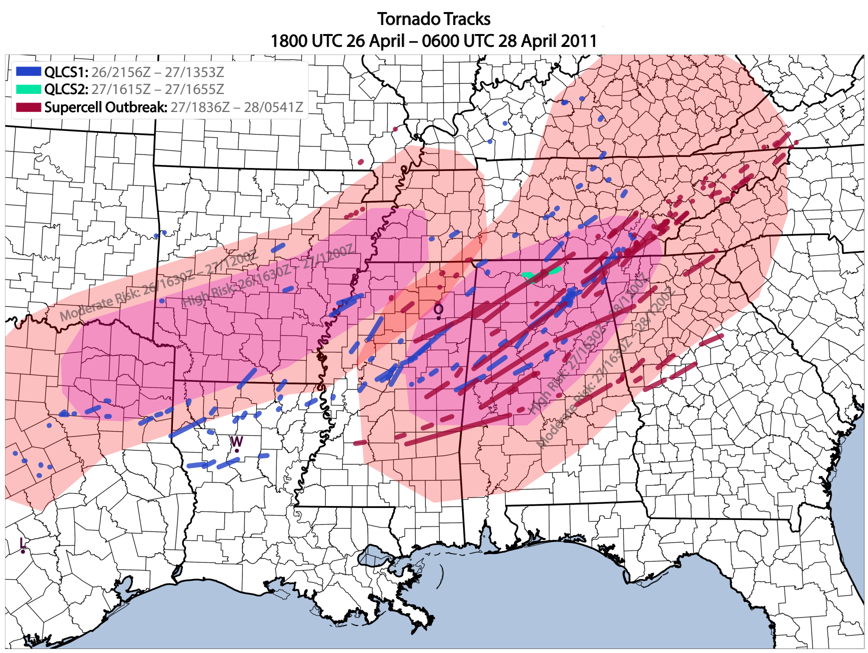

Figure 18: *Tracks of tornadoes that occurred between 1800 UTC 26 April and 0600 UTC 28 April 2011 in association with QLCS1 (blue lines), QLCS2 (green lines), and the afternoon supercell outbreak (maroon lines). The Day 1 SPC Categorical Convective Outlook (red) Moderate and (pink) High Risk areas issued at 1630 UTC on 26 April (centered over Arkansas) and 27 April 2011 (centered over Alabama) are both shown. Each outlook is valid from the time of issuance until 1200 UTC on the following day. The Ledbetter, TX, Winnfield, LA, and Okolona, MS, wind profiler sites are denoted with an "L", "W", and "O", respectively.*

formed over eastern Texas. Such strong, long-track, and wide tornadoes are rarely spawned by QLCSs (e.g., Trapp et al., 2005; Grams et al., 2012; Smith et al., 2012), making the severity of this system highly anomalous—a point emphasized by Knupp et al. (2014). Thus, the factors contributing to the evolution and exceptional severity of this primarily nocturnal system are of particular interest.

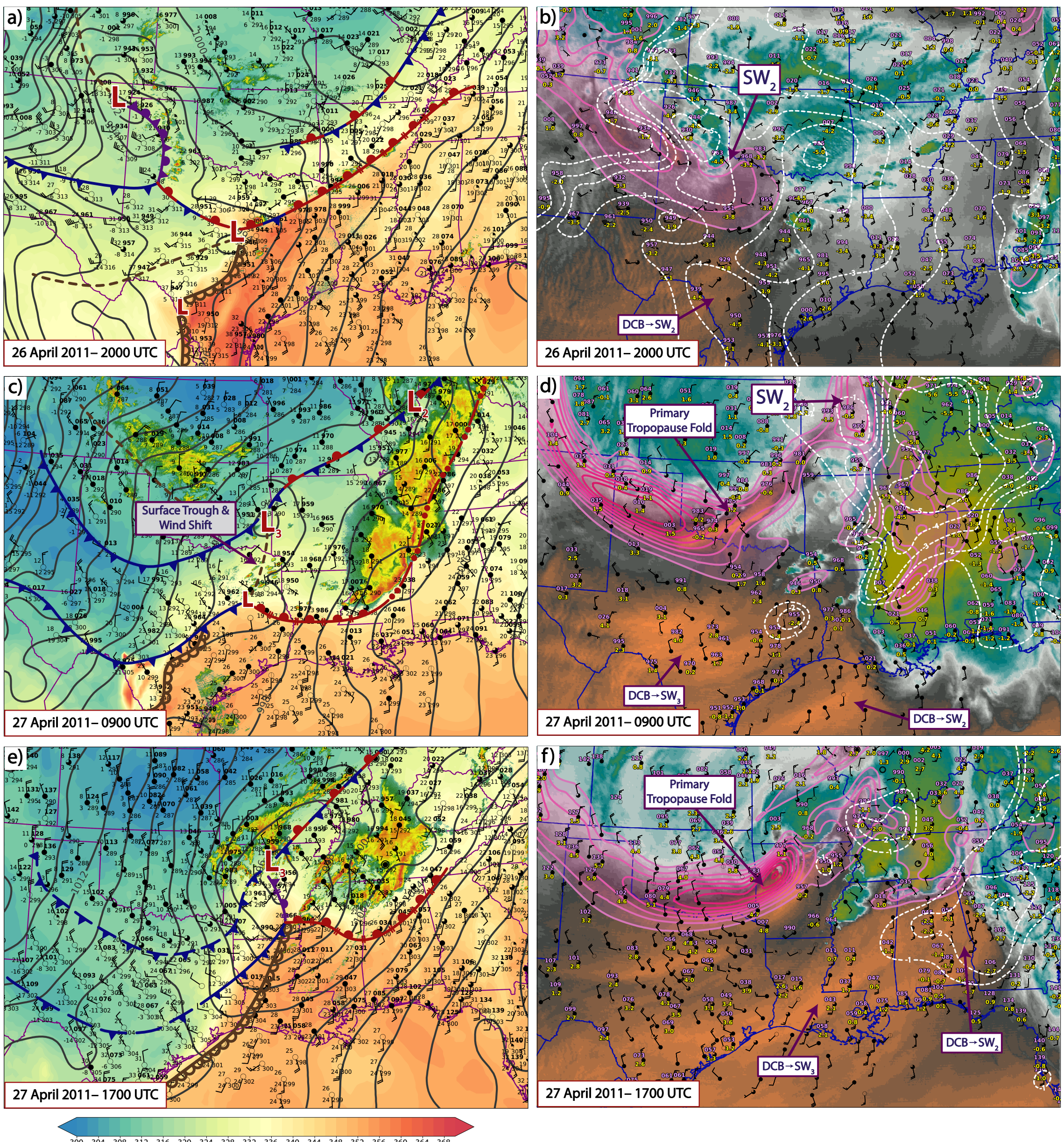

Figure 19: *On the left, composite radar reflectivity > 20 dBZ and surface observations (top left: temperature in °C; bottom left: dewpoint temperature in °C; top right: SLP to tenths of hPa with leading digit(s) omitted; bottom right: potential temperature in K; barbs: 10-m winds in kt) overlaid with surface equivalent potential temperature (shaded; K) and SLP (contours; hPa) from the RUC analyses valid at (a) 2000 UTC 26 April, (c) 0900 UTC 27 April, and (e) 1700 UTC 27 April 2011. Surface fronts and outflow boundaries are denoted using conventional notation, with double ticks to indicate effective warm fronts that are directly influenced by the presence of convection. On the right, GOES-13 water vapor imagery (shaded; warmer colors represent higher brightness temperatures), PV averaged over the 450-350 hPa layer from the corresponding RUC 1-h forecasts (pink contours; every 0.5 PVU ≥ 1 PVU), surface observations (top left: SLP, bottom left: 3-h SLP change in hPa), and manually analyzed isallobars (dashed contours every -1 hPa (3 h)$^{-1}$) valid at (b) 2000 UTC 26 April, (d) 0900 UTC 27 April, and (f) 1700 UTC 27 April 2011.*

3.3.1.1 Pre-convective environment and convection initiation

CI occurred at ~26/2000Z following the movement of SW_2 into the SGP. Pressure falls concentrated beneath the diffluent J_1 exit region and ahead of SW_2 (Figs. 20a, 21a) supported a deepening surface low along the quasi-stationary front in north-central Texas (Figs. 19a,d) and associated strengthening of low-level southerly flow and poleward moisture transport over the warm sector (Fig. 22a). A dryline extended southward from this low, east of which surface dewpoint temperatures of 21–22 °C (70–72 °F) were combined with PBL warming and steep midlevel lapse rates (Figs. 23a,b) to yield mixed-layer CAPE (MLCAPE) > 5000 J kg^{-1} during the afternoon (Fig. 24a). A corridor of MLCAPE > 2000 J kg^{-1} extended northeastward along the effective warm front and into central Arkansas (i.e., between the effective warm front and quasi-stationary front), where mixed-layer CIN was greater owing to cooler, drier near-surface air.

Farther to the northwest, pressure falls > 4 hPa (3 h)$^{-1}$ attending lee cyclogenesis were occurring over New Mexico and the Texas Panhandle (Figs. 19a,b), below the left exit region of J_1 (Figs. 20a, 21a) and downstream from the prominent upper-level PV maxima accompanying SW_3 (Figs. 15c,d). Owing to the lee cyclone and circulations accompanying J_1 and SW_2, strong midlevel subsidence (as inferred from GOES-13 water vapor satellite imagery; i.e., the descending DCB associated with SW_2) and downslope flow

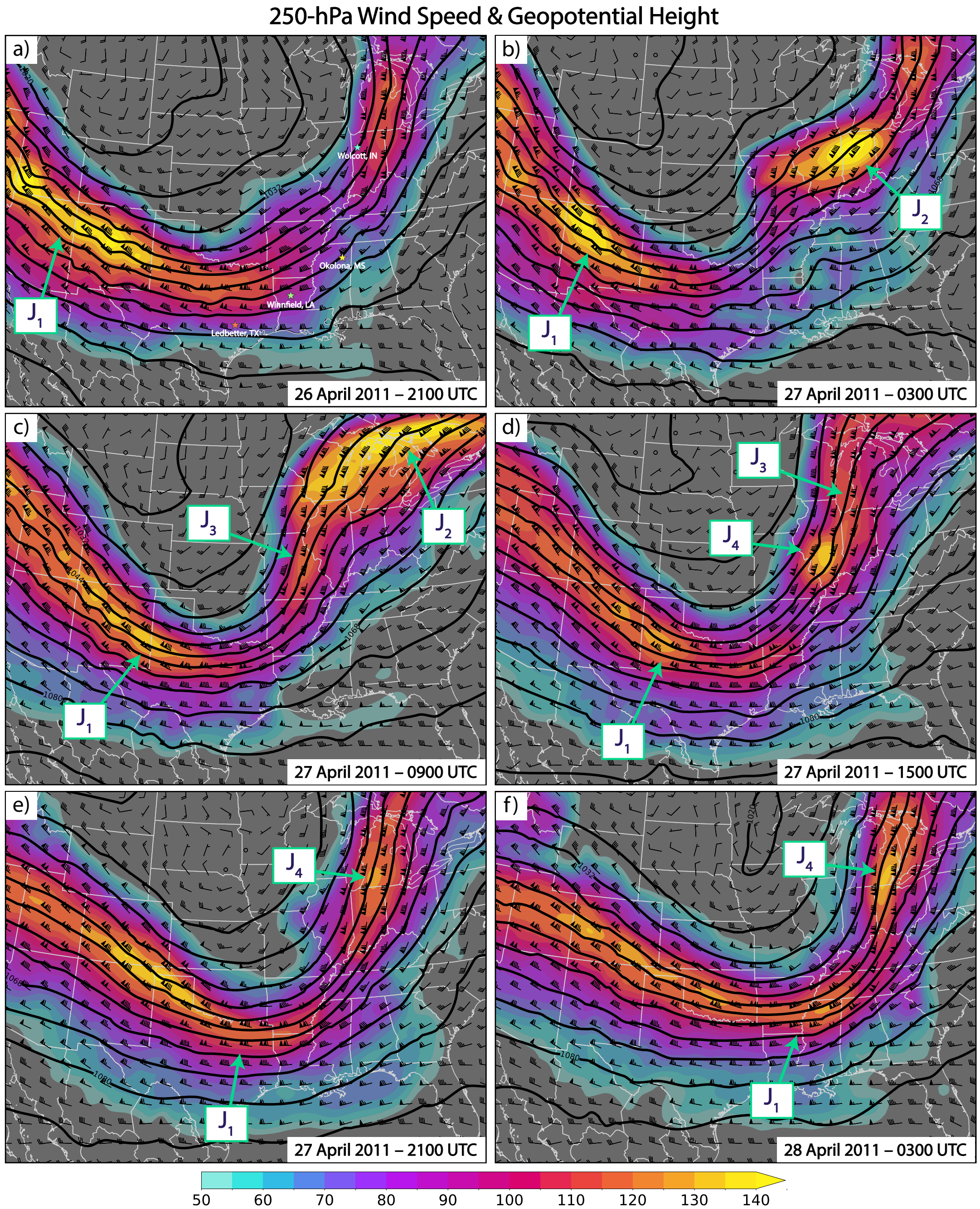

Figure 20: *250-hPa wind speed (shaded; kt), geopotential height (contours; dam), and horizontal winds (barbs; kt) from the corresponding RUC 1-h forecast valid at (a) 2100 UTC 26 April, (b) 0300 UTC 27 April, (c) 0900 UTC 27 April, (d) 1500 UTC 27 April, (e) 2100 UTC 27 April, and (f) 0300 UTC 28 April 2011. The wind profiler locations are displayed in (a).*

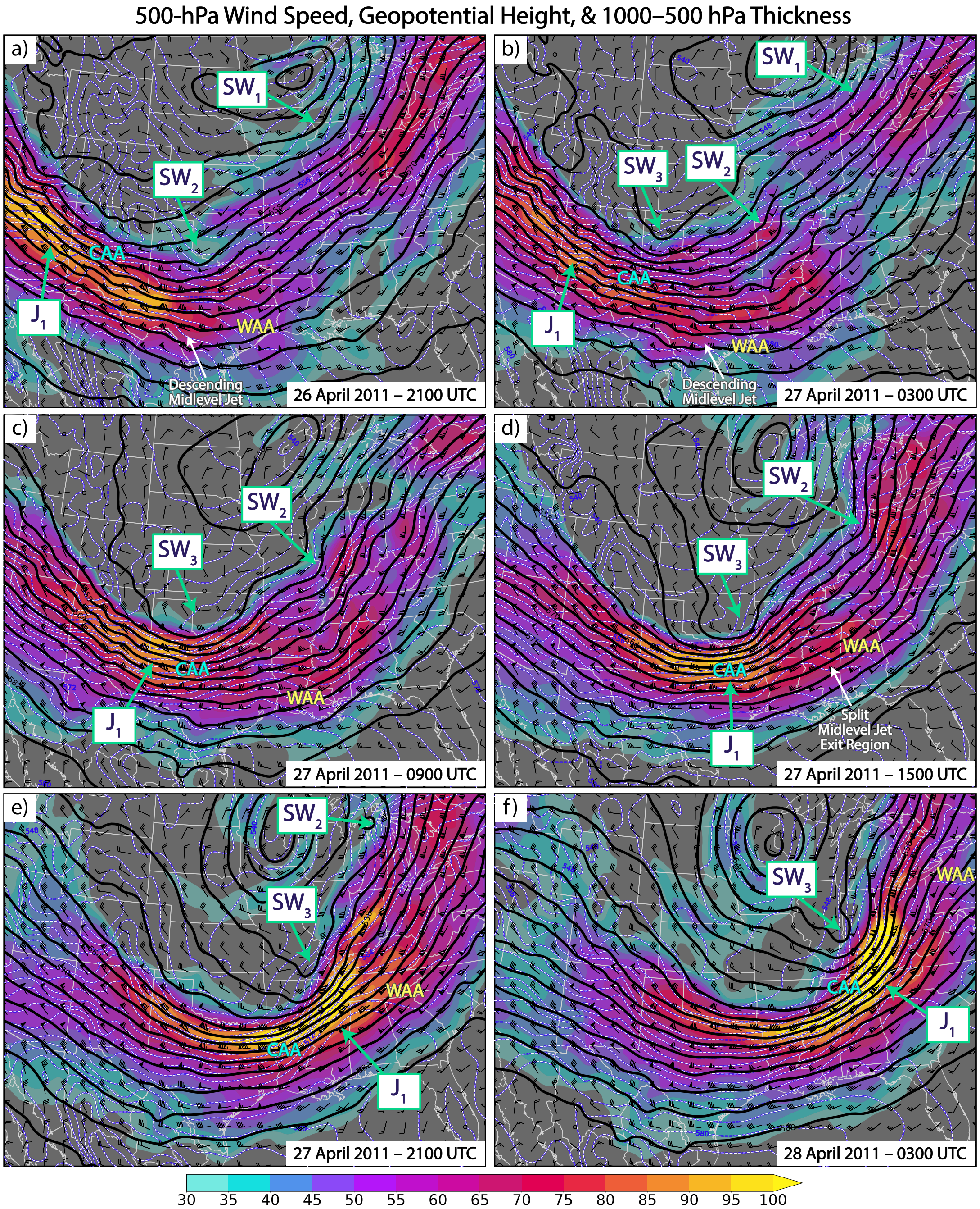

Figure 21: *As in Fig. 20, but for 500 hPa. 1000–500-hPa thickness (dashed contours; dam) is also shown. Prominent regions of geostrophic CAA and WAA are indicated.*

were occurring over the High Plains (Figs. 19a,b). Deep PBL mixing (up to ~600 hPa) was prevalent throughout this region, yielding the downward transport of strong momentum associated with the descending midlevel jet (Fig. 21a) and gusty surface winds (e.g., Danielsen, 1974; McCarthy and Koch, 1982). The first convective cells appeared ahead of the dryline in Texas and along the effective warm front in Arkansas as the descending

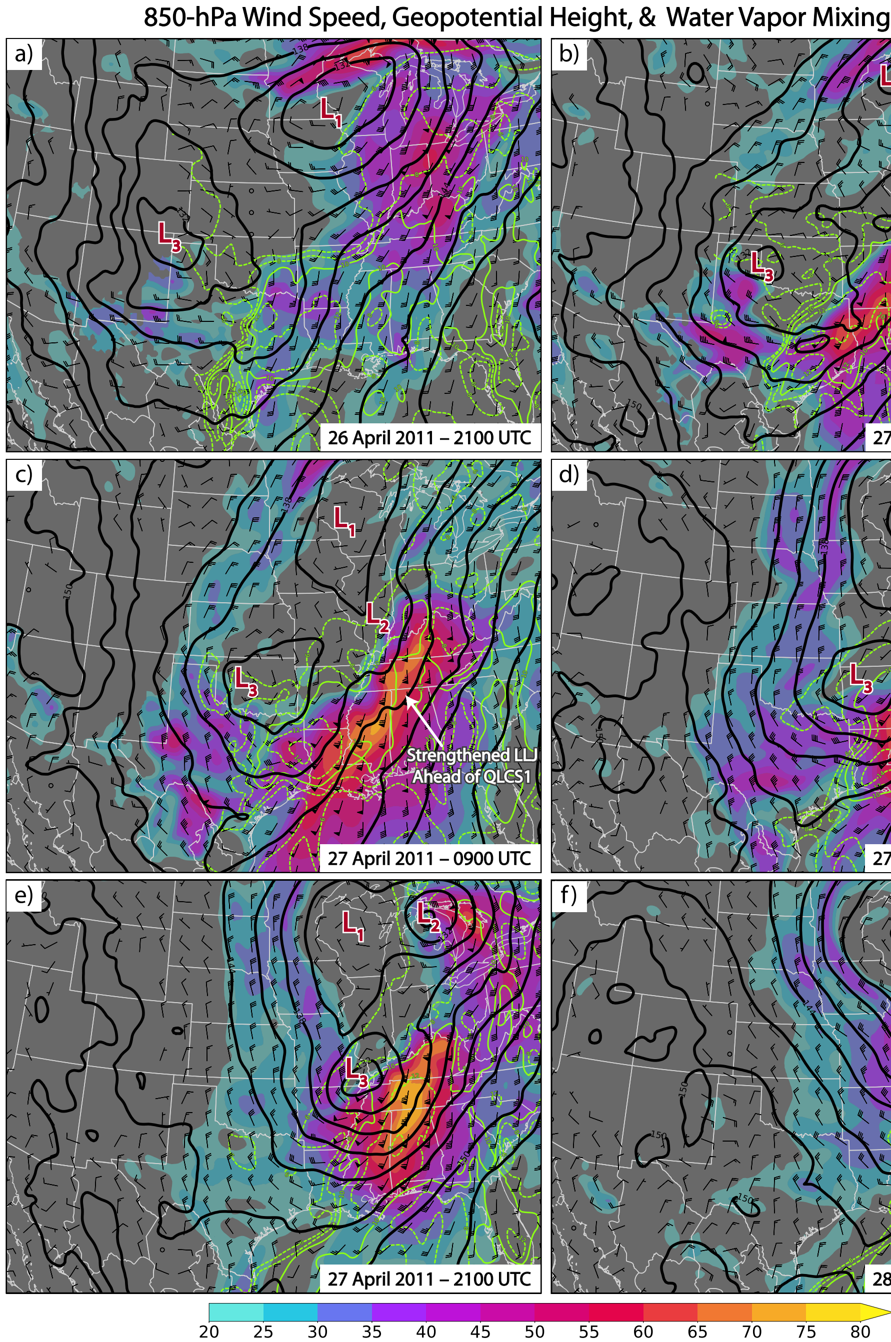

Figure 22: *As in Fig. 20, but for 850 hPa. 850-hPa mixing ratio (green contours; dashed every 2 g kg^{-1} $\geq$ 6 g kg^{-1} and solid for 10 g kg^{-1}) is also shown. Wind and mixing ratio fields are not shown where the 850-hPa surface lies below ground.*

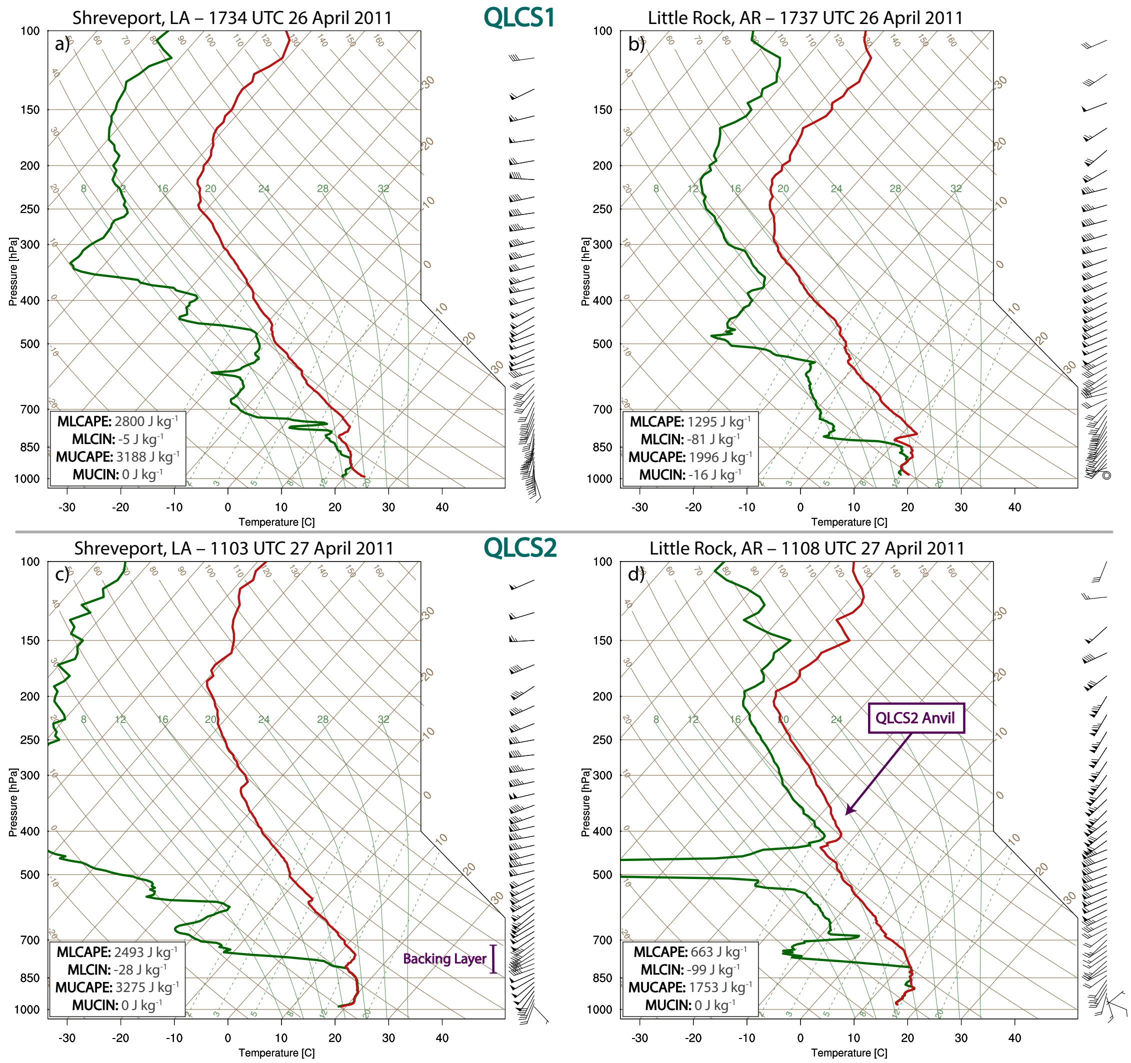

Figure 23: *Observed soundings released within the QLCS1 environment from (a) Shreveport, LA, and (b) Little Rock, AR, and the QLCS2 environment from (c) Shreveport, LA, and (d) Little Rock, AR. The sounding release times are shown in each panel. Sounding parameters were calculated using the SHARPpy program (Blumberg et al., 2017). The sounding locations are shown in Fig. 24.*

midlevel jet, DCB, and underlying deep EML plume crossed the dryline (Figs. 19a,b and 25a).

3.3.1.2 Environmental and convective evolution

The early convective evolution varied spatially due to differences in the mesoscale forcing and—in the presence of large-scale diffluence—heterogeneity in the vertical shear profiles.

Near the midlevel jet exit region and ahead of the dryline over Texas, deep-layer shear (calculated as the 0–6-km bulk wind difference) was approximately westerly (i.e., roughly orthogonal to the initiating boundary) and ranged from 60–70 kt at 26/2100Z (Figs. 24a, 25a). Consistent with the expected behavior in such a shear profile (e.g., Bluestein and Weisman, 2000; Dial et al., 2010) and in the presence of a progressive shortwave trough, the initial cells quickly moved eastward off the dryline, facilitating subsequent CI due to sustained low-level convergence. This evolution, coupled with storm splitting, led to the development of two supercell clusters (Figs. 16a,b) that collectively produced several tornadoes over eastern Texas (Fig. 18), with a peak in reports occurring between 27/0000Z–27/0100Z. The Ledbetter wind profiler (Fig. 25a) was located ~50–150 km south of these supercells and observed that the 0–1-km BWD increased from 13 kt to 27 kt between 26/2100Z–27/0000Z, which likely supported this uptick in tornadoes (e.g., Thompson et al., 2003, 2012). This temporal increase in low-level shear continued throughout the warm sector after 27/0000Z.

In Arkansas, a widespread convective region comprising several bands, bowing segments, and supercell clusters had formed by 27/0000Z (Fig. 16b). Based on the relatively large values of MLCIN over this region (Figs. 23b, 24a), much of this convection was likely elevated and supported by low-level WAA as the poleward-advancing moisture plume ascended north of the two surface fronts (Figs. 19a, 22a). Convection that formed along the effective warm front was likely rooted in the PBL (Figs. 23a), but these cells quickly became linear due to sustained frontal forcing and deep-layer shear that paralleled the boundary (Fig. 24a). Consequently, there was a sparsity of tornadoes throughout Arkansas and most of SPC's High Risk area (Fig. 18).

Over time, convection congealed into a QLCS that comprised several bowing segments, mesovortices, and embedded supercellular structures (Knupp et al., 2014) and was continually supported by deep-layer shear $\geq$ 50 kt (Figs. 24a-c). Nearly all tornadoes developed at night after convection had grown upscale, and the southern half of QLCS1 produced numerous significant (i.e., EF2+) and/or long-track tornadoes from Louisiana to Tennessee between ~27/0300Z–27/1330Z (Fig. 18). This unique evolution occurred although ML-CAPE throughout the environment decreased substantially after sunset. By 27/0900Z,

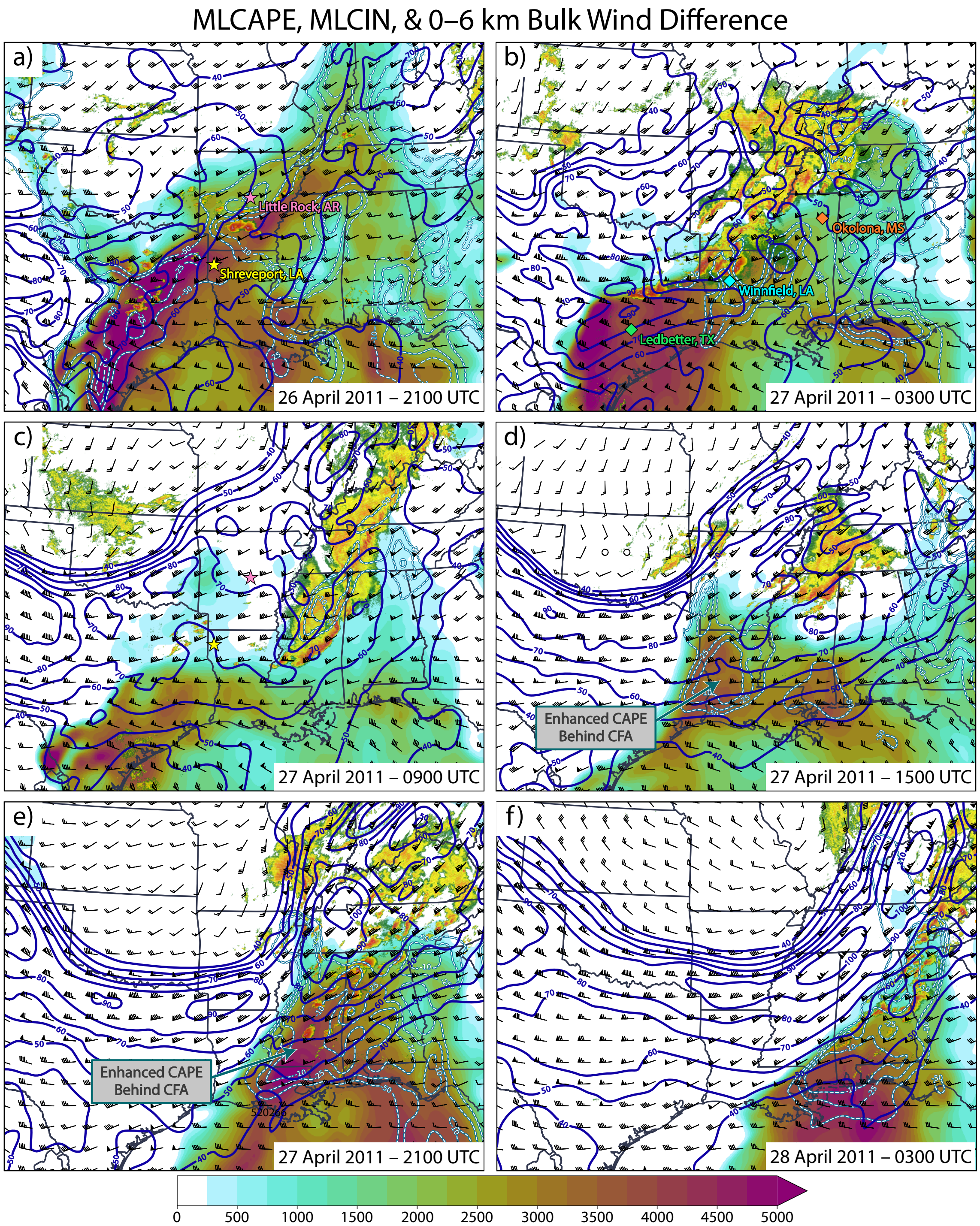

Figure 24: *NEXRAD composite radar reflectivity > 20 dBZ overlaid with MLCAPE (shaded; J kg^{-1}), MLCIN (dashed contours; -50, -25, and -10 J kg^{-1}), 0–6-km bulk wind difference magnitude (navy contours every 10 kt ≥ 40 kt), and 0–6-km bulk wind difference (barbs; kt) from the corresponding RUC 1-h forecast valid at (a) 2100 UTC 26 April, (b) 0300 UTC 27 April, (c) 0900 UTC 27 April, (d) 1500 UTC 27 April, (e) 2100 UTC 27 April, and (f) 0300 UTC 28 April 2011. The locations of the Shreveport, LA, and Little Rock, AR, soundings are denoted in (a) and (c) by the yellow and pink stars, respectively. The locations of the Ledbetter, TX, Winnfield, LA, and Okolona, MS, wind profilers are denoted in (b) by the green, cyan, and orange diamonds, respectively.*

MLCAPE values immediately ahead of QLCS1 were ≤ 750 J kg^{-1} (Fig. 24c), with higher MLCAPE coinciding with greater low-level θ_e values over the Southeast (Fig. 19c). While MLCAPE throughout the inflow region further decreased to ≤ 500 J kg^{-1} by 27/1200Z (not shown), at which point QLCS1 had noticeably weakened (Fig. 16f), tornado activity continued until 27/1400Z.

The rampant tornado activity accompanying QLCS1 as it moved into the Southeast likely stemmed from dramatic flow alterations that commenced immediately after CI—notably, rapid LLJ intensification that coincided with the formation of J_2 at upper levels. During the 6-h period between 26/2100Z–27/0300Z, J_2 rapidly developed north of QLCS1 and attained wind speeds > 140 kt over the Midwest (Figs. 20a,b and 25b), while 850-hPa winds strengthened by 20–25 kt ahead of QLCS1 (Figs. 22a,b). By 27/0900Z, a prominent LLJ comprising 60–70+ kt winds extended into the Ohio Valley beneath the J_2 entrance region (Figs. 20c, 22c), and 0–1-km BWD and corresponding SRH values within the inflow environment had increased to 45–50 kt and 300–600 m^2 s^{-2}, respectively (Fig. 26a); Thompson et al. (2012) found that such values are supportive of EF2+ QLCS tornadoes. The temporal increase in low-level shear was observed by the wind profilers in Winnfield and Okolona (Fig. 27), which were located in the QLCS1 inflow environment until approximately 27/0600Z and 27/0800Z, respectively. The 0–1-km BWD reached a temporal maxima of 46 kt at 27/0600Z in Winnfield (~44 km northeast of a developing EF2 tornado), while a maxima of 39 kt was observed at 27/0800Z in Okolona (~25 km north of a long-track EF3 tornado; Fig. 18).

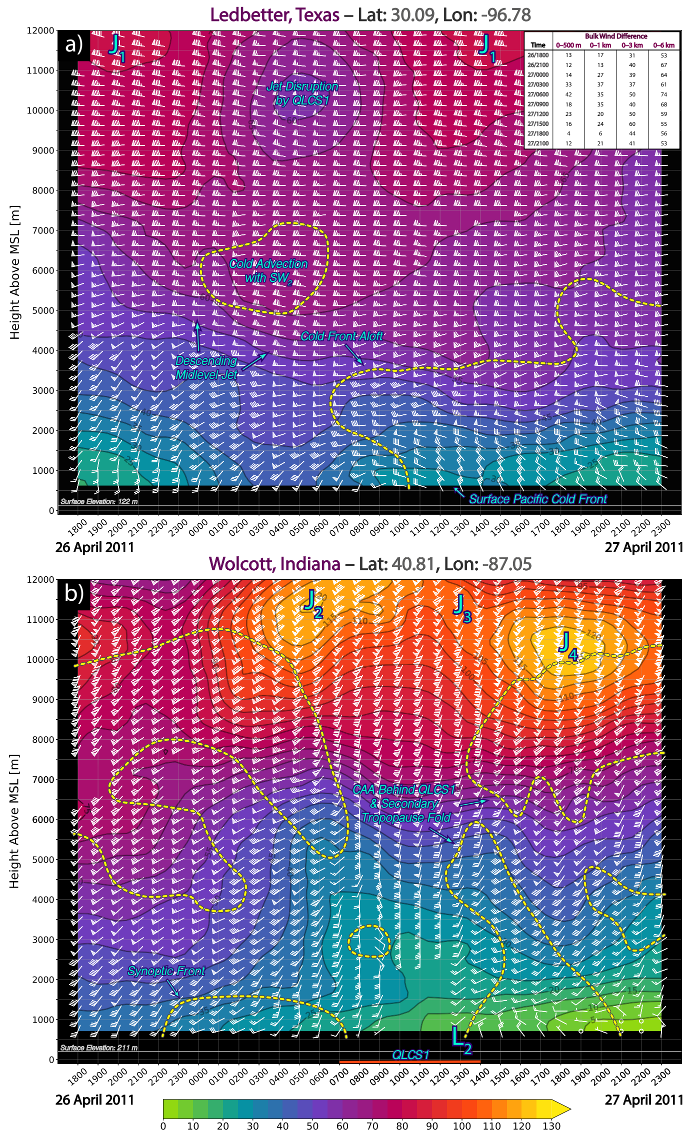

Figure 25: *Time-height diagrams of objectively analyzed horizontal wind speed (shaded; kt) and observed horizontal winds (barbs; kt) from the NOAA wind profilers located in (a) Ledbetter, TX, and (b) Wolcott, IN. Regions of derived geostrophic cold advection are denoted by the yellow dashed contours. BWD values (kt) computed from the surface to 500 m, 1 km, 3 km, and 6 km AGL are depicted every 3 h in the top right for the Ledbetter profiler. Since the lowest wind observation was located at 250 m AGL, the 10-m wind observation from the nearest operational surface observing site, which was the AWOS in Giddings, TX, (21 km WNW of Ledbetter), was used for the BWD computation. The profiler locations are shown in Fig. 20a.*

Figure 26 depicts the spatial distribution of hodographs plotted relative to the Bunkers et al. (2000) estimated right-moving supercell motion. Ahead of QLCS1, the strengthened

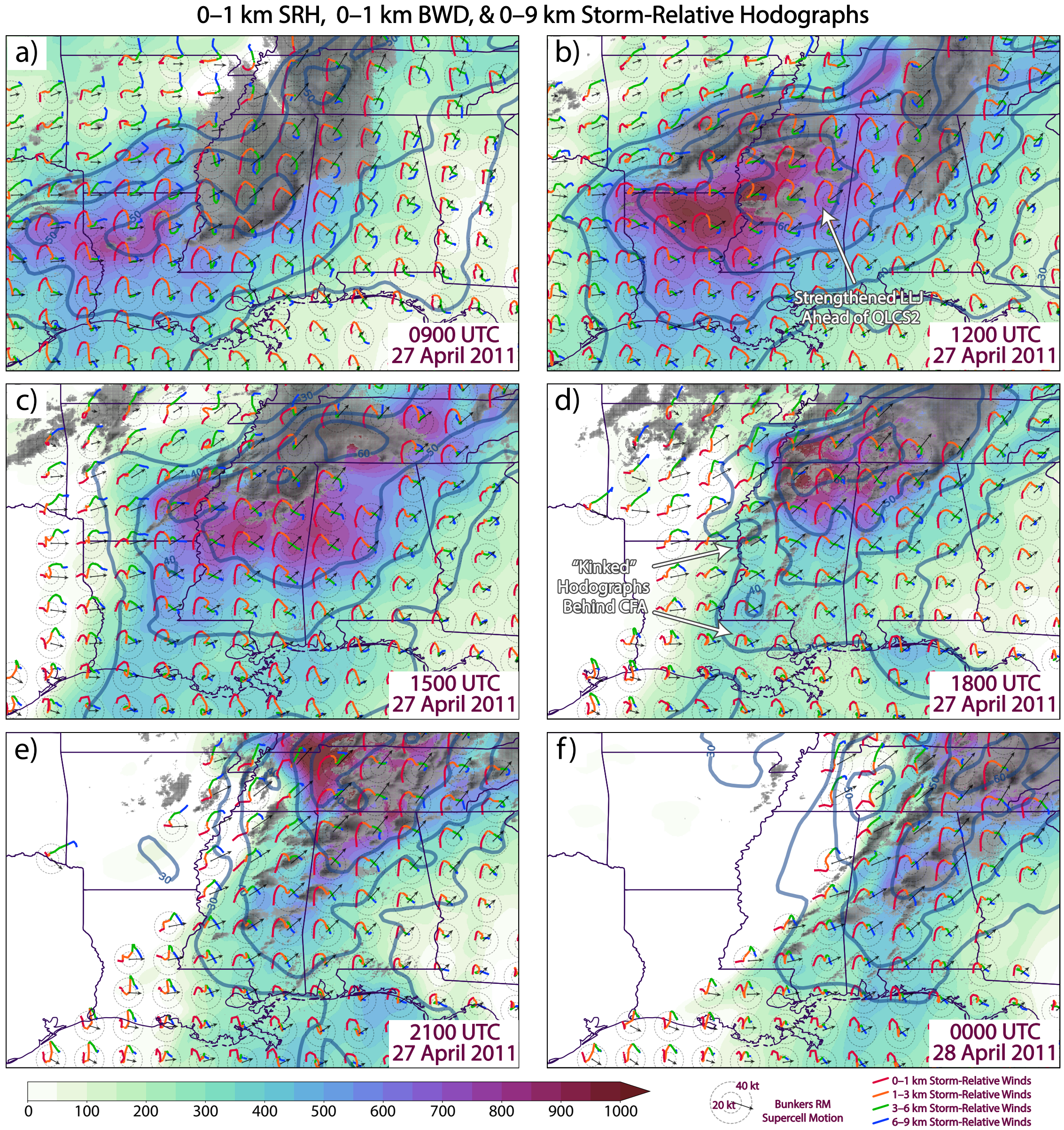

Figure 26: *NEXRAD composite radar reflectivity > 20 dBZ overlaid with 0–1-km SRH (shaded; m^2 s^{-2}), 0–1-km BWD (contours; kt), and a spatial depiction of 0–9 km AGL storm-relative hodographs from the corresponding RUC 1-h forecast valid at (a) 0900 UTC 27 April, (b) 1200 UTC 27 April, (c) 1500 UTC 27 April, (d) 1800 UTC 27 April, (e) 2100 UTC 27 April, and (f) 0000 UTC 28 April 2011. Concentric dashed circles represent wind speeds of 20 and 40 kt. The Bunkers et al. (2000) estimated motion for a right-moving supercell is depicted with the black vectors and is used for the SRH computation. The hodographs are colored according to the storm-relative winds within the following layers: (red) 0–1 km AGL, (orange) 1–3 km AGL, (green) 3–6 km AGL, and (blue) for 6–9 km AGL.*

LLJ supported hodographs that exhibited incredibly strong vertical shear over the lowest 1–3 km, with corresponding shear vectors oriented *approximately parallel to the system* (Figs. 26a,b). This shear configuration would yield appreciable streamwise vorticity for

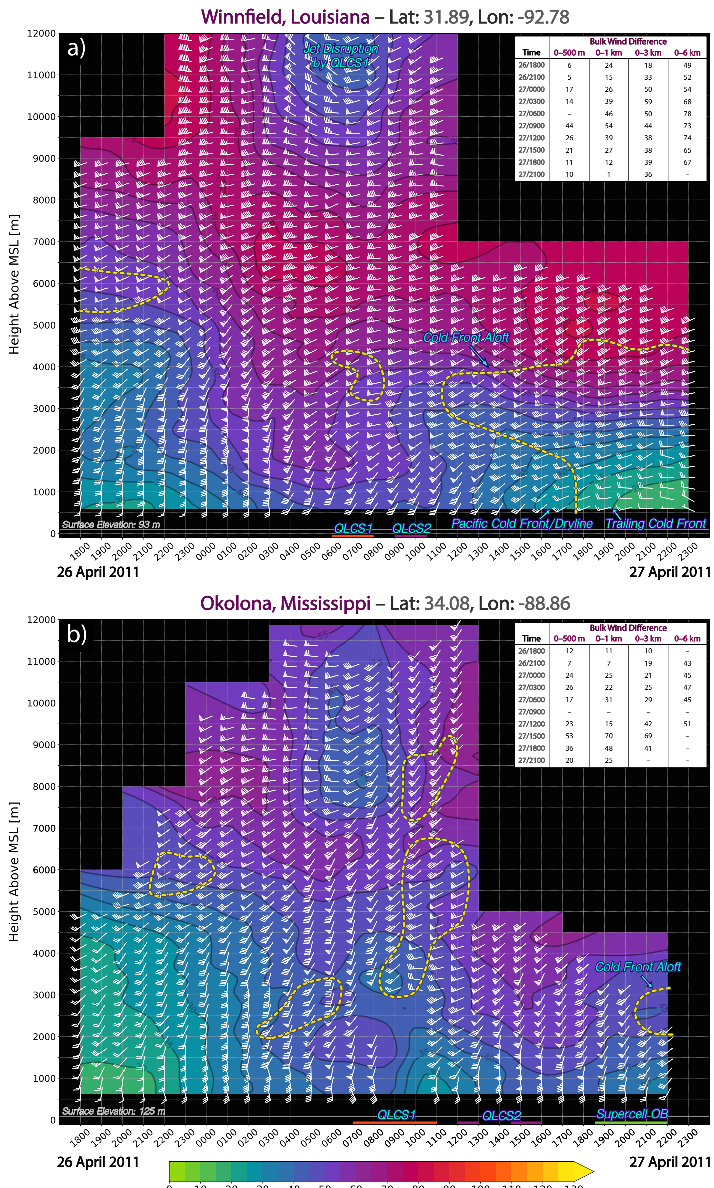

Figure 27: *As in Fig. 25 but for the NOAA wind profilers located in (a) Winnfield, LA, and (b) Okolona, MS. BWD values (kt) computed from the surface to 500 m, 1 km, 3 km, and 6 km AGL are depicted every 3 h in the top right for both profilers. Since the lowest wind observation was located at 250 m AGL, the 10-m wind observation from the nearest operational surface observing sites: AWOS in Natchitoches, LA, (35 km SW of Winnfield) and ASOS in Tupelo, MS, (22 km NNE of Okolona). The profiler locations are shown in Fig. 20a.*

low-level inflowing parcels, which may then be tilted into the vertical to promote cyclonic rotation within the QLCS (e.g., Lee and Wilhelmson, 1997; Wheatley and Trapp, 2008; Flournoy and Coniglio, 2019). We note that most foundational studies on the dynamics of quasi-linear convection employed both unidirectional wind and shear profiles and focused exclusively on the line-normal shear component (e.g., Rotunno et al., 1988; Weisman, 1993; Weisman and Trapp, 2003), which provided purely crosswise vorticity within this simplified framework.

3.3.2 QLCS2

The second system developed in the wake of QLCS1 just after 27/0900Z and grew upscale into a bow echo as it moved northeastward ahead of SW_3 (Figs. 16e-h), producing 7 weak EF0–EF1 tornadoes in northern Alabama between 27/1600–27/1700Z (Figs. 2 and 18). Although QLCS2 did not appreciably contribute to the tornado count during the outbreak, persistent outflow and cloud cover from the system induced a thermal boundary along which several tornadic supercells developed and/or tracked during the afternoon (Sherrer, 2014; Knupp et al., 2014). Thus, QLCS2 delimited the extent of the effective warm sector and the region of greatest tornado potential during the supercell outbreak, and whether the thermodynamic environment would subsequently recover to support tornadoes from northern Mississippi through the Tennessee Valley region during the afternoon was a major source of uncertainty in real-time.

3.3.2.1 Pre-convective environment and convection initiation

Convection associated with QLCS2 developed over the Ark-La-Tex region following the movement of SW_3 into the SGP (Figs. 20c,21c). Midlevel diffluence was present over the CI region in between SW_2 and SW_3—the latter of which was attended by a strong 1000–500-hPa thickness gradient representing a deep-tropospheric cold front that extended into eastern Oklahoma (Fig. 21c). The tropopause fold accompanying SW_3 (labeled "primary tropopause fold" in Fig. 19d) was continually deepening as the core of J_1 progressed into the longwave trough base, and a corridor of high 450–350-hPa PV values extended southeastward into the SGP by 27/0900Z. A sharp mesoscale band (width ≤ 100 km) of high GOES-13 WV brightness temperatures (indicating dry subsiding air of stratospheric origin) was situated over Oklahoma in association with the tropopause fold, while a widespread region of dry midlevel air that was descending within a prominent DCB was evident over Texas at this time (Fig. 19d).

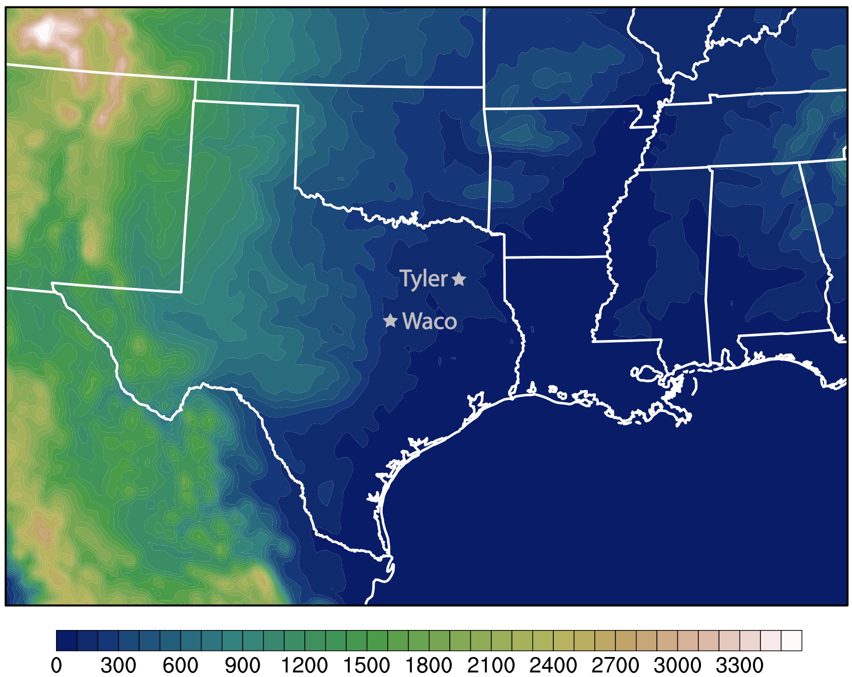

Figure 28: *Terrain height in meters over the southern United States.*

Ahead of the upper-level trough and in the wake of J_2, a broad region of surface pressure falls > 3 hPa (3 h)$^{-1}$ spanned from western Mississippi into central Indiana (where L_2 was developing; Figs. 19c,d) and supported the strengthening LLJ ahead of QLCS1 (Fig. 22c). The quasi-stationary front extended southwestward from L_2 into the SGP, where L_3 was reorganizing near the Arkansas-Oklahoma border ahead of SW_3 (Fig. 19c). Further, a surface trough and accompanying prefrontal wind shift (e.g., Schultz, 2005) extended southward from L_3 into east-central Texas, where a mesolow had formed at the intersection of a surface cold front (demarcating the leading surface position of the polar air mass originally over North Texas and the Pacific cold front farther toward the southwest) and an east-west-oriented outflow boundary produced by QLCS1, which served as an effective warm front.

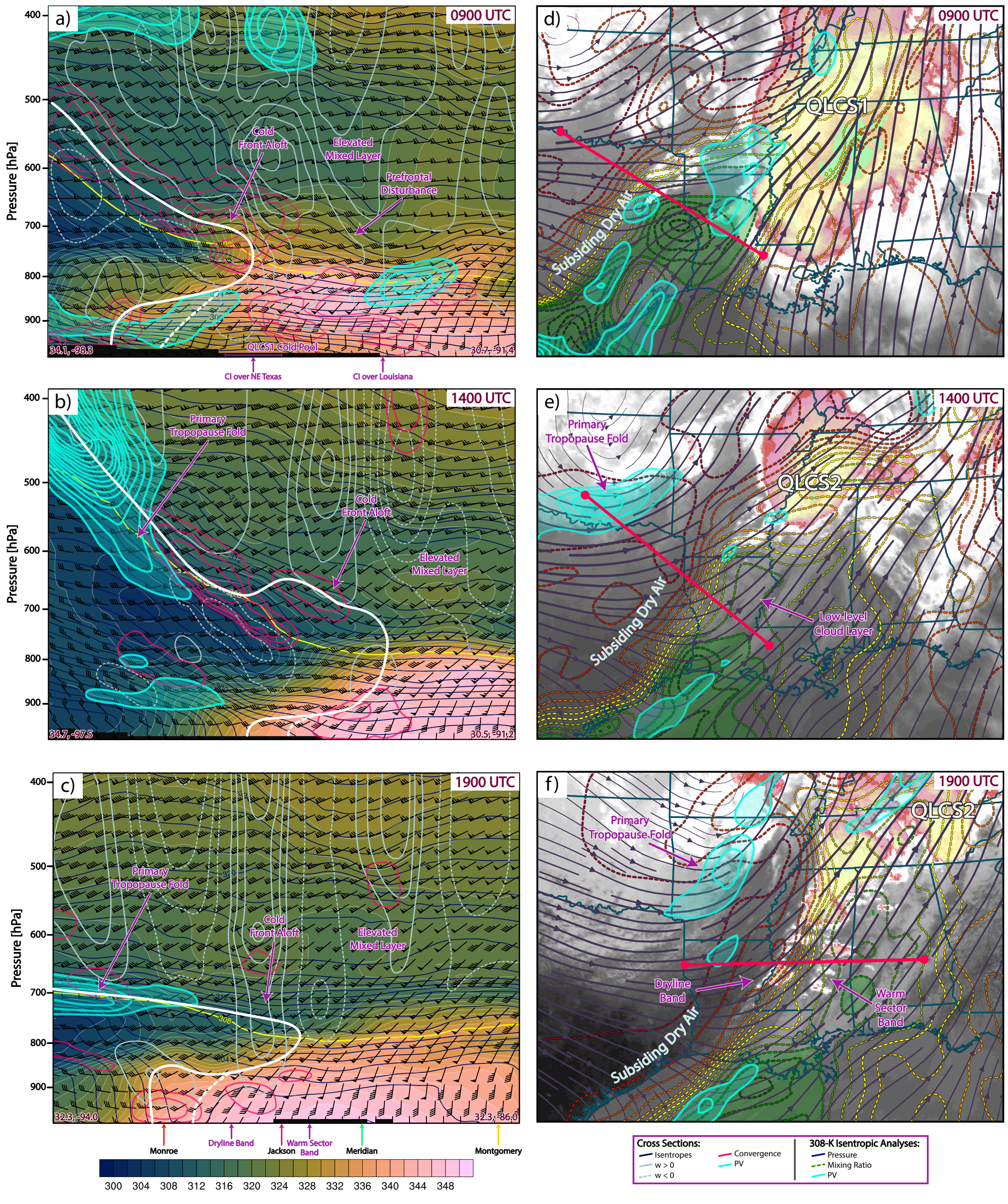

Over the elevated terrain in West Texas (topographic map shown in Fig. 28), near-surface air behind the Pacific cold front exhibited comparable or characteristically higher

Figure 29: *Vertical cross sections of equivalent potential temperature (shaded; K), potential temperature (navy contours with the 308 K surface shown in yellow; K), horizontal convergence (pink contours; every 2.5 × 10*$^{-5}$ *≥ 5 × 10*$^{-5}$ *s*$^{-1}$*), vertical velocity (gray contours; positive and negative values shown every 5 cm s*$^{-1}$ *with solid and dashed contours, respectively), PV (cyan contours; every 0.5 PVU ≥ 1.5 PVU), and horizontal winds (barbs; kt) from the corresponding RUC 1-h forecasts valid at (a) 0900 UTC, (b) 1400 UTC, and (c) 1900 UTC 27 April 2011. The analyzed location of the Pacific cold front is depicted by the white solid line, and the position of the prefrontal trough and developing dryline (at 27/1400Z and 27/1900Z) are shown using the dashed white line. On the right, GOES-13 IR imagery overlaid with 308-K isentropic analyses of water vapor mixing ratio (dashed contours; every 1 g kg*$^{-1}$ *with values > 10 g kg*$^{-1}$ *shaded), PV (cyan contours; every 0.5 PVU ≥ 1.5 PVU), streamlines (purple), and cross-section paths (red) at (d) 0900 UTC, (e) 1400 UTC, and (f) 1900 UTC 27 April 2011. All fields were lowpass filtered with a cutoff wavelength of 200 km prior to conducting the isentropic interpolation.*

potential temperatures (~299–303 K) than either of the prefrontal air masses found at lower elevations (~292–300 K; values shown on the station plots in Fig. 19c), and a CFA—which manifested primarily as an elevated intrusion of low-θ_e air (Fig. 29a)—accordingly developed as the Pacific cold front moved downslope and overran this relatively dense low-level air. The CFA passage was detectable at some surface observing sites as a wind shift followed by a hydrostatic pressure rise with no accompanying change in surface potential temperature (e.g., Waco and Tyler, TX, in Fig. 30), and its movement atop the polar air mass and QLCS1 cold pool contributed to the prefrontal wind shift evident over east-central Texas at 27/0900Z (Figs. 19c and 29a,d). Similar surface signatures have been observed to accompany CFA passages in previous studies (e.g., Neiman et al., 1998; Neiman and Wakimoto, 1999).

The eastward progression of the CFA was observed by the wind profilers in Ledbetter (at ~27/0900Z) and Winnfield (at ~27/1400Z), which showed backing winds with height and implied geostrophic CAA beginning at ~2–4 km and descending toward the surface over time—indicative of a forward-tilted structure (Figs. 25a and 27a). Owing to the sloping topography of Texas (Fig. 28) and the characteristic airflow structure within a descending DCB (Fig. 8), the CFA advanced most rapidly toward the south as the dry airstream penetrated into the lower troposphere and overran the shallow moist layer over

South Texas and the Gulf of Mexico (Figs. 29e,f). Unlike over land, where the surface has a lower heat capacity and thus the underlying air mass is subjected to considerable diurnal variations in static stability, the wind shift and thermal advection signature associated with the CFA remained coherent throughout the daytime over the Gulf of Mexico, where it was preceded by a distinct cloud band and spectacular long-lived undular bore (Lutzak, 2013). The mesoscale structure of the CFA and its interaction with the prefrontal moist air mass are discussed further in Chapter 6.

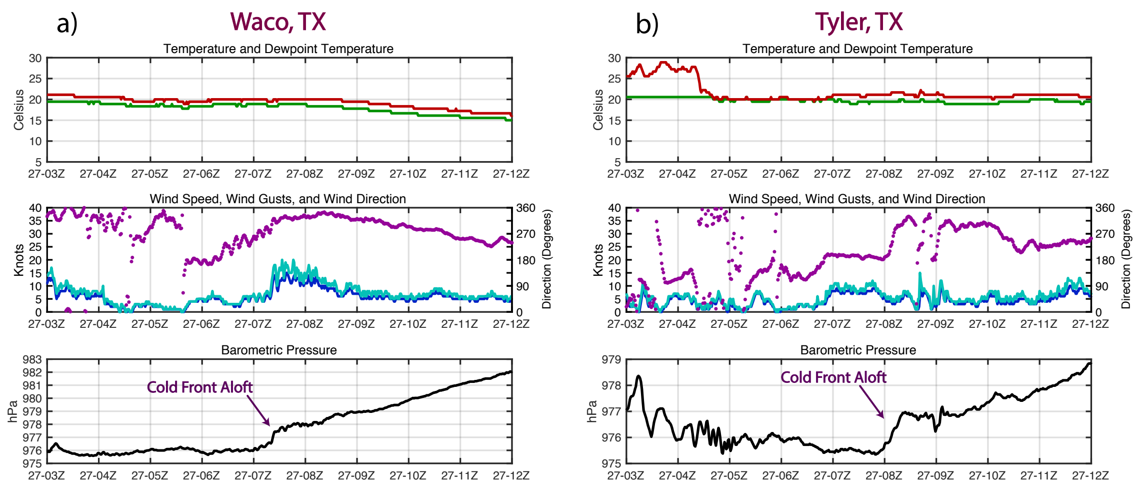

Figure 30: *Meteograms of 1-min ASOS observations from (a) Waco, TX, and (b) Tyler, TX, showing the inferred passage of the CFA. The locations of these two sites are shown in Fig. 28.*

Convection first developed over northeastern Texas ahead of the surface trough and CFA (Figs. 16e and 19c) and was quickly followed by the formation of multiple east-west-oriented bands north of the effective warm front over Louisiana and Arkansas by 27/1000Z (not shown). Although QLCS1 recently moved through the CI region, destabilization was supported by several factors: (1) large-scale forcing for ascent ahead of the longwave trough and SW_3 (Figs. 20c, 21c); (2) advection of an EML plume into the region at midlevels (Figs. 23c,d and 29a); (3) increased advection of warm, moist air by strengthening low-level southerly flow atop the remnant QLCS1 cold pool (Figs. 22c and 29d); and (4) mesoscale convergence ahead of the CFA and near the terminus of a 50–65-kt LLJ (Figs. 22c and 29a). Conditions remained unfavorable for surface-based convection (Fig. 24c), whereas elevated convection was supported by MUCAPE = 1000–1500 J kg^{-1} at 27/0900Z (not shown) that continued to increase with time (Figs. 23c,d). The 27/1103Z sounding from Shreveport, LA, (released < 50 km from the southwesternmost part of QLCS2) depicted a layer of backing winds between ~800–725 hPa (Fig. 23c), which coincided with an elevated layer of CAA within the RUC (not shown) and suggests that the CFA may have contributed to this MUCAPE increase. This sounding was also characterized by notably dry air above 800 hPa (i.e., air that descended within the DCB), which supported enhanced potential instability ahead of SW_3 and interacted with ongoing convection associated with QLCS2.

3.3.2.2 Environmental and convective evolution

QLCS2 exhibited a highly complex morphological evolution as it grew upscale ahead of SW_3 (Figs. 16f-i). For one, the east-west-oriented convective bands that developed near the LLJ terminus congealed as they lifted northward with time, while convection that formed near the CFA quickly advanced eastward and evolved into a bow echo with a widespread region of stratiform precipitation. Due to these considerably different motions, the system became reoriented as it moved northeastward during the morning. By 27/1800Z, the stratiform region had eroded over much of Tennessee as QLCS2 progressively evolved into a disorganized conglomeration of arc-shaped bands, clusters, and supercells (Fig. 16h).

QLCS2's complex evolution resulted at least partly from (1) interactions with the primary tropopause fold, accompanying DCB, and J_1 exit region (Figs. 21c-e and 29d-f); (2) the downstream formation of J_4 at upper levels following CI and its subsequent strengthening to 135+ kt by 27/1500Z (Figs. 20c-e); and (3) rapid LLJ intensification within the system's inflow environment (Figs. 22c-e and 27). The hodograph evolution presented in Fig. 26 nicely depicts how QLCS2 evolved relative to the background flow. The preconvective environment was characterized by 70–80-kt westerly deep-layer vertical wind shear (Fig. 24c) and a well-defined LLJ—which yielded elongated hodographs with strong low-level shear—that had appreciably strengthened ahead of QLCS2 by 27/1200Z (Figs. 26a,b). The east-west-oriented bands rapidly advanced northward within a region of implied convergence at the periphery of this accelerating LLJ, which contributed to the reorientation and expansion of QLCS2 over time. Furthermore, the rear portion of QLCS2 was interacting directly with dry midlevel air that had subsided within the primary tropopause fold and DCB (Figs. 29d-f), which likely supported its progression into a bow echo (e.g., Johns, 1993) and eventual disorganization (e.g., Browning et al., 1995; Browning, 2005).

Although QLCS2 remained elevated atop the remnant QLCS1 cold pool throughout much of its lifetime (Figs. 24c,d), significant surface cooling and strong outflow accompanied the system during its later stages (Knupp et al., 2014). Between 27/1500Z–27/1700Z, MLCAPE ahead of the system grew from < 250 J kg^{-1} to 500 J kg^{-1} as it encountered a destabilizing environment over northern Alabama (not shown). Furthermore, the reorientation of the bow echo throughout the late morning led to its increasing parallel alignment with the low-level shear vectors, which were south-southwesterly and corresponded to 0–1-km BWD = 50–60 kt (Fig. 26c). As this shear configuration has been shown to support the development of QLCS mesovortices (e.g., Wheatley and Trapp, 2008), we surmise that the reorientation of QLCS2 relative to the low-level shear occurring contemporaneously with the movement into a destabilizing environment contributed to the brief period of tornadic activity during the late morning.

3.3.3 Afternoon supercell outbreak

Owing to the amplified upper-level pattern and approaching J_1, the likelihood of a high-impact severe weather event transpiring east of the Mississippi River during the afternoon of 27 April was identified several days in advance by SPC forecasters. SPC issued a High Risk Convective Outlook at 27/0600Z (updated Outlook valid from 27/1630Z–28/1200Z is displayed in Fig. 18) that was centered over northern Alabama in anticipation of a forthcoming tornado outbreak. This afternoon supercell outbreak commenced at ~27/1830Z with the development of an EF3 tornado over northern Mississippi, which preceded another

14 EF3, 11 EF4, and 4 EF5 tornadoes between 27/1930Z–28/0501Z (Fig. 2). Unlike the first two systems, the afternoon episode comprised multiple bands of supercells that developed within the warm sector and were remarkably efficient at producing long-track tornadoes (Fig. 18). The unique development and mesoscale organization of numerous supercells that remained largely discrete for several hours was undeniably one of the most—if not foremost—essential components to the sheer severity of the supercell outbreak (e.g., Bunkers et al., 2006; Garner, 2012). We introduce some of the processes responsible for this development herein, but a more comprehensive mesoscale analysis is presented in Chapter 6.

3.3.3.1 Pre-convective environment and convection initiation

The supercell outbreak unfolded over the Southeast in association with the movement of SW_3 and the core of J_1 through the longwave trough base (Figs. 20d-f and 21d-f). A coupled upper-level jet streak configuration had developed following the downstream formation of J_4 such that the outbreak region was situated within the right exit region of J_1 and the right entrance region of J_4. SW_3 continued to amplify throughout the morning, and an elongated band of high PV extending downward to ~600 hPa in the primary tropopause fold had rotated into Arkansas by 27/1700Z (Fig. 19f). The tropopause fold was attended by a distinct DCB that spanned from southern Texas into the Southeast and a strengthening 100–105-kt midlevel jet streak (Figs. 21d,e). SW_3 was trending toward a positively tilted structure as it moved into the Mississippi Valley behind QLCS2, with increasing confluence downstream and an accompanying tightening of the 1000–500-hPa thickness gradient. *Thus, the supercell outbreak did not occur in association with a highly diffluent shortwave trough.*

Although a potent midlevel shortwave and deep tropopause fold advanced into the region, *rapid surface cyclogenesis was not a key factor in the culmination of this outbreak.* Between 27/0900Z and 27/1700Z, the minimum pressure within L_3 remained steady or even slightly increased (cf. Figs. 19c,e), while L_3 moved only ~250 km northeastward across Arkansas.

This gradual northeastward motion accompanied by negligible deepening continued through the bulk of the supercell outbreak. Despite the absence of substantial surface pressure falls, the pressure gradient over the Southeast had noticeably tightened throughout the morning as the isobars acquired a greater zonal orientation and the circulation about L_3 became increasingly contracted in scale (Figs. 19e,f). Accordingly, a prominent LLJ with 850-hPa

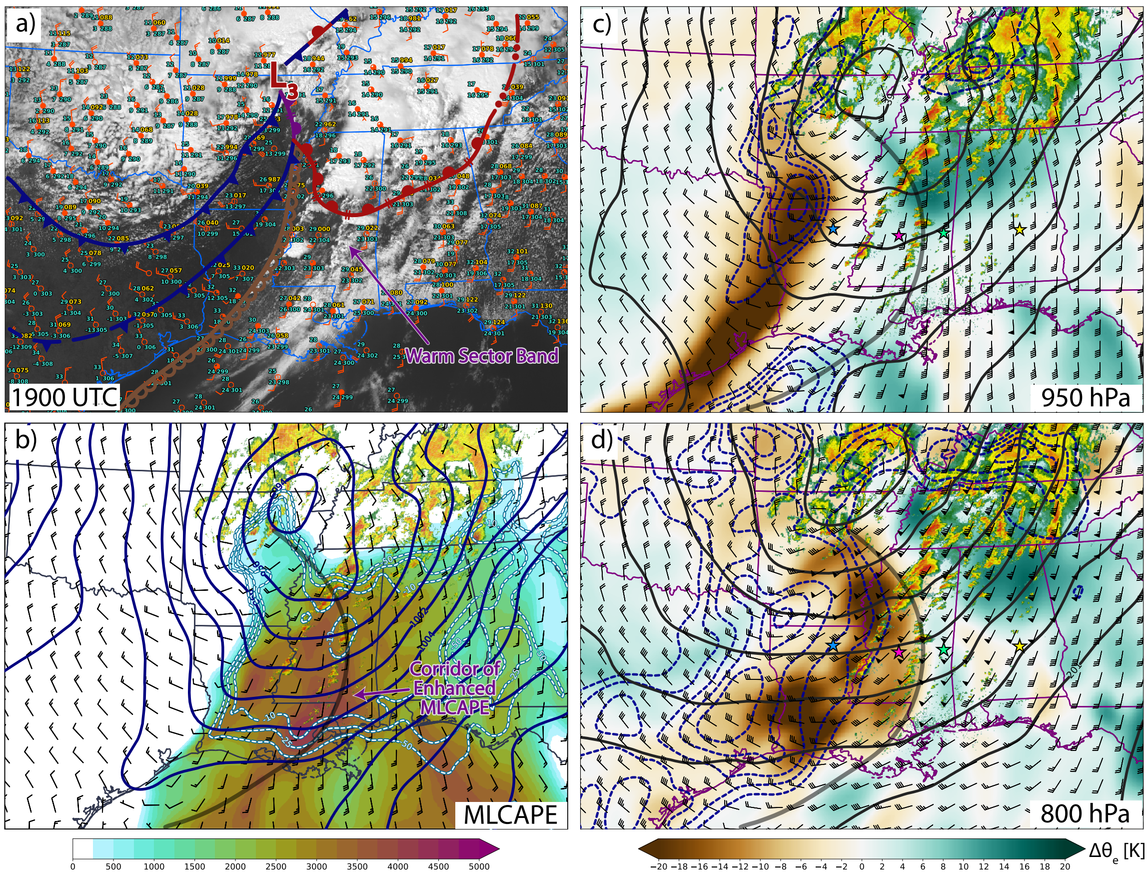

Figure 31: *Visible satellite imagery, surface observations, and subjectively analyzed fronts (depicted with conventional notation) are shown in (a) at 1900 UTC 27 April 2011. NEXRAD composite radar reflectivity > 20 dBZ is overlaid with (b) MLCAPE (shaded; J kg^{-1}), MLCIN (dashed contours; -50, -25, and -10 J kg^{-1}), SLP (navy contours; hPa), and 10-m winds (barbs; kt), and (c,d) 3-h equivalent potential temperature change (shaded; K), 3-h virtual potential temperature change (dashed navy contours; every 1 K ≤ -1 K), geopotential height (black contours; dam), and horizontal winds (barbs; kt) at (c) 975 hPa and (d) 800 hPa from the corresponding RUC 1-h forecasts valid at the same time. The estimated CFA location at 800 hPa is denoted by the gray contour in (b)-(d). The blue, magenta, green, and yellow markers denote the locations of Monroe, LA, Jackson, MS, Meridian, MS, and Montgomery, AL, respectively.*

wind speeds = 60–75 kt was established over the Southeast during the supercell outbreak (Figs. 22d,e).

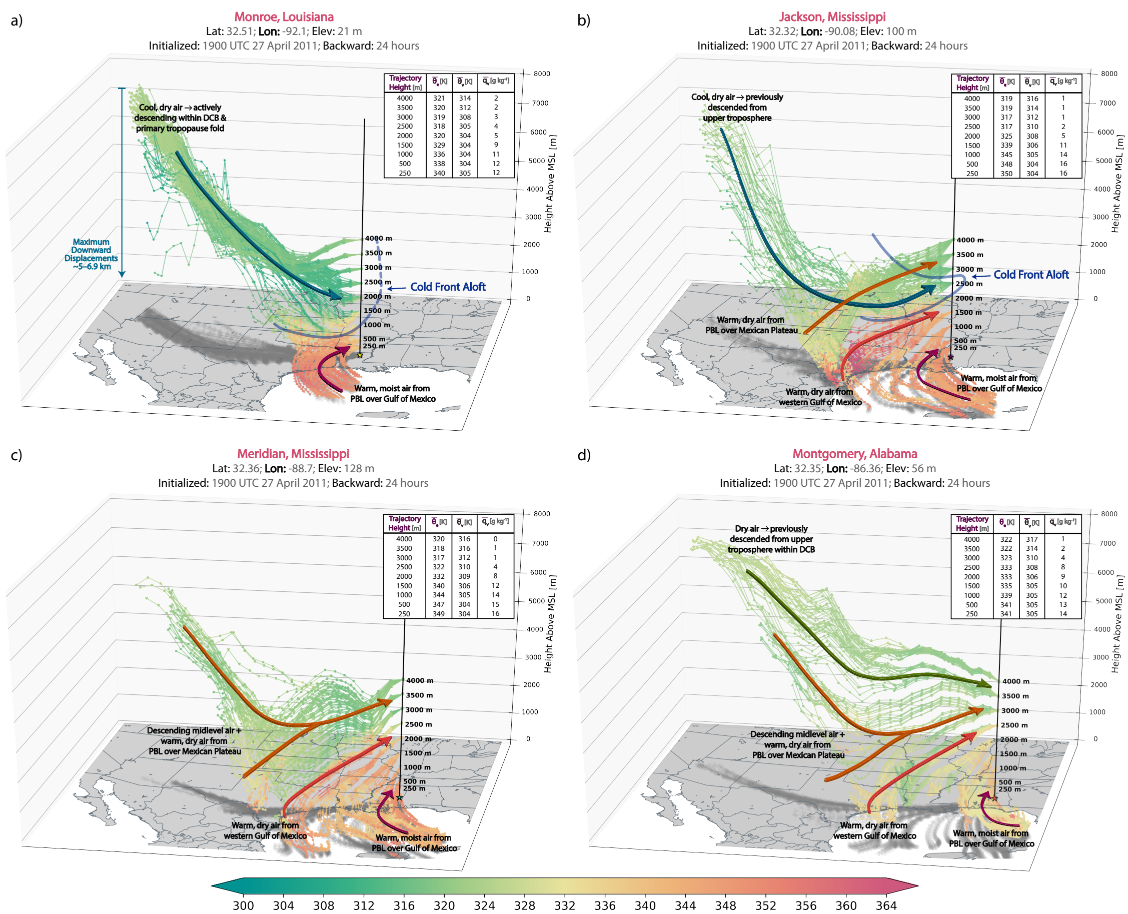

Figure 32: *Depiction of the three-dimensional flow evolution using HYSPLIT backward trajectories initialized at 1900 UTC 27 April 2011 from (a) Monroe, Louisiana, (b) Jackson, Mississippi, (c) Meridian, Mississippi, (d) Montgomery, Alabama. All trajectories are displayed in height above MSL. Values of equivalent potential temperature (K) along each 3D trajectory are shaded in color. Gray shading is shown to depict the horizontal locations of each trajectory as a projection onto the 2D map plane. Trajectory ensemble starting heights are labeled at the initialization location in meters AGL. The mean values of equivalent potential temperature ($\bar{\theta}_e$), virtual potential temperature ($\bar{\theta}_v$), and water vapor mixing ratio ($\bar{q}_v$) were calculated for each ensemble at the initialization time and location and are listed in the displayed table. The initialization locations are displayed in Fig. 31.*

The overall structure of L_3 and the character of its attendant fronts were influenced considerably by diabatic processes—primarily postfrontal sensible heating and widespread convection occurring within the *synoptic* warm sector. Owing to remnant cloud cover and convective outflow produced by both QLCSs, a notable cold pool comprising temperatures of 14–19 °C (57–66 °F) was situated east of L_3 and reduced the thermal contrast across the quasi-stationary front while displacing the strongest low-level baroclinity into the Southeast across an effective warm front (Fig. 19e). To the south of L_3, incredibly dry and potentially warm air that descended from the upper troposphere and overran the low-level moist layer behind the CFA was mixed downward through the PBL after sunrise. Consequently, the surface Pacific cold front acquired characteristics of a dryline[3] that preceded a corridor of temperatures > 30 °C and markedly low dewpoint temperatures (< 0 °C in many locations), while a warm occlusion developed over Arkansas as this potentially warm postfrontal air moved atop the stable cold pool. The wedge of warm, dry surface air expanded northeastward throughout the daytime due to the progression of the DCB and deepening PBL mixing (Figs. 29f, 31a). HYSPLIT trajectories initialized from Monroe, LA, (located in the northeastern portion of the surface dry wedge at 27/1900Z; Fig. 31) show the downward penetration of this dry postfrontal air to ≤ 1 km, where it was mixed vertically over a ~2–2.5-km deep dry adiabatic layer with moist low-level air that originated over the Gulf of Mexico (Fig. 32a). Most trajectories initialized above ~1 km had descended > 5 km over 24 h, with maximum displacements of ~6.9 km for some parcels in the ~1.5–2 km layer. Other prolific tornado outbreaks—including the 1965 Palm Sunday Outbreak (Fujita et al., 1970) and 1974 Super Outbreak (Hoxit and Chappell, 1975; Locatelli et al., 2002b)—also featured notably dry surface air that had descended into the lower troposphere within a DCB and was subsequently mixed downward through the PBL behind a surface boundary that was preceded by a CFA. *Thus, identification of an expanding postfrontal corridor of remarkably dry air in the Mississippi Valley during an impending severe event may indicate to forecasters that a CFA could be progressing into the Southeast.*

Owing to PBL heating and strong differential advection ahead of SW_3, the environment quickly destabilized in the wake of the two QLCSs, yielding MLCAPE > 2000 J kg^{-1}

[3]The Pacific cold front was classified as a dryline where it exhibited a diurnal reversal of the surface thermal gradient and a cross-boundary difference in mixing ratio ≥ 3 g kg^{-1} (e.g., Schaefer, 1974).

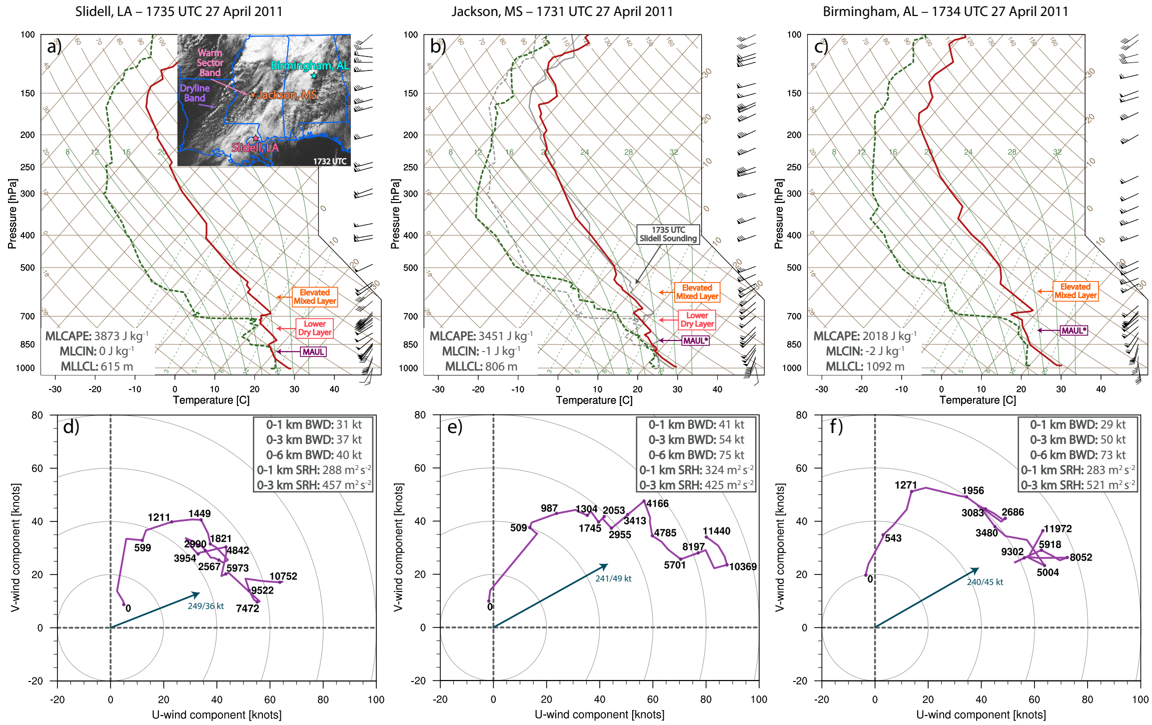

Figure 33: *Observed soundings and corresponding hodographs from (a,d) Slidell, LA, (b,e) Jackson, MS, and (c,f) Birmingham, AL, valid at 1800 UTC 27 April 2011. The actual release times are shown for each individual sounding. Sounding parameters were calculated using the SHARPpy program (Blumberg et al., 2017). The hodograph labels represent height AGL (m). The blue vector in panels (d)-(f) denote the predicted storm motion for a right-moving supercell (Bunkers et al., 2000). The sounding locations are overlaid with GOES-13 visible imagery from 1732 UTC in panel (a).*

throughout the warm sector by 27/1800Z. Three operational soundings released within the preconvective environment at ~27/1730Z depicted large MLCAPE, negligible MLCIN, and considerable vertical wind shear, hodograph curvature, and SRH (Fig. 33). The highest MLCAPE (3873 J kg^{-1}) was observed in Slidell, LA, where PBL moisture was greater, while the strongest 0–6-km BWD (73–75 kt) was observed closer to the midlevel jet in Jackson, MS, and Birmingham, AL. The high MLCAPE over the Southeast was evidently supported by steep midlevel lapse rates and an EML plume that HYSPLIT trajectories showed to originate over the Mexican Plateau during the previous afternoon (Figs. 32b-d). The base of the EML was characterized by a strong inversion at ~700 hPa (Fig. 33), which overlaid a low-level dry layer in Slidell and Jackson that originated as air descended from the Mexican Plateau to low levels over the western Gulf of Mexico before moving into the Southeast (Figs. 32b-d). This dry layer was absent in the Birmingham sounding, which depicted a ~150-hPa-deep nearly saturated and potentially unstable layer that began at the top of the dry adiabatic PBL. Shallower but similar layers—characteristic of a moist absolutely unstable layer (MAUL; Bryan and Fritsch, 2000) provided that saturation was achieved[4]—were also observed in Slidell and Jackson. Visible satellite imagery (shown in Fig. 33a) suggests that these MAUL signatures accompanied several low-level cloud bands that had developed over the warm sector—the depth of which increased northeastward from Slidell to Birmingham. The circulations supporting these bands were evidently insufficient for CI owing to the overlying inversion(s). The mesoscale processes responsible for the development of a MAUL over the Southeast are discussed further in Chapter 6.

The first cells developed gradually throughout the late morning and were apparent southwest of QLCS2 over Arkansas and Louisiana at 27/1500Z (Fig. 3g). Moisture transport on the 308-K isentropic surface overlaid with satellite imagery at 27/1400Z indicated that these cells erupted as a low-level stratocumulus layer was overrun by descending (or previously descended) dry air at ~800–750 hPa and subsequently broke up into several low-level cumulus bands (Fig. 29e). A corresponding vertical cross section showed that an elevated layer of low-θ_e air had progressed into central Louisiana by 27/1400Z (consistent with the CFA passage estimated from the wind profiler observations in Winnfield, LA; Fig. 27a), and low-level convergence and ascent were analyzed within the underlying moist layer at and just behind the CFA (Fig. 29b). Furthermore, potential instability had increased behind the CFA due to elevated drying and CAA, which manifested as a region of high MLCAPE and low MLCIN over the western half of Louisiana (Fig. 24d).

During the afternoon, CI occurred primarily (but not exclusively) along two bands (shown at ~27/1730Z in Fig. 33a) that were oriented approximately southwest-northeast—nearly parallel to the low-level flow (Figs. 19e and 22d,e) and conducive to long parcel

[4]In Figs. 33a-c, we labeled these layers with an asterisk if they were not fully saturated.

residence times within mesoscale updrafts. At 27/1700Z, multiple supercells were developing over northwestern Mississippi near and to the north of the effective warm front (Figs. 19e,f). These cells were aligned with the dryline but extended beyond where the dryline was detectable at the surface, and their formation largely resulted from forcing by the tropopause fold and accompanying CFA. CI was ongoing along much of the dryline by 27/1900Z, while the warm sector band over central Mississippi had become a prominent arc-shaped corridor of agitated cumulus and developing supercells that preceded a region of suppressed cloud cover and veered surface winds (Figs. 29f, 31a). This band coincided with a prefrontal trough and was attributed to mesoscale forcing ahead of the CFA (Figs. 31b-d).

A vertical cross section oriented across the warm sector band at 27/1900Z depicted an intrusion of low-θ_e air between 850–700 hPa that extended over Mississippi at the periphery of the sloping tropopause fold (Fig. 29c). The warm sector band was well aligned with the leading edge of this elevated intrusion layer, which was apparent in the isentropic analysis (Fig. 29f) and in plots of 3-h θ_e change at 800 hPa (Fig. 31d). Compared to the strong subsidence actively occurring behind the dryline in Monroe (Fig. 32a), trajectories initialized from Jackson depicted a shallow tongue of low-θ_e air between ~2–3 km that rapidly descended from the upper troposphere over West Texas before ~27/0300Z and continued to gradually subside as it flowed northeastward along the Texas Gulf Coast, ultimately overrunning the low-level moist layer while undercutting the EML plume from the Mexican Plateau (Fig. 32b). This signature was absent in trajectories initialized from Meridian and Montgomery as the CFA remained upstream (Figs. 32c,d).

Although baroclinity was weak across the CFA, the disturbance was evidently capable of promoting CI over central Mississippi. As shown in Fig. 29c, winds in the lower troposphere shifted behind the CFA and became increasingly veered farther toward the west where the layer of elevated CAA and PBL mixing were both deeper. Accordingly, a broad region of confluence, enhanced cyclonic vorticity, and convergence had developed within the underlying moist PBL and was apparent over much of Mississippi and Louisiana at

27/1900Z (Figs. 31b,c). Additionally, an axis of enhanced MLCAPE (3000–4500 J kg^{-1}) had formed over central Mississippi owing to destabilization (via lifting and differential advection) stemming from the CFA. The net effect of this destabilization was evident in the Jackson sounding, which was released *within the warm sector cloud band* at ~27/1730Z (Fig. 33). Compared to the Slidell and Birmingham soundings, the Jackson sounding exhibited steeper lapse rates throughout the lower and middle troposphere and greater veering within the PBL. *Thus, mesoscale ascent and cooling aloft associated with the CFA concurrent with continued surface heating and PBL destabilization were likely responsible for producing the warm sector band of supercells in Mississippi.* This evolution is explored further in Chapter 6.

3.3.3.2 Environmental and convective evolution

By 27/2100Z, numerous tornadic supercells were ongoing over the Southeast and persisted for several hours before eventually growing upscale during the late evening (Figs. 16i-l). MLCAPE continued to increase throughout the afternoon, and a widespread region of MLCAPE = 4000–5500 J kg^{-1} was located over Mississippi behind the CFA by 27/2100Z, while MLCAPE > 2000 J kg^{-1} extended into the destabilizing cold pool over northern Mississippi and Alabama (Fig. 24e). These remarkably high MLCAPE values were noted by Thompson et al. (2013) to lie above the 90th percentile for all significant tornadic supercell events in the Southeast. The vertical shear profiles over the Southeast were also incredibly conducive to the formation of long-lived tornadic supercells. 0–1-km and 0–6-km BWD values of 40–65 kt and 60–80 kt, respectively (Figs. 24d-f and 26d-f), and 0–1-km SRH values of 300–800+ m^2 s^{-2} persisted throughout the supercell outbreak and were on the extreme end of the parameter space for significant tornado environments, especially when paired with such high MLCAPE (e.g., Rasmussen and Blanchard, 1998; Rasmussen, 2003; Thompson et al., 2003; Garner, 2012).

The effective warm front bounded a mesoscale region of extremely high (> 500 m^2 s^{-2}) 0–1-km SRH along which several long-track, violent tornadoes formed, while SRH > 300 m^2 s^{-2} extended south of this boundary throughout the warm sector (Figs. 18 and 26d-f). Storm-relative hodographs indicate that such high SRH was attributable to ample streamwise vorticity and notably strong storm-relative winds in the lower troposphere that resulted from ~45–55-kt storm motions oriented at a large angle to the LLJ (Figs. 26d-f). The hodographs also depict how the wind profiles were modified behind the CFA, which yielded a slight reduction in low-level curvature as the winds veered and induced a "kink" between 1–3 km (e.g., over western Mississippi at 27/1800Z). However, considerable SRH remained in this environment—likely due to the shallowness of the intrusion layer, as a deeper layer of CAA would presumably promote greater disruption to the hodograph shape and thus diminish the potential for sustained mesocyclones and tornadoes. Although the majority of tornadoes formed within the environment ahead of the CFA, several significant and/or long-track tornadoes were produced by supercells that developed along the dryline (e.g., those over south-central Mississippi in Fig. 18), which solidifies that the hodograph modifications behind the CFA were not detrimental—consistent with recent findings by Parker (2017).

Considerable low-level shear and hodograph curvature were established over the Southeast well before strong deep-layer shear (Fig. 26) due to the accumulated LLJ intensification that began during the previous evening and primarily occurred over two periods *prior to the onset of the supercell outbreak at ~27/1800Z* (Figs. 22). The first and most significant period transpired immediately after QLCS1 developed—the overall effects of which persisted through the remainder of the outbreak. At 1 km, the Winnfield profiler observed that wind speeds doubled from 32 kt to 64 kt between 26/2100Z–27/0400Z, while the Okolona profiler observed an increase from 18 kt to 57 kt between 26/2100Z–27/0700Z (Figs. 25). A second intensification episode ensued ahead of SW_3 after the development of QLCS2, yielding additional wind maxima of 59 kt in Winnfield at 27/1100Z and 58 kt in Okolona at 27/1400Z, which followed a 24-kt increase over 2 h. This secondary LLJ enhancement was concentrated near QLCS2 and thus primarily augmented the low-level shear over the northern portion of the outbreak region (Figs. 26b-d). In contrast, deep-layer shear strengthened over the Southeast throughout the morning as the approaching midlevel jet exit region was split into two branches around QLCS2, yielding a southwesterly branch of J_1 that was adjacent to the system's southern flank (Fig. 21d). This evolution supported elongated hodographs with considerable deep-layer shear that was oriented ~35–45° to the dryline and warm sector bands by 27/1800Z (Fig. 26d). Such a shear configuration favors discrete right-moving supercells given a lack of strong linear forcing and a significant component of the storm motion off the initiating boundary (Bluestein and Weisman, 2000; Dial et al., 2010), which was true during the afternoon. However, the northeastward progression of the midlevel jet core and its intensification throughout the evening led to temporal changes in the storm motion and shear orientation relative to the mesoscale forcing (Figs. 21e,f and 26e,f). This evolution—paired with the increase in linear forcing along the occluded and surface cold fronts—resulted in convection growing upscale with time, particularly in the northern and western portions of the outbreak region (Figs. 16j-l). Although the LLJ had become increasingly coupled to the J_1 exit region and further intensified as the jet advanced northeastward into the Ohio Valley (Figs. 21f, 22f), this overall progression promoted a growing separation between the region of strongest shear and the favorable thermodynamic environment over the Southeast (Figs. 24f, 26f). Consequently, tornado activity generally waned during the nighttime congruent with this upscale growth.

3.4 Summary and discussion

Herein we provided a multiscale assessment of the environmental conditions present during this extended tornado outbreak, with emphasis given to the ~36-h period spanning QLCS1 through the afternoon supercell outbreak. The primary findings of this chapter are summarized below.

- The outbreak occurred ahead of a highly amplified longwave trough and prominent upper-level jet streak that stemmed from a preceding upstream Rossby wave breaking event. The trough base persisted over the south-central U.S. for multiple days, enabling continued replenishment of potential instability and supporting episodic CI ahead of three successive shortwaves.

- QLCS1 formed ahead of SW_2 and was supported by increasingly strong vertical wind shear to yield conditions known to support significant QLCS tornadoes. Low-level shear rapidly strengthened as the LLJ intensified over the warm sector after CI and was oriented largely parallel to QLCS1, providing ample streamwise vorticity for inflowing parcels. Tornadic QLCSs in the Southeast are often preceded by strong line-parallel shear associated with the LLJ (e.g., Sherburn et al., 2016; King et al., 2017), but most studies on the dynamics of quasi-linear convection have solely emphasized the line-normal shear component (e.g., Weisman, 1993; Weisman and Trapp, 2003), warranting that greater attention be given to the behavior of quasi-linear convection in such environments.

- The movement of SW_3 into the SGP preceded the development of QLCS2 and was accompanied by continued deepening of the tropopause fold, intensification of the midlevel jet, and the formation of a CFA. Destabilization in the wake of QLCS1 plus convergence ahead of the CFA and near the LLJ terminus enabled the formation of QLCS2. QLCS2 remained elevated throughout most of its lifetime and exhibited a complex morphological evolution as it interacted with dry midlevel air and a rapidly intensifying LLJ. The system developed into a bow echo during the late morning before transitioning into a widespread region of disorganized convection.

- The afternoon supercell outbreak was associated with a coupled upper-level jet configuration and commenced as SW_3 moved into the Lower Mississippi Valley behind

QLCS2. However, the supercell outbreak was neither associated with a highly diffluent shortwave trough nor rapid surface cyclogenesis, and the strong LLJ present over the Southeast largely originated from the accumulated flow intensification that followed the development of QLCS1 and QLCS2.

- The surface Pacific cold front acquired characteristics of a dryline owing to postfrontal sensible heating and PBL mixing, which promoted the downward transport of incredibly dry air that descended atop the moist layer behind the CFA. The dryline advanced northeastward during the daytime and remained preceded by a CFA, which manifested as an elevated intrusion of low-θ_e air that promoted the formation of a band of supercells over the warm sector. A distinct surface cold front—which would have promoted strong linear forcing for ascent and hindered the ability for storms to remain discrete—was absent over the Southeast until later in the evening.

- The unique overlap of anomalously large buoyancy, significant vertical wind shear and SRH, and organized CI within the warm sector supported the prolific nature of the supercell outbreak. High MLCAPE was supported by PBL destabilization, strong differential advection ahead of SW_3, and steep midlevel lapse rates within an EML; further destabilization occurred following the CFA passage. Deep-layer shear increased as the midlevel jet approached the region and was split around QLCS2, yielding elongated hodographs with ample curvature and shear vectors that were oriented favorably to the dryline and CFA for the development and sustenance of discrete supercells.

Several findings obtained from this analysis warrant further investigation. In particular, the remarkable large-scale flow evolution that occurred after QLCS1 developed motivates our hypothesis that the system—which was expansive and contained a sustained region of latent heating—was directly responsible for producing environmental modifications that enhanced its own severity and persisted throughout the remainder of the outbreak. Furthermore, interactions between QLCS2 and the midlevel jet and the possibility that QLCS2 provoked or contributed significantly to the second period of LLJ intensification should be evaluated, as this evolution directly influenced the environment during the supercell outbreak. The significance and dynamics of the environmental modifications produced by the QLCSs are thoroughly examined in the following chapter. Additionally, the evolution of the CFA and how it promoted mesoscale destabilization and CI over the Southeast are explored further in Chapter 6.

Chapter 4

Environmental modifications and upscale feedbacks arising from latent processes

4.1 Introduction

In this chapter, we expand upon the findings in Chapter 3 by providing a detailed dynamical investigation into the upscale environmental modifications produced by QLCS1 and QLCS2 and how they contributed to the overall outbreak severity and evolution. Specifically, we use environmental fields from the RUC model and convection-permitting WRF-ARW simulations configured with and without latent heating to demonstrate that the QLCSs collectively altered the environment on multiple scales prior to the afternoon supercell outbreak. Particular attention is given to evaluating whether the dramatic environmental modifications produced by QLCS1 may have ultimately heightened the system's severity and longevity—an upscale feedback effect. Furthermore, we investigate the physical processes responsible for establishing highly favorable shear profiles over the Southeast during the supercell outbreak and—through partitioning the hodographs into their geostrophic and ageostrophic counterparts—demonstrate the overwhelming control by ageostrophic motions on the shape of the hodograph and the strength of the vertical wind shear. The contents of this chapter were recently published as Part II of a two-part paper in *Monthly Weather Review* (Chasteen and Koch, 2021b).

4.2 Background on environmental adjustments to convection

Various environmental modifications stemming from deep moist convection have been documented in the literature over the past few decades. These include the development of pressure perturbations and resultant (unbalanced) divergent secondary circulations comprising upper-level outflow, low-level inflow, and compensating subsidence and the environmental adjustments that occur via the outward propagation of low-frequency gravity waves (e.g., Bretherton and Smolarkiewicz, 1989; Nicholls et al., 1991; Olsson and Cotton, 1997; Lane and Reeder, 2001; Liu and Moncrieff, 2004). For simplicity, these adjustments have often been studied within the context of idealized convection that develops in isolation and is thus not interacting with a background baroclinic environment. An additional subset of studies has focused on the upscale effects and circulations that arise from organized mesoscale convective systems (MCSs; the largest of which are classified as mesoscale convective complexes) that typically develop within weakly forced environments during the midlatitude warm season (e.g., Maddox, 1980). Unlike with ordinary convection, MCSs persist for several hours, occupy a much larger spatial scale at which Coriolis effects are significant (i.e., a scale comparable to the Rossby radius of deformation; Cotton et al., 1989), and have considerably more complex heating profiles that vary between the convective and stratiform regions of the system (e.g., Houze, 1989).

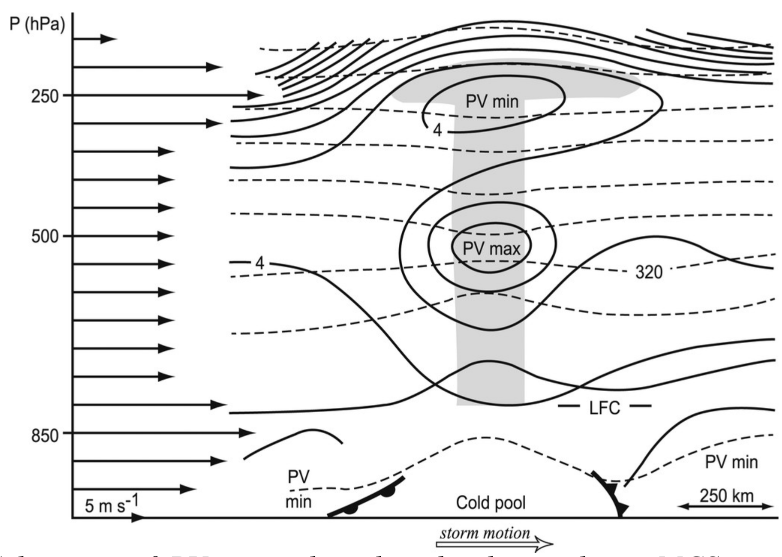

Figure 34: *Schematic of PV anomalies that develop in large MCSs owing to vertical gradients in latent heating. Dashed lines represent potential temperature (every 5 K), and solid lines are PV (every 2×10^{-7} m^2 s^{-1} K kg^{-1}; a contour value of 4 represents 0.4 PVU). Figure adapted from Houze (2018) based on an original schematic in Fritsch et al. (1994).*

As convection grows upscale into a large MCS, geostrophic adjustment promotes the gradual transition from divergent circulations toward rotational (balanced) circulations and accompanying PV anomalies (e.g., Cotton et al., 1989; Raymond and Jiang, 1990; Olsson and Cotton, 1997). The timescale of this balance adjustment process is inversely related to the Coriolis parameter f and is thus dependent upon the latitude at which the MCS develops (e.g., Blumen, 1972). For MCSs in midlatitudes, studies have shown that these balanced circulations tend to develop after ~3–6 hours (e.g., Davis and Weisman, 1994; Olsson and Cotton, 1997). The formation of these PV anomalies results from spatial variations in diabatic heating occurring in the presence of preexisting vorticity and is understood through the tendency equation for Ertel's PV (Ertel, 1942), which in isobaric coordinates can be approximated by its vertical component[1] as follows if the effects of friction are neglected:

$$\frac{d(PV)}{dt} \approx -g(\zeta + f)\frac{\partial \dot{\theta}}{\partial p}, \tag{4.1}$$

where g is the gravitational acceleration, ζ is the relative vertical vorticity, and $\dot{\theta}$ is the diabatic heating rate. Accordingly, a negative PV anomaly and perturbation anticyclone generally develop in the upper troposphere above the level of maximum heating, and a positive PV anomaly and perturbation cyclone (i.e., a mesoscale convective vortex; MCV) generally develop in the middle to lower troposphere beneath the level of maximum heating within an MCS (e.g., Maddox, 1980; Bartels and Maddox, 1991; Fritsch and Maddox, 1981; Cotton et al., 1989; Davis and Weisman, 1994; Olsson and Cotton, 1997). These diabatic PV anomalies are shown schematically in Fig. 34.

The height and wind perturbations accompanying MCSs are often large and may promote upscale flow modifications and jetogenesis (Bluestein, 1993, p. 394–395)—particularly downstream from the system at upper levels (i.e., an outflow jet) and along its flanks

[1]More precisely, PV generation arises from gradients in diabatic heating that exist along the total vorticity vector. In the absence of vertical wind shear and ambient relative vertical vorticity, the total vorticity vector is entirely dictated by f and thus points upward. However, in a strongly sheared environment, the resultant PV dipole acquires a slope owing to the dominance of horizontal vorticity and is thus more complicated than the simplified description presented herein.

where the background height gradient becomes amplified (e.g., Ninomiya, 1971; Maddox et al., 1981; Anthes et al., 1982; Wetzel et al., 1983; Keyser and Johnson, 1984; Wolf and Johnson, 1995; Rowe and Hitchman, 2016). Furthermore, MCSs may influence surface cyclogenesis—both through diabatic amplification and enhancing the background baroclinity—a process that is sensitive to the MCS location relative to the baroclinic wave (e.g., Zhang and Harvey, 1995; Stensrud, 1996). Overall, numerous studies have demonstrated that latent heating may notably impact the structure and dynamics of baroclinic waves and extratropical cyclones (e.g., Kuo et al., 1991; Davis and Emanuel, 1991; Whitaker and Davis, 1994; Stoelinga, 1996; Dickinson et al., 1997; Wernli et al., 2002; Zhang et al., 2007).

Highly amplified and slowly moving synoptic patterns are common during tornadic events in the Southeast (e.g., Galway and Pearson, 1981; Guyer et al., 2006; Sherburn et al., 2016) and—in general—often support prolonged periods of active convection (e.g., Stensrud, 1996; Hamill et al., 2005). Sustained interactions between mesoscale regions of latent heating and a strongly baroclinic environment may induce considerable upscale flow modifications that ultimately act as feedbacks to enhance the severity and persistence of ongoing or subsequent convection. This may occur through upper-level alterations that enhance forcing for ascent near the convection and/or through LLJ intensification, which yields stronger vertical wind shear, poleward moisture transport, and moisture convergence (e.g., Ninomiya, 1971; Keyser and Johnson, 1984; Wolf and Johnson, 1995; Lackmann, 2002). Such modifications often compound during multiepisode convective events. Stensrud (1996) found that multiple convective systems occurring over 2–3 days collectively amplified the large-scale flow pattern, strengthened the LLJ, and increased poleward moisture transport throughout the warm sector—favorable conditions for subsequent convective development. Furthermore, Trapp (2014) found that tornado outbreaks often culminate following multiday periods of severe weather and hypothesized that this tendency may be attributable to upscale feedbacks produced by convection during the previous days. Owing to the established difficulty in accurately predicting convective events in the Southeast (e.g., Dean and Schneider, 2008; Rasmussen, 2015) and the general predictability challenges inherent in forecasting individual convective episodes (e.g., Zhang et al., 2007; Melhauser and Zhang, 2012; Weisman et al., 2015), an evaluation of the scale interactions and upscale feedbacks that occur during multiepisode severe outbreaks in the Southeast is warranted.

4.3 Environmental modifications and scale interactions

4.3.1 Role of convection in upper-level flow modifications

Based on the environmental evolution presented in Chapter 3, we hypothesize that complex scale interactions and upper-level flow modifications—including alterations to the height field and jetogenesis—occurred in response to the development of QLCS1 and QLCS2. Processes driving these modifications are now examined within the context of: (1) PV modifications by diabatic heating and upper-level convective outflow, and (2) flow imbalance and upper-level accelerations.

Upper-level PV modifications and jet streak formation Modifications to the upper-level PV field by convection occur through two primary processes: (1) the vertical redistribution of PV by latent heating (i.e., upper-level PV "erosion" owing to negative diabatic PV tendency via Eq. 4.1), and (2) the vertical transport and subsequent horizontal advection of low-PV air by divergent upper-level convective outflow (hereafter "negative PV advection"). Studies have demonstrated that latent heat release occurring near a strong background PV gradient (i.e., near the jet stream) and ahead of a midlatitude trough may promote downstream ridge amplification and a decrease in the wavelength of the large-scale flow pattern, which enhances forcing for ascent downstream from the trough while simultaneously hindering its eastward propagation (e.g., Davis and Emanuel, 1991; Stoelinga, 1996; Stensrud, 1996; Riemer et al., 2008; Archambault et al., 2015; Steinfeld and Pfahl, 2019; Winters and Martin, 2016; Winters et al., 2020). Furthermore, convection may steepen the PV gradient across the tropopause to promote upper-level jetogenesis[2] (e.g., Archambault et al., 2013;

[2]Within a balanced (e.g., quasi-geostrophic) framework, this process can be understood through a derived relationship between PV and anomalies in the geopotential height field. Following this relationship, a strengthening horizontal PV gradient would correspond to a strengthening geopotential height gradient, which yields an intensification of the *balanced* component of the horizontal wind field (e.g., Davis, 1992; Morgan and Nielsen-Gammon, 1998; Pyle et al., 2004).

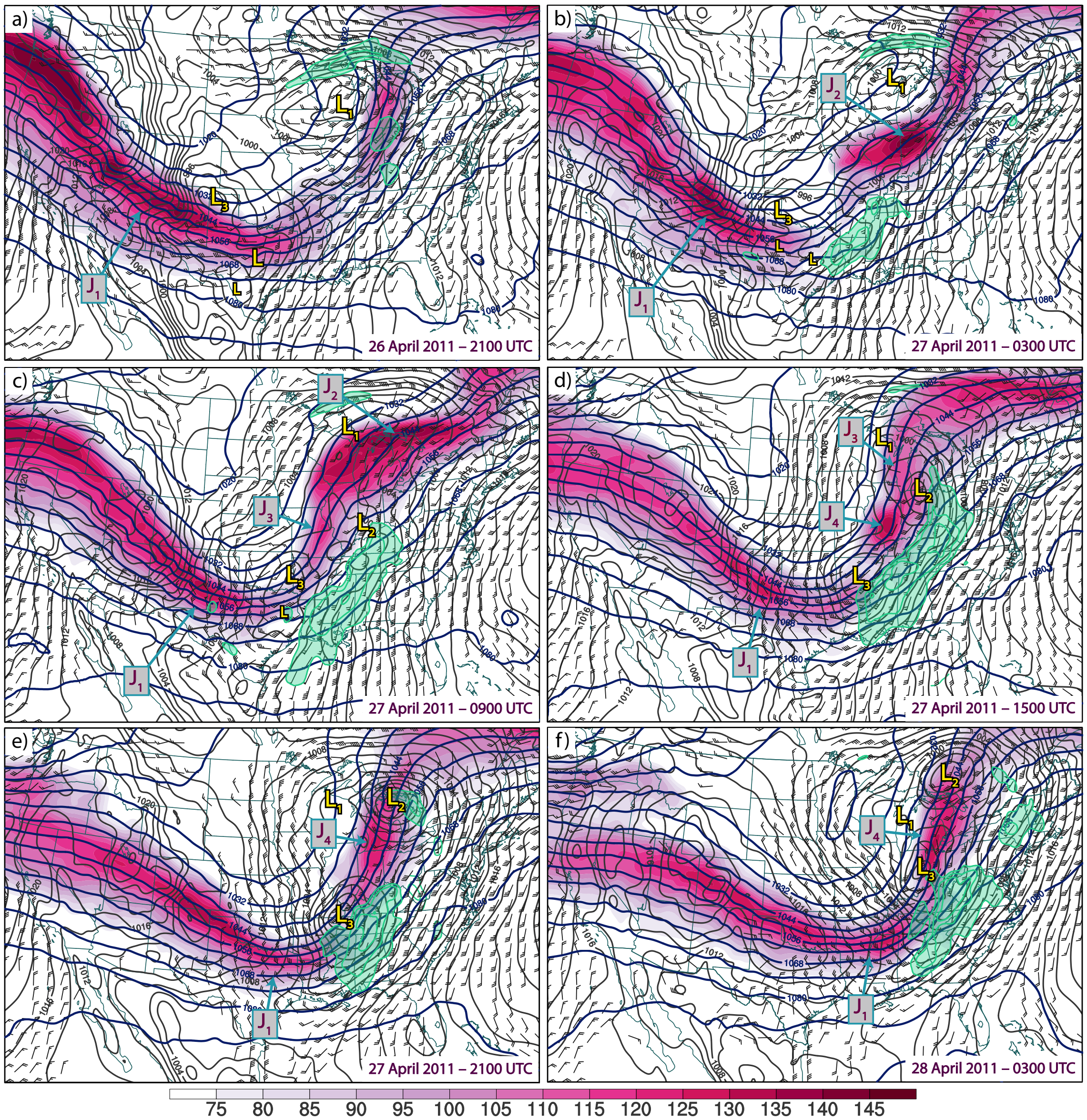

Figure 35: *250-hPa wind speed (pink shading; kt), 250-hPa geopotential height (blue contours; dam), SLP (gray contours; hPa), 850-hPa winds (barbs; kt), and 850-hPa wind speed (green shading > 50 kt with contours every 10 kt ≥ 50 kt) from the corresponding RUC 1-h forecast valid at (a) 2100 UTC 26 April, (b) 0300 UTC 27 April, (c) 0900 UTC 27 April, (d) 1500 UTC 27 April, (e) 2100 UTC 27 April, and (f) 0300 UTC 28 April 2011. Low pressure centers are denoted by a yellow "L".*

Grams et al., 2013; Grams and Archambault, 2016; Rowe and Hitchman, 2016) and—in some instances—tropopause folding (e.g., Atallah and Bosart, 2003; Rowe and Hitchman, 2015).

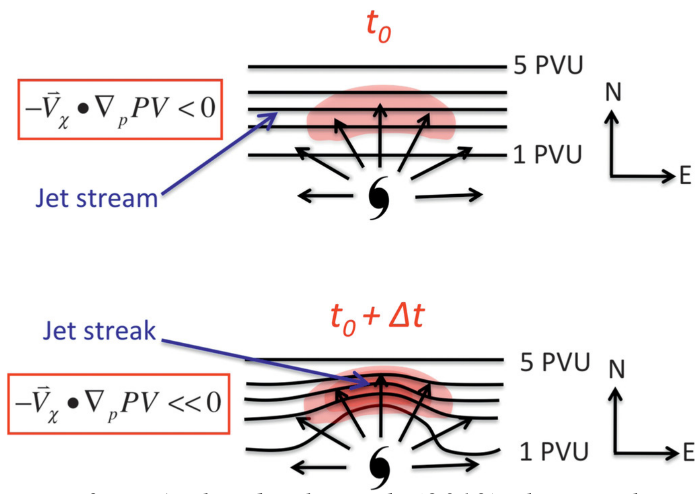

Figure 36: *Schematic from Archambault et al. (2013) showing how the divergent outflow from a tropical cyclone impinging upon the upper-level waveguide leads to ridge amplification and jetogenesis. Vectors represent the upper-level divergent (irrotational) wind component associated with convective outflow, and shading represents negative PV advection by the divergent wind component.*

Figure 36 shows conceptually how upper-level ridge amplification and jetogenesis can arise as a mesoscale region of convection—in this case, associated with a tropical cyclone—distorts the waveguide (Archambault et al., 2013). As in Fig. 36, the influence of convection on the upper-level PV field may be ascertained by (1) partitioning the horizontal wind into its rotational and divergent components ($\vec{V}_\psi = \hat{k} \times \nabla\psi$ and $\vec{V}_\chi = \nabla\chi$, respectively, where ψ is streamfunction, χ is velocity potential, and $\hat{k}$ is the unit normal vector along the z axis), and (2) computing PV advection by the divergent wind component ($-\vec{V}_\chi \cdot \nabla_p PV$, where the subscript p represents an isobaric surface), which is dominated by strong convective outflow. We employ this technique herein.

The manner in which QLCS1 altered the PV distribution and upper-level flow pattern is explained with reference to Fig. 37, which shows the temporal evolution of 250-hPa wind speed, 250-hPa PV, 300–200-hPa layer-averaged divergent winds, negative PV advection by the divergent wind component, and observed radar reflectivity. The onset of CI during

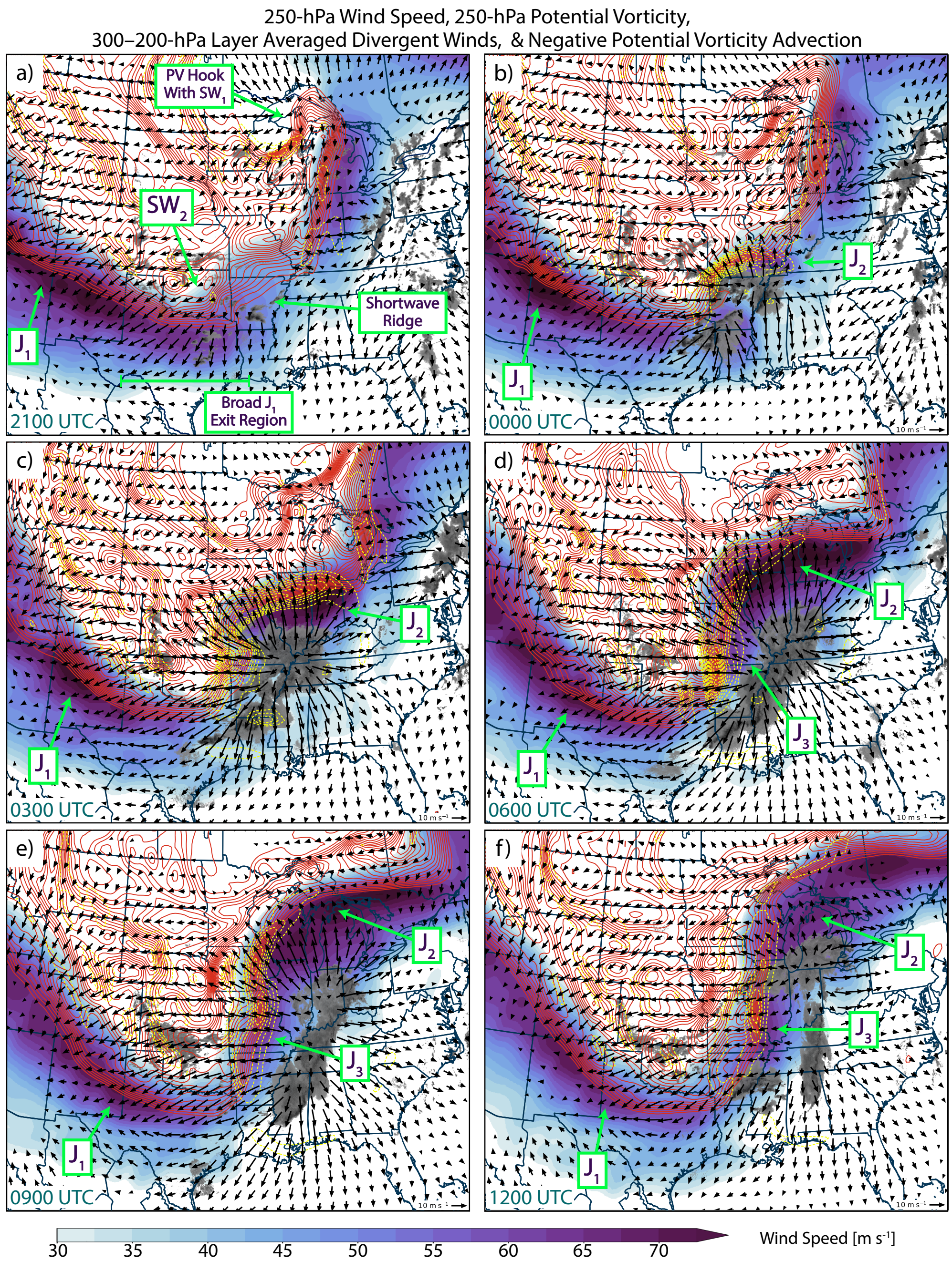

Figure 37: *Composite radar reflectivity > 20 dBZ (gray shading) overlaid with 250-hPa wind speed (purple shading; m s^{-1}), 250-hPa PV (orange contours; every 0.5 PVU ≥ 2 PVU), divergent winds averaged over the 300–200-hPa layer (vectors; m s^{-1}), and negative 250-hPa PV advection by the layer-averaged divergent winds (yellow dashed contours; contoured every 10^{-4} PVU s^{-1} ≤ -1 × 10^{-4} PVU s^{-1}) from the corresponding RUC 1-h forecast valid at (a) 2100 UTC 26 April, (b) 0000 UTC 27 April, (c) 0300 UTC 27 April, (d) 0600 UTC 27 April, (e) 0900 UTC 27 April, and (f) 1200 UTC 27 April 2011.*

the evening of 26 April was accompanied by the rapid development of strong convective outflow within broader J_1 exit region over the SGP and immediately downstream from SW_2 (Figs. 37a,b). Over eastern Texas, pre-dryline convection produced convective outflow that largely opposed the background westerly flow within the upper-level jet (Figs. 37b,c). Additionally, widespread convection developed over Arkansas beneath a shortwave ridge (i.e., a region of relatively higher tropopause and reduced 250-hPa PV) and adjacent to a largely meridional upper-level PV gradient that was established in the wake of SW_1 (Fig. 37a). Following CI, diabatic PV erosion acting together with strong negative PV advection quickly sharpened the preexisting PV gradient over western Missouri and Arkansas (i.e., steepened the tropopause) and consequently induced J_2 immediately downstream (Figs. 37b-e). J_2 rapidly strengthened and advanced poleward with time in conjunction with sustained negative PV advection, which promoted upper-level ridge amplification and effectively shifted the longwave trough axis westward (by reducing its horizontal wavelength while counteracting its eastward progression; Figs. 35a-c). As QLCS1 grew upscale into a meridionally elongated system, the upper-level PV gradient to its west strengthened considerably, leading to the genesis of J_3 and ultimately the formation of a tropopause fold with SW_2 (hereafter the "secondary tropopause fold"; Figs. 16c-f and 37c-f). This evolution effectively led to a westward shift in the longwave trough axis (i.e., a decrease in the wavelength of the midlatitude trough) and promoted the amplification of the downstream ridge (Figs. 35a-c). *Therefore, the widespread development of deep moist convection immediately on the equatorward side of a preexisting upper-level PV gradient promoted upstream jet modifications, downstream J_2 development, downstream ridge amplification, and a notable decrease in the wavelength of the upper-level pattern.*

Just after 27/0900Z, QLCS2 formed ahead of SW_3 and adjacent to the tightened PV gradient that had become established over Arkansas behind QLCS1 (Figs. 16e, 37e). Overall, QLCS2 produced upper-level flow modifications that were qualitatively similar but comparatively less substantial than those arising from QLCS1—likely due to its smaller spatial scale (O(500–600) km versus O(1200–1300) km for QLCS1) and the location where it formed relative to the background PV distribution, which had been dramatically altered by QLCS1. The PV modifications produced by QLCS2 were more discernible at a slightly

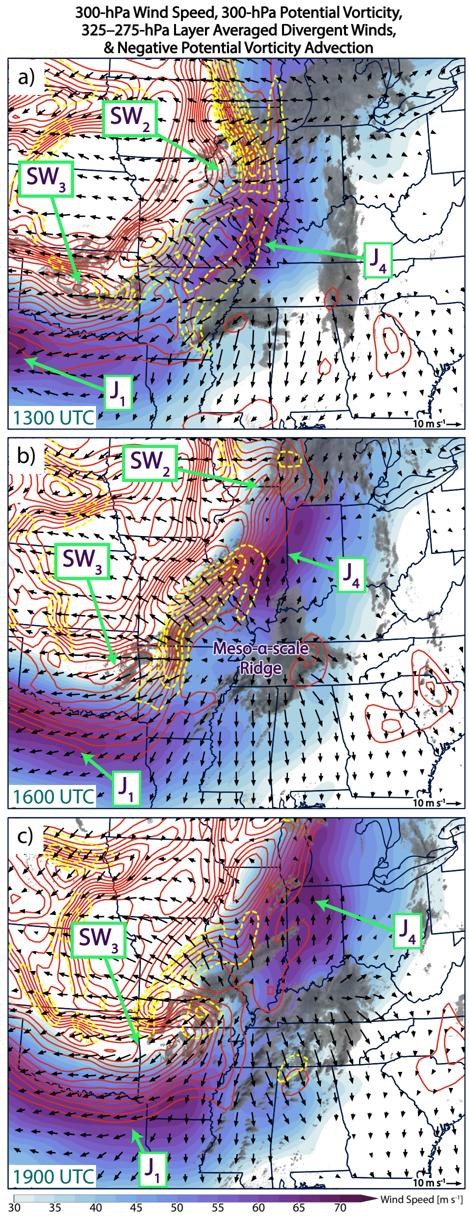

Figure 38: *Composite radar reflectivity > 20 dBZ (gray shading) overlaid with 300-hPa wind speed (purple shading; m s^{-1}), 300-hPa PV (orange contours; every 0.5 PVU ≥ 2 PVU), divergent winds averaged over the 325–275-hPa layer (vectors; m s^{-1}), and negative 300-hPa PV advection by the layer-averaged divergent winds (yellow dashed contours; contoured every 10^{-4} PVU s^{-1} ≤ -1 × 10^{-4} PVU s^{-1}) from the corresponding RUC 1-h forecast valid at (a) 1300 UTC, (b) 1600 UTC, and (c) 1900 UTC 27 April 2011.*

lower level than those stemming from QLCS1, so the same fields displayed in Fig. 37 are shown for the 325–275 hPa layer in Fig. 38. As depicted in Fig. 38a, QLCS2 had moved into northwestern Mississippi by 27/1300Z and was located east of SW_3 and immediately south of an eastward PV protrusion that corresponded to the amplifying SW_2. Owing to strong negative PV advection and diabatic PV erosion, a meso-α-scale ridge developed just downstream from SW_3, and the background PV gradient sharpened to the northwest of QLCS2 (Fig. 38b). J_4 formed over the Midwest in association with this sharpened PV gradient and advanced poleward with time, being situated ~800–1000 km downstream from the warm sector at 27/1900Z as the supercell outbreak was commencing over the Southeast (Fig. 38c).

Dynamical flow imbalance and upper-level adjustments Within the context of flow imbalance and jet dynamics, we now further analyze these upper-level modifications. From the inviscid equation for horizontal motion,

$$\frac{d\vec{v}}{dt} = f\,\vec{v_a} \times \hat{k}\,, \tag{4.2}$$

where $\vec{v}$ is the horizontal wind vector and $\vec{v_a}$ is the ageostrophic wind vector, one can deduce that parcel accelerations occurring under the influence of Coriolis effects are directed orthogonal and to the right of the ageostrophic wind vector. For a straight jet streak that obeys quasi-geostrophic (QG) or semi-geostrophic balanced dynamics (Hoskins, 1975), a four-cell pattern of divergence and vertical motion develops in association with thermally direct and indirect transverse ageostrophic circulations that straddle the jet entrance and exit regions, respectively, and constantly act to restore thermal wind balance (e.g., Uccellini and Johnson, 1979; Keyser and Shapiro, 1986). The cross-isohypse upper branches of these ageostrophic circulations provide along-stream accelerations and decelerations for parcels in the jet entrance and exit regions, respectively. Owing to complexities like flow curvature and thermal advection, the distribution of ageostrophic and vertical motions may deviate significantly from this simplified jet model while still maintaining thermal wind balance (e.g., Keyser and Shapiro, 1986).

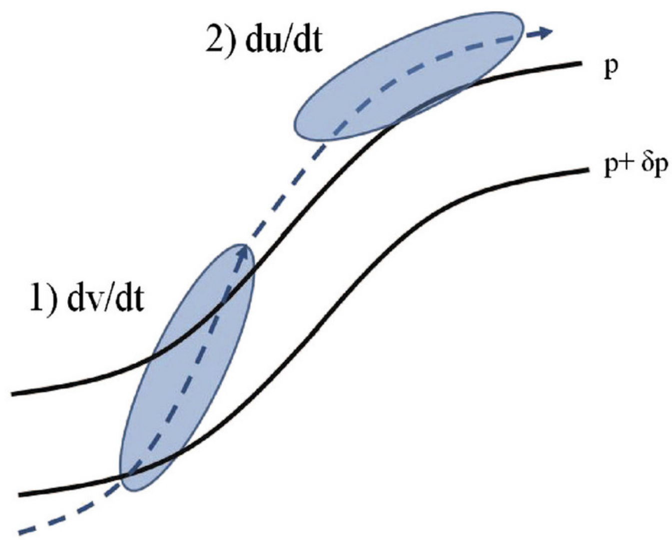

Figure 39: *Schematic from Rowe and Hitchman (2016) showing the relationship between dynamical imbalance, inertial instability, and poleward jet surges. In Stage 1, the meridional flow accelerates down the meridional pressure gradient in the presence of negative zonal ageostrophic flow. In Stage 2, the zonal flow accelerates because of the Coriolis torque on the strong meridional flow in the presence of a weak zonal pressure gradient.*

In contrast, jet streaks may instead be *dynamically unbalanced* and thus comprise circulations cannot be satisfactorily explained using the geostrophic momentum approximation (i.e., $\frac{d\vec{v_a}}{dt}$ is non-negligible; Hoskins, 1975) or other balance conditions (e.g., Charney, 1955). These disturbances are typically accompanied by large parcel accelerations, considerable mass divergence, and strong vertical motions (e.g., Van Tuyl and Young, 1982; Keyser and Johnson, 1984; Uccellini et al., 1984; Rowe and Hitchman, 2016). Moreover, unbalanced jet streaks often are displaced downstream from their geostrophic counterparts, develop in response to abrupt changes in flow curvature, and induce an exceptionally strong LLJ via isallobaric forcing (e.g., Uccellini et al., 1984; Uccellini and Koch, 1987; Koch and Dorian, 1988). Highly unbalanced jets may be characterized by dynamical instabilities, such as inertial instability or symmetric instability, which facilitate enhanced parcel accelerations (e.g., Emanuel, 1979; Koch et al., 1998; Schultz and Schumacher, 1999; Rowe and Hitchman, 2016). For example, Rowe and Hitchman (2016) show that the formation of convection immediately downstream from a midlatitude trough may induce inertial instability and promote the development of an unbalanced upper-level jet streak, which rapidly strengthens and surges poleward until it regains balance at higher latitudes (shown schematically in Fig. 39). Additionally, the development of flow imbalance is known to coincide with the emission of (often high amplitude) mesoscale inertia-gravity waves (e.g., Uccellini and Koch, 1987; Koch and Dorian, 1988; Zhang et al., 2001), which play a significant dynamical role in the mass-momentum adjustment process and aid in the restoration of balance (e.g., Rossby, 1938; Cahn, 1945; Blumen, 1972; Van Tuyl and Young, 1982). These wave disturbances may then promote CI or act to modulate preexisting precipitation systems as they propagate away from their unbalanced source regions (e.g., Miller and Sanders, 1980; Stobie et al., 1983; Koch et al., 1988; Ruppert and Bosart, 2014).

A commonly used diagnostic for evaluating the degree to which mass and momentum fields are dynamically "balanced" is the nonlinear balance equation (NBE), which arises from a scale analysis of the forcing terms in the divergence tendency equation and has proven applicability in highly curved flow and on relatively short timescales (e.g., Charney, 1955; Raymond, 1992; Zhang et al., 2000). The NBE residual diagnostic is given by

$$NBE = 2J(u, v) + f\zeta - \beta u - \nabla^2\Phi\,, \tag{4.3}$$

where $J(u, v)$ is the Jacobian of the horizontal wind components (related to horizontal variations in the momentum field), f is the Coriolis parameter, ζ is the relative vertical vorticity, β is the Rossby parameter, and $\nabla^2\Phi$ is the 2D horizontal Laplacian of geopotential (related to horizontal variations in the mass field). Regions of large positive (negative) values of NBE residual are characterized by large divergence (convergence) tendency and thus do not satisfy nonlinear balance. The NBE and geostrophic wind fields presented herein were low-pass filtered using a Lanczos filter (Duchon, 1979) with a cutoff wavelength (50%

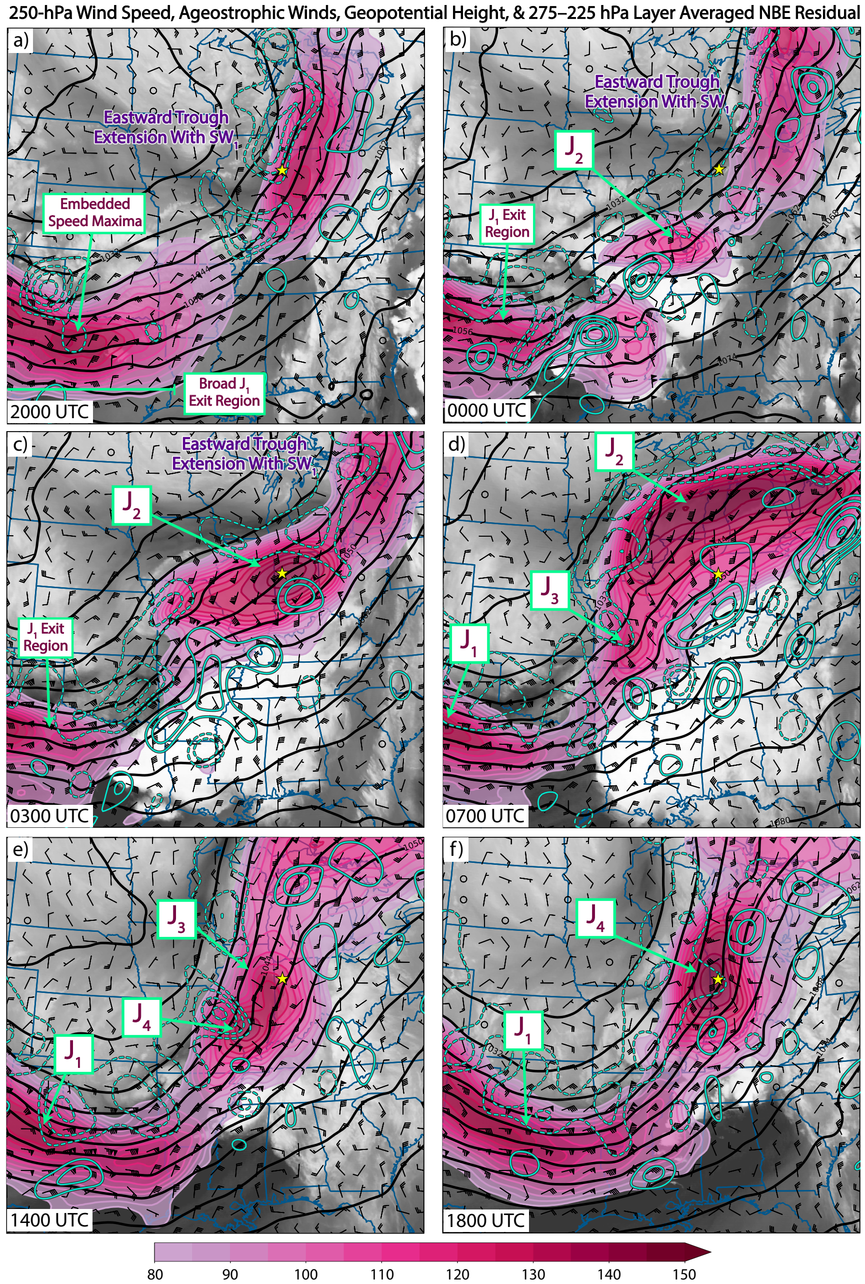

Figure 40: *GOES-13 water vapor imagery overlaid with 250-hPa wind speed (shaded; kt), 250-hPa ageostrophic winds (barbs; kt), 250-hPa geopotential height (black contours; dam), and 275–225-hPa layer averaged NBE residual (positive values shown by solid cyan contours every 1×10*$^{-8}$ *s*$^{-2}$ ≥ *2×10*$^{-8}$ *s*$^{-2}$*; negative values shown by dashed cyan contours every 1×10*$^{-8}$ *s*$^{-2}$ ≤ *-2×10*$^{-8}$ *s*$^{-2}$*) from the corresponding RUC 1-h forecasts valid at (a) 2000 UTC 26 April, (b) 0000 UTC 27 April, (c) 0300 UTC 27 April, (d) 0700 UTC 27 April, (e) 1400 UTC 27 April, and (f) 1800 UTC 27 April 2011. The NBE field was low-pass filtered. The Wolcott, IN, wind profiler location is denoted by the yellow marker.*

response) of 325 km to reduce the signal from gravity waves, which yield large values of $\nabla\Phi$ and $\nabla^2\Phi$ owing to their associated short-wavelength geopotential height perturbations.

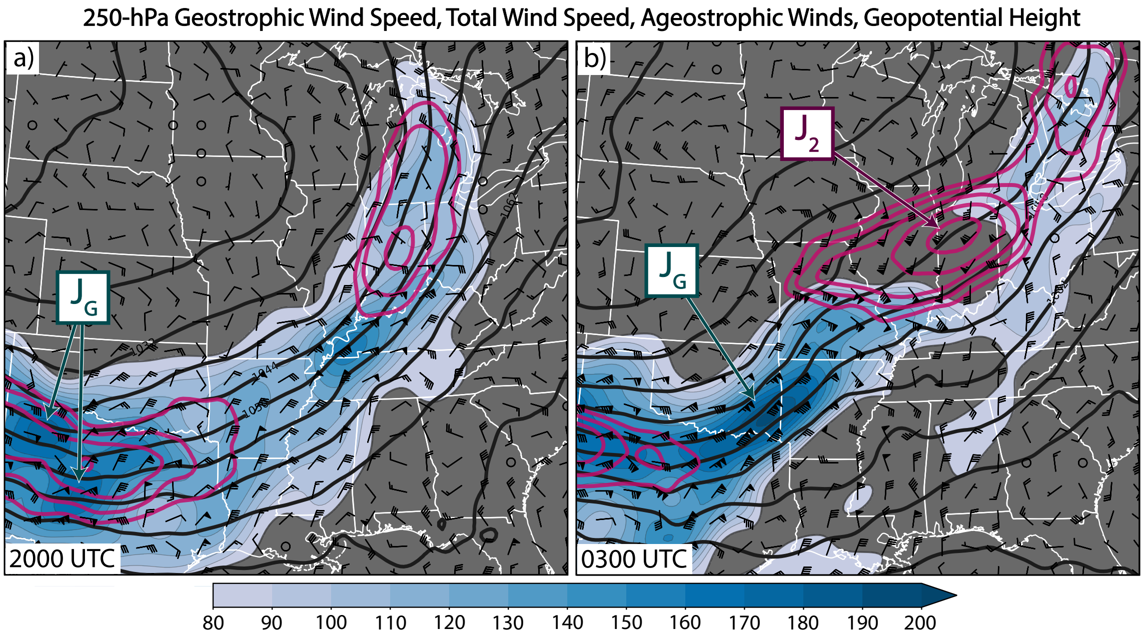

Figure 41: *250-hPa geostrophic wind speed (shaded; kt), 250-hPa total horizontal wind speed (magenta contours; every 10 kt ≥ 100 kt), 250-hPa ageostrophic winds (barbs; kt), and 250-hPa geopotential height (black contours; dam) from the corresponding RUC 1-h forecasts valid at (a) 2000 UTC 26 April and (b) 0300 UTC 27 April 2011. Geostrophic wind maxima are denoted by the teal arrows. The geostrophic wind fields were low-pass filtered.*

The development of strong upper-level ageostrophic motions and flow imbalance is described with reference to Figs. 40 and 41. The upper-level flow was largely balanced at 26/2000Z prior to the formation of QLCS1, when both an embedded upper-level wind maxima associated with SW_2—which was situated within the broader J_1 exit region—and its corresponding geostrophic wind maxima ("J_G") were collocated in the trough base over northern Texas (Figs. 40a, 41a). However, geopotential heights suddenly increased downstream from the trough base and within the jet exit region following CI, yielding a force imbalance that had three primary effects. First, parcel decelerations and mass convergence were dramatically enhanced west of the convection over eastern Texas (as inferred from the increased along-stream gradient in wind speed and large negative values of NBE residual), while the height gradient strengthened immediately upstream (Figs. 40b,c). Accordingly, the thermally indirect circulation about the jet exit region intensified as it became disrupted by convection. Second, the curvature of the height field was amplified, which—combined with the strengthened height gradient—induced notably strong ($>$ 100 kt) upstream-directed ageostrophic flow over the SGP. Finally, widespread convection over Arkansas—which formed south of the eastward trough extension that was established over the Midwest by SW_1—induced a strong isallobaric component that was preferentially directed northwestward *down the height gradient*, yielding considerable accelerations within the J_G exit region (Fig. 41b) and the rapid formation of J_2 downstream over the Midwest.

The onset of flow imbalance and strong upper-level accelerations was accompanied by a dramatic increase in mass divergence within the J_2 entrance region (as evidenced by the region of large positive NBE residual values in Figs. 40c,d), which reinforced the convection and facilitated its rapid upscale growth. Within 5 hours of developing, the maximum 250-hPa wind speeds within J_2 had increased by more than 45 kt to 140 kt as QLCS1 and its outflow jet synchronously advanced poleward with time—an evolution highly analogous to the poleward momentum surges described by Rowe and Hitchman (2016). Additionally, J_3 had formed within the strengthened height gradient to the west of QLCS1 by 27/0700Z, and strong cross-isohypse ageostrophic flow, implied accelerations, and upper-level divergence were prevalent over Arkansas at this time (Fig. 40d). Both of the jet streaks produced by QLCS1 were observed by a NOAA wind profiler located in Wolcott, IN, and are evident in the time-height diagram of wind speed shown in Fig. 25b (see Chapter 3).

In a similar manner, J_4 developed and quickly intensified over the Midwest in response to strong cross-isohypse convective outflow and implied accelerations that resulted from QLCS2 (Figs. 40e,f). As QLCS2 grew upscale throughout the morning, the system remained coupled to the right-entrance region of J_4, which was characterized by strong upper-level divergence and flow imbalance as the jet streak was continually bolstered by convective outflow. J_4 had strengthened to > 140 kt by 27/1800Z (Fig. 40f) and was also observed by the wind profiler in Wolcott (Fig. 25b).

Relationship of flow imbalance to mesoscale gravity waves detected over the region. As we noted above, the onset of dynamical flow imbalance coincides with the emission of mesoscale inertia-gravity waves that alter the mass and momentum fields as they propagate away from their unbalanced source region to yield a newly adjusted balanced state (e.g., Blumen, 1972; Plougonven and Zhang, 2014). Although mesoscale gravity waves were not a primary focus of this investigation, we note that observations from the USArray Transportable Array network were used to study mesoscale pressure perturbations during

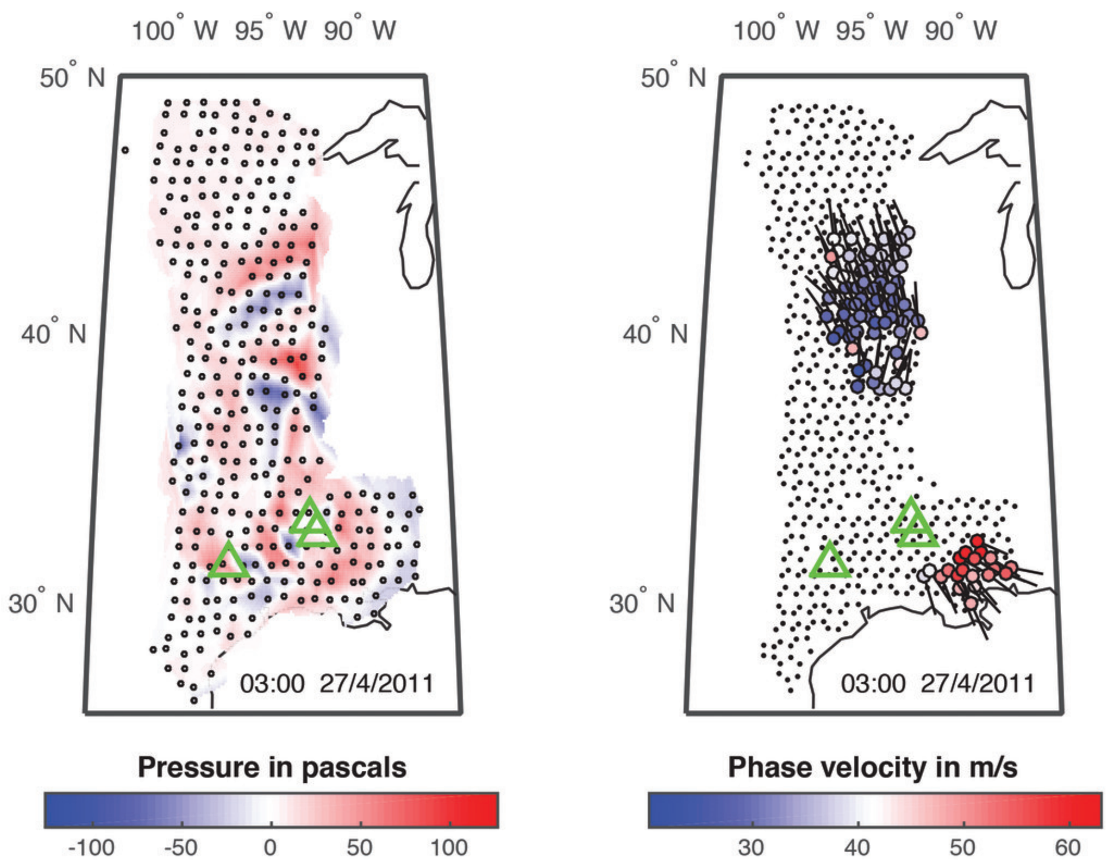

Figure 42: *Spatially interpolated surface pressure perturbations from the USArray at 0300 UTC 27 April 2011 from Tytell et al. (2016). The pressure observations from each station were bandpassed with a period of 2–6 h. The green triangles represent tornado locations that occurred within 15 min of the time stamp. The colored dots denote the wave phase speed, and the lines indicate the direction of wave propagation.*

this outbreak by de Groot-Hedlin et al. (2014), Tytell et al. (2016), and Jacques et al. (2017). Figure 42 from Tytell et al. (2016) shows pressure perturbations[3] at 27/0300Z that were bandpass filtered with a period of 2–6 h such that the propagating disturbances seen over the domain were primarily mesoscale gravity waves (e.g., Uccellini and Koch, 1987). Two main wave packets were evident in the pressure observations at this time: one that was propagating north-northwestward over the Upper Midwest with phase speeds of ~30–45 m s^{-1}, and a second that was propagating southeastward over the Gulf Coast with phase speeds of ~45–60 m s^{-1} (compare to Fig. 14 for improved geographical context).

Figure 43 depicts the temporal evolution of surface pressure perturbations with a period of 2–4 h from de Groot-Hedlin et al. (2014). Prior to CI associated with QLCS1 at 26/1900Z, the pressure perturbations detected by the USArray network had small amplitudes (i.e., much less than 1 hPa). However, the amplitude of pressure perturbations over the region had increased by 26/2100Z following CI, and significant propagating mesoscale disturbances had developed by 27/0100Z—largely downstream from the system but also in its wake. *The emission of these disturbances therefore coincided with the timing and location of the dynamical flow imbalance induced by QLCS1.* The pressure perturbations accompanying these gravity waves suggest that they maintained high amplitudes for several hours as QLCS1 grew progressively upscale and the flow gradually regained balance. By 27/0900Z, the pressure perturbations detected by the observing network over the Upper Midwest had weakened considerably, while larger amplitude mesoscale perturbations continued over the Southeast near the southernmost bowing segment of QLCS1 and over the Ark-La-Tex region where QLCS2 was actively developing.

[3]Animations of these pressure perturbations from de Groot-Hedlin et al. (2014) are available online at `https://ars.els-cdn.com/content/image/1-s2.0-S0012821X13003658-mmc1.mp4` and `https://ars.els-cdn.com/content/image/1-s2.0-S0012821X13003658-mmc2.mp4`.

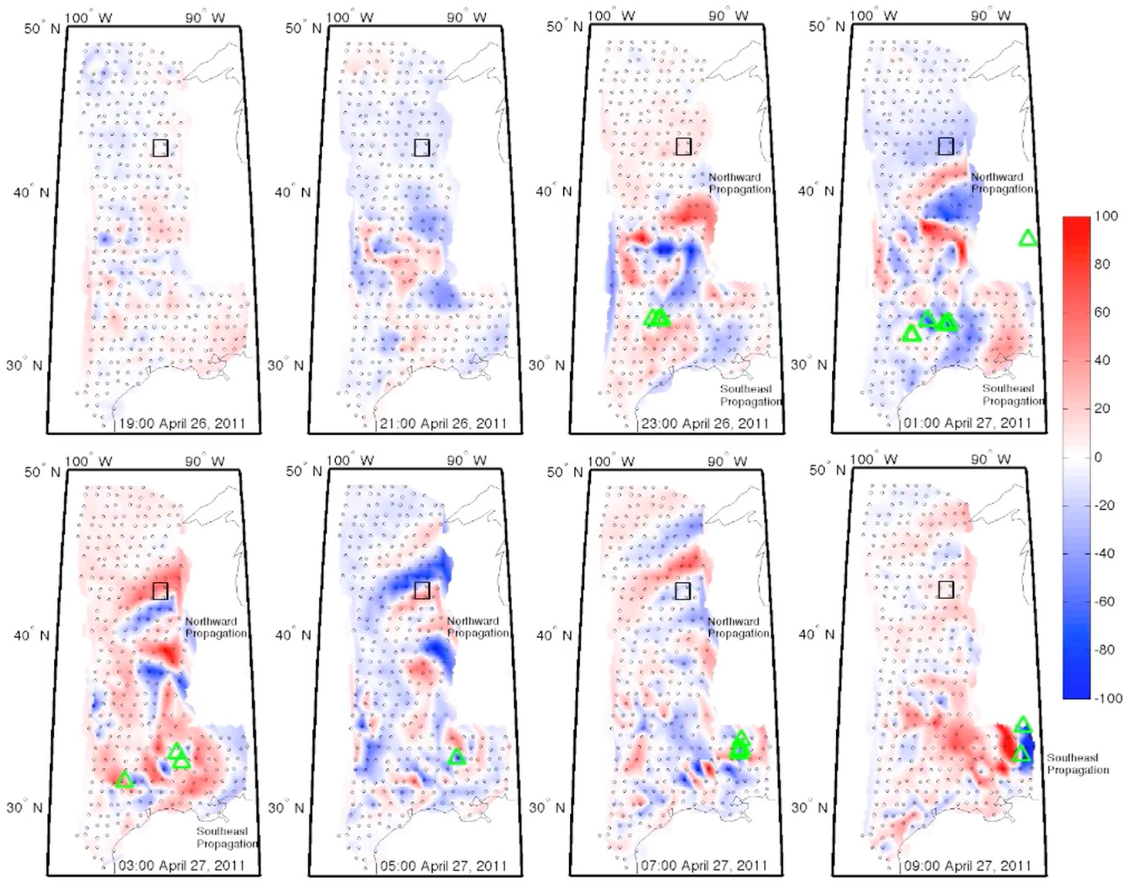

Figure 43: *Spatially interpolated surface pressure perturbations from the USArray every 2 h between 1900 UTC 26 April and 0900 UTC 27 April 2011 from de Groot-Hedlin et al. (2014). The pressure observations from each station were bandpassed with a period of 2–4 h.*

4.3.2 Mid- to upper-tropospheric modifications and tropopause folding

Recall that J_3 formed in association with tropopause steepening behind QLCS1 following its upscale growth. We now describe how this evolution related to the development of the secondary tropopause fold and associated amplification of SW_2 over the Midwest. Shown in Fig. 44 are the potential temperature and geostrophic potential temperature advection fields averaged over the 550–450-hPa layer between 27/0700Z–27/1900Z. As QLCS1 grew progressively upscale overnight, the potential temperature gradient $\nabla\theta$ within the upper and middle troposphere strengthened along the system's northern and western flanks owing to differential thermal advection and diabatic heating. This resultant frontogenesis would induce a thermally direct transverse ageostrophic circulation about the baroclinic zone such that subsidence was enhanced on the polar (cool) side to yield downward transport of high-PV air and tropopause steepening (e.g., Keyser and Shapiro, 1986). Consistent with this expected evolution, a distinct corridor of enhanced midlevel $\nabla\theta$ had developed below the steepened tropopause accompanying J_3 by 27/0700Z (Figs. 37d, 44a) and was paralleled by a band of midlevel subsidence (not shown), with maximum downward motion collocated with a 400-hPa PV anomaly over Missouri that represented the developing tropopause fold (Fig. 45a).

Geostrophic cold advection (hereafter simply CAA in this chapter) increased behind QLCS1 and within the strengthening front as the system moved northeastward throughout the morning (Figs. 44a-c). This supported QG forcing for subsidence and upper-level height falls, and a distinct region of 400-hPa height falls remained situated above the strongest midlevel geostrophic CAA over the Midwest during this period (Figs. 45a-c). Furthermore, Keyser and Shapiro (1986) described how geostrophic CAA occurring along an upper-level front shifts the secondary ageostrophic circulation such that subsidence forms beneath the jet axis and tilting effects become frontogenetical—a positive feedback that produces stronger subsidence and tropopause folding. Accordingly, the region of geostrophic CAA became increasingly collocated with the strongest midlevel subsidence behind QLCS1 over time (not shown), and $\nabla\theta$ further intensified in consequence—yielding greater geostrophic CAA, continued amplification of SW_2 (via sustained forcing for upper-level height falls), and further deepening of the secondary tropopause fold beneath J_3 (Figs. 44, 45). Overall, the longevity of differential vertical motions that coincided with the western periphery of QLCS1 and a tightened upper-level PV gradient played a critical role in this evolution. Ultimately, the amplification of SW_2 supported greater forcing for ascent over the QLCS1 stratiform region and surface cyclogenesis with L_2, which we discuss in the following subsection. This progression was supported by the wind profiler observations from Wolcott, which depicted a deep region of derived geostrophic CAA behind QLCS1 and below J_3 and the subsequent passage of L_2 at ~27/1300Z (Fig. 25b).

Owing to the amplification of SW_2, the large-scale flow curvature and overall diffluence were diminished downstream from the longwave trough and SW_3, yielding broad and fairly unidirectional southwesterly flow over the Southeast in the wake of QLCS1 (Figs. 45b-d). The mid- to upper-tropospheric flow was further altered following the formation and upscale growth of QLCS2, which induced a meso-α-scale region of height rises and

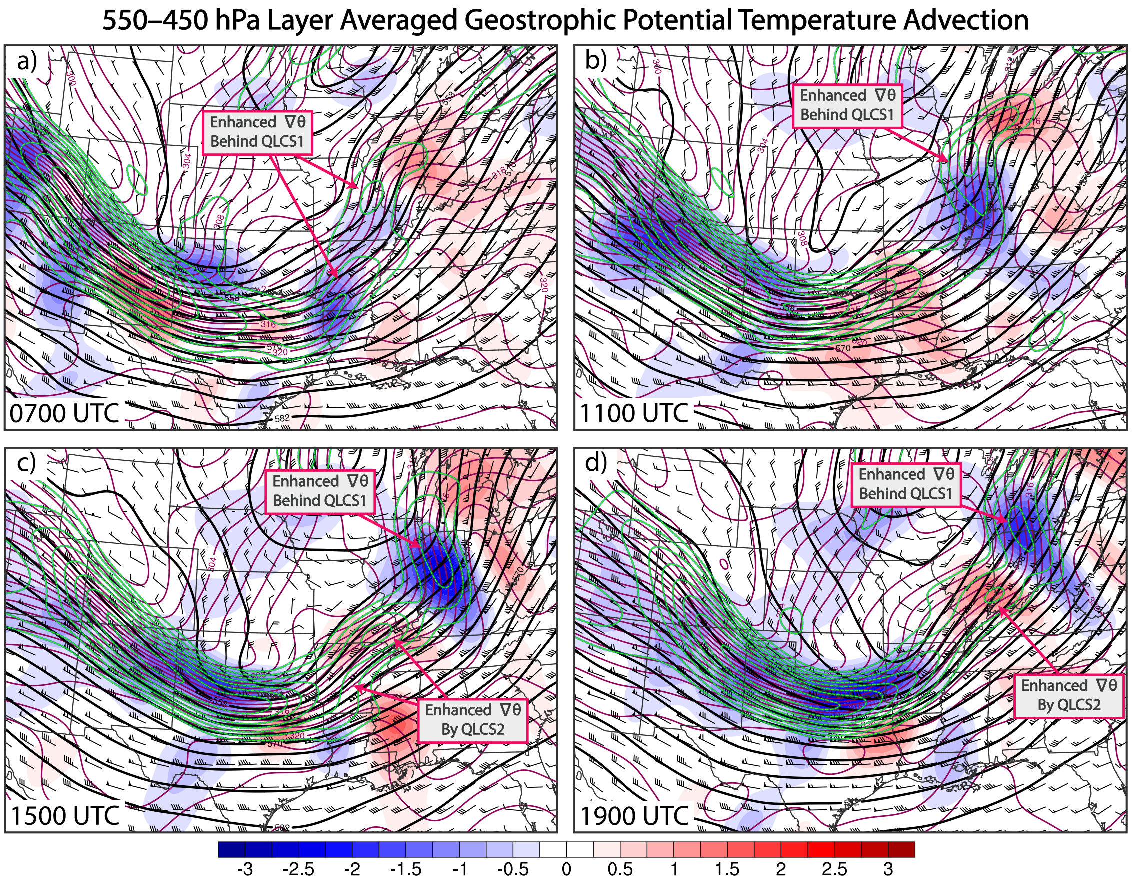

Figure 44: *Geostrophic potential temperature advection averaged over the 550–450-hPa layer (shaded; K h^{-1}), 550–450-hPa layer-averaged potential temperature (magenta contours; K), 550–450-hPa layer-averaged geostrophic winds (barbs; kt), 500-hPa geopotential height (black contours; dam), and 550–450-hPa layer-averaged potential temperature gradient (dashed green contours; every 0.5 K (100 km)$^{-1}$ $\geq$ 1.5 K (100 km)$^{-1}$) from the corresponding RUC 1-h forecasts valid at (a) 0700 UTC, (b) 1100 UTC, (c) 1500 UTC, and (d) 1900 UTC 27 April 2011. The plotted fields were low-pass filtered with a cutoff horizontal wavelength of 500 km.*

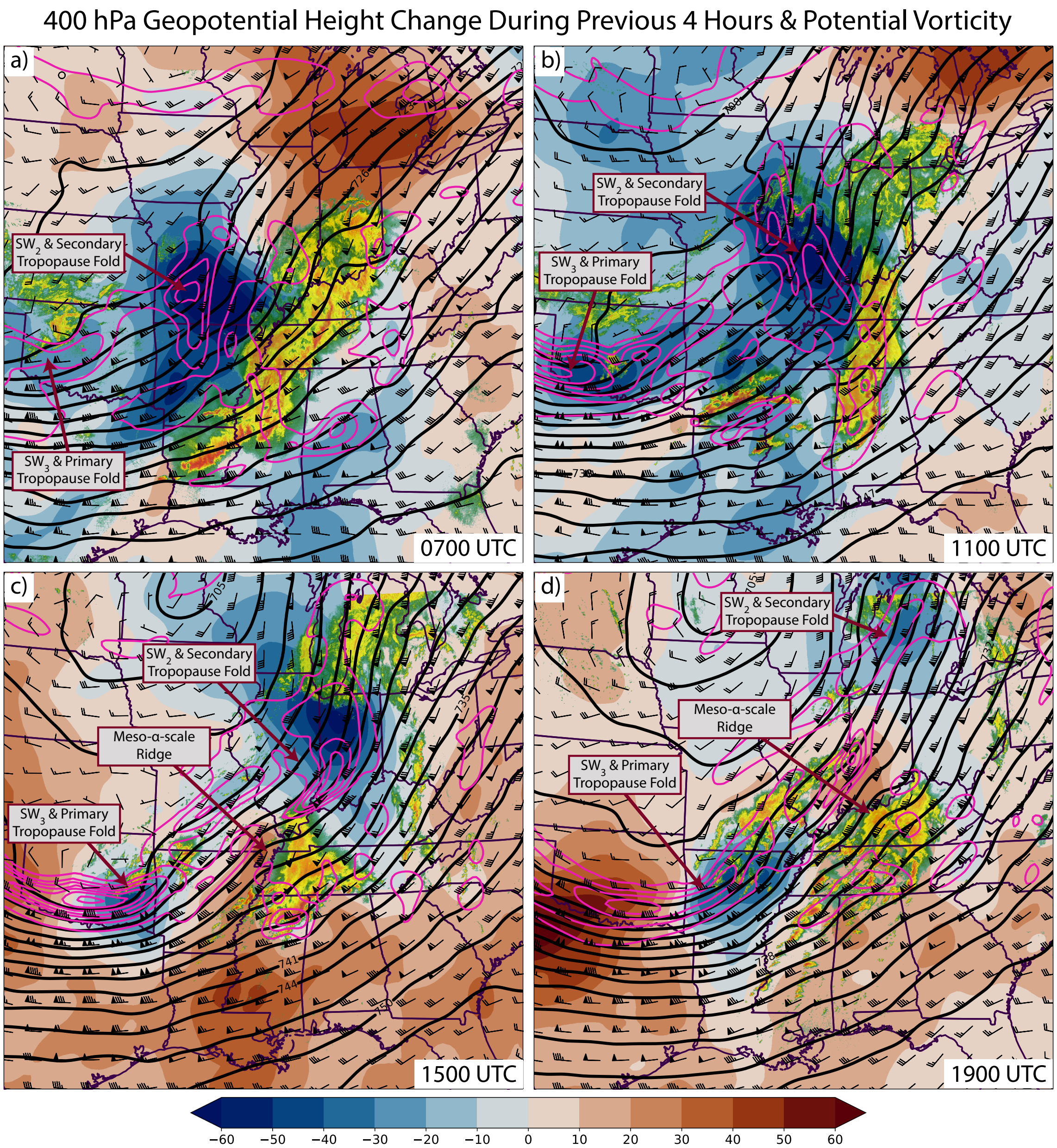

Figure 45: *Composite radar reflectivity > 20 dBZ overlaid with 400-hPa geopotential height change during the previous 4 hours (shaded; m), 400-hPa potential vorticity (pink contours; every 1 PVU ≥ 1 PVU), 400-hPa geopotential height (black contours; dam), and 400-hPa horizontal winds (barbs; kt) from the corresponding RUC 1-h forecasts valid at (a) 0700 UTC, (b) 1100 UTC, (c) 1500 UTC, and (d) 1900 UTC 27 April 2011.*

midlevel warming (Figs. 44c,d and 45c,d) immediately downstream from SW_3 and within the J_1 exit region during the morning and early afternoon (Fig. 46). Accordingly, QLCS2

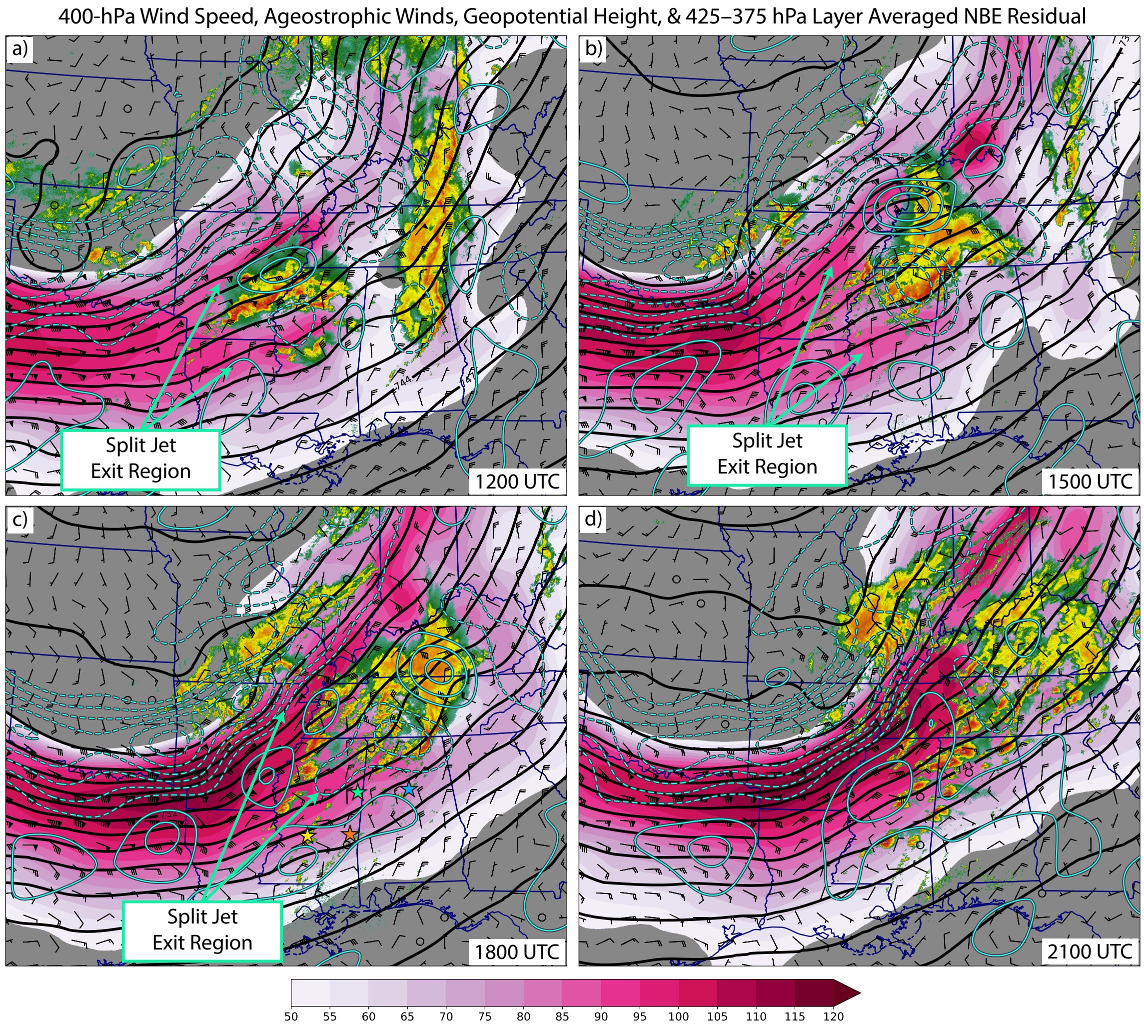

Figure 46: *Composite radar reflectivity > 20 dBZ overlaid with 400-hPa horizontal wind speed (shaded; kt), 400-hPa geopotential height (black contours; dam), 400-hPa ageostrophic winds (barbs; kt), and 425–375-hPa layer averaged NBE residual (positive values shown by solid cyan contours every* 1×10^{-8} $s^{-2} \geq 1\times10^{-8}$ s^{-2}*; negative values shown by dashed cyan contours every* 1×10^{-8} $s^{-2} \leq -1\times10^{-8}$ s^{-2}*) from the corresponding RUC 1-h forecasts valid at (a) 1200 UTC, (b) 1500 UTC, (c) 1800 UTC, and (d) 2100 UTC 27 April 2011. The location of Columbus, MS, Birmingham, AL, Jackson, MS, and Meridian, MS, are shown in (c) with the green, blue, yellow, and orange markers, respectively.*

effectively amplified the cyclonic perturbations accompanying SW_2 and SW_3 and enhanced the *mesoscale* flow curvature ahead of SW_3 prior to the supercell outbreak.

The midlevel warming accompanying QLCS2 intensified and reoriented the background thermal gradient to its north and west, promoting increased geostrophic CAA (and thus forcing for height falls) ahead of SW_3 (Figs. 44c,d and 45c,d). Furthermore, the 400-hPa height rises stemming from QLCS2 strengthened (weakened) the height gradient on the cyclonic (anticyclonic) flank of the jet (Figs. 45c,d) while forking the J_1 exit region into two branches around the system (Fig. 46). The northern branch—which was supported by the bolstered height gradient—was characterized by a narrow corridor of ~90–105 kt south-southwesterly winds and large positive values of NBE residual at 27/1500Z. Accordingly, accelerations were occurring within this branch as it pivoted cyclonically over time, yielding an extensive region of strengthened winds by 27/1800Z. Conversely, the southern branch was diverted over the Southeast and comprised weaker (~80–95 kt at 27/1800Z) and considerably more veered southwesterly winds. Large negative values of NBE residual, strong equatorward-directed ageostrophic flow, and implied decelerations accompanied this southern branch and—combined with the thermally indirect ageostrophic circulation attending the upper-level J_1 exit region (Figs. 40e,f)—supported midlevel subsidence over much of the Southeast prior to the afternoon supercell outbreak.

4.3.3 Low-level jet evolution and surface cyclogenesis

Recall that the low-level flow intensification that commenced immediately after QLCS1 formed was postulated to have supported this system's exceptional severity. Prior to any upper-level flow modifications produced by QLCS1, a broad region of southerly 30–40-kt winds extended from central Texas into Alabama at 850 hPa (Fig. 47a). However, the sudden increase in upper-level divergence (and resultant low-level geopotential height falls) that accompanied the formation of J_2 caused the LLJ to rapidly strengthen and expand northward with time ahead of QLCS1 (Figs. 40b,c and 47b,c). Specifically, the LLJ was tightly coupled to the highly unbalanced J_2 entrance region, and its intensification and poleward advancement occurred as an isallobaric response to the intensification and poleward advancement of J_2. By 27/0700Z, an elongated corridor of 60–75-kt 850-hPa winds extended into the Ohio Valley, which was situated beneath the J_2 entrance region and accompanying maxima in NBE residual (Figs. 40d and 47d) and coincided with low-level height falls > 20 m (4 h)$^{-1}$ (Fig. 48a).

Additionally, cyclogenesis corresponding to L_2 commenced over the Midwest below the J_2 entrance region and ahead of SW_2 as an upshear tilt in the PV field associated with the secondary tropopause fold developed behind QLCS1 (Fig. 49). At 27/0900Z, the 2-PVU contour within the tropopause fold extended down to 500 hPa and was located ~200 km west of vertically aligned midlevel and low-level PV anomalies that corresponded to a diabatically generated MCV and a quasi-stationary front, respectively (Figs. 49a,c). By 27/1200Z, a coherent ~995-hPa surface low had formed along the surface front and remained collocated with the overlying diabatic PV anomaly and downshear from the secondary tropopause fold (Figs. 49d,f). L_2 deepened over time due to sustained low-level height falls (Fig. 48b-d) ahead of SW_2 and beneath the highly divergent J_2 entrance region (Figs. 40e-f and 45b-d). Meanwhile, L_3 was slowly reorganizing ahead of SW_3 throughout this period, yielding two subsynoptic-scale lows that were separated by $\leq$ 1000 km at 27/1500Z (Fig. 48c). L_3 was not supported by appreciable height falls until SW_3 began to noticeably amplify over Arkansas (i.e., near the beginning of the supercell outbreak), after which time L_3 gradually deepened and became increasingly compact (Fig. 48d).

In the hours before the supercell outbreak, the LLJ structure reflected the presence of both lows and was influenced by convectively driven flow modifications aloft in addition to the approaching SW_3. At 27/1400Z, an uninterrupted corridor of 850-hPa winds > 50 kt extended from the Gulf Coast into the Great Lakes region and included two embedded LLJ maxima—the southernmost of which comprised 65–80-kt winds over the Southeast (Fig. 47e). In Chapter 3, we attributed this secondary maxima to rapid low-level accelerations that occurred following the formation of QLCS2 ahead of SW_3. Indeed, the LLJ further strengthened throughout the morning as a coherent region of 900-hPa height falls > 20 m (4 h)$^{-1}$ developed within the QLCS2 inflow environment and expanded poleward with time (Figs. 48b-d). By the beginning of the supercell outbreak, a mesoscale corridor comprising

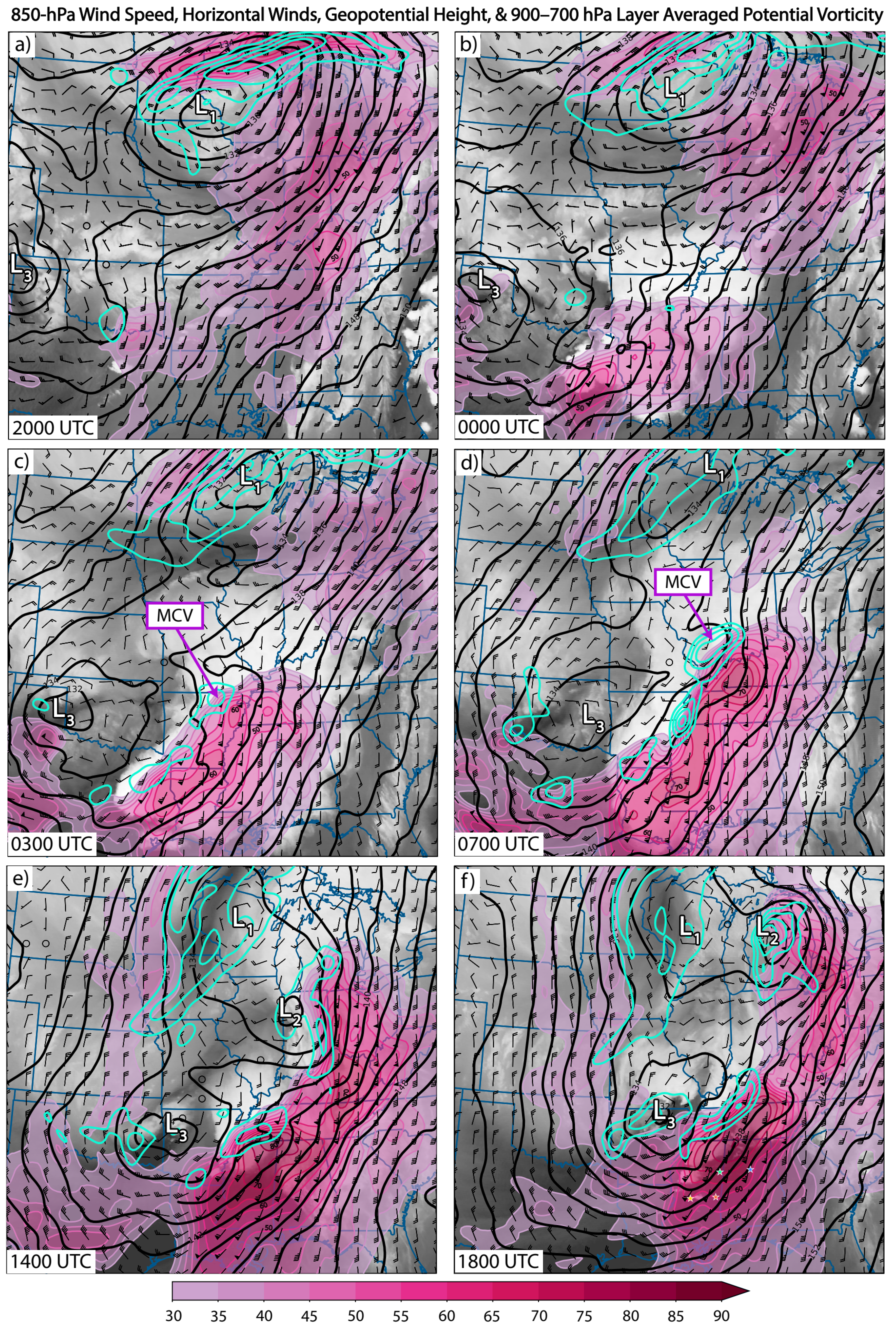

Figure 47: *GOES-13 water vapor imagery overlaid with 850-hPa wind speed (shaded; kt), 850-hPa horizontal winds (barbs; kt), 850-hPa geopotential height (contours; dam), and 900–700-hPa layer averaged PV (cyan contours; every 0.5 PVU ≥ 1 PVU) from the corresponding RUC 1-h forecasts valid at (a) 2000 UTC 26 April, (b) 0000 UTC 27 April, (c) 0300 UTC 27 April, (d) 0700 UTC 27 April, (e) 1400 UTC 27 April, and (f) 1800 UTC 27 April 2011. The location of Columbus, MS, Birmingham, AL, Jackson, MS, and Meridian, MS, are shown in (f) using the same notation as in Fig. 46.*

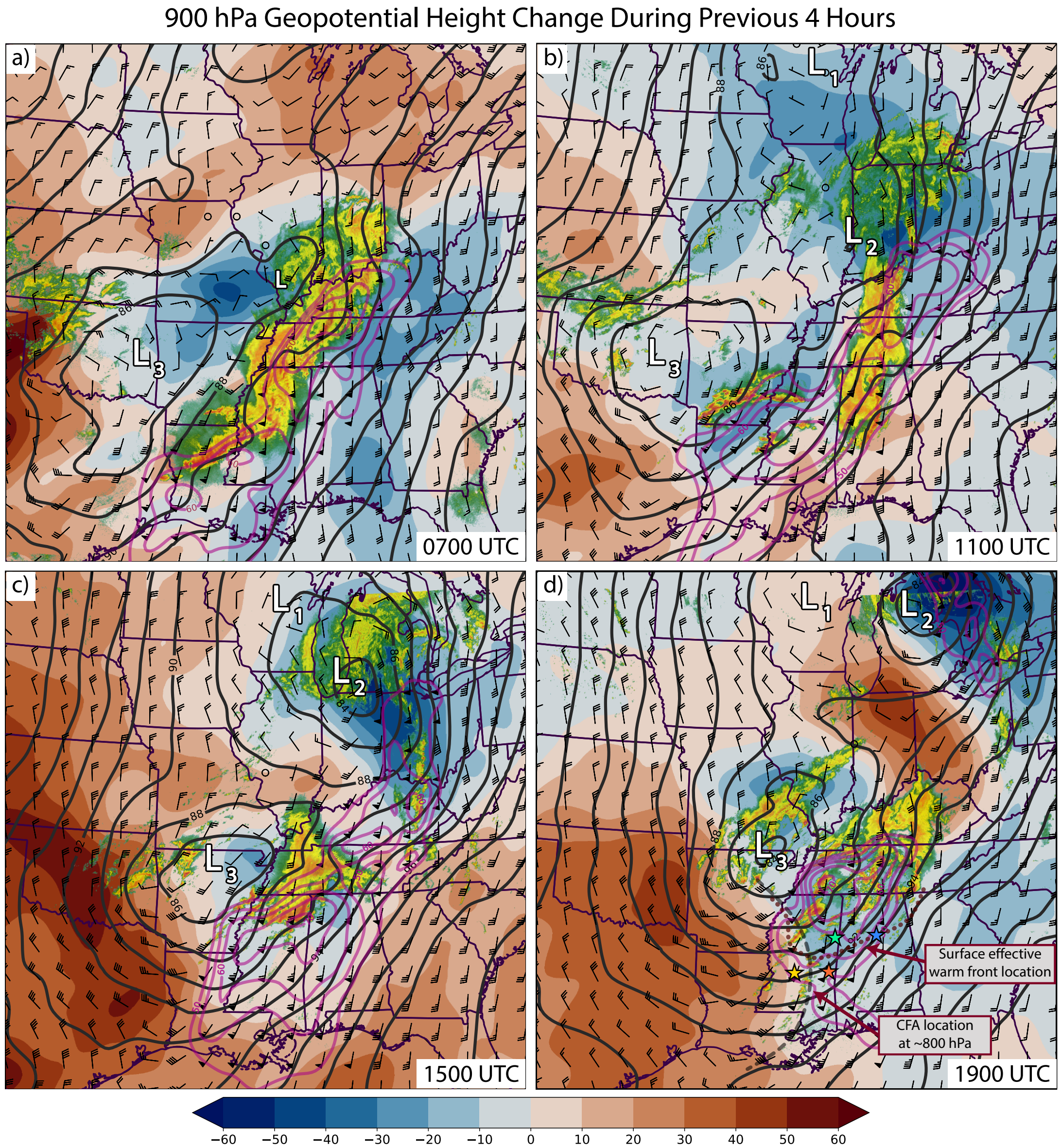

Figure 48: *Composite radar reflectivity > 20 dBZ overlaid with 900-hPa geopotential height change during the previous 4 hours (shaded; m), 900-hPa geopotential height (black contours; dam), 900-hPa wind speed (magenta contours; every 5 kt ≥ 50 kt), and 900-hPa horizontal winds (barbs; kt) from the corresponding RUC 1-h forecasts valid at (a) 0700 UTC, (b) 1100 UTC, (c) 1500 UTC, and (d) 1900 UTC 27 April 2011. The location of Columbus, MS, Birmingham, AL, Jackson, MS, and Meridian, MS, are shown in (d) using the same notation as in Fig. 46. The manually analyzed positions of the effective warm front and CFA are shown with the red dotted line and gray dashed line, respectively, based upon Fig. 31 in Chapter 3.*

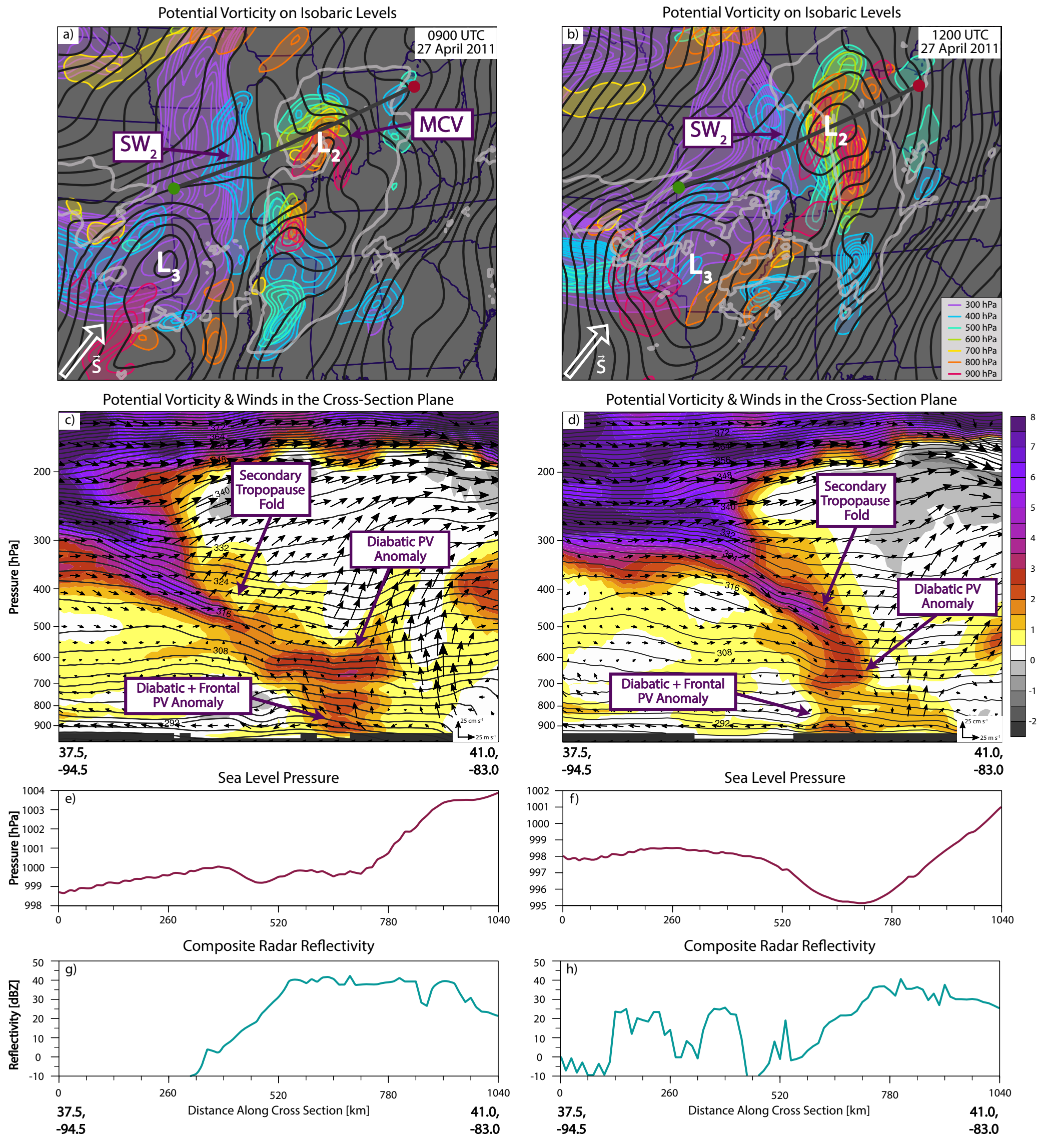

Figure 49: *RUC depiction of PV calculated on different isobaric levels (colored contours; every 0.5 PVU ≥ 1.5 PVU), SLP (black contours; hPa), and simulated composite radar reflectivity (white contours; 25 dBZ) at (a) 0900 UTC and (b) 1200 UTC; vertical cross sections of PV (shaded; PVU), potential temperature (gray contours; K), and total winds within the plane of the cross section (vectors; scale shown on the figure) at (c) 0900 UTC and (d) 1200 UTC; SLP along the cross section path at (e) 0900 UTC and (f) 1200 UTC; simulated composite radar reflectivity along the cross section path at (g) 0900 UTC and (h) 1200 UTC. The cross section path is denoted by the gray line in panels (a) and (b) and is oriented from the green (left) to red (right) filled circles at each end. The estimated mean shear vector over the 1000–400-hPa layer within the vicinity of L_2 is depicted by the gray arrow. Note that the y-axis ranges differ between panels (e) and (f).*

850-hPa winds of 70–80 kt and considerable cross-isohypse ageostrophic flow was centered over middle Tennessee and northwestern Alabama (Fig. 47f) beneath an area of large positive NBE residual and pronounced upper-level divergence accompanying the right-entrance region of J_4 and the split J_1 exit region (Figs. 40f,46c). We note that the greatest low-level wind speeds throughout this evolution were displaced to the north and northwest of the strongest height gradient—indicative of the highly ageostrophic and unbalanced nature of the LLJ over the Southeast. This notably strong and highly ageostrophic LLJ present at the onset of the supercell outbreak was therefore partially attributable to isallobaric forcing that accompanied the formation of QLCS2, which augmented the background forcing ahead of SW_3 and supplemented the persistent low-level flow enhancement that stemmed from QLCS1.

4.4 Relationship of flow modifications to vertical shear profiles during the supercell outbreak

We now evaluate how these flow modifications influenced the vertical shear profiles over the Southeast during the afternoon supercell outbreak. Numerous studies have collectively established that long-lived, right-moving supercells (in the NH) are favored within environments that contain strong deep-layer vertical wind shear and a shear vector that veers with height (particularly throughout the lower troposphere), yielding a "long" hodograph with appreciable clockwise curvature and SRH (e.g., Rotunno and Klemp, 1982; Weisman and Klemp, 1984; Davies-Jones, 1984; Rotunno and Klemp, 1985; Brooks and Wilhelmson, 1993; Weisman and Rotunno, 2000; McCaul and Weisman, 2001). Furthermore, shear and SRH computed over shallow near-surface layers (i.e., 0–500 m and 0–1 km) have proven to discriminate well between tornadic and nontornadic supercell environments (e.g., Rasmussen, 2003; Thompson et al., 2003; Markowski et al., 2003; Coffer et al., 2019).

Although these studies defined what constitutes a favorable shear environment for supercells and tornadoes, less attention has been given to explicitly diagnosing the processes responsible for creating such hodographs within tornado outbreak environments[4] (e.g., Roebber et al., 2002; Gold and Nielsen-Gammon, 2008). In the conceptually straightforward scenario of geostrophic flow and thermal wind balance, the vertical wind shear is solely a function of the background thermal gradient. Accordingly, the magnitude of the geostrophic shear depends upon the strength of the background baroclinity, and the geostrophic hodograph shape is determined by how the orientation and strength of the thermal gradient vary with height. Through this relationship, meteorologists frequently assume that much of the hodograph curvature found in tornado environments is due to geostrophic veering in the presence of ample WAA (e.g., Maddox et al., 1980; Maddox and Doswell, 1982; Doswell and Bosart, 2001; Markowski and Richardson, 2011). However, tornado outbreaks—including the one described herein—often occur in the warm sector where baroclinity is generally weak (e.g., Hoxit and Chappell, 1975; Koch et al., 1998; Thompson and Edwards, 2000; Bunkers et al., 2006; Garner, 2012). Furthermore, severe weather environments typically comprise jet streaks and may evolve rapidly (i.e., the flow is dynamically unbalanced), yielding large pressure tendencies and strong accelerations (e.g., Kocin et al., 1986; Zack and Kaplan, 1987; Kaplan et al., 1998). In such environments, the ageostrophic component may contribute significantly to the vertical shear profile such that the oft-assumed thermal wind relationship has limited applicability (e.g., Doswell, 1991; Doswell and Bosart, 2001). The effects of flow curvature and friction also promote ageostrophic motions—the latter of which tends to induce or enhance veering throughout the PBL and increase low-level hodograph curvature (e.g., Maddox et al., 1980; Davies-Jones, 1984; Banacos and Bluestein, 2004; Markowski and Richardson, 2011).

In Chapter 3, we noted that the vertical shear, hodograph shapes, and SRH values during the afternoon were more than sufficient for persistent mesocyclones and tornadoes and were largely attributed to the deflection of the midlevel jet over the Southeast by QLCS2 and the accumulated low-level flow intensification that accompanied the formation of QLCS1

[4]We are specifically concerned with external processes that preceded CI within a particular tornadic episode.

and QLCS2. Knupp et al. (2014) also emphasized these notable shear profiles and related their existence—specifically over northern Alabama at 27/2100Z—to isallobaric forcing ahead of SW_3, friction, and the thermally direct circulation accompanying the effective warm front. However, we stress that strong low-level shear and high SRH were established

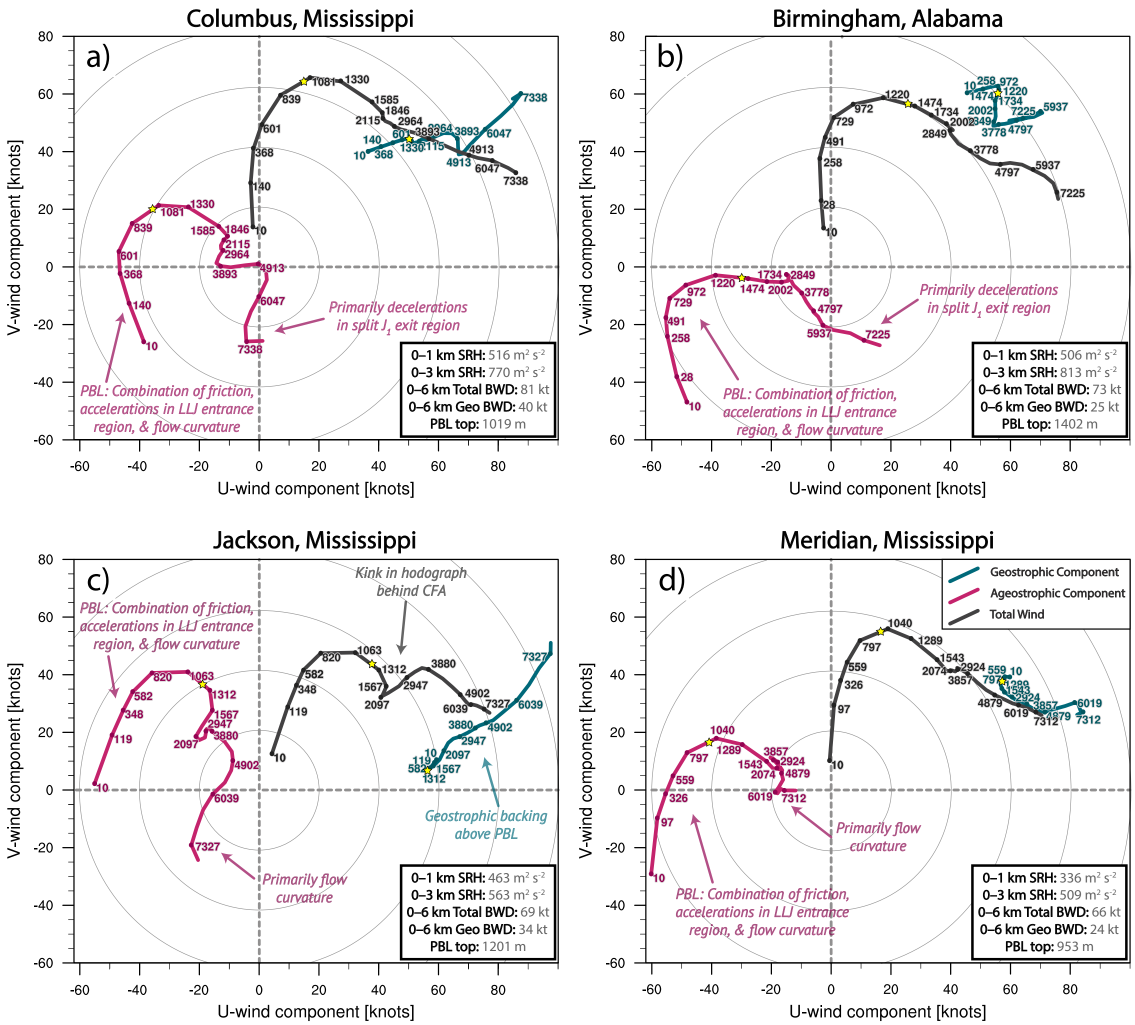

Figure 50: *Hodographs showing the vertical profiles of the total horizontal wind (gray; kt), geostrophic wind component (blue; kt), and ageostrophic wind component (magenta; kt) at (a) Columbus, MS, (b) Birmingham, AL, (c) Jackson, MS, and (d) Meridian, MS from the RUC 1-h forecast valid at 1900 UTC 27 April 2011. The hodograph labels represent height AGL (m). The yellow star denotes the approximate height of the PBL. Wind and geopotential height fields were low-pass filtered with a cutoff horizontal wavelength of 325 km prior to computing the geostrophic and ageostrophic components. The hodograph locations are displayed in Fig. 47f.*

over the Southeast several hours prior to 27/2100Z (see Fig. 26 in Chapter 3.1), when SW_3 remained far upstream. In order to assess the relative importance of ageostrophic motions—due to both convective feedbacks and other processes—on the shear profiles *at the beginning of the supercell outbreak*, we show in Fig. 50 hodographs of the total horizontal wind, geostrophic wind component, and ageostrophic wind component at 27/1900Z from four locations: Columbus, MS, Jackson, MS, Meridian, MS, and Birmingham, AL.

Overall, the geostrophic hodographs from all four locations exhibited strong southwesterly flow (particularly within the middle to upper troposphere), which developed following the downstream amplification of SW_2 and was furthered by the flow modifications produced ahead of SW_3 by QLCS2. Geostrophic veering (and implied WAA) was apparent in the hodographs from Columbus, Birmingham, and Meridian, but the accompanying geostrophic shear was largely unidirectional and generally weak at all levels—consistent with the expectation of minimal baroclinity and thermal advection in the warm sector—and alone would not likely support a prolific tornado outbreak (e.g., Rasmussen and Blanchard, 1998; Rasmussen, 2003; Thompson et al., 2003). Conversely, the geostrophic hodograph from Jackson—which was located behind the CFA but within the surface warm sector (Fig. 48d)—exhibited backing with height (and implied CAA) beginning near the top of the PBL and extending throughout the depth of the troposphere. Notably, only subtle backing within a shallow layer was evident in the total wind hodograph and existed exclusively due to a "kink" in the ageostrophic hodograph between ~1.5–3 km, which corresponded to the elevated layer of CAA analyzed behind the CFA in Fig. 29.

At all locations, the shape of the hodograph and the strength of the vertical wind shear—particularly throughout the lower to middle troposphere—were dictated almost entirely by the ageostrophic wind profile. The ageostrophic hodographs over the lowest ~1.5–2 km exhibited considerable low-level shear and clockwise curvature as the ageostrophic wind veered with height. The near-surface ageostrophic winds were incredibly strong (i.e., up to 67 kt at 10 m; Fig. 50d), largely opposed their geostrophic counterparts, and resulted predominantly due to a combination of friction (the effects of which diminished with height throughout the PBL) and flow curvature. However, a large cross-isohypse component of the ageostrophic flow (i.e., the component orthogonal to the geostrophic wind) also existed throughout the lower troposphere (including above the PBL) and was related primarily to accelerations occurring within the LLJ entrance region (Figs. 47f and 48d). Aloft, ageostrophic component winds > 25 kt were found above 7 km in Columbus and Birmingham (owing primarily to decelerations within the southern split branch of J_1) and in Jackson (owing primarily to flow curvature), which further improved the shape of the total wind hodograph.

Overall, strong ageostrophic motions that veered with height throughout the lower troposphere combined with appreciable deep-layer southwesterly geostrophic flow to create the notably favorable shear profiles present during the supercell outbreak. Together, the largely opposing near-surface ageostrophic component, accelerations occurring within the LLJ entrance region, and weak background geostrophic shear yielded strong deep-layer total vertical wind shear, while the strong southwesterly geostrophic flow effectively translated the highly curved ageostrophic hodographs into the first quadrant (typical of Southeast tornado environments; Markowski and Richardson, 2006) and primarily supported the length and shape of the total wind hodographs in the middle to upper troposphere.

4.5 WRF simulations

4.5.1 Model configuration

In order to directly evaluate how latent processes contributed to the flow modifications discussed thus far, two simulations were conducted using version 4.2.1 of the WRF-ARW model (Skamarock et al., 2008; Powers et al., 2017): one configured using full model physics (LH), and one without latent heating or cooling (NOLH). Both simulations were initialized at 26/1800Z and run for 36 h to capture the outbreak entirely (Table 4.1). Initial conditions (ICs) for atmospheric and soil fields were obtained from the NCEP GFS 0.5°

analysis valid at 26/1800Z, and lateral boundary conditions (BCs) were updated every 6 h using the corresponding GFS analyses.

Table 4.1: *WRF-ARW Model, version 4.2.1, configuration and physics parameterizations.*

	Outer Domain	**Inner Domain**
Grid Configuration		
Initial conditions	0.5° GFS analysis from 1800 UTC 26 April 2011	0.5° GFS analysis from 1800 UTC 26 April 2011
Lateral boundary conditions	6-h 0.5° GFS analyses	Outer WRF domain
Horizontal grid spacing	15 km	3 km
Number of grid points	420×320	1151×981
Number of vertical levels	70	70
Model top	10 hPa	10 hPa
Time step	60 s	5 s
Physics parameterizations		
Cumulus	New Tiedtke (LH only)	None
PBL	MYNN level 2.5	MYNN level 2.5
Surface layer	MYNN	MYNN
Land surface model	Unified Noah	Unified Noah
Microphysics	Thompson	Thompson
Shortwave radiation	RRTMG	RRTMG
Longwave radiation	RRTMG	RRTMG

Both simulations were run using a two-way nested grid configuration, with an outer domain of $\Delta x = \Delta y = 15$ km, and a convection-permitting inner domain of $\Delta x = \Delta y = 3$ km (Fig. 51). A stretched vertical grid comprising 70 levels below a 10-hPa model top was used. Within the lowest 1 km AGL, Δz ranged from approximately 54–67 m. Identical physics parameterization schemes were used for both simulations, except that the New Tiedtke cumulus scheme (Zhang et al., 2011) was only employed on the outer domain of the LH simulation. The Thompson microphysics scheme (Thompson et al., 2004, 2008) was used for both simulations, but no microphysics heating tendency was permitted in the NOLH simulation. The Mellor-Yamada-Nakanishi-Niino (MYNN) level 2.5, TKE-based PBL scheme was used in tandem with the MYNN surface layer scheme (Nakanishi and Niino, 2006, 2009) and coupled Unified Noah LSM (Ek et al., 2003). Shortwave and longwave radiation were parameterized using the respective RRTMG schemes (Iacono et al., 2008). Radiative effects of clouds were permitted in both simulations.

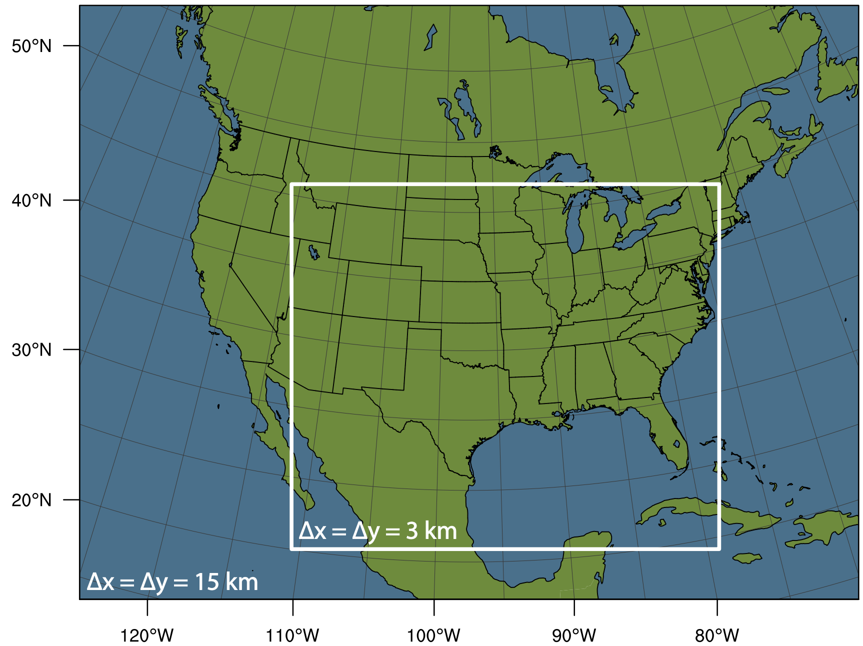

Figure 51: *The domain configuration used for the WRF-ARW simulations presented herein and in Chapter 5.*

4.5.2 Validity of simulation

The LH simulation was validated using the radar observations and RUC 1-h forecasts. Overall, the evolution of QLCS1 was well-depicted, and a widespread region of strong convection had developed over Arkansas and Texas by 27/0000Z (cf. Figs. 16b and 52a). This convection quickly grew upscale into an expansive QLCS, but the southernmost bowing segment that resulted from the upscale growth of convection over eastern Texas and produced numerous tornadoes throughout the Southeast overnight was absent in the simulation[5] (cf. Figs. 16d-f and 52b,c). Although this discrepancy will inevitably influence any simulated modifications to the mesoscale environment over the Southeast, the adequate depiction of the initiation and rapid upscale growth of QLCS1 provides confidence that the LH simulation should reasonably portray the most significant upscale modifications described in the previous sections. However, QLCS2 developed ~4–5 h too early and ~150–200 km too far west in the LH simulation. The resultant environmental modifications

[5]Forecasts from the convection-permitting ensembles presented in Chapter 5 suggest that this bowing segment had limited predictability.

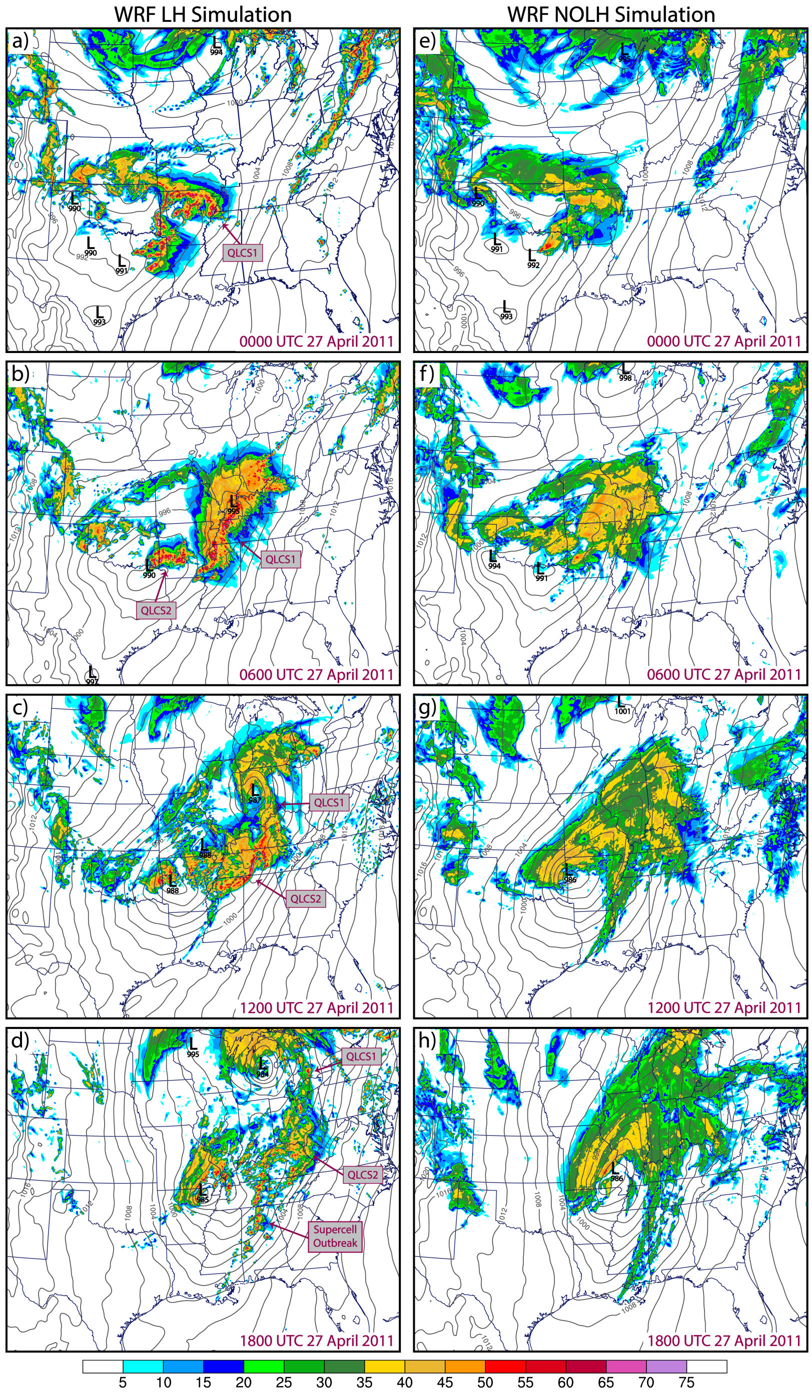

Figure 52: *Simulated radar reflectivity (shaded; dBZ) and SLP (gray contours; hPa) from the LH simulation at (a) 0000 UTC, (b) 0600 UTC, (c) 1200 UTC, and (d) 1800 UTC, and the NOLH simulation at (e) 0000 UTC, (f) 0600 UTC, (g) 1200 UTC, and (h) 1800 UTC 27 April 2011. The reflectivity fields and SLP are shown on the 3-km inner domain and 15-km outer domain, respectively.*

from QLCS2—including the development and evolution of J_4, the intensification of the LLJ, and the system's interactions with SW_3 and J_1—and how they influenced conditions during the supercell outbreak were therefore depicted inaccurately. Thus, the WRF simulations are primarily used to further assess how QLCS1 altered the large-scale pattern and its own inflow environment. In order to mitigate the influence of QLCS2 on our analyses, we describe the flow modifications that had occurred by 27/0600Z—just before QLCS1 produced its first EF3 tornado (see Fig. 3 in Knupp et al., 2014). *We emphasize that the environmental conditions present at this time did not represent those during the supercell outbreak, which began ~12 h later.*

The LH simulation compared well with the corresponding RUC 1-h forecast at 27/0600Z in its depiction of the flow modifications occurring both at upper levels (particularly with regard to the development and strength of J_2; Figs. 53a,c) and at low levels (particularly with regard to the strength of the LLJ ahead of QLCS1; Figs. 53b,d). Specifically, simulated 250-hPa winds within J_2 were > 130 kt over the Great Lakes region, and cross-isohypse ageostrophic flow, inferred accelerations, and mass divergence were apparent in the J_2 entrance region. At 850 hPa, the simulated LLJ intensified and advanced northward in conjunction with J_2, and a corridor of 55–70-kt winds extended into the Ohio Valley ahead of QLCS1 by 27/0600Z.

4.5.3 Simulated flow modifications

4.5.3.1 Upper-level modifications

The environmental modifications stemming from QLCS1 were quantified by computing the difference between the LH and NOLH simulations (calculated as LH − NOLH) for several fields, including geopotential height and wind speed[6] At 27/0600Z, 250-hPa height perturbations > 125 m were centered over southern Illinois (coincident with the QLCS1 stratiform region), while height perturbations > 50 m spanned much of the Midwest (Fig.

[6]The wind speed difference was calculated from the differences in u and v components as $\sqrt{(\Delta u)^2 + (\Delta v)^2}$.

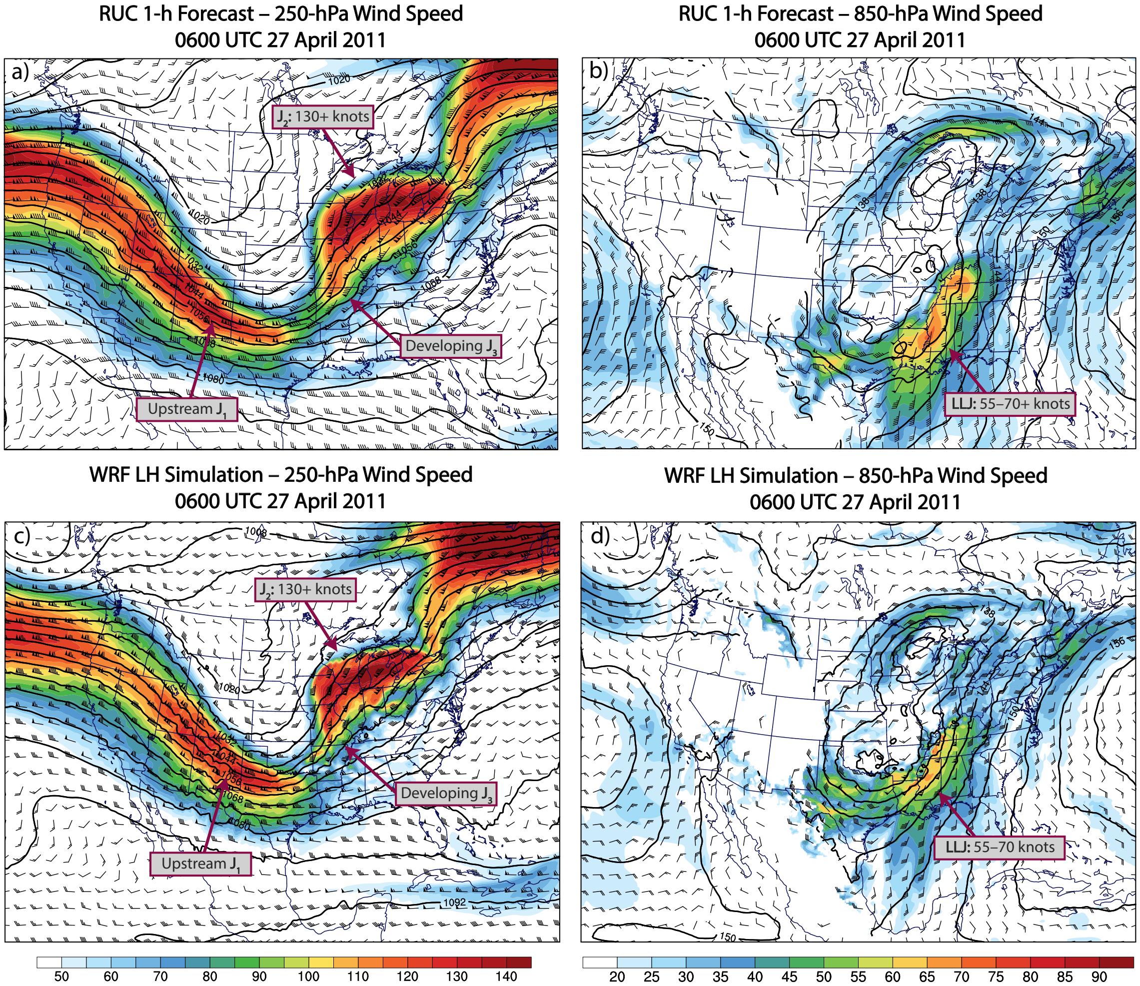

Figure 53: *Comparison of wind speed (shading; kt), geopotential height (contours; dam), and total winds (barbs; kt) valid at 0600 UTC 27 April as depicted by (top) the corresponding RUC 1-h forecast and (bottom) the WRF LH simulation at (a),(c) 250 hPa and (b),(d) 850 hPa. The fields are shown on the 15-km outer domain.*

54a). This broad region of greater height values in the LH simulation signified the amplified downstream ridge and was centered within a perturbation anticyclone (Fig. 54b). The northern and western flanks of this anticyclone comprised wind speed perturbations of ~70–110 kt and ~70–100 kt and corresponded to J_2 and J_3, respectively. Additionally, relatively strong (~30–50 kt) easterly perturbations were evident along the southern flank, which opposed the background flow over the SGP (Fig. 53c) and supported enhanced decelerations within the J_1 exit region—consistent with our previous findings in Chapter 4.3.1.

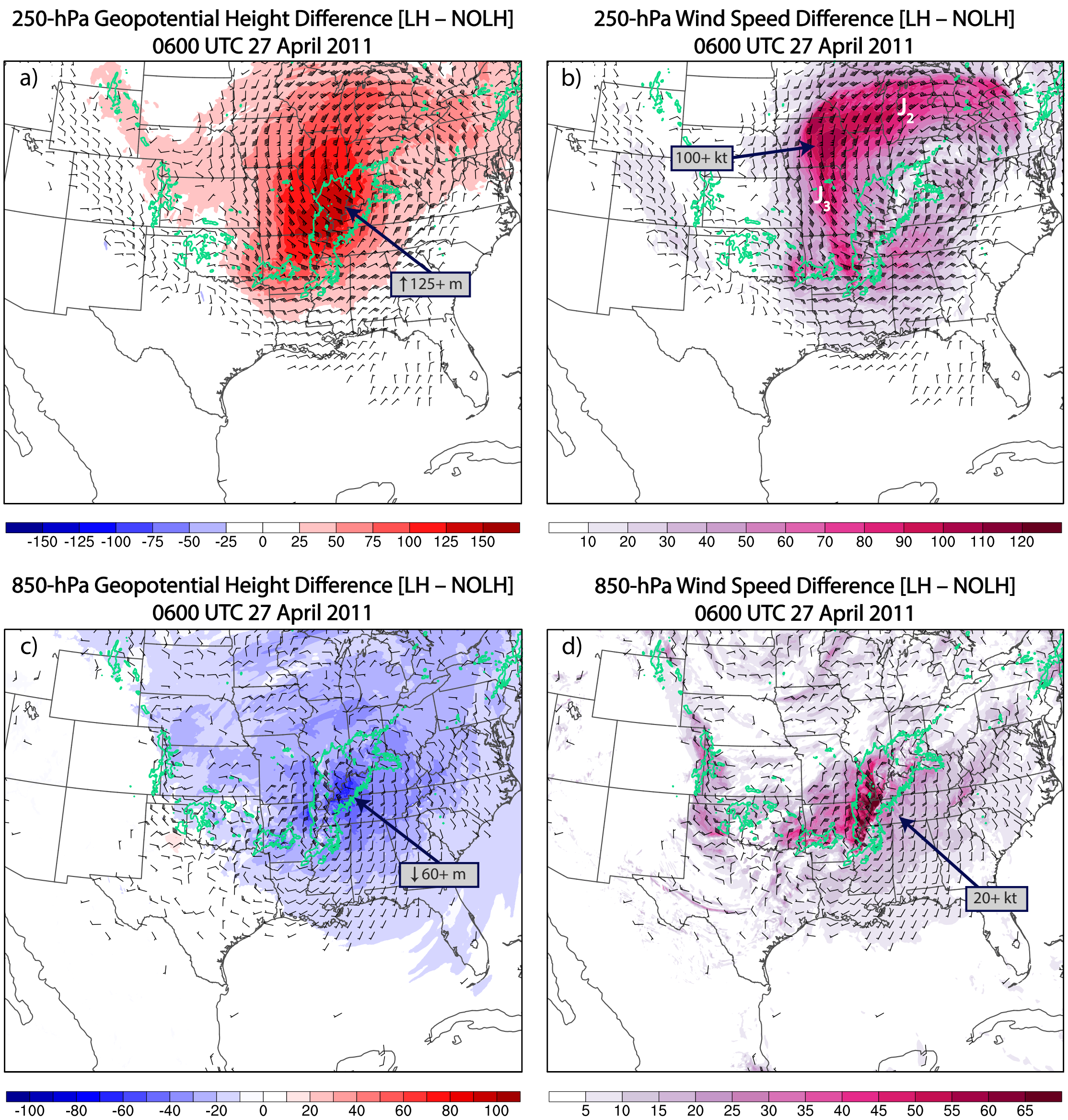

Figure 54: *Differences between the LH and NOLH WRF simulations of (a) 250-hPa geopotential height (shaded; m) and horizontal winds (barbs; kt), (b) 250-hPa wind speed (shaded; kt) and horizontal winds (barbs; kt), (c) 850-hPa geopotential height (shaded; m) and horizontal winds (barbs; kt), and (d) 850-hPa wind speed (shaded; kt) and horizontal winds (barbs; kt) at 0600 UTC 27 April. Simulated radar reflectivity = 35 dBZ from the LH simulation is displayed in all panels (green contours). All fields are shown on the 3-km inner domain.*

Furthermore, QLCS1 had considerably altered the tropopause structure in the LH simulation. As depicted in Fig. 55, the 2-PVU surface within the NOLH simulation (denoted by the blue contour) gradually sloped upward toward the east and was located at 9–11 km

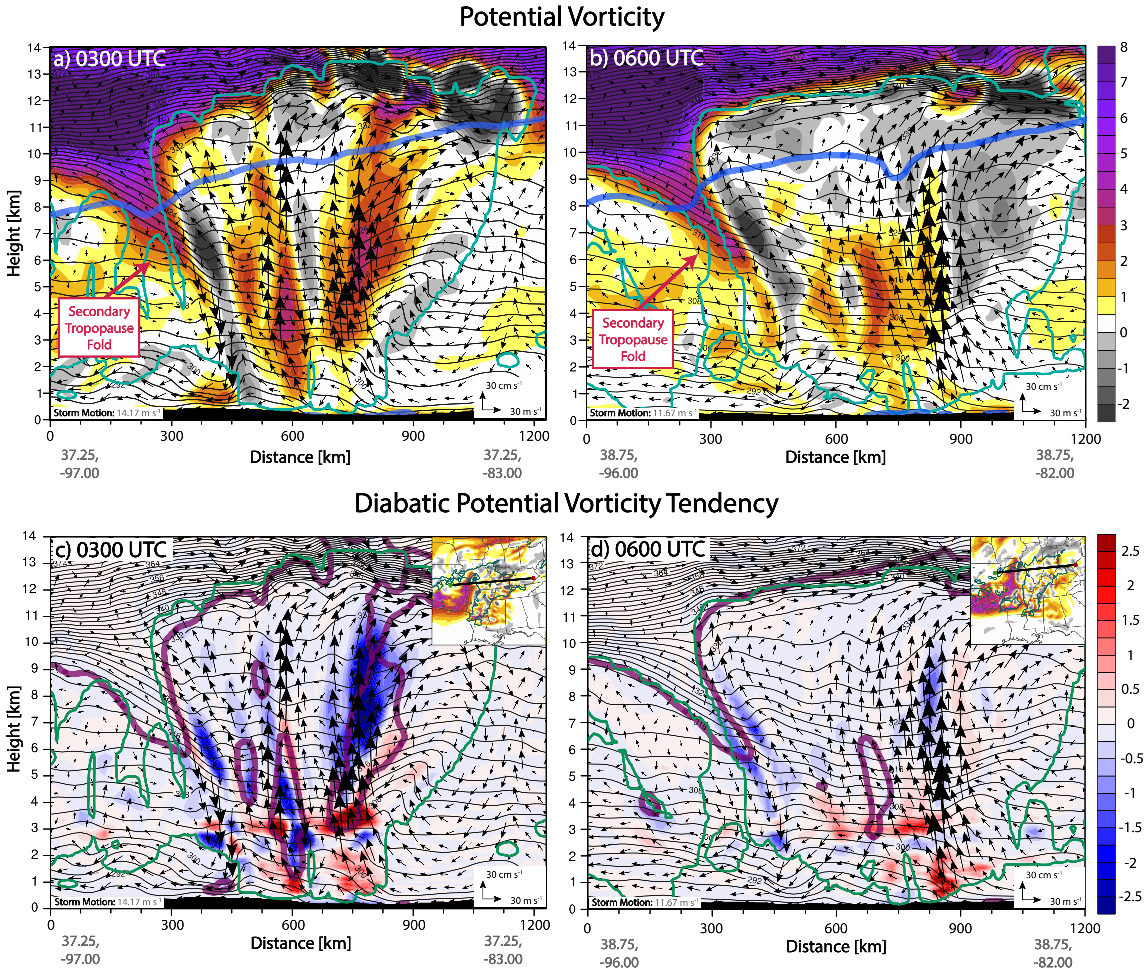

Figure 55: *Vertical cross sections of (top row) PV from the LH simulation (shaded; PVU), potential temperature (gray contours; K), cloud boundary (cyan contour; defined as the sum of the cloud water, cloud ice, and snow mixing ratios = 0.001 g kg^{-1}), system-relative winds (vectors; scale shown on figure), and the 2-PVU contour from the NOLH simulation (blue) at (a) 0300 UTC and (b) 0600 UTC, and (bottom row) diabatic PV tendency (shaded; PVU h^{-1}), potential temperature (gray contours; K), cloud boundary (green contour), system-relative winds (vectors; scale shown on figure), and the 2-PVU contour from the LH simulation (purple) at (c) 0300 UTC and (d) 0600 UTC 27 April 2011. The cross-section paths, overlaid with 350-hPa PV (~8 km MSL) from the LH simulation, are shown in the bottom row. Plotted fields are from the 15-km outer domain.*

MSL within the vicinity of QLCS1. In contrast, this surface had been lifted by ~3–4 km in the LH simulation, and a steepened tropopause and accompanying tropopause fold had developed behind QLCS1, which were absent in the NOLH simulation. The steepened tropopause and developing fold first appeared shortly after CI (owing to mass conservation and compensating subsidence; e.g., Phoenix et al., 2019) and progressively deepened with time as QLCS1 grew upscale (Figs. 55a,b). This secondary tropopause fold was not collocated with any appreciable positive PV tendency—i.e., the high-PV values were not generated by diabatic processes occurring within QLCS1 (Figs. 55c,d). Rather, this high-PV intrusion comprised stratospheric air and resulted from sustained differential vertical motions occurring along the western periphery of QLCS1 and the formation of a strong underlying convective downdraft. We note that this downdraft also supported the formation of a distinct wake low signature in the low-level isentropes (e.g., Johnson and Hamilton, 1988; Stumpf et al., 1991; Ruppert and Bosart, 2014) and that numerous surface observing sites detected strong negative pressure perturbations following the passage of QLCS1 that were consistent with a wake low (not shown).

4.5.3.2 Low-level modifications

At 850 hPa, the geopotential height and horizontal wind perturbations were in opposition to those aloft—consistent with the expected hydrostatic and low-level PV response to diabatic processes occurring within QLCS1 (Figs. 54c,d). At 27/0600Z, a negative height perturbation < -60 m was centered over western Kentucky (nearly aligned with the greatest positive upper-level height perturbation), and a broad region of height difference values < -30 m spanned much of the Ohio Valley. This region of lower height values in the LH simulation coincided with a perturbation cyclonic circulation that was most pronounced at midlevels (i.e., ~500–700 hPa; not shown) in accordance with a positive PV anomaly that developed within QLCS1. 850-hPa wind perturbations of 15–30 kt accompanied this circulation and augmented the background southerly flow throughout the QLCS1 inflow environment.

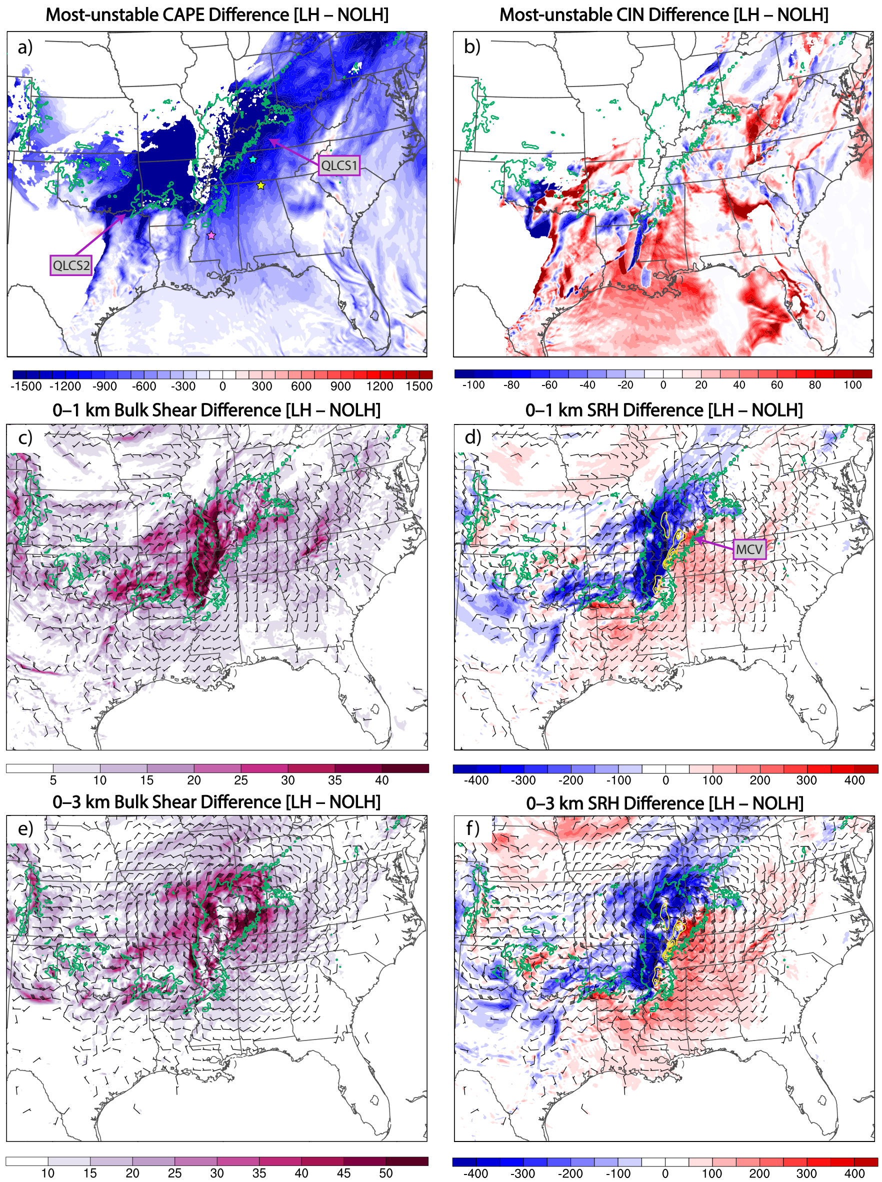

Figure 56: *Differences between the LH and NOLH WRF simulations of (a) CAPE (shaded; J kg^{-1}) and (b) CIN (shaded; J kg^{-1}) corresponding to the most-unstable parcel at 0600 UTC 27 April. CIN values are taken to be positive such that positive differences represent greater values of inhibition within the LH simulation. Bottom two rows show (left) difference in bulk wind shear (barbs; kt) and bulk wind shear magnitude (shaded; kt) calculated over the (c) 0–1 km and (e) 0–3 km layers, and (right) difference in bulk wind shear (barbs; kt) and SRH (shaded; m^2 s^{-2}) calculated over the (d) 0–1 km and (f) 0–3 km layers at 0600 UTC 27 April 2011. Simulated radar reflectivity = 35 dBZ from the LH simulation is displayed in all panels (green contours). PV averaged within the 900–700-hPa layer (yellow contours; every 2 PVU ≥ 2 PVU) is displayed in panels (d) and (f). All fields except for PV are shown on the 3-km inner domain.*

4.5.4 Alterations to CAPE and CIN

It is reasonable to conjecture that enhanced poleward advection of warm, moist air by the strengthened LLJ might yield greater CAPE (and reduced CIN) within the QLCS1 inflow environment. Difference fields for CAPE and CIN corresponding to the most-unstable parcel[7] at 27/0600Z are shown in Figs. 56a,b. Conversely, CAPE decreases > 300 J kg^{-1} were widespread throughout the warm sector, and a corridor of CAPE decreases > 800 J kg^{-1} extended ~250 km ahead of the convective line beneath the anvil. The lateral extent of this diminished CAPE region quickly expanded away from QLCS1 following CI (not shown) and was due primarily to midlevel warming that resulted from deep-tropospheric subsidence—the manifestation of which is evident in Fig. 57. Although the LLJ had strengthened ahead of QLCS1, the adverse effects of subsidence warming were not offset by low-level advective processes owing to the presence of weak background thermal and moisture gradients. Consequently, the near-surface temperature and moisture profiles were essentially identical between the LH and NOLH simulations (Fig. 57). Thus, the net effect of latent heating was to diminish CAPE throughout the inflow environment—a finding consistent with previous studies (e.g., Lane and Reeder, 2001; Adams-Selin and Johnson, 2013).

Considerable mesoscale variability was evident in the CIN difference field, particularly in the environment ahead of QLCS1, where alternating bands of increased and decreased CIN values spanned from northern Mississippi into Kentucky (Fig. 56b). Overall, CIN was greater within the LH simulation—especially over Mississippi and Louisiana, where increases ranged from 30–60 J kg^{-1}. As CIN is primarily affected by thermodynamic

[7]These quantities from the WRF output presented herein and in Chapter 6 were computed using either NCL or wrf_python, which both employ the same method of finding the level of maximum θ_e within the lowest 3 km AGL and then averaging the thermodynamic properties over a 500-m deep layer to determine the properties of the "most-unstable parcel". Thus, if the highest θ_e value in the lowest 3 km lies at the surface, the MUCAPE computed by this routine is analogous to mixed-layer CAPE and will yield a value less than the surface-based CAPE. Unfortunately, this nuance was not discovered until very late into the dissertation writing process, hence why the MUCAPE and MUCIN fields were not recomputed using different methods. Note that this does not apply to MUCAPE and MUCIN values obtained from the RUC or computed from observed soundings.

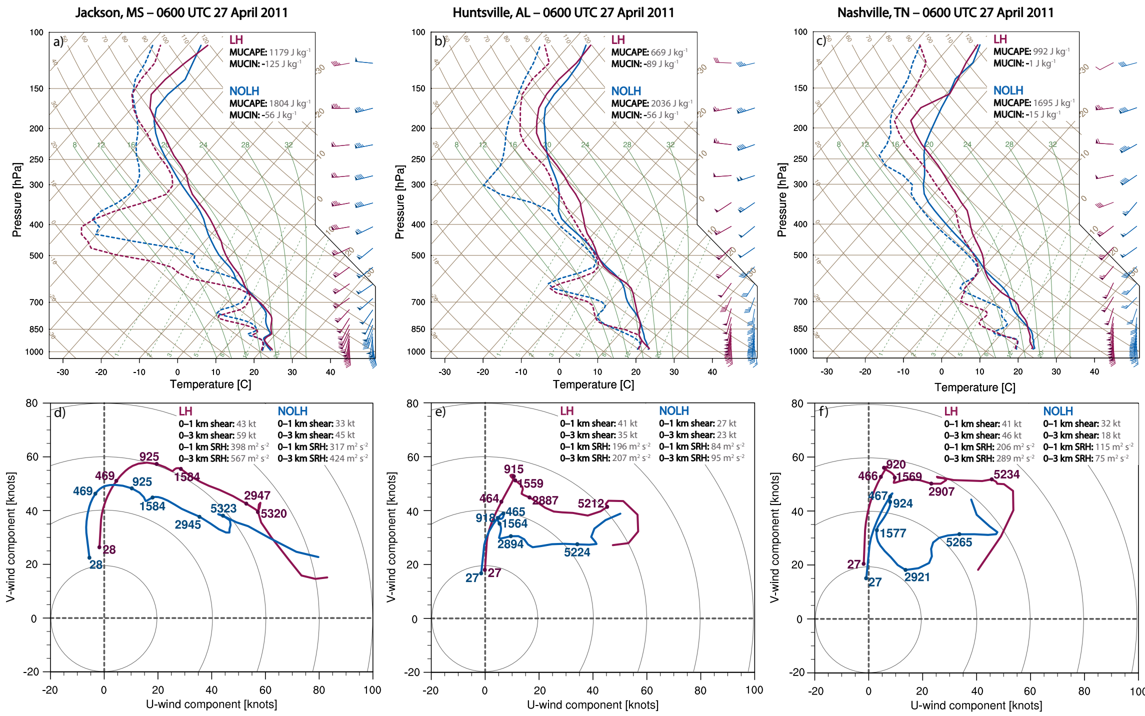

Figure 57: *Soundings and corresponding hodographs (displayed below 8 km AGL) from the LH (magenta) and NOLH (blue) WRF simulations valid at 0600 UTC 27 April 2011 for the locations of (a,d) Jackson, MS, (b,e) Huntsville, AL, and (c,f) Nashville, TN. The locations of Jackson, Huntsville, and Nashville are denoted by the pink, yellow, and cyan markers in Fig. 56a, respectively.*

modifications that manifest within the lower to middle troposphere, these increases were predominantly due to subsidence warming below ~700 hPa that strengthened a capping inversion beneath an EML in the LH simulation (Fig. 57a). Although this result might suggest that another important effect of latent processes was to yield thermodynamic conditions that were less conducive to cell regeneration and system longevity over the Southeast, we cannot affirm whether such a pronounced CIN enhancement would have occurred ahead of the southernmost bowing segment had it properly developed within the LH simulation.

4.5.5 Alterations to vertical wind shear

The vertical wind shear within the inflow environment was enhanced relative to the NOLH simulation. Difference fields of BWD and SRH[8] calculated over the 0–1-km and 0–3-km layers are displayed in Figs. 56c-f. The greatest low-level shear increases occurred over the Ohio and Tennessee Valleys, where changes in 0–1-km (0–3-km) BWD magnitude ranged from 10–30 kt (15–40 kt). Such increases were related to the strengthened LLJ and perturbation cyclonic circulation (i.e., positive PV anomaly) that developed within the lower to middle troposphere. Low-level shear also increased over the Southeast—particularly just ahead of QLCS1—although the overall BWD enhancements were ~5–10 kt weaker in this region. The 0–1-km shear difference vector within the inflow environment was oriented approximately parallel to QLCS1—consistent with the findings in Chapter 3 in that the low-level shear profiles yielded considerable streamwise vorticity for inflowing parcels.

Unsurprisingly, the greatest increases in SRH and low-level shear were largely collocated, and a notable area of enhanced SRH—particularly when calculated over the 0–3-km layer—was situated east of a band of low-level cyclonic vorticity in Kentucky and Tennessee. Wind profiles from Nashville, TN, and Huntsville, AL, indicate that these large SRH increases resulted from strengthened winds throughout the lowest ~5 km and significant changes in the hodograph shape (Figs. 57). SRH increases were also evident over the Southeast, and the hodograph from the LH simulation at Jackson, MS, exhibited stronger vertical shear and greater low-level curvature than in the NOLH simulation, although the background shear and SRH values were already considerable. We note that the actual magnitude of differences over the Southeast may have been underrepresented by the WRF simulations because the observed QLCS extended ~400 km farther to the southwest at 27/0600Z. Comparisons with the RUC fields at Jackson suggest that the LH simulation underestimated 0–1-km BWD and 0–1-km SRH values by ~4 kt and ~120 m^2 s^{-2}, respectively (not shown). Overall, the WRF simulations indicate that *low-level shear and SRH*

[8]All SRH calculations employed the right-moving supercell motion estimated using the Bunkers et al. (2000) technique, as this was used to compute SRH within the RUC model.

increased markedly within the QLCS1 inflow environment and thus supported the system's notable severity and longevity—an upscale feedback effect.

4.5.6 Accumulated effects of latent heat release on the baroclinic environment

We now discuss how the accumulated effects of latent heating occurring over 24 h modified the environment within the WRF simulation. Owing to (1) the absence of the southernmost bowing segment with QLCS1 in the LH simulation, (2) the premature development of QLCS2 and misrepresentation of its upscale modifications in the LH simulation, and (3) errors in the strength and forward progression of J_1 into the Southeast (i.e., too strong and too fast) in both WRF simulations, *the following analyses are not expected to replicate the environmental conditions during the supercell outbreak*, but rather serve to demonstrate how dramatically the simulated environment adjusted to prolonged convection. The composite radar reflectivity and SLP evolution for both simulations is shown in Fig. 52. Despite the lack of deep convection in the NOLH simulation, the precipitation distribution was generally comparable between the two simulations from 27/0000Z–27/1800Z. However, appreciable differences in the SLP field had arisen by 27/1200Z—particularly due to alterations in the evolution of L_1 and the formation of L_2 over the Midwest in the LH simulation. Notably, L_2 was completely absent in the NOLH simulation, solidifying that latent processes and upscale modifications were essential for cyclogenesis to occur with SW_2.

Considerable differences in the simulated baroclinic environment had become evident by 27/1800Z (Fig. 58). At midlevels, SW_2 had become amplified over the Great Lakes region in the LH simulation (Fig. 58a), whereas a distinct cyclonic perturbation with SW_2 was absent in the NOLH simulation (Figs. 58d,g). Consequently, the NOLH simulation featured a negatively tilted and highly diffluent midlevel baroclinic wave supportive of broad forcing for ascent over the Midwest, while the baroclinic wave in the LH simulation exhibited an elongated structure with limited downstream diffluence owing to the added presence of SW_2. Differences in the low-level kinematic and thermodynamic environments

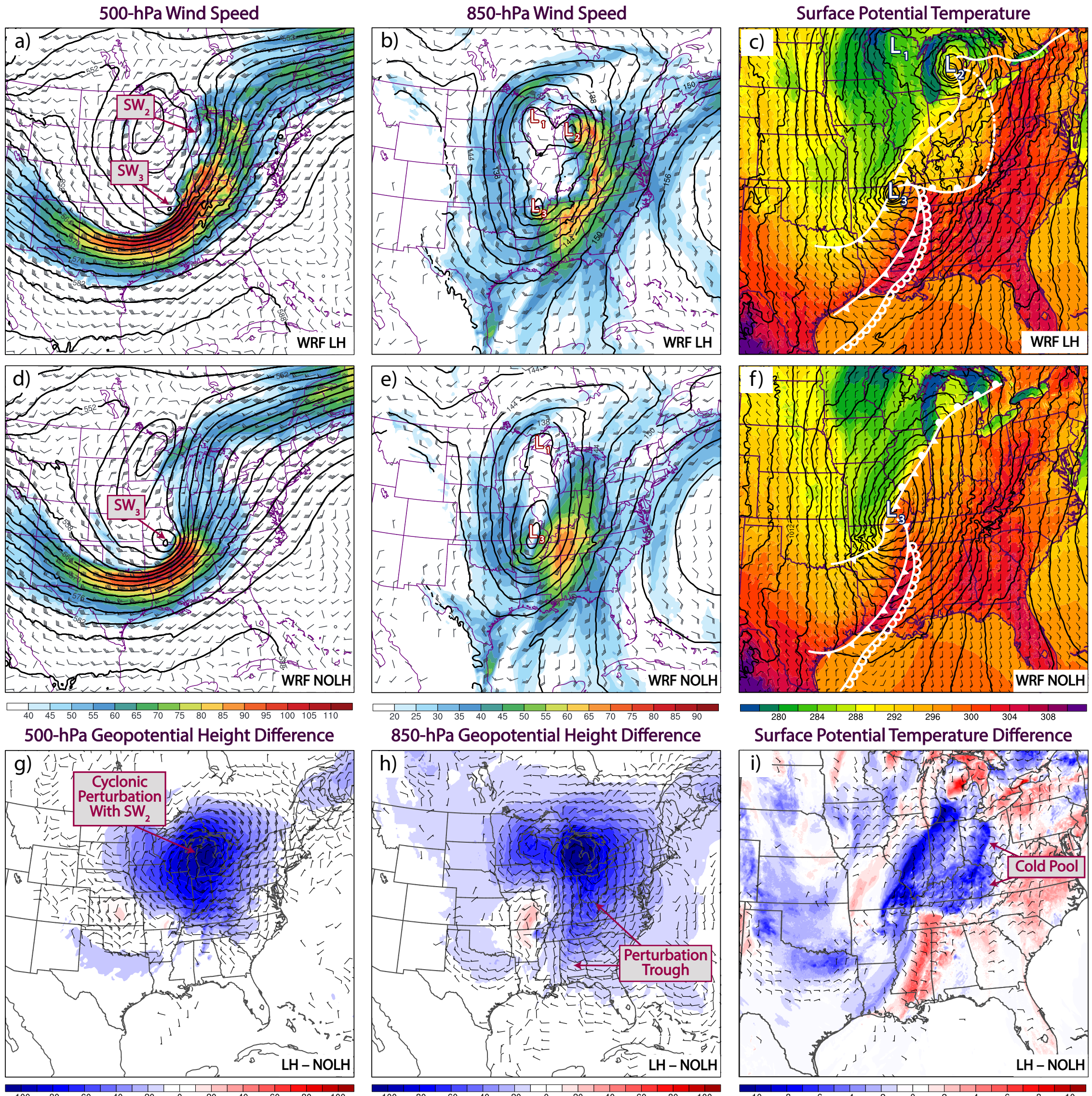

Figure 58: *Comparison of wind speed (shading; kt), geopotential height (contours; dam), and total winds (barbs; kt) valid at 1800 UTC 27 April from the (top) LH simulation at (a) 500 hPa and (b) 850 hPa and (middle) NOLH simulation at (d) 500 hPa and (e) 850 hPa. Difference fields of geopotential height (shaded; m) and horizontal winds (barbs; kt) at 500 hPa and 850 hPa are displayed in (g) and (h), respectively. Corresponding analyses of 2-m potential temperature (shaded; K), SLP (contours; hPa), 10-m winds (barbs; kt), and manually analyzed surface fronts are shown for the LH and NOLH simulations in (c) and (f), respectively. Difference fields of surface potential temperature (shaded; K) and 10-m winds (barbs; kt) are displayed in (i). The upper-level fields are shown on the 15-km outer domain, and the surface fields are shown on the 3-km inner domain.*

were also apparent and resulted both directly from the QLCSs (e.g., production of cool surface outflow) and indirectly (e.g., modifications to the baroclinic wave structure and thus dynamical forcing for low-level height falls and cyclogenesis). The NOLH simulation featured an elongated trough that extended northward from L_3 into the Great Lakes region and supported a highly amplified warm sector comprising uninterrupted southerly flow with an embedded LLJ that was actively strengthening beneath the J_1 exit region at this time (Figs. 58e,f). In contrast, L_3 was deeper and more contracted in scale in the LH simulation (Figs. 58b,c), and the added height perturbations accompanying L_2 and its appendage trough—which extended southwestward into the Gulf of Mexico and was collocated with a perturbation cyclonic wind shift (Fig. 58h)—promoted more veered southwesterly low-level flow over the Southeast. Moreover, two LLJ maxima had formed in association with L_2 and L_3, and the southern maxima (which comprised 60–70-kt winds—slower than in the RUC, primarily due to the misrepresentation of J_4) was bounded to the north by the residual cold pool (Figs. 58b,c).

Overall, the structure of the thermal wave was significantly modified by convection in the LH simulation, with differences evident in the baroclinity and position of surface fronts (e.g., the cold front in Mississippi) and the confinement of the "warm sector" to the south of the effective warm front (Fig. 58i). Moreover, these differences were consequential for the cyclone structure—even more so in reality than the LH would suggest. Specifically, in the absence of outflow from the QLCSs, L_3 acquired a structure that was generally reminiscent of a Shapiro-Keyser cyclone (e.g., Shapiro and Keyser, 1990; Schultz et al., 1998, 2019), with a broad warm sector and weak cold front that was moving roughly orthogonal to the quasi-stationary synoptic front.[9] In contrast, an warm-type occlusion developed at the interface between the Pacific cold front and effective warm front in the LH simulation and in the observations (Figs. 19e and 31a), which is lacking in the Shapiro-Keyser cyclone

[9]Note that this frontal fracture structure was evident in the potential temperature field in Fig. 58f but was not reflected in the annotated cold frontal position over the Central Mississippi Valley.

model and highlights the significance that mesoscale processes often have in influencing the structure and evolution of synoptic-scale disturbances.

4.6 Summary and discussion

In this chapter, we evaluated the environmental modifications produced by the two successive QLCSs. Overall, QLCS1 drastically altered the large-scale pattern and induced flow modifications that contributed to its upscale growth and notable severity, while QLCS2 modified the mesoscale environment and enhanced the shear profiles over the Southeast prior to the afternoon supercell outbreak. Collectively, these multiscale modifications yielded conditions that likely enhanced the severity of convection during the multiepisode outbreak.

Specific and noteworthy findings were as follows:

- Following CI associated with QLCS1 on the evening of 26 April, upper-level geopotential heights increased downstream from SW_2, which amplified the flow curvature and induced dynamical imbalance. Over eastern Texas, convection interrupted the upper-level jet exit region and yielded greater parcel decelerations and a stronger thermally indirect transverse circulation. Over Arkansas, widespread convection rapidly sharpened the preexisting upper-level PV gradient that was established in the wake of SW_1 (via diabatic PV erosion and negative PV advection by strong divergent outflow) and consequently promoted the downstream formation of J_2.
- The J_2 entrance region was dynamically unbalanced and highly divergent, which facilitated QLCS1's upscale growth as J_2 rapidly strengthened and advanced poleward overnight. This evolution promoted downstream ridge amplification and reduced the wavelength and eastward progression of the large-scale pattern. Moreover, J_2 was accompanied by an isallobaric response that rapidly intensified the LLJ ahead of QLCS1.

- The upper-level height and PV gradients strengthened to the west of QLCS1 following its upscale growth and promoted the formation of J_3 by 27/0600Z. Furthermore, differential vertical motions and sustained midlevel subsidence induced a tropopause fold behind QLCS1, which did not form in the absence of latent heating. This secondary tropopause fold was directly attributable to the development and upscale growth of convection near a preexisting PV gradient and prolonged environmental modifications arising from this convection.

- Cyclogenesis occurred along the quasi-stationary front behind QLCS1 as the secondary tropopause fold and amplified SW_2 interacted with a prominent low- to midlevel PV anomaly. L_2 did not develop in the absence of latent heating and was therefore a direct consequence of the upscale modifications from QLCS1. The height perturbations accompanying L_2 and its associated trough supported more veered low-level flow over the Southeast during the afternoon. Moreover, continued amplification of SW_2 diminished the large-scale flow curvature downstream from the upper-level trough and helped establish strong southwesterly flow aloft over the Southeast.

- Using WRF simulations configured with and without latent heating, we evaluated whether the thermodynamic and kinematic environmental modifications arising from QLCS1 may have furthered its longevity and severity. In the LH simulation, low-level wind shear increased throughout the inflow environment, and the 0–1-km shear difference vector was oriented nearly parallel to QLCS1 at 27/0600Z—supportive of the strong line-parallel shear emphasized in Chapter 3. SRH also increased in conjunction with greater shear and hodograph curvature. Therefore, QLCS1 provided more favorable kinematic conditions for the production of severe convective hazards (e.g., damaging winds and tornadoes)—an upscale feedback effect that likely enhanced its own severity. Conversely, CAPE decreased throughout the environment in the LH simulation, predominantly due to warming aloft congruent with deep-tropospheric subsidence and mass conservation. However, coherent CIN increases were primarily confined to the south of QLCS1, with alternating mesoscale regions of increased and decreased CIN found within the immediate inflow environment.

- QLCS2 was accompanied by a meso-α-scale region of upper-level height rises and midlevel warming that enhanced the mesoscale flow curvature and baroclinity ahead of SW_3 during the morning of 27 April and promoted the generation of J_4 downstream over the Midwest. The right-entrance region of J_4 was unbalanced and characterized by considerable upper-level divergence. Furthermore, the J_1 exit region was split into two branches around QLCS2, and the southern branch contributed to the strong deep-layer shear present over the Southeast during the afternoon. This flow disruption—coupled with the rapid strengthening of J_4—yielded an isallobaric response that further intensified the LLJ ahead of SW_3 and established a regional maxima in low-level wind speed (and accordingly low-level shear) over northern Mississippi and Alabama during the supercell outbreak.

- The respective contributions of geostrophic and ageostrophic motions to the total wind hodographs over the Southeast at the beginning of the supercell outbreak were evaluated. The geostrophic hodographs all depicted strong southwesterly flow but overall weak vertical wind shear that alone would not have supported a prolific tornado outbreak. In contrast, the highly curved hodographs and strength of the vertical wind shear throughout the lower to middle troposphere were due almost entirely to the ageostrophic wind profile, which veered appreciably with height and resulted from a combination of frictional effects, flow curvature, and—of particular importance—strong accelerations within the LLJ entrance region. Thus, ageostrophic motions were absolutely essential to creating the highly favorable shear profiles present during the prolific afternoon supercell outbreak.

- Of notable importance in this event was the development and rapid strengthening of convectively forced jet streaks downstream from the upper-level trough—specifically, the formation of J_2 with QLCS1 and J_4 with QLCS2. Both jet streaks resulted from convection intruding upon preexisting geopotential height and PV gradients that were established in the wake of a preceding shortwave trough and thus had a substantial meridional component. Consequently, the upper-level outflow that developed along

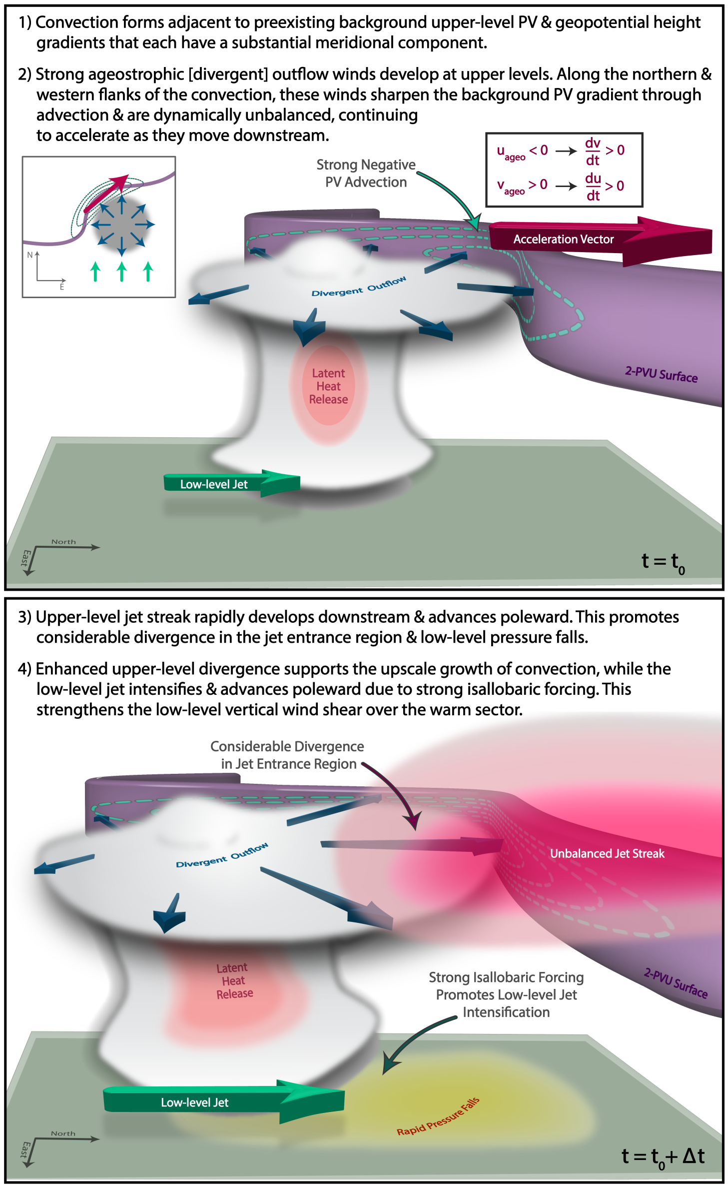

Figure 59: *Schematic summarizing how convection interacting with background PV and geopotential height gradients along the southeastern flank of an amplified upper-level trough can induce an unbalanced jet streak that rapidly advances poleward, aiding in the upscale growth of convection and yielding intensification of the LLJ and low-level shear within the warm sector.*

the northern and western flanks of the QLCSs became dynamically unbalanced, yielding strong accelerations as these outflow jets quickly advanced poleward with time—analogous to the poleward momentum surges described by Rowe and Hitchman (2016). This unique evolution augmented the strength of the LLJ and vertical wind shear over the warm sector throughout the outbreak and is schematized in Fig. 59.

Chapter 5

Convection-permitting ensemble simulations

5.1 Introduction

An ensemble of convection-permitting WRF-ARW simulations was sought to (1) further investigate the influence of latent heat release and upscale feedbacks on the outbreak evolution, and (2) study the mesoscale processes that influenced CI and convective morphology during the supercell outbreak (described in Chapter 6).

Several studies over the past decade have used convection-permitting ensembles to investigate the relevant physical processes that lead to differences or errors in the forecast evolution of severe weather events. Many of these studies have employed ensemble-based sensitivity analysis (ESA; Torn and Hakim, 2008), which is a statistical technique used to quantify the sensitivity of a forecast metric (e.g., maximum vertical velocity within convective updrafts) to prior characteristics of the model environment (e.g., initial conditions or low-level moisture 3-h earlier; Bednarczyk and Ancell, 2015; Torn and Romine, 2015; Hill et al., 2016; Torn et al., 2017; Berman et al., 2017). Another commonly used approach involves constructing subgroups of ensemble members (or ensemble subsets) that vary based on some metric or property (e.g., CI location, convective mode, etc.) and evaluating the differences between their composites (e.g., Schumacher, 2011; Hanley et al., 2013; Trier et al., 2015, 2019, 2021).

Trier et al. (2021) recently applied this subsetting approach to investigate the physical processes responsible for CI and the environmental factors influencing the severity of convection within a 50-member ensemble forecast of a VORTEX-SE case. In their study, two subsets were configured by grouping the ensemble members with the strongest and weakest convection, and the environmental conditions for each subset were averaged to produce composites. These composites were then compared with each other and with the ensemble mean to provide insight into how environmental factors governed the initiation and intensity of convection over the Southeast. We take a similar approach herein and analyze composites generated from two ensemble subsets to further study the upscale environmental modifications produced by QLCS1.

5.2 Ensemble design and validation

5.2.1 Ensemble configuration

Two 50-member convection-permitting ensemble forecasts were configured using mean initial conditions (ICs) from the NCEP 0.5° GFS analysis (hereafter "GFS ensemble") and European Centre for Medium-Range Weather Forecasts (ECMWF) 0.25° ERA5 reanalysis (Hersbach et al., 2020, hereafter "ERA5 ensemble") valid at 1800 UTC 26 April 2011. Both ensembles were run using WRF-ARW version 4.2.1 and employed the same nested grid configuration and physics parameterization schemes as the deterministic full-physics WRF LH simulation described in Chapter 4.5. These specifications are summarized in Table 5.1 for the GFS ensemble. The model configuration used in the ERA5 ensemble was identical except for the mean ICs and lateral boundary conditions (LBCs).

Overall, the ensemble design presented herein was fairly similar to that used in the NCAR real-time convection-permitting ensemble (Schwartz et al., 2015, 2019). Unique ICs for the ensemble forecasts were generated using flow-dependent perturbations derived from a continuously cycled ensemble adjustment Kalman filter (EAKF; Anderson, 2001) analysis system implemented within the Data Assimilation Research Testbed (DART; Anderson et al., 2009) software. Several steps were required to obtain these flow-dependent IC perturbations before conducting the 50-member ensemble forecasts. To begin, an 80-member mesoscale ensemble with 15-km grid spacing (i.e., over the outer WRF domain shown in Fig. 51) was produced by applying random Gaussian perturbations with NCEP global background error covariances taken from the WRF data assimilation (WRFDA) system (Barker et al., 2012) to the GFS analysis from 1200 UTC 24 April 2011. This ensemble provided ICs for an

Table 5.1: *Model configuration and physics parameterizations used in the GFS ensemble simulations generated with WRF-ARW version 4.2.1.*

	Outer Domain	**Inner Domain**
Grid Configuration		
Initial conditions	Perturbed 0.5° GFS analysis from 1800 UTC 26 April 2011	Perturbed 0.5° GFS analysis from 1800 UTC 26 April 2011
Lateral boundary conditions	6-h 0.5° GFS analyses	Outer WRF domain
Horizontal grid spacing	15 km	3 km
Number of grid points	420×320	1151×981
Number of vertical levels	70	70
Model top	10 hPa	10 hPa
Time step	30 s	6 s
Physics parameterizations		
Cumulus	New Tiedtke	None
PBL	MYNN level 2.5	MYNN level 2.5
Surface layer	MYNN	MYNN
Land surface model	Unified Noah	Unified Noah
Microphysics	Thompson	Thompson
Shortwave radiation	RRTMG	RRTMG
Longwave radiation	RRTMG	RRTMG

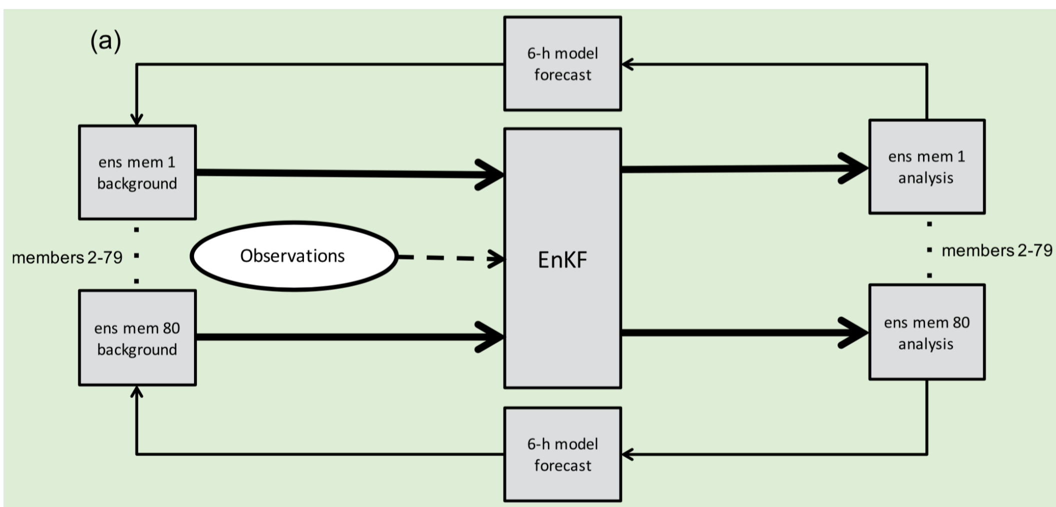

Figure 60: *Schematic from Schwartz et al. (2019) depicting the continuously cycling EnKF DA system used in the NCAR ensemble analysis system with 80 members and a 6-h cycle period. In the EnKF, an ensemble of backgrounds is combined with conventional observations to produce an ensemble of analyses, which then initialize ensembles of 6-h forecasts that become backgrounds for a subsequent DA cycle 6 h later.*

80-member short-term forecast, and the ensemble valid at 1800 UTC 24 April was then used as the background (prior) for the first ensemble Kalman filter (EnKF) assimilation cycle.

Conventional observations obtained through NCEP's Meteorological Assimilation Data Ingest System (MADIS) archive were assimilated every 6 h through DART's ensemble Kalman filter (EnKF) system using continuous cycling with the previous 6-h ensemble forecast serving as the new background state (see Fig. 60 for a schematic of this cycled DA procedure based on the NCAR ensemble). This continuously cycling EnKF procedure generated an updated *ensemble of 15-km analyses every 6 h between 1800 UTC 24 April and 1800 UTC 28 April* with perturbations (defined relative to the EnKF analysis mean) that acquired flow dependence over time. These perturbations included potential temperature; geopotential height; dry surface pressure; horizontal wind components; mixing ratios for water vapor, rain, cloud water, cloud ice, snow, and graupel; and number concentrations for rain and cloud ice. Unique LBCs were derived by applying random perturbations to either the GFS analyses or ERA5 reanalyses following the method described by Torn et al. (2006) and updated every 6 h for the outer 15-km domain of each ensemble analysis member.

The ensemble forecasts described herein used unique ICs that were produced by extracting the flow-dependent perturbations from the first 50 ensemble analysis members valid at 1800 UTC 26 April (by subtracting the EnKF analysis mean from each member for all perturbation fields except for hydrometeor mixing ratios and number concentrations, for which the full EnKF analysis fields were used as the GFS and ERA5 hydrometeor values were set to zero by the WRF Preprocessing System) and adding them to either the GFS analysis (for the GFS ensemble) or ERA5 reanalysis (for the ERA5 ensemble) valid at this same time. This approach provided two independent sets of 50 ICs centered on either the GFS analysis and ERA5 reanalysis mean state wherein each member of a given set could be considered equally likely to represent the true atmospheric state at 1800 UTC (e.g., Schwartz et al., 2019). Schwartz et al. (2020) recently demonstrated that applying this recentering perturbation technique to GFS analyses yields superior forecasts of convective events owing to its higher quality and greater abundance of assimilated observations (including satellite radiances) compared to continuously cycled regional EnKF analyses (Schwartz et al., 2020). These perturbed GFS and ERA5 ICs were then used to initialize two 30-h convection-permitting ensemble forecasts over the two-way nested grid configuration shown in Fig. 51.

5.2.2 Comparisons and validation

Output from both ensembles were compared to each other and validated against radar observations, surface observations, and upper-air fields from the corresponding 1-h RUC forecasts to determine which set of simulations provided a better representation of the outbreak evolution. Overall, all members of both ensembles depicted the initial formation and upscale growth of QLCS1, secondary CI associated with QLCS2, and the development of multiple quasi-discrete cells over the Southeast during the afternoon of 27 April. Within each individual ensemble, variations in the timing, location, and extent of CI and in the convective organization were evident among members. Despite these nuances, the individual members of either ensemble were fairly consistent in their general depiction of the outbreak (i.e., the ensemble spread was relatively low overall), while notable systematic differences were evident between the two ensemble sets.

5.2.2.1 Evolution of the simulated convection

Simulated composite radar reflectivity from two representative members of each ensemble (i.e., Members 20 and 44) is displayed every 6 h between 27/0000Z–27/1800Z in Figs. 61 and 62[1]. Initial convective development associated with QLCS1 was slightly slower in the ERA5 ensemble compared to the GFS ensemble (not shown). However, both ensembles had produced a widespread region of strong convection that extended from northeastern Arkansas into eastern Texas by 27/0000Z. This initial convective organization within the GFS ensemble better corresponded with the observed system—which comprised a combination of supercell clusters and line segments at this time (Fig. 3b)—while supercell clusters

[1]All figures herein are shown on the 3-km inner WRF domain unless specified otherwise.

dominated overall in the ERA5 ensemble. Despite these differences, both ensembles similarly depicted the upscale growth of convection into an expansive QLCS by 27/0600Z, although QLCS1 had acquired a greater meridional orientation in the GFS ensemble.

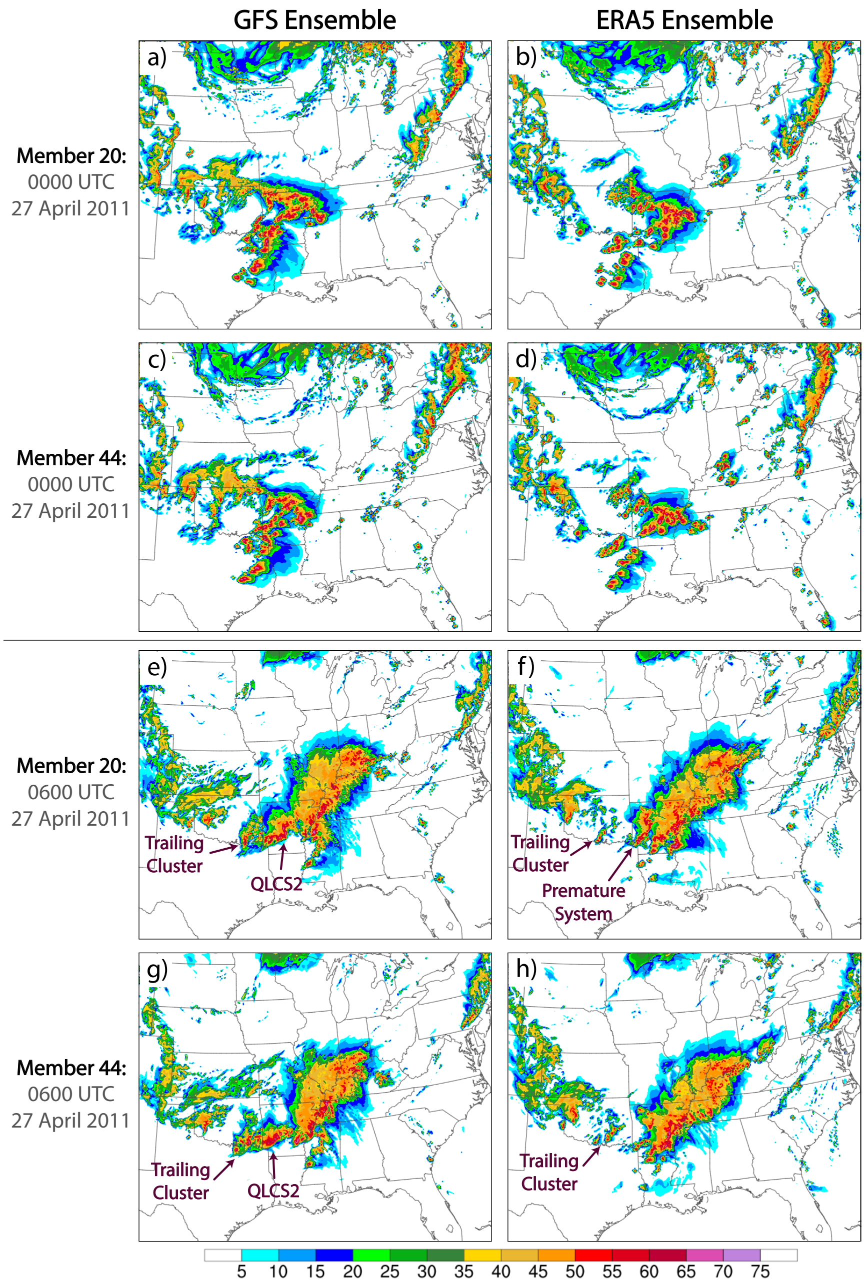

Figure 61: *Simulated composite radar reflectivity (shaded; dBZ) for members 20 and 44 of the (left) GFS ensemble and (right) ERA5 ensemble at (a)–(d) 0000 UTC and (e)–(h) 0600 UTC 27 April 2011.*

By 27/0600Z, the observed system comprised a quasi-linear band of strong convection that extended southwestward through northern Louisiana and primarily originated from the upscale growth of convection that developed ahead of the dryline over eastern Texas (Figs. 3c-d). As was previously discussed in Chapter 3, this convective band subsequently evolved into the prolific bowing segment that produced severe winds and numerous significant and/or long-track tornadoes overnight throughout much of the Southeast (Figs. 3e-f). Although numerous mature convective cells were situated over eastern Texas at 27/0000Z in the simulations, these cells failed to grow upscale and instead weakened considerably and eventually dissipated as they moved eastward with time. This progression consistently occurred in all members of both ensembles, while specific details of this morphological evolution varied among the individual members. For example, the remnants of these cells corresponded to the broken band of weakening convection over Mississippi at 27/0600Z in Members 20 and 44 of the GFS ensemble, whereas several other members (e.g., Members 4, 8, and 40; not shown) retained little to no active convection over Mississippi or Louisiana from these initial cells. *Consequently, both ensembles fundamentally failed to develop and sustain the southern portion of QLCS1, which suggests that the predictability of the most severe and impactful part of this system—the notably tornadic bowing segment that moved through the Southeast—was limited and that both ensembles were underdispersed.* The poleward bias in the southward extent of convection was more pronounced in the GFS ensemble as QLCS1 moved through the Southeast and was partly due to a faster system motion, which seemed to be influenced by the early formation of QLCS2 immediately upstream from the system. Accordingly, the placement and evolution of QLCS1 through the Southeast at later times (e.g., 27/0900Z) within the ERA5 ensemble better matched the observations (not shown).

Whereas the evolution of QLCS2 differed considerably between the GFS and ERA5 ensembles, they both failed to correctly represent this system's complex morphological evolution and its resultant upscale environmental modifications. The CI episode that led

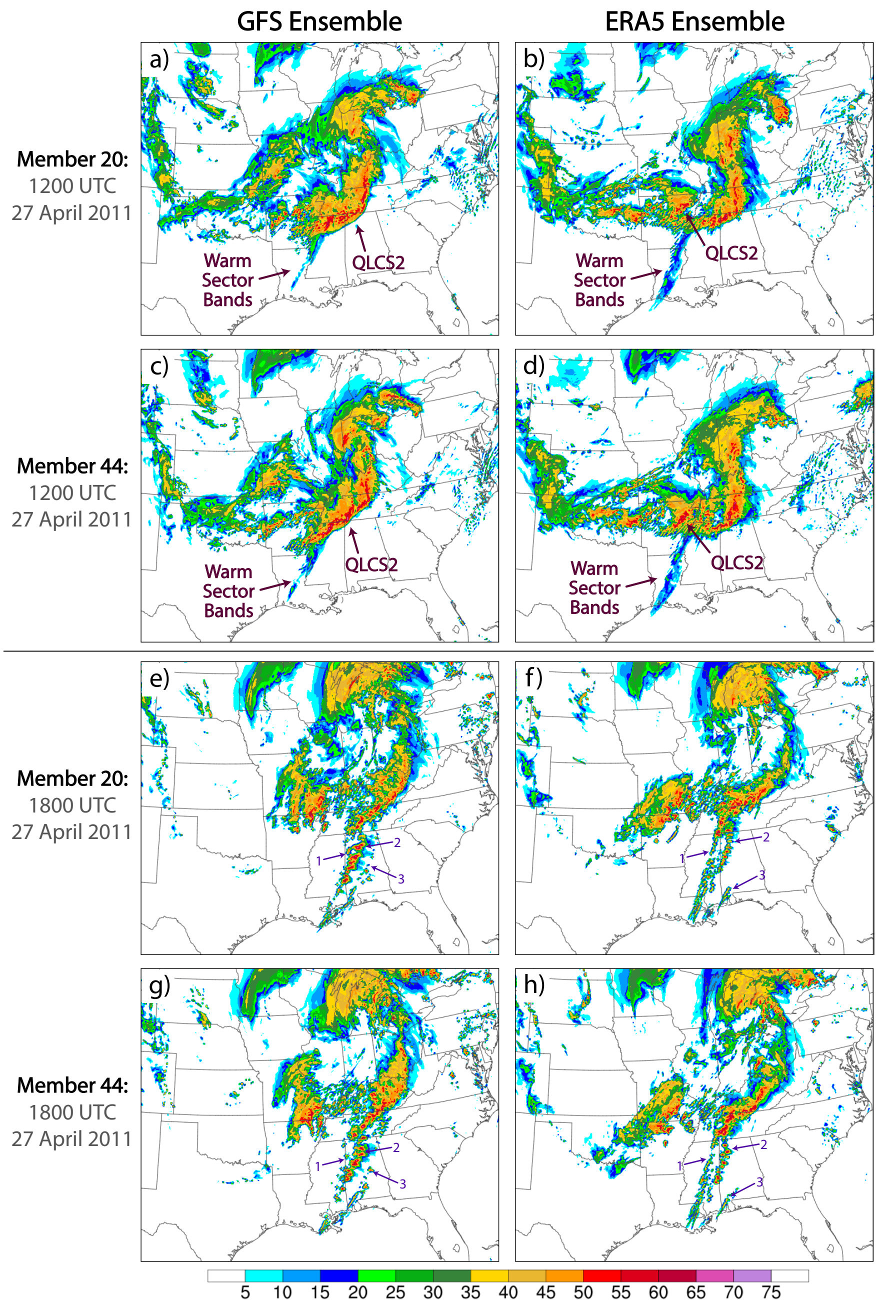

Figure 62: *As in Fig. 61, but for (a)–(d) 1200 UTC and (e)–(h) 1800 UTC 27 April 2011.*

to the formation of QLCS2 occurred several hours too early and too far west in the GFS ensemble (i.e., beginning around 27/0400Z over southeastern Oklahoma). By 27/0600Z, this convection had coalesced into a strengthening bow echo over Arkansas and was situated immediately behind QLCS1, while a secondary trailing cluster of convection had formed over Oklahoma in several ensemble members (Figs. 61e,g). By 27/0900Z—at which time convection associated with the observed QLCS2 was just beginning to form over the Ark-La-Tex region (Fig. 3e)—the leading edge of the simulated bow echo had progressed into the Lower Mississippi Valley within the GFS ensemble (not shown). Owing to the premature development and maturation of QLCS2, this system's separation from QLCS1 was reduced considerably relative to the observations, and its influence on the morphological evolution of QLCS1 was enhanced beginning several hours too early. QLCS2 therefore became largely indistinct from the southern portion of QLCS1 over time, and several ensemble members had completely merged the two systems together by 27/1200Z (e.g., Fig. 62a). However, the latter evolution of the simulated QLCS2 was reminiscent of the observed system in that it became increasingly disorganized throughout the late morning and had evolved into a widespread region of broken convection over Tennessee and Kentucky by 27/1800Z (Figs. 62e,g).

In contrast, some members of the ERA5 ensemble (e.g., Member 20) also showed a premature cluster of convection developing behind QLCS1 by 27/0400Z (e.g., the "premature system" labeled in Fig. 61f), but this convection did not mature into a dominant and sustained bow echo. Instead, the system corresponding to QLCS2 emerged from the trailing cluster of convection located over Oklahoma at 27/0600Z (Figs. 61f,h) and began to organize over Arkansas at approximately the same time as the observed system. While the timing of CI that led to QLCS2 was better represented in the ERA5 ensemble, this system initially manifested as stronger convective clusters that were embedded within a widespread region of broken convection and coalesced over time (Figs. 62b,d). However, this convection never organized into a coherent bow echo and instead attained its peak intensity over Arkansas before rapidly weakening after ~27/1200Z. By 27/1800Z, several clusters of strong convection had developed over Kentucky and Tennessee (Figs. 62f,h), but these clusters evolved separately from the initial convection associated with QLCS2 and seemed to be more closely related to the third episode of CI that led to the afternoon supercell outbreak.

Overall, the CI signatures associated with the premature system that ultimately became QLCS2 in the GFS ensemble and the trailing cluster that developed into QLCS2 in the ERA5 ensemble were present in both ensembles. *Therefore, it seems highly plausible that the simulated QLCS2 originated from the premature and spurious upscale growth of convection that formed over Oklahoma and Arkansas in the GFS ensemble.* This spurious system then dominated over the trailing cluster of convection, which evolved into QLCS2 in the ERA5 ensemble and better aligned with the timing and location of observed CI. Regardless of the origin of this convection, QLCS2 became increasingly disorganized and weakened considerably with time in both ensembles as it progressed northeastward in advance of SW_3, which was consistent with the observed system.

Both ensembles depicted the formation of quasi-discrete convection over the warm sector during the afternoon supercell outbreak, and this convection primarily developed near the Mississippi-Alabama border between 27/1700Z–27/1900Z (Figs. 62e-h). Thus, the simulated timing of CI was generally consistent with the observed onset of the supercell outbreak, but an eastward bias in the CI location occurred in both ensembles (cf. Figs. 3h and 62e-h). CI during the afternoon was focused along multiple bands (labeled "1", "2", and "3" in Figs. 62e-h) that largely stemmed from an initially coherent comma-shaped disturbance in simulated radar reflectivity, which had appeared over the warm sector by 27/1200Z and intersected the strongest convection within QLCS2 at this time (Figs. 62a-d). The nature and evolution of these three bands are described further using the GFS ensemble in Chapter 6.

Overall, convection developed slightly earlier and farther to the east in the GFS ensemble than in the ERA5 ensemble. In both ensembles, CI first occurred along Band 2 and was followed by a secondary CI episode along Band 1 shortly thereafter. These two bands were largely superposed in the GFS ensemble and had produced a broken line of strong convection by 27/1800Z (Figs. 62e,g). In contrast, Bands 1 and 2 exhibited greater separation in the ERA5 ensemble, and two distinct corridors of developing convection were evident at 27/1800Z (Figs. 62f,h), in better agreement with the observations. Additionally, a third arc-shaped band of weak convective echoes associated with attempted CI was situated over Alabama—particularly within the GFS ensemble, where it was ~100–150 km ahead of the primary convective line associated with Band 2. Although Band 3 became more distinct with time, it did not produce any sustained deep convection within most members of either ensemble. By 27/2100Z, both ensembles had produced an elongated corridor of quasi-discrete rotating updrafts that spanned from northeastern Kentucky through southern Alabama (not shown). Compared to the observed radar reflectivity at 27/2100Z (Fig. 3i), the simulations (1) extended the supercell outbreak too far northward and eastward, (2) produced more widespread convective coverage, and (3) led to an overall convective distribution that was more disorganized and exhibited a greater meridional and linear orientation. *Thus, while the ensembles supported the development of numerous supercells, the simulated mesoscale organization was generally less conducive to these storms remaining discrete for several hours as they traversed the warm sector.*

5.2.2.2 Evolution of the simulated mean environments

Mean fields from both ensembles were compared with each other and the RUC 1-h forecasts to (1) identify systematic differences in how each ensemble depicted various features and processes within the environment, and (2) determine which ensemble produced a better representation of the environmental conditions throughout the outbreak. To assess how the upper-level flow evolved within the two ensembles, the mean 250-hPa wind speed from each ensemble and the corresponding ensemble mean wind speed difference (calculated as *GFS ensemble mean − ERA5 ensemble mean*) are shown every 3 h from 27/0000Z–28/0000Z in Figs. 63–65.

Following CI with QLCS1, both ensembles had produced disruption to the upper-level jet exit region over eastern Texas and the downstream formation of J_2 over Missouri by 27/0000Z (Figs. 63a,d). However, differences between the two ensembles were evident

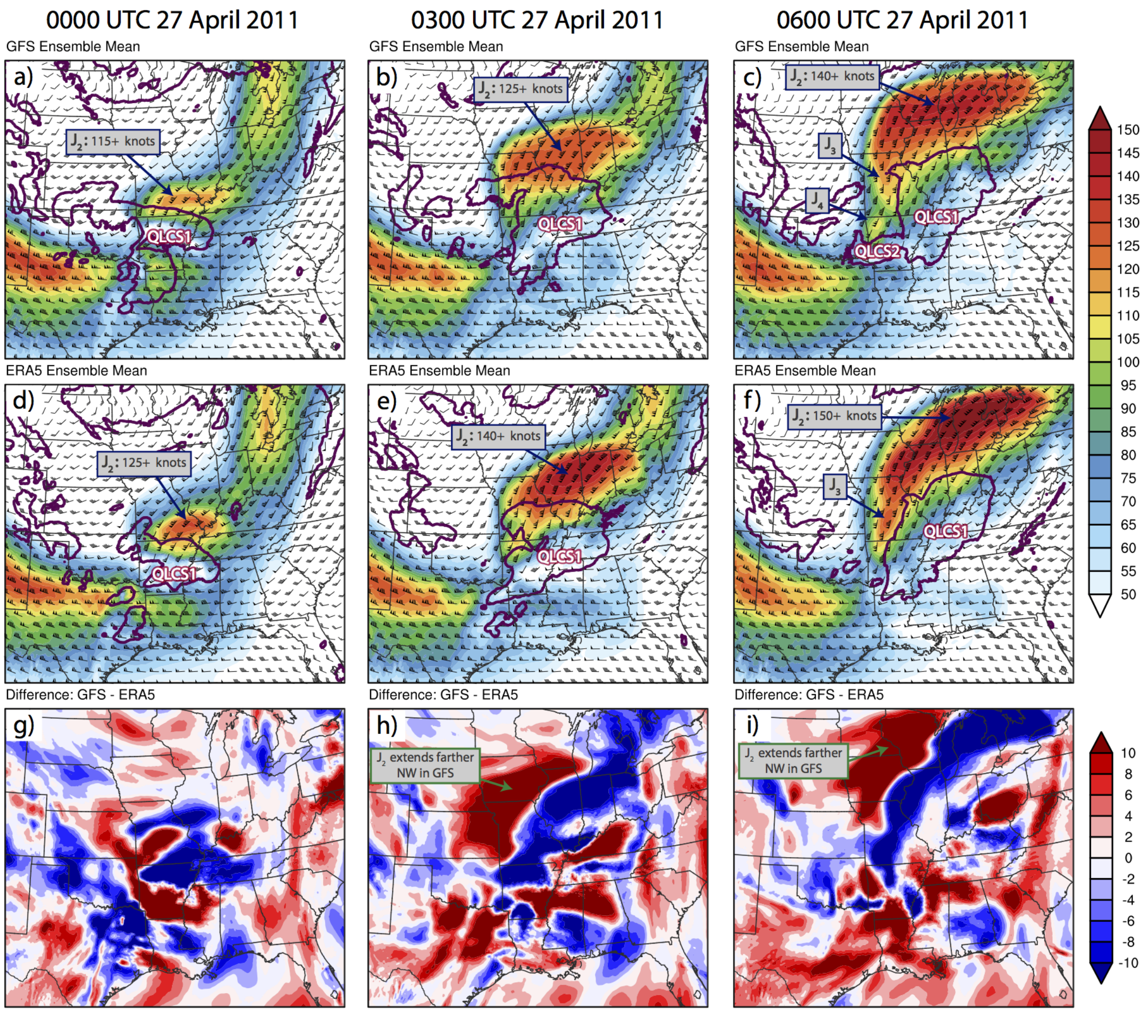

Figure 63: *Mean 250-hPa wind speed (shaded; kt), horizontal winds (barbs; kt), and simulated composite radar reflectivity = 10 dBZ (purple contours) from the (top) GFS and (middle) ERA5 ensembles, and (bottom) the mean wind speed difference between the GFS and ERA5 ensembles (shaded; kt) at (a),(d),(g) 0000 UTC 27 April, (b),(e),(h) 0300 UTC 27 April, and (c),(f),(i) 0600 UTC 27 April 2011.*

in the mean intensity and extent of J_2, which were related to systematic differences in how each ensemble represented the jet structure (i.e., physical differences between the two ensembles) and/or relative differences in ensemble spread. Specifically, J_2 exhibited a more elongated structure at 27/0000Z in the GFS ensemble mean and extended farther toward the northwest as it advanced poleward over time. By 27/0600Z, mean wind speeds in J_2 exceeded 140 kt over the Great Lakes in the GFS ensemble (Fig. 63c), compared to 150+ kt mean wind speeds in the ERA5 ensemble (Fig. 63f) and 135–140+ kt peak wind speeds in the corresponding RUC 1-h forecast (Fig. 53a). Furthermore, geopotential height increases were larger over the Upper Midwest in the GFS ensemble (not shown), promoting a more amplified upper-level flow pattern and the faster meridional reorientation of QLCS1.

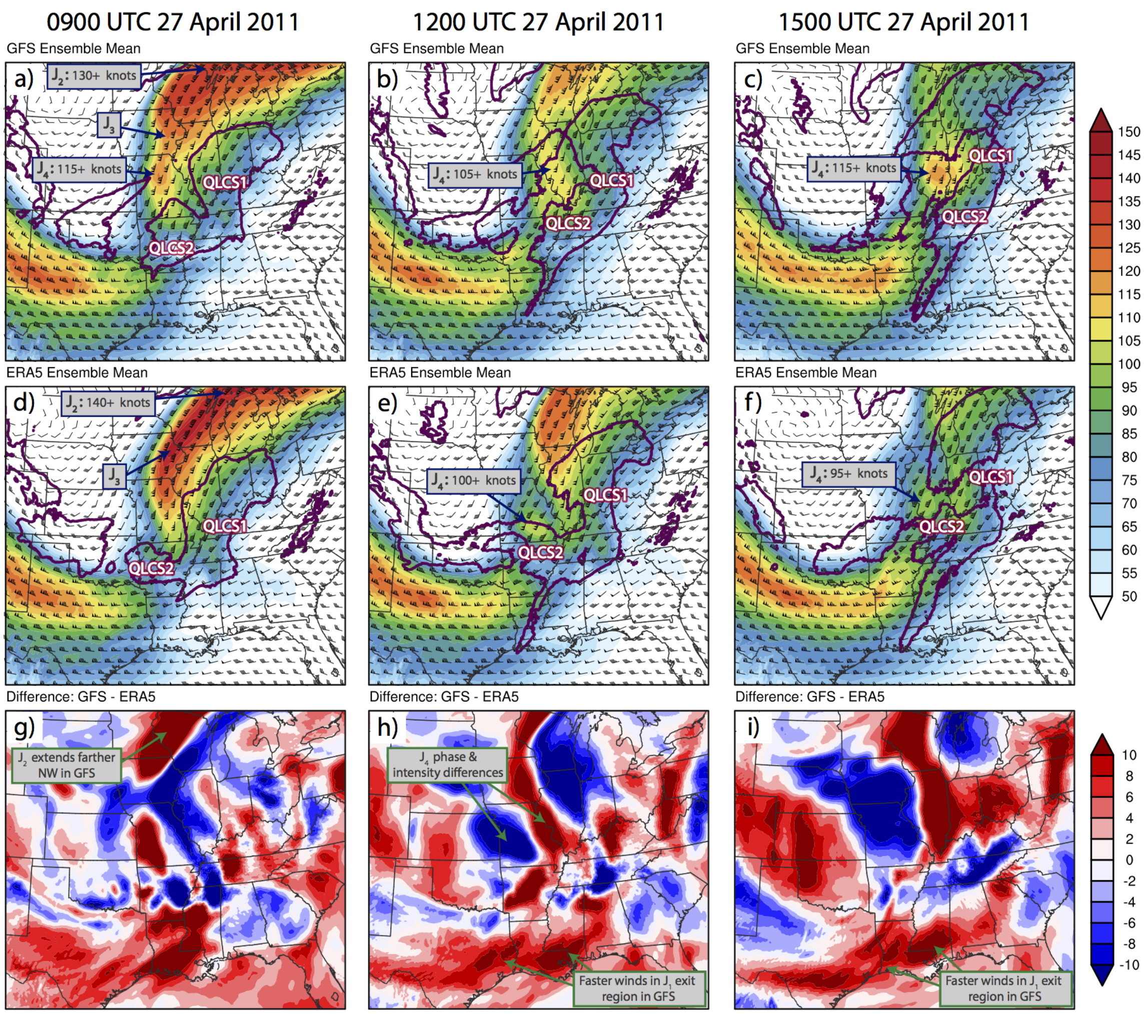

Figure 64: *As in Fig. 63, but for (a),(d),(g) 0900 UTC 27 April, (b),(e),(h) 1200 UTC 27 April, and (c),(f),(i) 1500 UTC 27 April 2011.*

Systematic differences in the evolution of QLCS1 plus the premature formation of QLCS2 within the GFS ensemble had translated into differences in the mean upper-level flow structure by 27/0900Z. In particular, the upper-level pattern remained markedly more amplified in the GFS ensemble, with J_2 exhibiting a broader structure and extending farther northwestward over Minnesota and Wisconsin (Figs. 64a,g). While the flow enhancement along the western flank of QLCS1 that corresponded to J_3 had developed in both ensembles by 27/0900Z, this jet was better defined and more persistent in the ERA5 ensemble owing to the system's overall slower meridional reorientation (Figs. 63f and 64d). In contrast, the premature development of QLCS2 in the GFS ensemble had promoted the genesis of J_4 over Arkansas by 27/0600Z, which merged with J_3 as it advanced poleward behind QLCS1 (Figs. 63c and 64a). J_4 quickly strengthened to 115+ kt by 27/0900Z in the GFS ensemble, but the jet subsequently weakened over the Midwest despite the persistence of strong convection with QLCS2 (Figs. 64a,b).

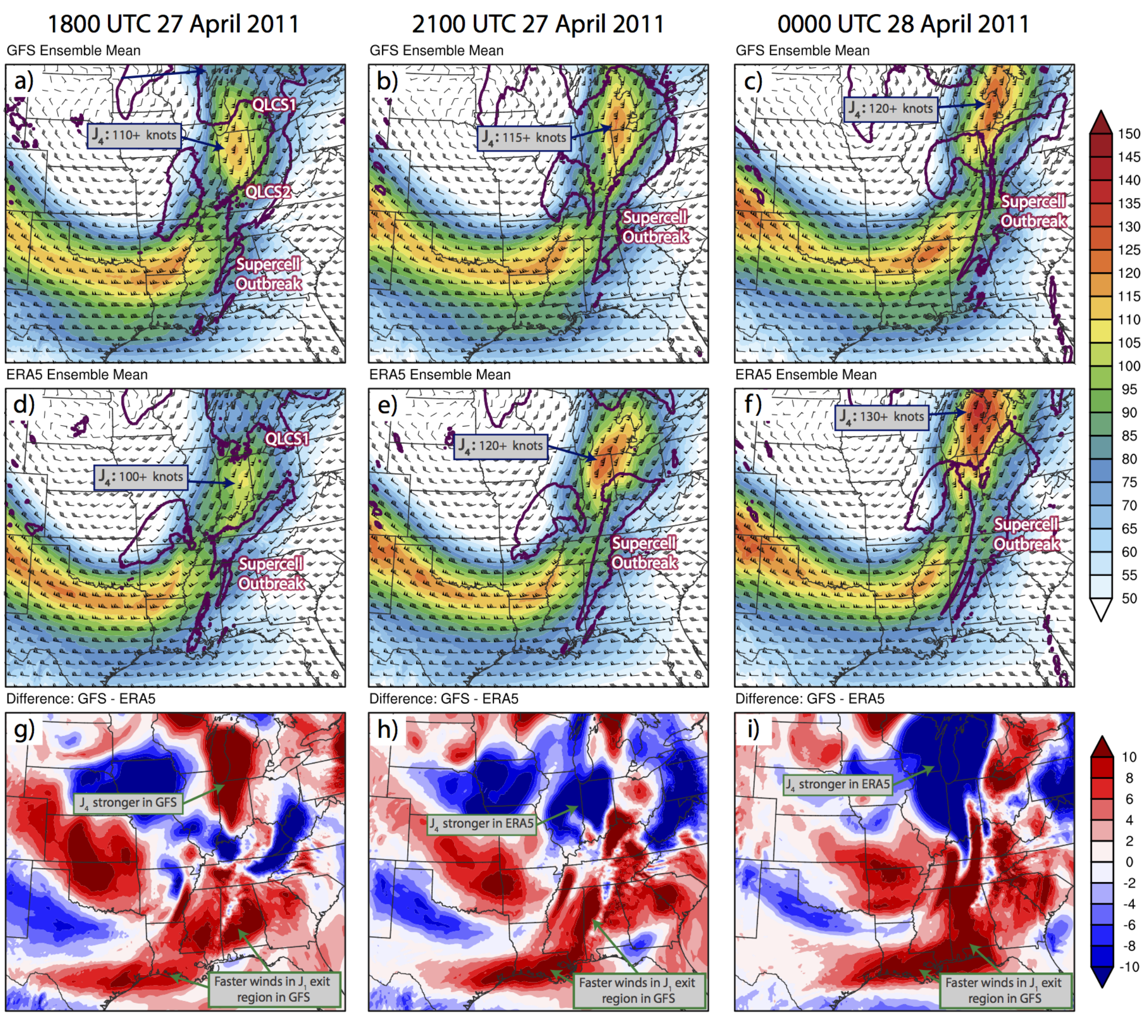

Figure 65: *As in Fig. 63, but for (a),(d),(g) 1800 UTC 27 April, (b),(e),(h) 2100 UTC 27 April, and (c),(f),(i) 0000 UTC 28 April 2011.*

Because convection associated with QLCS2 formed later in the ERA5 ensemble and was considerably weaker and less organized, J_4 was only beginning to develop at 27/0900Z and had attained a peak intensity of ~100 kt by 27/1200Z before subsequently weakening (Figs. 64e,f). J_4 exhibited pulsed behavior in both ensembles, gradually restrengthening over the Midwest throughout the late morning and afternoon in the GFS ensemble (Figs. 64c and 65a-c) and abruptly reintensifying during the afternoon in the ERA5 ensemble (Figs. 65d-f). However, by the onset of the supercell outbreak at 27/1800Z, wind speeds within J_4 were only ~110–115 kt and 100–105 kt in the GFS and ERA5 ensembles, respectively—much weaker than the ~140-kt jet streak that had formed in the RUC by this time (Fig. 40f).

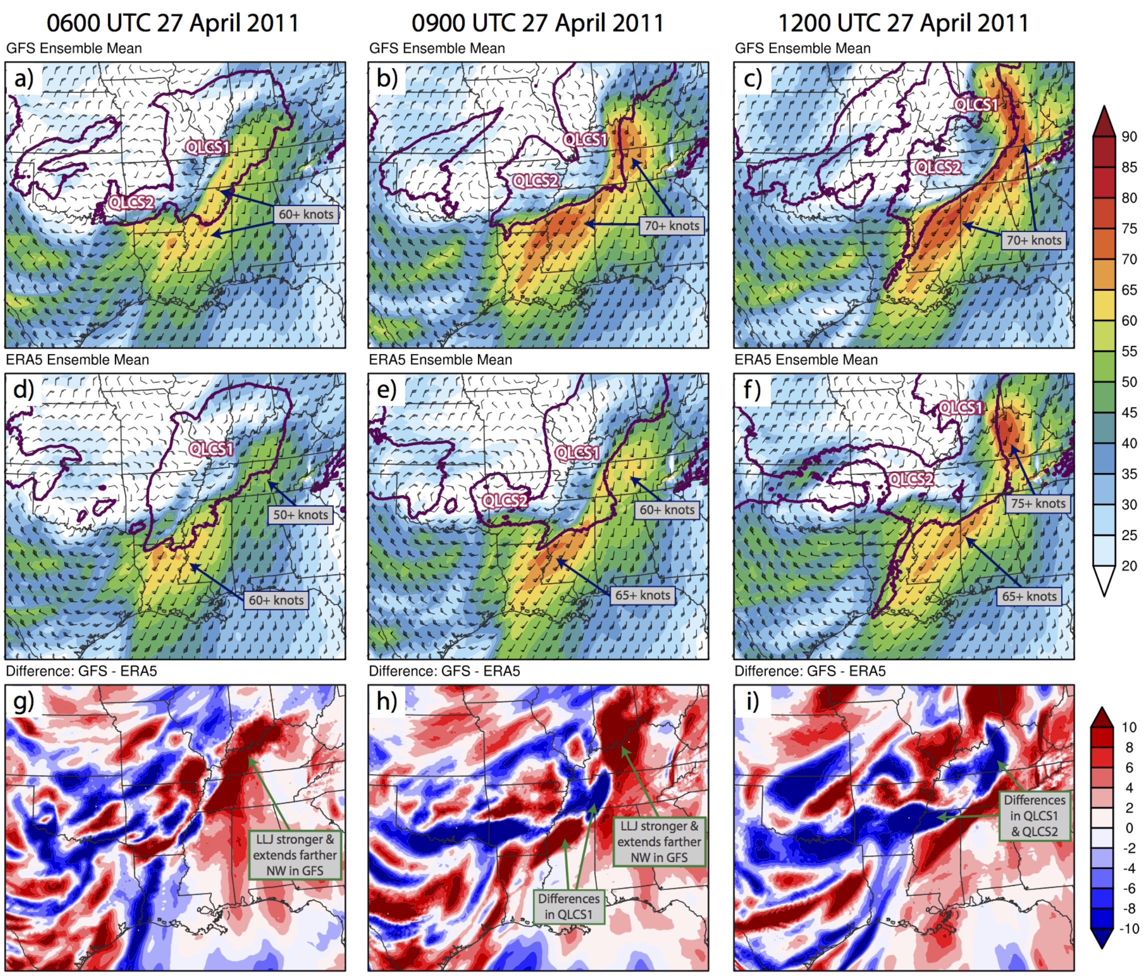

Figure 66: *Mean 850-hPa wind speed (shaded; kt), horizontal winds (barbs; kt), and simulated composite radar reflectivity = 10 dBZ (purple contours) from the (top) GFS and (middle) ERA5 ensembles, and (bottom) the mean wind speed difference between the GFS and ERA5 ensembles (shaded; kt) at (a),(d),(g) 0600 UTC 27 April, (b),(e),(h) 0900 UTC 27 April, and (c),(f),(i) 1200 UTC 27 April 2011.*

These fluctuations in upper-level jet intensity are expected to affect the timing and strength of supplemental isallobaric forcing for the LLJ ahead of SW_3 and yield differences in the LLJ evolution when compared to the RUC.

The mean 850-hPa wind speed from each ensemble and the corresponding mean wind speed difference field are shown every 3 h from 27/0600Z–27/1200Z in Fig. 66 and from 27/1800Z–28/0000Z in Fig. 67. In both ensembles, the LLJ intensified within the warm sector following CI and the development of J_2 over the Midwest (not shown). By 27/0600Z, 850-hPa wind speeds $\geq$ 60 kt extended northward into Kentucky ahead of QLCS1 in the GFS ensemble (generally consistent with the RUC; Fig. 53b), while the strongest low-level winds were largely confined to Mississippi and Louisiana in the ERA5 ensemble (Figs. 66a,d). The LLJ had further intensified and advanced northward by 27/0900Z in both ensembles, but wind speeds throughout the warm sector remained stronger (i.e., 65–70+ kt) in the GFS ensemble (Figs. 66b,e). Overall, the stronger and more extensive LLJ in the GFS ensemble during this period primarily resulted from the greater amplification of the upper-level flow pattern, which led to larger low-level height falls over the Mississippi and Ohio Valleys (not shown) and the faster meridional reorientation of QLCS1—thus enabling the uninterrupted LLJ to extend farther poleward ahead of the system.

The LLJ structure had become more complex in both ensembles by 27/1200Z (Figs. 66c,f). Further intensification of the low-level flow had occurred ahead of QLCS1 and over the Southeast in the GFS ensemble, but both the LLJ strength and the later morphological evolution of QLCS1 were influenced to some degree by the premature development of QLCS2 and J_4. In contrast, the LLJ had strengthened to 75+ kt over the Ohio Valley in the ERA5 ensemble, but the low-level flow had weakened discernibly over central Mississippi despite the initial development of J_4 (cf. Figs. 66e-f). This tendency was due to the movement of a mesoscale disturbance (i.e., a bore; see Chapter 6) over the Southeast—which promoted low-level ascent and a net decrease in 850-hPa wind speed in its wake—rather than diminished large-scale forcing in the ERA5 ensemble. An associated decrease

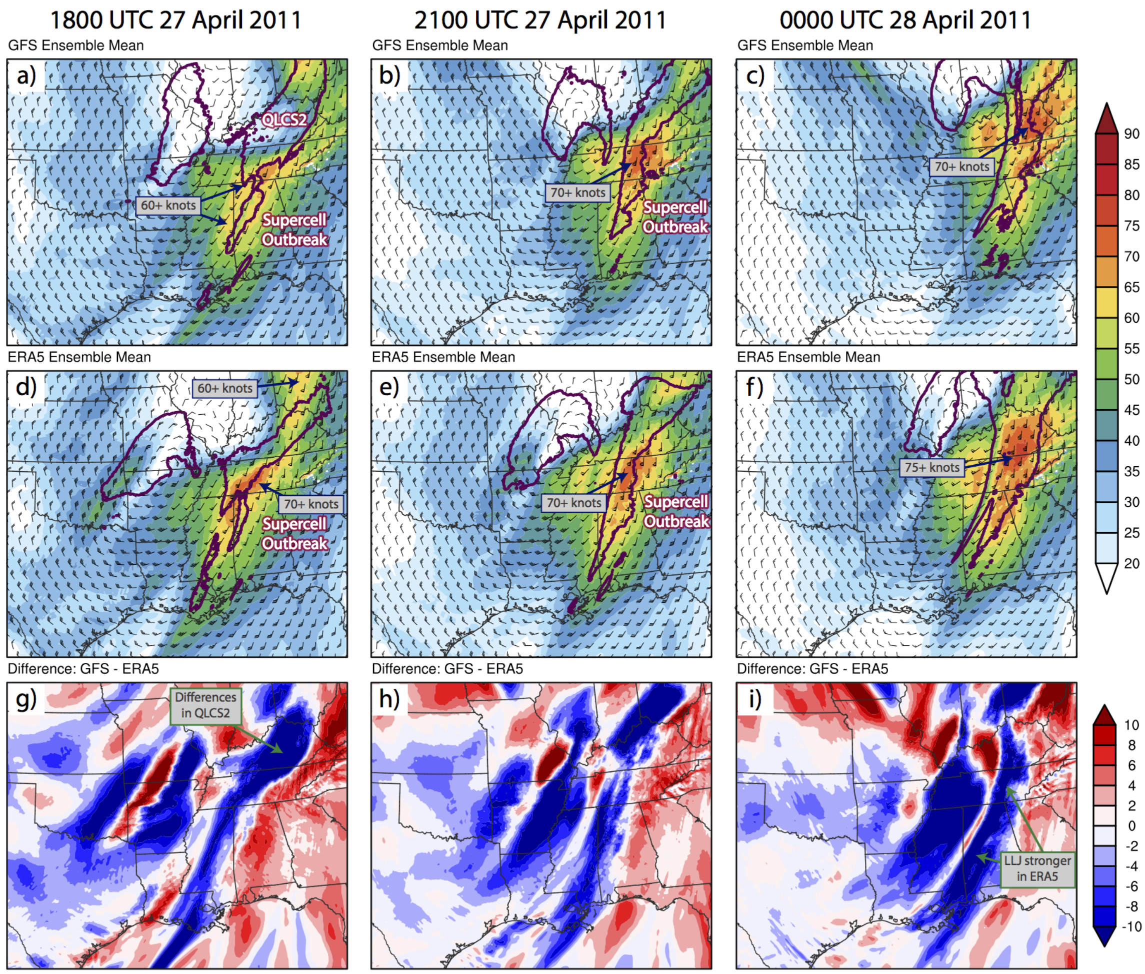

Figure 67: *As in Fig. 66, but for (a),(d),(g) 1800 UTC 27 April, (b),(e),(h) 2100 UTC 27 April, and (c),(f),(i) 0000 UTC 28 April 2011.*

in low-level wind speed behind the bore had occurred throughout much of Mississippi and Alabama by 27/1500Z in the GFS ensemble (not shown).

The LLJ subsequently restrengthened and advanced poleward after 27/1500Z in the ERA5 ensemble (Figs. 67d-f) and after 27/1800Z in the GFS ensemble (Figs. 67a-c) due to the movement of the J_1 exit region into the Southeast and the reintensification of J_4 downstream (Figs. 65 and 68b,d). Overall, 850-hPa wind speeds throughout much of Mississippi, Alabama, and Tennessee were slightly weaker in both ensembles (i.e., 60–65+ kt and 60–70+ kt in the GFS and ERA5 ensembles, respectively; Figs. 67a,d) than in the RUC (i.e., 65–75+ kt; Fig. 47f) at the beginning of the supercell outbreak but became more comparable throughout the afternoon as the LLJ continued to strengthen ahead of SW_3 (Figs. 67b-c,e-f).

Substantial differences between the two ensembles had become apparent in the mean 500-hPa geopotential height and wind fields by the onset of the afternoon supercell outbreak

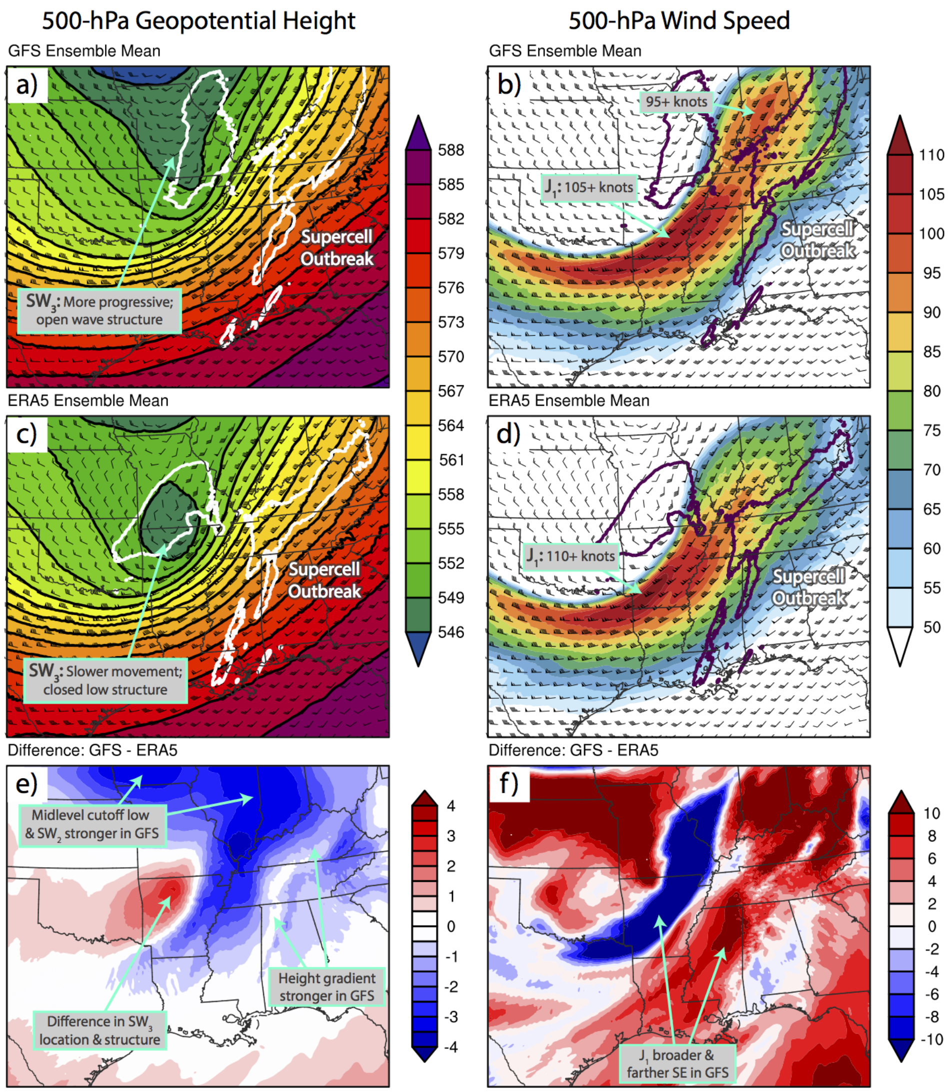

Figure 68: *Mean fields from the (top) GFS and (middle) ERA5 ensembles of (a),(c) 500-hPa geopotential height (shaded; dam), horizontal winds (barbs; kt), and composite radar reflectivity = 10 dBZ (white contours), and (b),(d) 500-hPa wind speed (shaded; kt), horizontal winds (barbs; kt), and composite radar reflectivity = 10 dBZ (purple contours) at 1800 UTC 27 April 2011. Corresponding mean difference fields between the GFS and ERA5 ensembles of (e) 500-hPa geopotential height (shaded; dam) and (f) 500-hPa wind speed (shaded; kt) are displayed in the bottom row.*

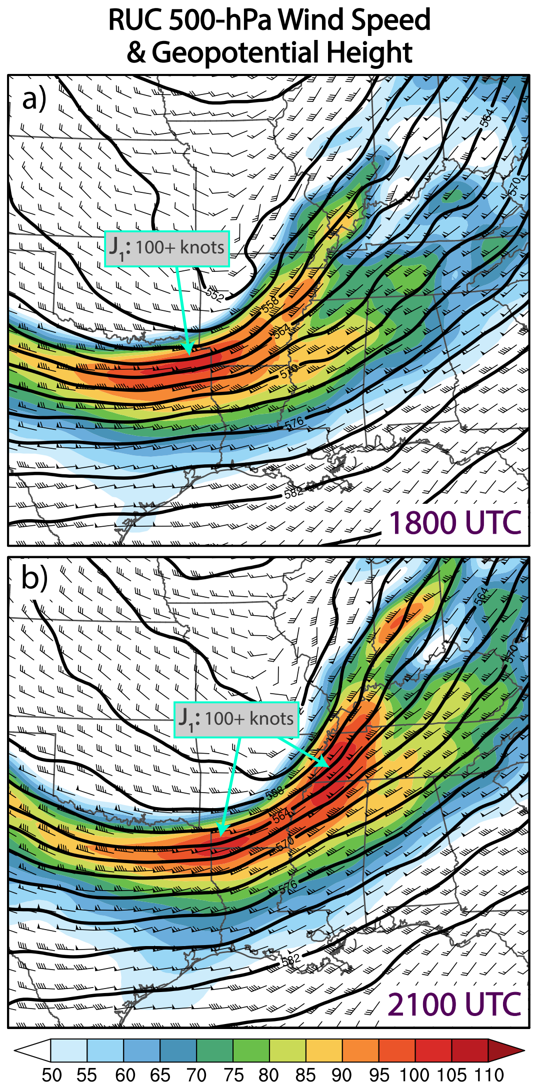

Figure 69: *500-hPa wind speed (shaded; kt), geopotential height (contours; dam), and horizontal winds (barbs; kt) from the corresponding RUC 1-h forecasts valid at (a) 1800 UTC and (b) 2100 UTC 27 April 2011.*

(Fig. 68). Specifically, SW_3 exhibited a more progressive open-wave structure in the GFS ensemble (Fig. 68a), while a midlevel closed low was centered over southwestern Missouri in the ERA5 ensemble (Fig. 68c). Furthermore, geopotential height values were lower throughout the Midwest in the GFS ensemble and were associated with a more amplified SW_2 and the greater southward migration of a midlevel cutoff low that stemmed from SW_1 (Fig. 68e). Accordingly, a stronger midlevel height gradient extended from the Lower Mississippi Valley through the Ohio Valley in the GFS ensemble, yielding higher wind speeds over much of the Southeast—primarily to the west of the ongoing convection within a more progressive jet streak—and supporting the downstream extension of J_1 into Indiana (Figs. 68b,f). Overall, the structure of SW_3 and J_1 produced by the GFS ensemble at 27/1800Z better resembled that in the RUC, albeit slightly later in the afternoon (i.e., RUC

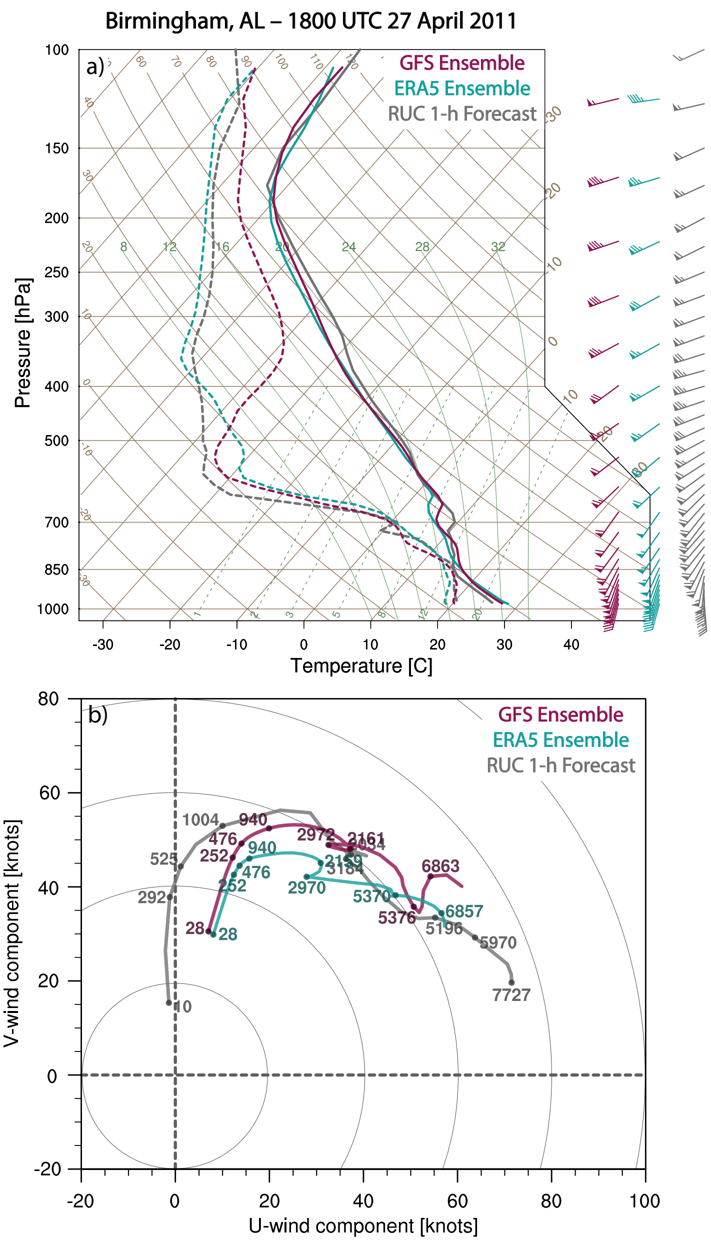

Figure 70: *Overlays of (a) mean soundings from the GFS ensemble (maroon), ERA5 ensemble (teal), and RUC 1-h forecast (gray), and (b) corresponding mean hodographs valid at 1800 UTC 27 April 2011 for Birmingham, AL.*

fields at 27/2100Z) due to the faster shortwave progression in the WRF simulations (cf. Figs. 68 and 69).

One notable issue with both ensembles was their failure to adequately capture the influence of QLCS2 on the midlevel J_1 exit region and SW_3 as they approached the Southeast. Specifically, both the premature development of QLCS2 in the GFS ensemble and the lack of an organized convective system in the ERA5 ensemble meant that the midlevel jet was not split into two branches around the QLCS, ultimately influencing the deep-layer shear profiles over the Southeast during the supercell outbreak (Fig. 70). Moreover, any potential influences that QLCS2 had on slowing the forward motion of SW_3, enhancing the baroclinity ahead of the midlevel shortwave, and affecting surface cyclogenesis were misrepresented within the ensembles. Thus, it may be presumed that the poor depiction of QLCS2 may have further enabled the positive bias in the propagation speed of SW_3 and J_1, which—in addition to the differences in deep-layer shear profiles—would tend to favor greater linear forcing for convection during the supercell outbreak, a quicker upscale progression toward a QLCS-type convective mode, and the eastward bias in convective placement noted in Section 5.2.2.1.

Differences in the sea level pressure (SLP) distribution and in the intensity and location of surface boundaries were also evident between the GFS and ERA5 ensembles at 27/1800Z (Fig. 71). The structure of L_3 in the GFS ensemble better matched the RUC and surface observations at this time, with a more compact SLP anomaly situated over northeastern Arkansas; a secondary SLP anomaly was centered over Michigan in association with L_2 (Fig. 71a). In contrast, L_3 was a broader and deeper circulation in the ERA5 ensemble and was located farther to the west due to the slower forward progression of SW_3 (Figs. 71b-c). Moreover, L_2 was weaker and more concentrated in scale than in the GFS ensemble such that its SLP signature was located outside the domain shown in Fig. 71b. Owing to the stronger circulation about L_3 in the ERA5 ensemble and the poor depiction of QLCS2, the residual cold pool over Tennessee and Kentucky was weaker than in the GFS ensemble,

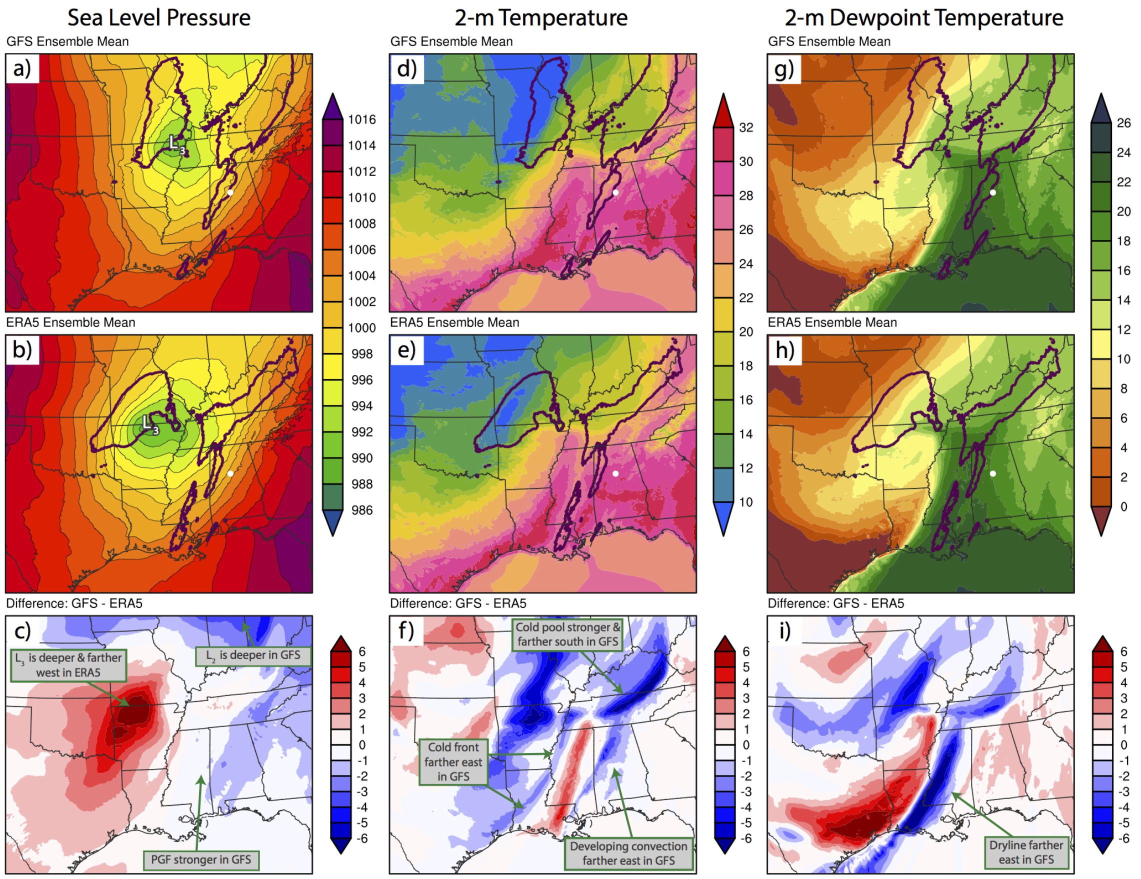

Figure 71: *Mean fields from the (top) GFS and (middle) ERA5 ensembles of (a),(b) sea level pressure (shaded; hPa), (d),(e) 2-m temperature (shaded; °C), and (g),(h) 2-m dewpoint temperature (shaded; °C) at 1800 UTC 27 April 2011. Simulated composite radar reflectivity = 10 dBZ from each respective ensemble is overlaid in purple contours. Corresponding mean difference fields between the GFS and ERA5 ensembles of (c) sea level pressure (shaded; hPa), (f) 2-m temperature (shaded; °C), and (i) 2-m dewpoint temperature (shaded; °C) are displayed in the bottom row. The location of Birmingham, AL, is indicated by the white marker.*

and the warm sector extended farther poleward (Figs. 71d-f). However, both the dryline and surface cold front were located farther to the east in the GFS ensemble (Figs. 71d-i), which largely resulted from differences in the structure and northeastward progression of the midlevel jet. Additionally, convection was located farther into the warm sector in the GFS ensemble than the ERA5 ensemble at 27/1800Z, and the region comprising ample surface moisture extended farther to the east. This difference in moisture was evident in the ensemble mean soundings from Birmingham, which depict higher mixing ratio values throughout the PBL in the GFS ensemble that were highly comparable to those from the RUC 1-h forecast valid at 27/1800Z (Fig. 70a).

5.2.2.3 Discussion and implications for predictability

Considering the differences between the two ensembles and the overall better agreement between the GFS ensemble and RUC fields throughout the outbreak, *the GFS ensemble will be employed for all subsequently discussed analyses involving WRF model output.* Primary characteristics and shortcomings of the GFS ensemble simulations are reiterated below.

- All members of the GFS ensemble depicted well the initial development and upscale growth of QLCS1 and the primary flow modifications that arose from this system, including amplification of the upper-level ridge, rapid generation of J_2, and intensification of the LLJ. Thus, the predictability of this overall evolution was high given GFS analysis mean initial conditions and lends confidence to the results obtained using the deterministic WRF simulations in Chapter 4.

- However, all members of the GFS ensemble failed to sustain the convection that developed east of the dryline over Texas and thus did not represent the prolific southernmost bowing segment with QLCS1 that moved through the Southeast overnight and produced numerous tornadoes. Consequently, the southern extent of the QLCS1 cold pool was misrepresented in the GFS ensemble, altering the low-level thermodynamic environment over the Southeast ahead of SW_3.

- QLCS2 formed too early and too far west in all GFS ensemble members, which may have resulted—at least in part—from the consistent absence of the southernmost bowing segment in the simulations. The upscale flow modifications from this system were therefore misrepresented by the GFS ensemble, including the generation and evolution of J_4, interactions with SW_3 and J_1, and augmented isallobaric forcing for LLJ intensification over the Southeast prior to the supercell outbreak. Furthermore, differences in this system's morphological evolution further influenced the cold pool extent and characteristics prior to the supercell outbreak and thus enabled the warm sector to extend farther poleward than in reality.

- All GFS ensemble members depicted J_1 and SW_3 progressing too quickly into the Southeast during the afternoon, yielding an eastward bias in the location of convection during the supercell outbreak and a mesoscale organization that was generally more linear and meridionally oriented, with quasi-discrete rotating convection largely concentrated along a single dominant band.

- Despite these shortcomings, the *overall outbreak evolution* was reasonably depicted by the GFS ensemble given the significance of scale-interactive processes with the two QLCSs and the abundance of possible error pathways that are inherent in forecasts of multiple convective episodes. In other words, while the noted discrepancies with QLCS1 and QLCS2 had implications on the forecasts at later times, many of these implications could be readily identified (e.g., errors in the poleward extent of the warm sector) and did not preclude the supercell outbreak from transpiring altogether.

5.3 Environmental analysis using the GFS ensemble

5.3.1 Ensemble mean and spread

The temporal evolution of the ensemble mean and standard deviation—a measure of ensemble spread—for several fields was examined to gauge which aspects of the environment exhibited appreciable variability among the GFS ensemble members. Particular attention was given to (1) the representation of upscale feedbacks and jetogenesis stemming from QLCS1 and (2) the varying depictions of mesoscale features that were present over the Southeast during the afternoon supercell outbreak. The findings from this examination were then used to help motivate the analyses of QLCS1 feedbacks using ensemble subsets described in Section 5.3.2 and the analyses of mesoscale processes leading to CI presented in Chapter 6.

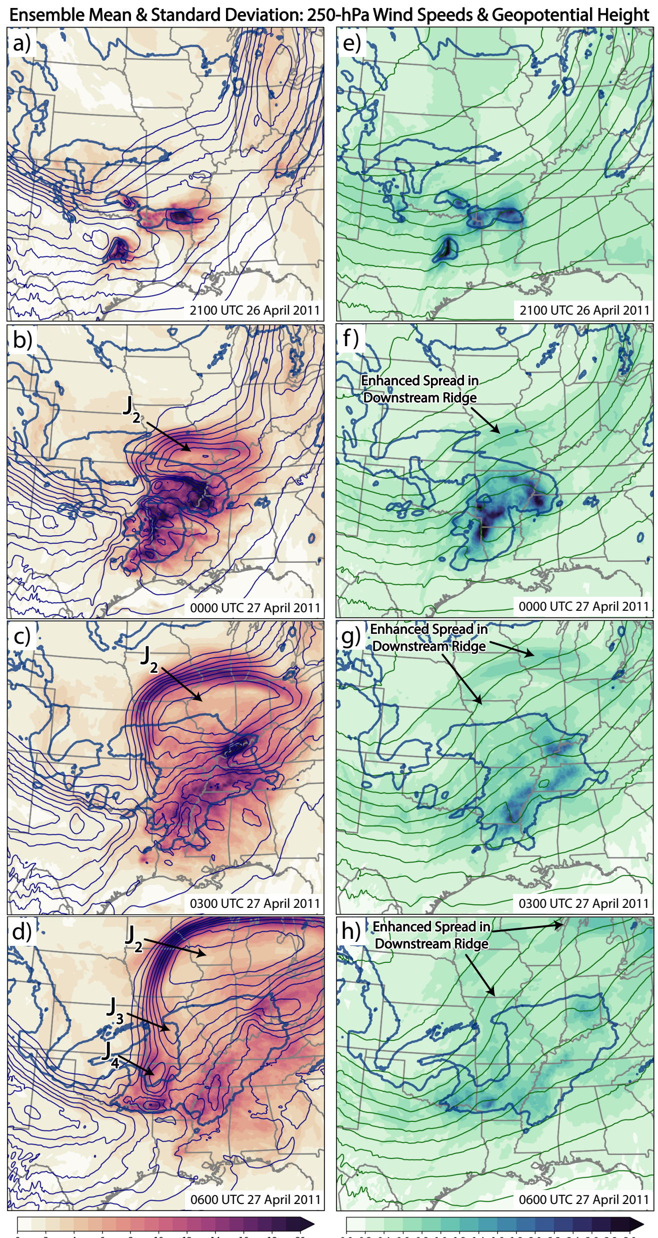

Figure 72: *GFS-initialized ensemble mean (thin contours) and standard deviation (shaded) for (left) 250-hPa wind speed (contours every 10 kt ≥ 50 kt) and (right) 250-hPa geopotential height (contours every 6 dam) at (a),(e) 2100 UTC 26 April, (b),(f) 0000 UTC 27 April, (c),(g) 0300 UTC 27 April, and (d),(h) 0600 UTC 27 April 2011. Ensemble mean composite radar reflectivity = 10 dBZ is overlaid in blue contours for each time.*

Upscale modifications from QLCS1. The ensemble depiction of upper-level and low-level flow modifications stemming from QLCS1 are first described. Shown in Fig. 72 is the temporal evolution of 250-hPa wind speed and geopotential height mean and standard deviation fields following CI associated with QLCS1 and accompanying the development and intensification of J_2. Large standard deviations of these upper-level fields were both

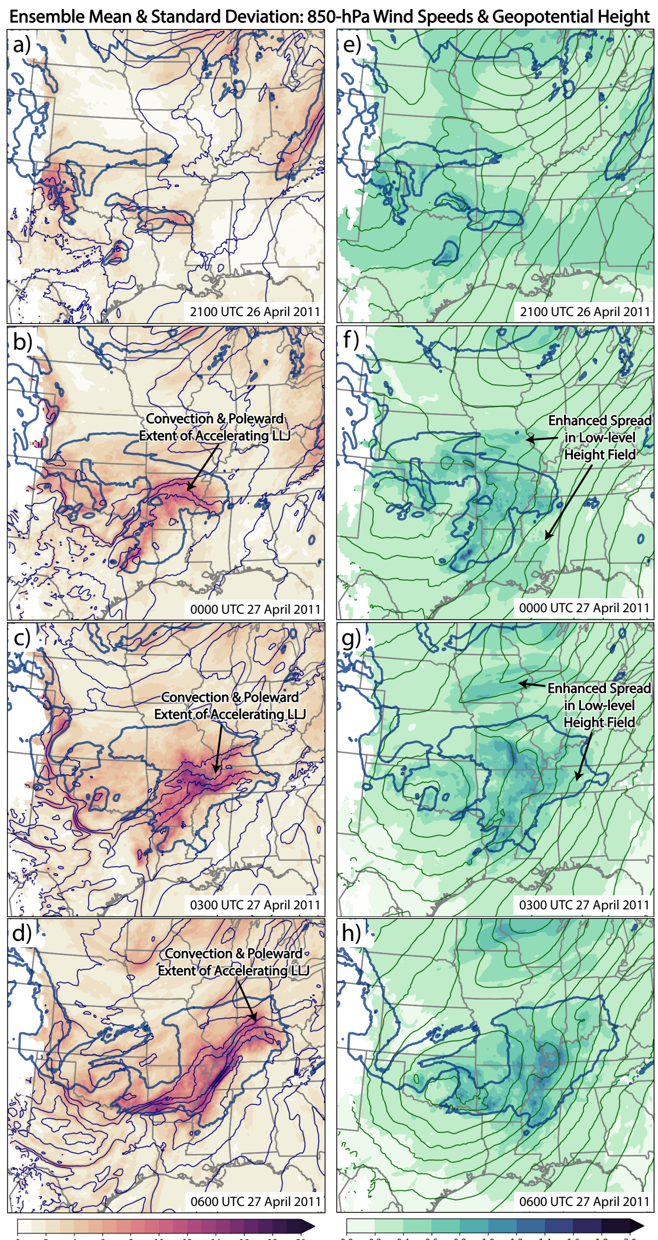

Figure 73: *As in Fig. 72, but for 850-hPa wind speed (contours every 10 kt ≥ 20 kt) and geopotential height (contours every 3 dam).*

collocated with the convection itself (e.g., over southern Arkansas at 26/2100Z in Figs. 72a,e) and extended downstream into the Southeast and Upper Midwest with time as the environment became increasingly modified by QLCS1. Notably, enhanced standard deviations in the 250-hPa geopotential height field can be seen propagating away from QLCS1 with time and signify increasing spread in the strength and extent of the amplifying upper-level ridge (Figs. 72f-h). Furthermore, large standard deviations of both geopotential height and 250-hPa wind speed (Figs. 72b-d) remained concentrated along the northern and western flanks of J_2 as it advanced poleward between 27/0000Z–27/0600Z, *indicating that details in the structure, location, and northwestward extent of this convectively forced jet streak varied appreciably among the individual ensemble members.*

The temporal evolution of 850-hPa wind speed and geopotential height mean and standard deviation fields are shown for this same 9-h period in Fig. 73. Unsurprisingly, large standard deviations of both wind speed and geopotential height were present where active convection was occurring within the ensemble members and became concentrated near the leading edge of QLCS1 as the system organized and grew upscale with time (Fig. 73d). Within the inflow environment, a region of enhanced standard deviation values—particularly for 850-hPa wind speed—was located near the terminus of the LLJ as it strengthened and advanced poleward ahead of QLCS1 (Figs. 73b-d). The large ensemble spread within this region and adjacent to the leading edge of QLCS1 following its upscale growth was likely due to differences in the system's orientation and variations in isallobaric forcing among the individual members. Both factors are expected to be related to differences in the upper-level flow response (i.e., ridge amplification and the structure of J_2) and are postulated to have important implications for the severity of QLCS1. These hypothesized relationships are explored further in Section 5.3.2.

Similar to the evolution of the upper-level geopotential height standard deviation field, an arc-shaped region of enhanced 850-hPa geopotential height standard deviation values can be seen originating near the convection and propagating northward into the Upper

Midwest away from the QLCS (Figs. 73f-h). This region was at least partly associated with a negative geopotential height perturbation (e.g., the sharp trough over Iowa in Fig. 73g) and was situated beneath the propagating corridor of large standard deviation values flanking J_2 at 250 hPa (Figs. 72f-h). Thus, it is likely that this disturbance manifested as a deep-tropospheric gravity wave (or wave train) that developed on the downstream flank of J_2—analogous to the high-amplitude mesoscale gravity waves documented over this region by de Groot-Hedlin et al. (2014) following the development of QLCS1 (see Chapter 4).

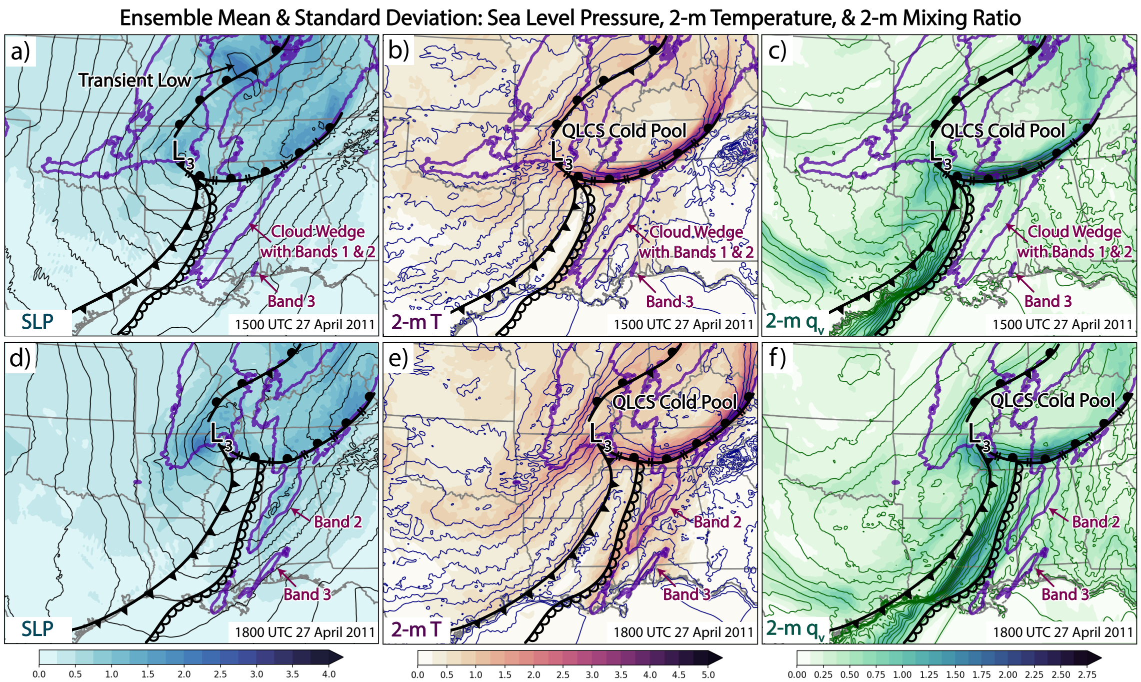

Figure 74: *GFS-initialized ensemble mean (thin contours) and standard deviation (shaded) for (a),(d) sea level pressure (contours every 2 hPa), (b),(e) 2-m temperature (contours every 2 °C), and (c),(f) 2-m mixing ratio (contours every 1 g kg^{-1}) at (top) 1500 UTC and (bottom) 1800 UTC 27 April 2011. Ensemble mean composite radar reflectivity = 10 dBZ is overlaid in purple contours for each time.*

Mesoscale environment during the supercell outbreak. The remainder of this discussion focuses on understanding how the structure and placement of surface boundaries and other relevant mesoscale disturbances varied within the ensemble during the afternoon supercell outbreak. Mean and standard deviation fields of SLP, 2-m temperature, and 2-m mixing ratio are shown every 3 h from 27/1500Z–28/0000Z in Figs. 74–75. At 27/1500Z, the ensemble mean depicted L_3 over central Arkansas, with the residual QLCS cold pool and its associated effective warm front extending eastward through northern Mississippi and Tennessee (Figs. 74a-c). L_3 was attended by a cold front that draped southwestward through Louisiana and was preceded by a dryline that had moved into the Lower Mississippi Valley. Unsurprisingly, the ensemble members varied considerably in their representation of the effective warm front, which coincided with large standard deviation values of SLP, 2-m temperature, and 2-m mixing ratio and whose character and location were primarily determined by convection within the southern portions of both QLCS1 and QLCS2. Large ensemble spread was also found in the surface moisture near and behind the dryline—likely due to its dependence on PBL mixing, possible differences in the representation of the DCB, and ultimately variations in dryline propagation speed among the individual members. Additionally, enhanced standard deviation values—particularly in 2-m temperature—were located over the warm sector throughout Mississippi and southeastern Louisiana in association with a coherent wedge of cloud cover and weak simulated reflectivity that evolved into Bands 1 and 2. A similar corridor of enhanced 2-m temperature standard deviation values was situated over western Alabama in association with Band 3. Neither Band 2 nor Band 3 was adjacent to any discernible surface boundaries in the ensemble mean during the period of CI over the Southeast (Figs. 74b-c, e-f), and the mesoscale processes responsible for their development are investigated further in Chapter 6.

Overall, the greatest ensemble spread remained concentrated near L_3 and the predominant surface boundaries as the baroclinic system evolved over time, while standard deviation values increased over the warm sector following the development of deep convection during the afternoon (Figs. 74d-f and 75). L_3 advanced northeastward throughout the supercell outbreak, yielding the poleward expansion of the warm sector and the movement of the effective warm front—which weakened substantially during the afternoon—into the Ohio Valley. By 28/0000Z, little thermal contrast remained across the effective warm front, and the surface cold front had overtaken the dryline from central Kentucky through central

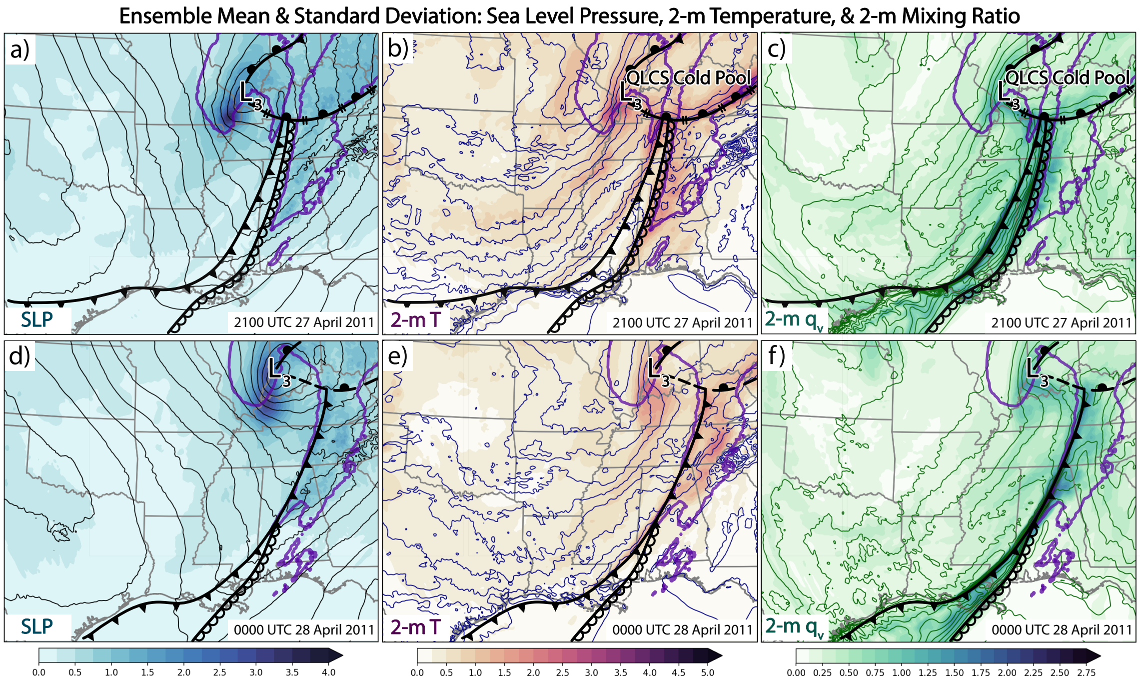

Figure 75: *As in Fig. 74, but for (top) 2100 UTC 27 April and (bottom) 0000 UTC 28 April 2011.*

Alabama (Figs. 75d-f). Owing to the breakdown of the effective warm front and in the absence of a coherent mesoscale baroclinic zone east of the low, L_3 increasingly took on the character of a Shapiro-Keyser-type cyclone (Shapiro and Keyser, 1990; Schultz et al., 1998), with a distinct T-bone frontal structure becoming apparent by 28/0000Z.

5.3.2 Ensemble subsets: Upscale feedbacks and initial CI

Further investigation of the upscale feedback effects that stemmed from QLCS1 are now presented using subsets from the 50-member GFS ensemble. Based on the environmental evolution previously described in Chapters 3 and 4, *it is hypothesized that the character of the dramatic upscale flow response that began with the genesis and rapid intensification of* J_2 *was directly related to the strength and spatial extent of convection that developed over eastern Oklahoma and Arkansas during the evening of 26 April.* The fundamental objectives of this analysis were to evaluate this hypothesis by (1) sorting the ensemble members by a given forecast metric that characterizes the intensity and coverage of convection during the period immediately following CI; (2) segregating the 10 ensemble members with the strongest, most expansive convection and the 10 ensemble members with the weakest, least expansive convection into TOP and BOTTOM composite subsets, respectively; (3) identifying any coherent environmental differences between the TOP and BOTTOM subsets that developed throughout the forecast evolution; and (4) assessing whether these environmental differences influenced the morphological evolution and overall severity of QLCS1.

5.3.2.1 Composition of ensemble subsets

Previous studies employing ensemble-based sensitivity techniques to WRF ensemble forecasts of convective events have used the maximum vertical kinetic energy $^{1}/_{2}w_{max}^{2}$ averaged over a geographic area as a proxy for the strength and spatial extent of convection (e.g., Berman et al., 2017; Torn et al., 2017). In the former expression, w_{max} is a diagnostic quantity representing the maximum upward vertical velocity that was calculated below 400 hPa at each horizontal grid point for every model time step within the previous hour[2] (or otherwise defined history interval; Kain et al., 2010). Herein, the hourly maximum vertical kinetic energy (VKE) was aggregated from 26/2100Z–27/0000Z to produce swaths of 3-h maximum VKE for each grid point within a specified domain that encompassed the primary CI region over eastern Oklahoma and Arkansas (34°N, 96°W to 37°N, 90°W; shown in Fig. 76). The domain-averaged values of 3-h maximum VKE calculated for each ensemble member were then used to discriminate between the ensemble members with the most and least expansive regions of strong convection. All 50 ensemble members were ranked according to this metric, and the members with the 10 highest values (i.e., top 20%) and 10 lowest values (i.e., bottom 20%) were initially designated as the TOP and BOTTOM subsets, respectively.

Members 32 and 50 both differed appreciably from the other 48 ensemble members in their depictions of QLCS1—including differences in the CI timing, location, and orientation

[2]For example, the w_{max} field at 27/0100Z would account for all updraft velocity values computed within the model beginning at the first time step after 27/0000Z.

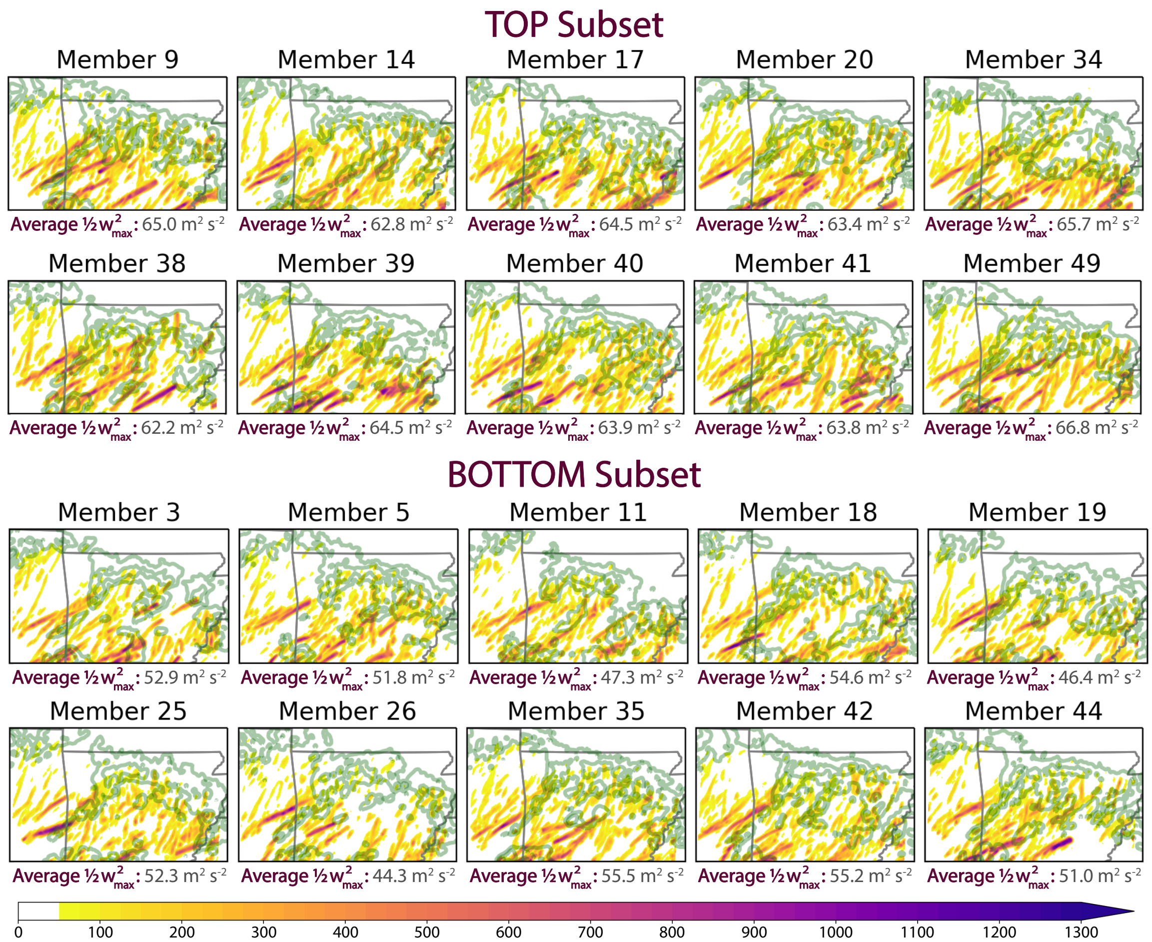

Figure 76: *Swaths of 3-h aggregated grid-point maximum vertical kinetic energy from 26/2100Z–27/0000Z (shaded; m^2 s^{-2}) and composite radar reflectivity at 27/0000Z (contours; every 15 dBZ ≥ 35 dBZ) for the TOP and BOTTOM ensemble subsets. The domain-averaged value of 3-h aggregated VKE is listed for each member.*

(cf. Figs. 77 and 79); differences in the system's morphological evolution and severity; and differences in the resultant environmental modifications—and were consequently omitted from the subset analysis based on member rankings. Therefore, Member 50 (the 4^{th} lowest ranked member) was replaced in the BOTTOM subset by Member 35 (the 11^{th} lowest ranked member) for all subset mean composites presented herein, which facilitated clearer interpretation of any differences in CI characteristics and resultant upscale environmental modifications that occurred between the TOP and BOTTOM subsets. Note that these two members were still included in calculations of the full ensemble mean, which were used to compute anomaly fields for each of the two subsets.

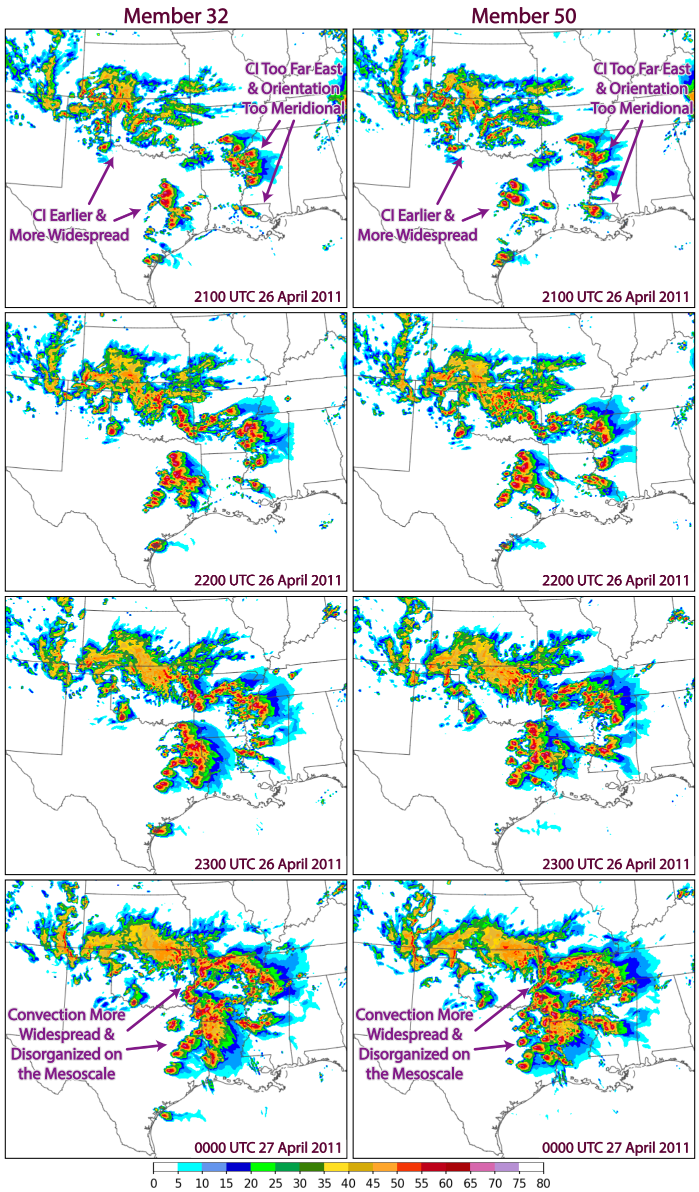

Figure 77: *Simulated composite radar reflectivity (shaded; dBZ) from (left) Member 32 and (right) Member 50 every hour from 2100 UTC 26 April – 0000 UTC 27 April 2011.*

Domain-averaged average VKE values for each member in the finalized TOP and BOTTOM subsets and for the omitted Member 50 are listed in Table 5.2, and VKE swaths from 26/2100Z–27/0000Z overlaid with simulated composite radar reflectivity at 27/0000Z are shown for each subset member in Fig. 76. Overall, swaths of large VKE values covered a greater area in the TOP subset and signified the presence of more extensive, stronger convection throughout eastern Oklahoma and central Arkansas in the period immediately

Table 5.2: *Values of domain-averaged VKE between 26/2100Z–27/0000Z for the TOP and BOTTOM CI subsets. The maximum value within the ensemble is shown in red. The replacement member in the BOTTOM subset is denoted with an asterisk.*

TOP Subset Member	$^1/_2\mathbf{w}^2_{max}$ [m^2 s^{-2}]	**BOTTOM Subset Member**	$^1/_2\mathbf{w}^2_{max}$ [m^2 s^{-2}]
9	65.0	3	52.9
14	62.8	5	51.8
17	64.5	11	47.3
20	63.4	18	54.6
34	65.7	19	46.4
38	62.2	25	52.3
39	64.5	26	44.3
40	63.9	35*	55.5
41	63.8	42	55.2
49	**66.8**	44	51.0
		Omitted Member	
		50	49.3

following CI. Moreover, the VKE swaths in the TOP subset extended farther north—on average—than the swaths in the BOTTOM subset, suggesting that differences between the two subsets may exist in placement of convection during this period.

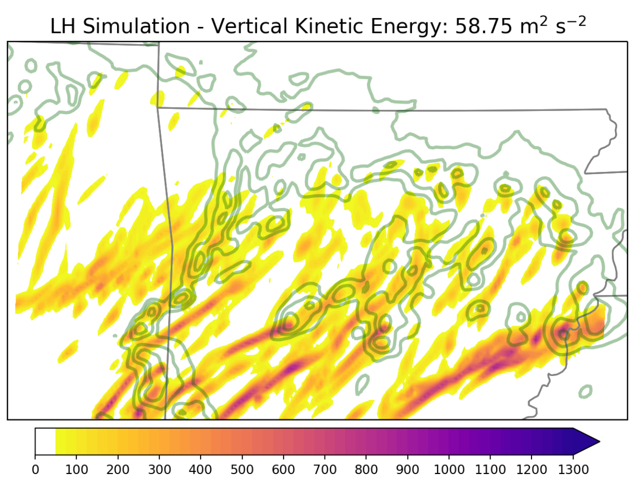

Figure 78: *As in Fig. 76, but for the LH simulation discussed in Chapter 4.*

Because the model configuration and physics parameterizations used in the GFS ensemble members were nearly identical[3] to those used in the deterministic LH simulation presented in Chapter 4, this simulation can effectively be treated as the CONTROL (51^{st}) member of the GFS ensemble, although it was not included in the subset analyses presented herein. However, this permits an assessment of where the LH simulation would be ranked relative to the 50 ensemble members in its representation of the coverage and intensity of convection shortly after CI. Corresponding VKE swaths from the LH simulation are displayed in Fig. 78 and suggest that a widespread region of moderate to strong convection developed throughout eastern Oklahoma and much of Arkansas between 26/2100Z–27/0000Z. The domain-averaged VKE value for the LH simulation was 58.75 m^2 s^{-2}, which puts it in between the 27^{th} and 28^{th} ensemble members when ranked from lowest to highest average VKE. Thus, the LH simulation was located near the center of the ensemble VKE distribution—which had mean and median values of 58.05 m^2 s^{-2} and 58.34 m^2 s^{-2}, respectively—and provided an average representation of possible outcomes in terms of the upscale flow enhancements produced by QLCS1 and their potential implications for the system's severity. This lends further credence to the conclusions drawn from this simulation in Chapter 4.

5.3.2.2 Subset analysis

Analyses derived from the TOP and BOTTOM ensemble subsets are now presented. As was previously described in Chapter 4, pronounced modifications to the upper-level flow commenced concurrently with the onset of CI associated with QLCS1. In particular, the genesis of J_2 was tied to the initial development and upscale growth of convection over Arkansas, and the unbalanced nature of J_2 supported strong low-level isallobaric forcing that rapidly strengthened the LLJ and low-level vertical wind shear within the

[3]There were slight differences in the time steps used in the GFS ensemble and LH simulation. Additionally, no hydrometeors were present in the GFS analysis used to initialize the deterministic LH simulation, whereas hydrometeors spun up through the EnKF procedure were included in the GFS ensemble ICs.

QLCS1 inflow environment. This flow intensification was postulated to have supported the anomalously tornadic nature of QLCS1 such that the system enhanced its own severity via upscale feedback effects. Based upon this key hypothesis and the previously established relationship between widespread CI over Arkansas and unbalanced upper-level jetogenesis, the following hypotheses are proposed:

- *The TOP and BOTTOM ensemble subsets were constructed based upon dissimilarities in the intensity, structure, and extent of convection that formed throughout eastern Oklahoma and Arkansas during the 26/2100Z–27/0000Z period. Accordingly, coherent differences in environmental conditions are expected to develop between the subset composites (or subset means) during this time period as this convection begins to alter its surrounding environment.*

- *These environmental differences are anticipated to exhibit temporal continuity such that they can be traced forward in time to subsequent forecast hours and should become increasingly amplified as they grow upscale in a manner consistent with multistage error-growth dynamics (Zhang et al., 2003, 2007; Baumgart et al., 2019; Baumgart and Riemer, 2019).*

- *Ultimately, the resultant differences in the mesoscale environment are expected to yield differences in the morphological evolution and severity of QLCS1 overnight.*

Differences in severity between the two subsets will be evaluated during the period from 27/0600Z–27/0800Z. This time period was chosen because (1) it encompassed the first period of increased tornadic activity with QLCS1, including two EF-3 tornadoes that formed in association with a long-lived mesovortex (see Fig. 2), and (2) the most dramatic upscale flow modifications produced by QLCS1 had occurred by 27/0600Z.

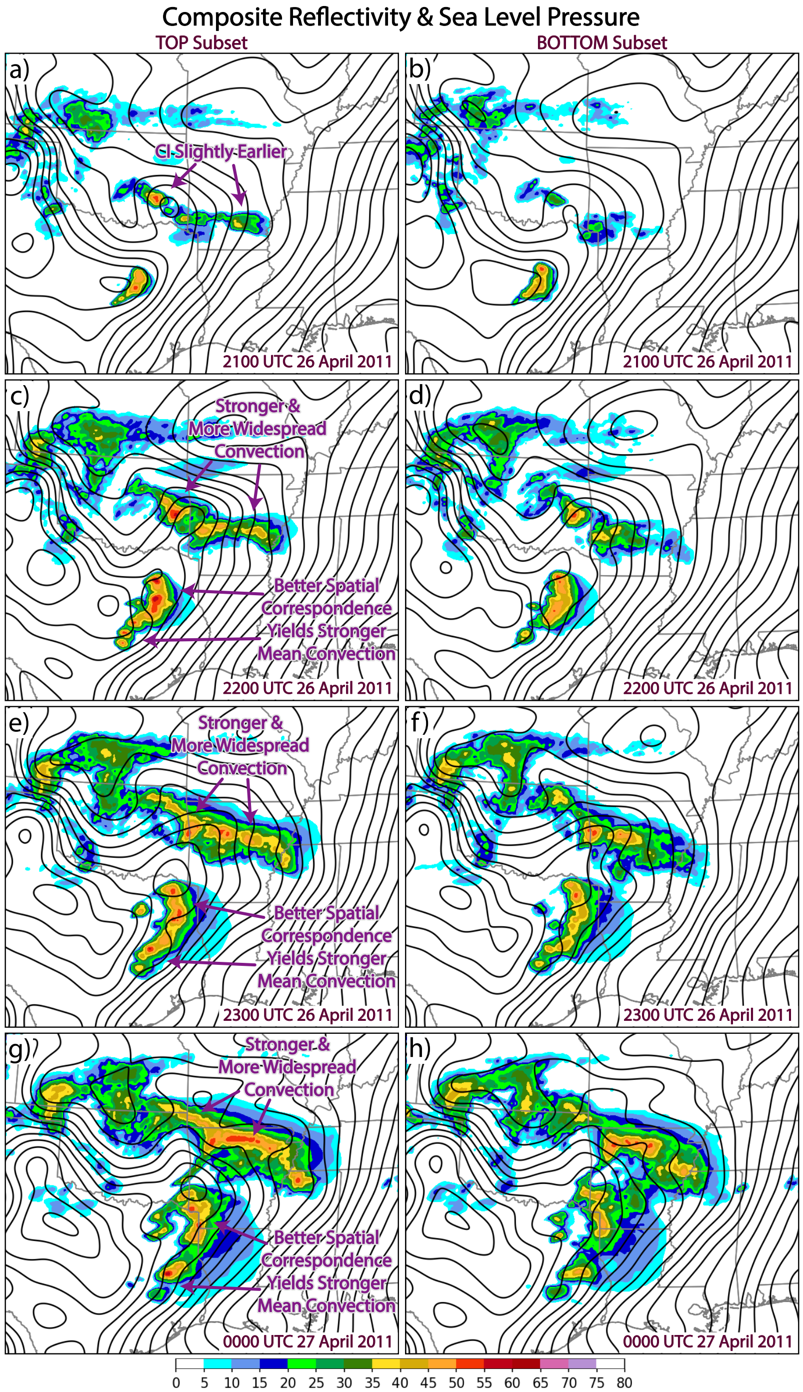

Figure 79: *Simulated mean composite radar reflectivity (shaded; dBZ) and sea level pressure (contours; every 1 hPa) from the (left) TOP subset and (right) BOTTOM subset every hour from 2100 UTC 26 April – 0000 UTC 27 April 2011. The SLP field was low-pass filtered with a cutoff wavelength of 200 km.*

Mean differences in QLCS1 and the simulated environment. Subset mean simulated composite radar reflectivity and sea level pressure[4] are shown in Fig. 79 from 26/2100Z–27/0000Z. In both subsets, CI occurred both ahead of the dryline over eastern Texas and

[4]Environmental fields shown herein on the inner WRF domain were low-pass filtered with a cutoff wavelength of 200 km to better convey coherent differences between the two ensemble subsets.

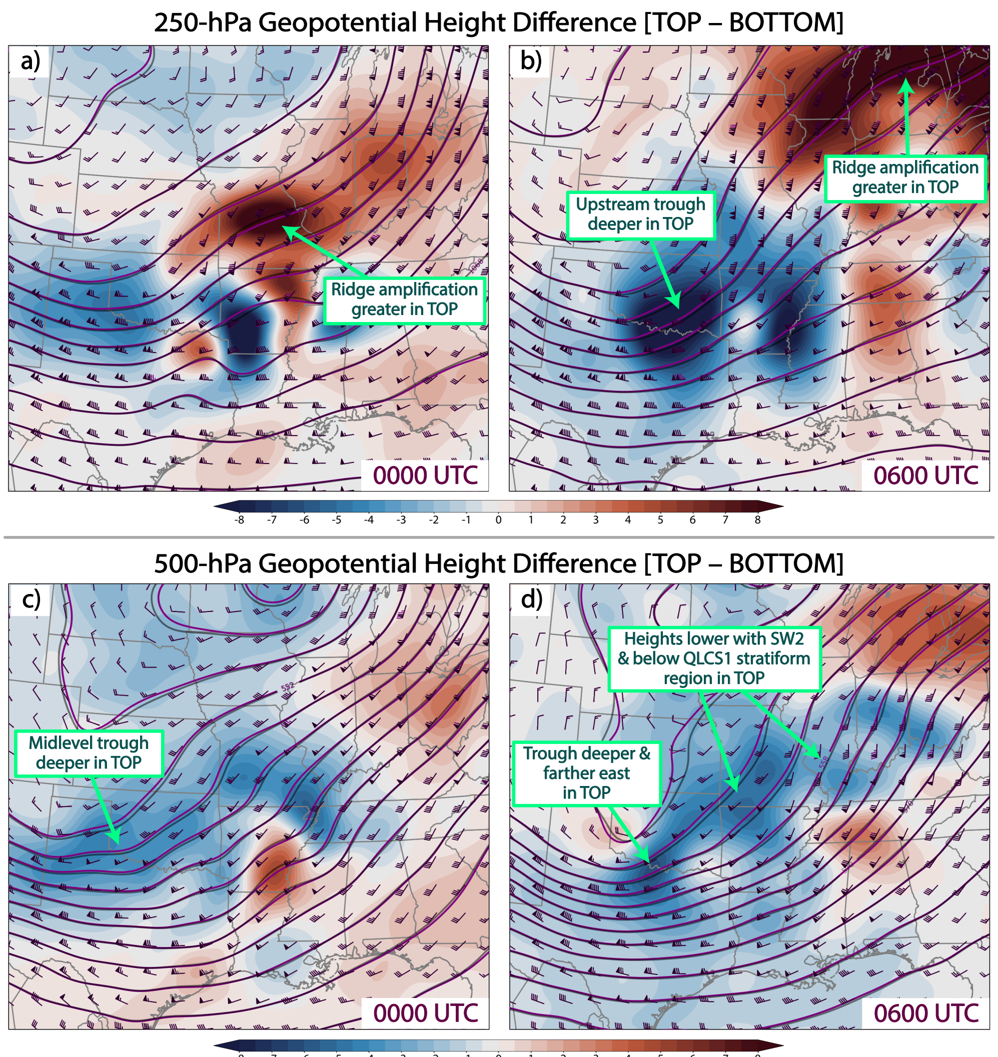

Figure 80: *Subset mean differences (defined as TOP – BOTTOM) in (top) 250-hPa geopotential height (shaded; m) and (bottom) 500-hPa geopotential height (shaded; m) at (a),(c) 0000 UTC and (b),(d) 0600 UTC 27 April 2011. Mean geopotential height (contours; dam) and horizontal winds (barbs; kt) are also shown in black and magenta for the TOP and BOTTOM subsets, respectively, at each corresponding level and time. These plotted fields were taken from the outer 15-km WRF domain and were low-pass filtered with a 325-km cutoff wavelength.*

north of the effective warm front in eastern Oklahoma and Arkansas. Overall, both subsets were comparable in their mean representations of the timing, location, and extent of CI ahead of the dryline, although this convection appeared stronger in the TOP subset mean—primarily because there was better spatial correspondence in convective placement among these individual subset members than among individual members in the BOTTOM subset. However, CI occurred earlier throughout Arkansas and eastern Oklahoma in the TOP subset and resulted in stronger and more widespread convection that was located slightly farther north by 27/0000Z. We note that the depiction provided by the BOTTOM subset better agreed with the observed convection that formed over eastern Oklahoma and Arkansas (Figs. 3a-b).

Examination of the surface and low-level kinematic and thermodynamic fields during the period of CI suggests that stronger winds over northeastern Texas and throughout southern Arkansas in the TOP subset may have provided more favorable thermodynamic conditions (via advection) and enhanced low-level convergence and frontogenesis along the effective warm front to better support CI (not shown). The upper-level geopotential height fields at 26/1800Z (i.e., when the forecasts were initialized) indicate that the upstream trough over Texas and Oklahoma was more amplified in the TOP subset mean initial conditions (not shown), which would have supported these aforementioned low-level differences.

To demonstrate how the upper-level mass fields varied between the two subsets after CI, subset mean 250-hPa and 500-hPa geopotential height difference fields (calculated as *TOP – BOTTOM*) are displayed in Fig. 80 at 27/0000Z and 27/0600Z. Note that these fields were derived from the 15-km outer WRF domain (output files only available every 6 h) and were filtered with a 325-km cutoff wavelength to better depict environmental differences on the meso-α-scale. At 27/0000Z, a prominent region of negative 250-hPa and 500-hPa height differences extended through much of Oklahoma and northern Texas and signified that the upstream trough remained deeper in the TOP subset (Figs. 80a,c). Furthermore, the earlier development of stronger and more widespread convection over eastern Oklahoma and

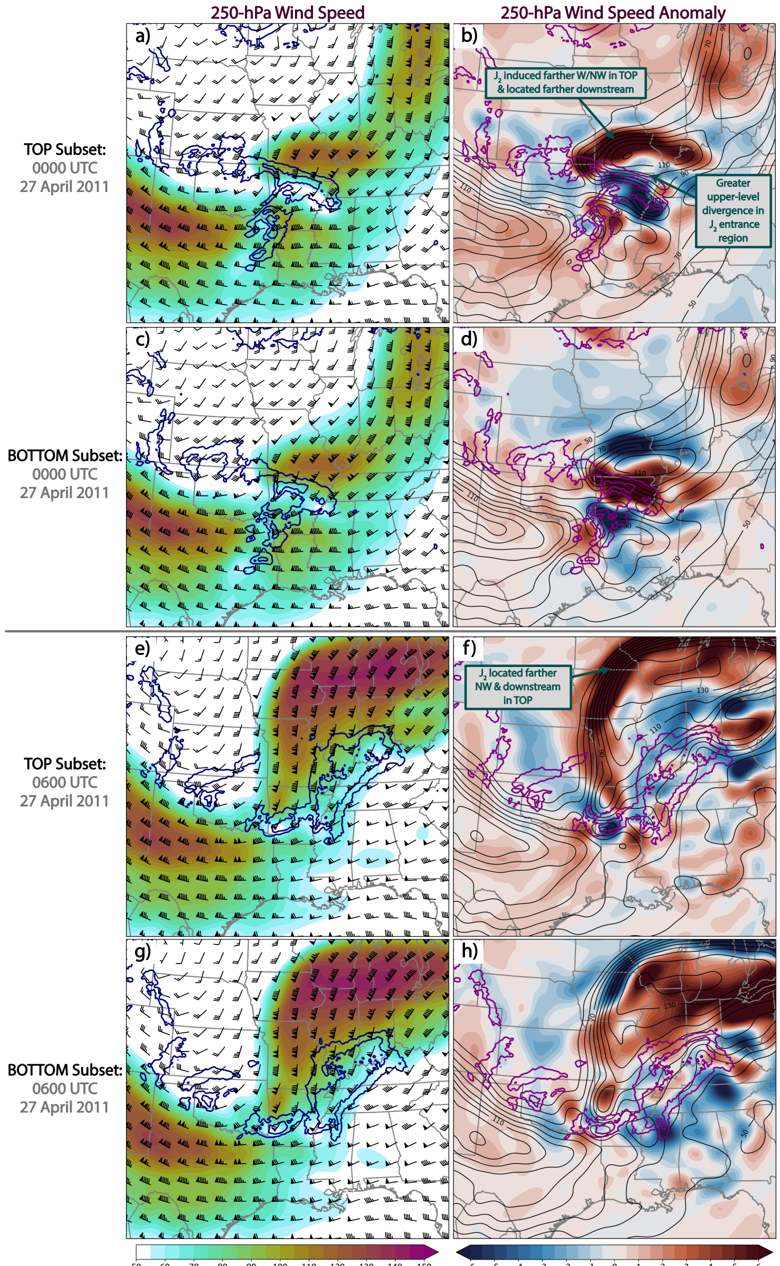

Figure 81: *Subset mean fields of (left) 250-hPa wind speed (shaded; kt), 250-hPa winds (barbs; kt), and composite radar reflectivity (navy contours 20 dBZ ≥ 20 dBZ), and (right) 250-hPa wind speed anomaly (shaded; kt), 250-hPa wind speed (black contours; every 10 kt ≥ 50 kt), and composite radar reflectivity (purple contours; every 20 dBZ ≥ 20 dBZ) for (a),(b) TOP and (c),(d) BOTTOM at 0000 UTC 27 April, and (e),(f) TOP and (g),(h) BOTTOM at 0600 UTC 27 April 2011. The wind fields were low-pass filtered with a 200-km cutoff wavelength.*

Arkansas in the TOP subset had promoted greater upper-level height rises and thus more pronounced downstream ridge amplification over Missouri. Accordingly, 250-hPa wind fields from the inner 3-km domain indicate that J_2 developed faster in the TOP subset and was both more intense and located farther downstream by 27/0000Z (Figs. 81a-d). Subset anomaly fields (calculated as *subset mean – full 50-member ensemble mean*) of 250-hPa wind speed depict large positive anomalies along the western and northern flanks of J_2 in the TOP subset (Fig. 81b), whereas large negative wind speed anomalies were collocated with the northern flank in the BOTTOM subset (Fig. 81d). These anomaly signatures indicate that J_2 was induced and continued to propagate farther toward the northwest in the TOP subset than in either the full ensemble mean or BOTTOM subset. This wind speed anomaly pattern persisted at 27/0600Z such that J_2 extended farther northwestward into Minnesota (Figs. 81e-h) and was consistent with the more amplified upper-level flow pattern that had developed in the TOP subset by this time (Fig. 80b).

The formation of J_2 coincided with the onset of considerable upper-level divergence within the jet entrance region and (1) contributed to the rapid upscale growth and meridional reorientation of QLCS1, and (2) provided strong isallobaric forcing for LLJ intensification within the warm sector. This upper-level divergence was more pronounced in the TOP subset and can be inferred from the dipole in 250-hPa wind speed anomaly across the jet in Fig. 81b—namely, the large positive wind speed anomaly situated downstream from the large negative wind speed anomaly over central Arkansas at 27/0000Z. This dipole signature remained more distinct in the TOP subset at 27/0600Z (cf. Figs. 81f and 81h), which—when coupled with the more amplified upper-level flow pattern in the TOP subset—suggests that *the initial formation of stronger and more extensive convection over eastern Oklahoma and Arkansas produced an upscale environmental response that yielded stronger large-scale dynamics.* The effects of these differences in upper-level forcing are evident in the morphological evolution and meridional reorientation of QLCS1, the northern part of which remained anchored to the J_2 entrance region as the outflow jet quickly advanced poleward and promoted upper-level ridge amplification over the Midwest. Subset mean composite radar reflectivity fields from 27/0200Z–27/0800Z reveal that QLCS1 became reoriented faster in the TOP subset and extended farther poleward—particularly convection within the northeastern flank of the system, which was situated near the LLJ terminus (Fig.

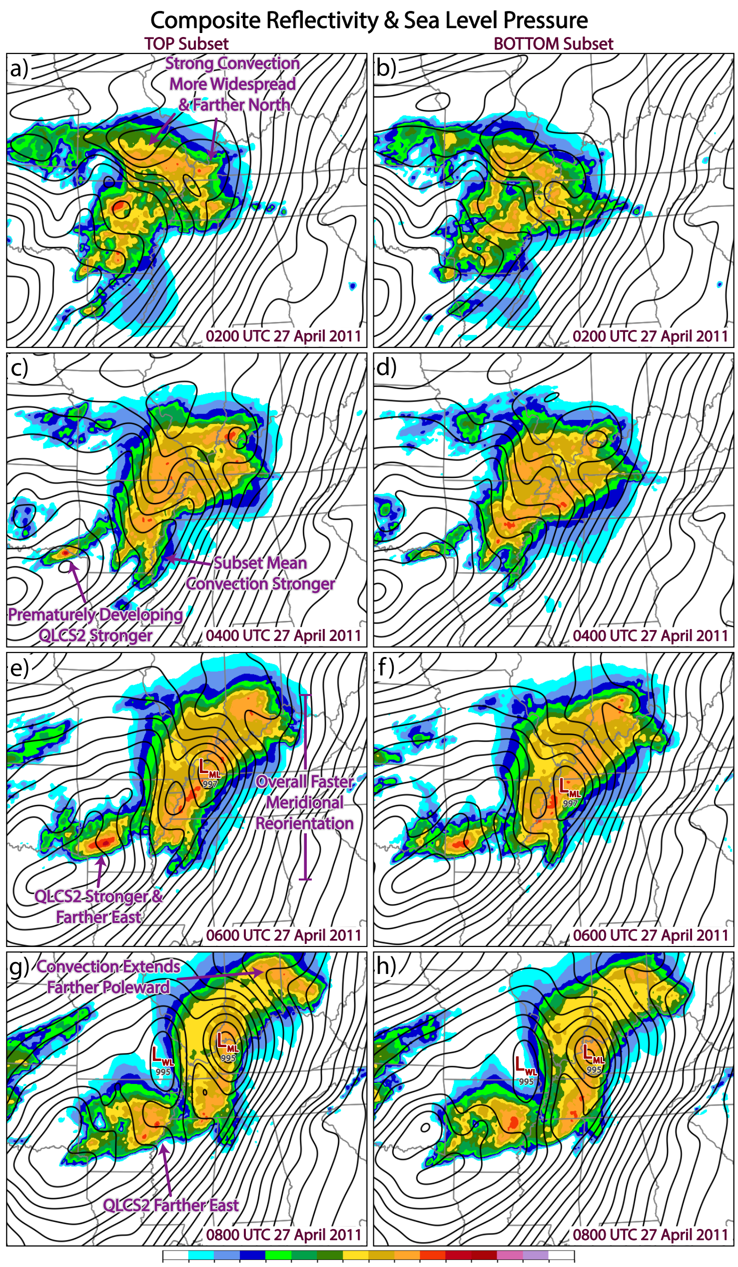

Figure 82: *As in Fig. 79, but every 2 h from 0200 UTC – 0800 UTC 27 April 2011. A prominent embedded mesolow and wake low are denoted by* L_{ML} *and* L_{WL}*, respectively.*

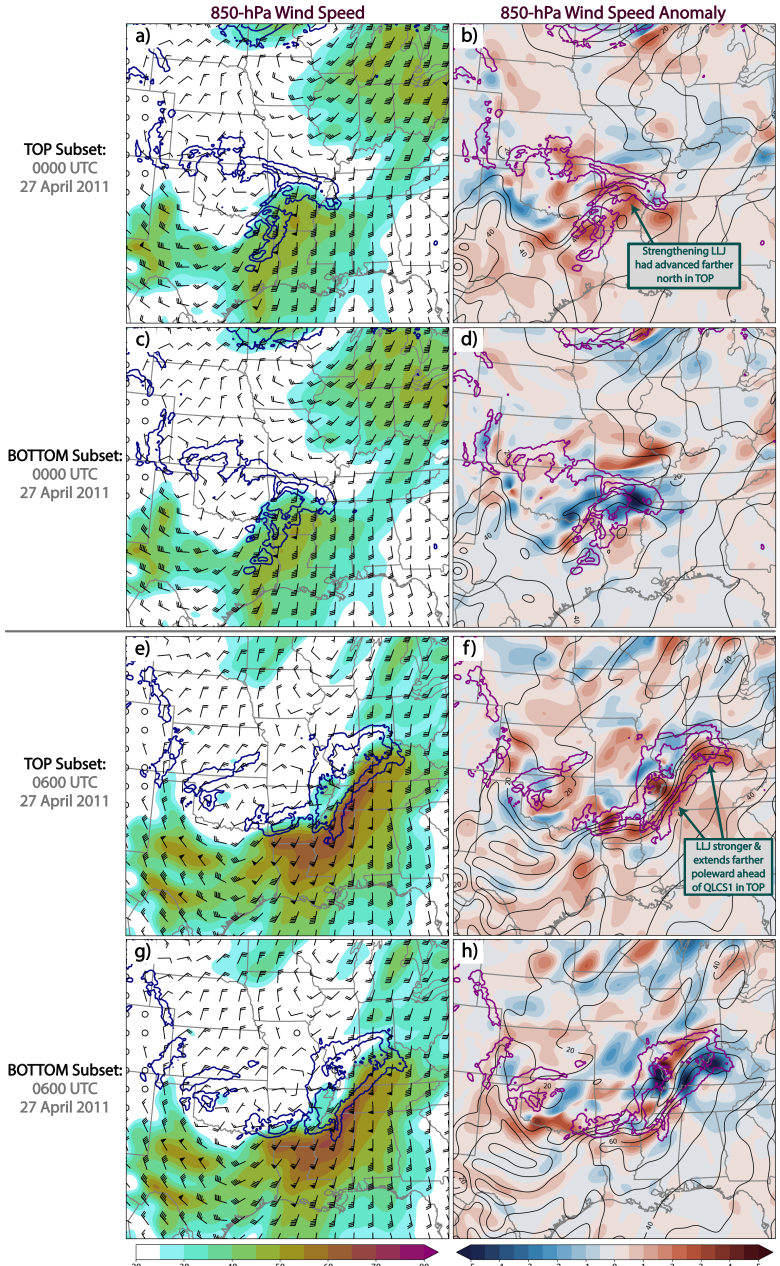

Figure 83: *Subset mean fields of (left) 850-hPa wind speed (shaded; kt), 850-hPa winds (barbs; kt), and composite radar reflectivity (navy contours 20 dBZ ≥ 20 dBZ), and (right) 850-hPa wind speed anomaly (shaded; kt), 850-hPa wind speed (black contours; every 10 kt ≥ 20 kt), and composite radar reflectivity (purple contours; every 20 dBZ ≥ 20 dBZ) for (a),(b) TOP and (c),(d) BOTTOM at 0000 UTC 27 April, and (e),(f) TOP and (g),(h) BOTTOM at 0600 UTC 27 April 2011. The wind fields were low-pass filtered with a 200-km cutoff wavelength.*

82). However, the orientation in the BOTTOM subset was more similar to the observed QLCS1 orientation throughout this period (cf. Figs. 3d and 82e,f).

When the simulations were initialized at 26/1800Z, 850-hPa wind speeds were 30–40 kt throughout much of the Ark-La-Tex region (not shown). The LLJ intensified after CI occurred in both subsets, with enhanced low-level winds becoming readily apparent south of the convection over Arkansas and Oklahoma by 26/2100Z. By 27/0000Z, 850-hPa wind speeds had increased to 45–50 kt throughout a corridor extending northward from the Texas Gulf Coast into central Arkansas, with the TOP subset retaining slightly stronger low-level winds within the inflow environment east of the dryline (Figs. 83a,c). However, a positive 850-hPa wind speed anomaly of approximately 1.5–2.5 kt was evident throughout much of Arkansas in the TOP subset (Fig. 83b) and indicates that the strengthened LLJ extended farther northward in the TOP subset than in the ensemble mean—likely due to greater isallobaric forcing and slight differences in the placement of convection at this time. In contrast, a distinct negative wind speed anomaly was present over central Arkansas in the BOTTOM subset (Fig. 83d).

By 27/0600Z, 850-hPa wind speeds of 55–65 kt had developed throughout the QLCS1 inflow environment in both subsets and extended northward into the Ohio Valley beneath the highly divergent J_2 entrance region (Figs. 83e,g). The LLJ remained stronger and had continued to advance farther poleward in the TOP subset, and a coherent positive 850-hPa wind speed anomaly extended northeastward from Mississippi into southern Indiana within the environment immediately ahead of QLCS1 (Fig. 83f). Although this positive anomaly reflected to some degree the difference in QLCS1 orientation between the TOP subset and the full ensemble mean (i.e., the faster meridional reorientation in the TOP subset meant that the northern portion of the system had pivoted farther toward the northwest; Fig. 82), the low-level flow within the system's inflow environment had become discernibly stronger in the TOP subset. In contrast, a negative wind speed anomaly was situated over Ohio and

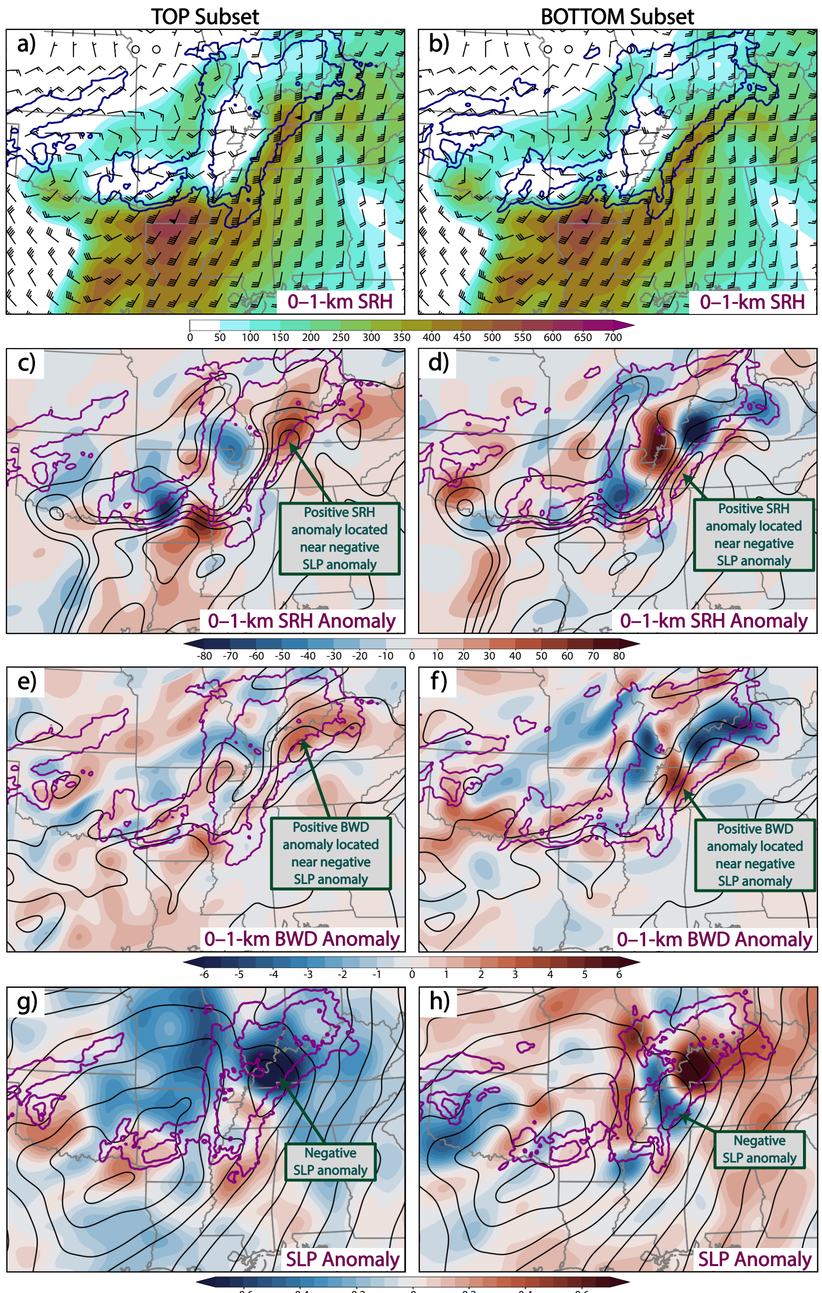

Figure 84: *Mean fields from the (left) TOP subset and (right) BOTTOM subset of (a),(b) 0–1-km SRH (shaded; $m^2\ s^{-2}$) and 0–1-km BWD (barbs; kt); (c),(d) 0–1-km SRH anomaly (shaded; $m^2\ s^{-2}$) and 0–1-km SRH (black contours; every 100 $m^2\ s^{-2} \geq 100\ m^2\ s^{-2}$); (e),(f) 0–1-km BWD anomaly (shaded; kt) and 0–1-km BWD (black contours; every 10 kt $\geq$ 20 kt); and (g),(h) SLP anomaly (shaded; hPa) and SLP (black contours; every 2 hPa) at 0600 UTC 27 April 2011. Composite radar reflectivity is contoured every 20 dBZ $\geq$ 20 dBZ in (a),(b) navy and (c)-(h) purple. All environmental fields were low-pass filtered with a 200-km cutoff wavelength.*

Kentucky in the BOTTOM subset and reflected both the reduced poleward extent of the LLJ and the more zonally slanted system orientation (Figs. 82 and 83h).

The influence that the strengthened LLJ had on the low-level shear and SRH values within the warm sector at 27/0600Z can be discerned by examining Fig. 84. A mesoscale corridor comprising 0–1-km BWD values of 35–45+ kt and 0–1-km SRH values of 350–400+ $m^2 s^{-2}$ stretched from Mississippi into Kentucky immediately ahead of QLCS1 in both subsets (Figs. 84a,b). Compared to the ensemble mean and BOTTOM subset, the inflow environment in the TOP subset was generally characterized by stronger low-level shear and higher SRH values (i.e., localized maxima greater than 50 kt and 450 $m^2 s^{-2}$, respectively) that extended farther northward in conjunction with the LLJ (Figs. 84c-f). However, the low-level shear and SRH anomaly fields exhibited greater mesoscale variability than the 850-hPa wind speed anomaly field and were strongly influenced by the strength and location of pressure perturbations within QLCS1. Specifically, the most prominent positive anomalies in 0–1-km BWD and SRH were situated near and to the east of prominent negative SLP anomalies (i.e., mesolows) within both subsets (Figs. 84g,h). The primary mesolow in the TOP subset was slightly deeper and centered ~150 km farther to the north than the primary mesolow in the BOTTOM subset (denoted L_{ML} in Fig. 82), and each supported a line echo wave pattern reflectivity structure (Nolen, 1959) with a strengthening bowing segment (or segments) located to its south. Note that the filter cutoff wavelength (i.e., wavelength at which the response function amplitude is 0.5; Duchon, 1979) applied to these plotted fields was 200 km such that these mesolows were meso-α-scale circulations.

Thermodynamic conditions were also evaluated for the two subsets. SBCAPE, SBCIN, and SBCAPE anomaly fields are shown at 27/0600Z and 27/0800Z in Fig. 85, and corresponding 2-m potential temperature and 2-m water vapor mixing ratio anomaly fields (θ' and q_v', respectively) are displayed in Fig. 86. We chose to emphasize surface-based quantities owing to their relevance to tornadic convection (i.e., tornadoes require vortex stretching by

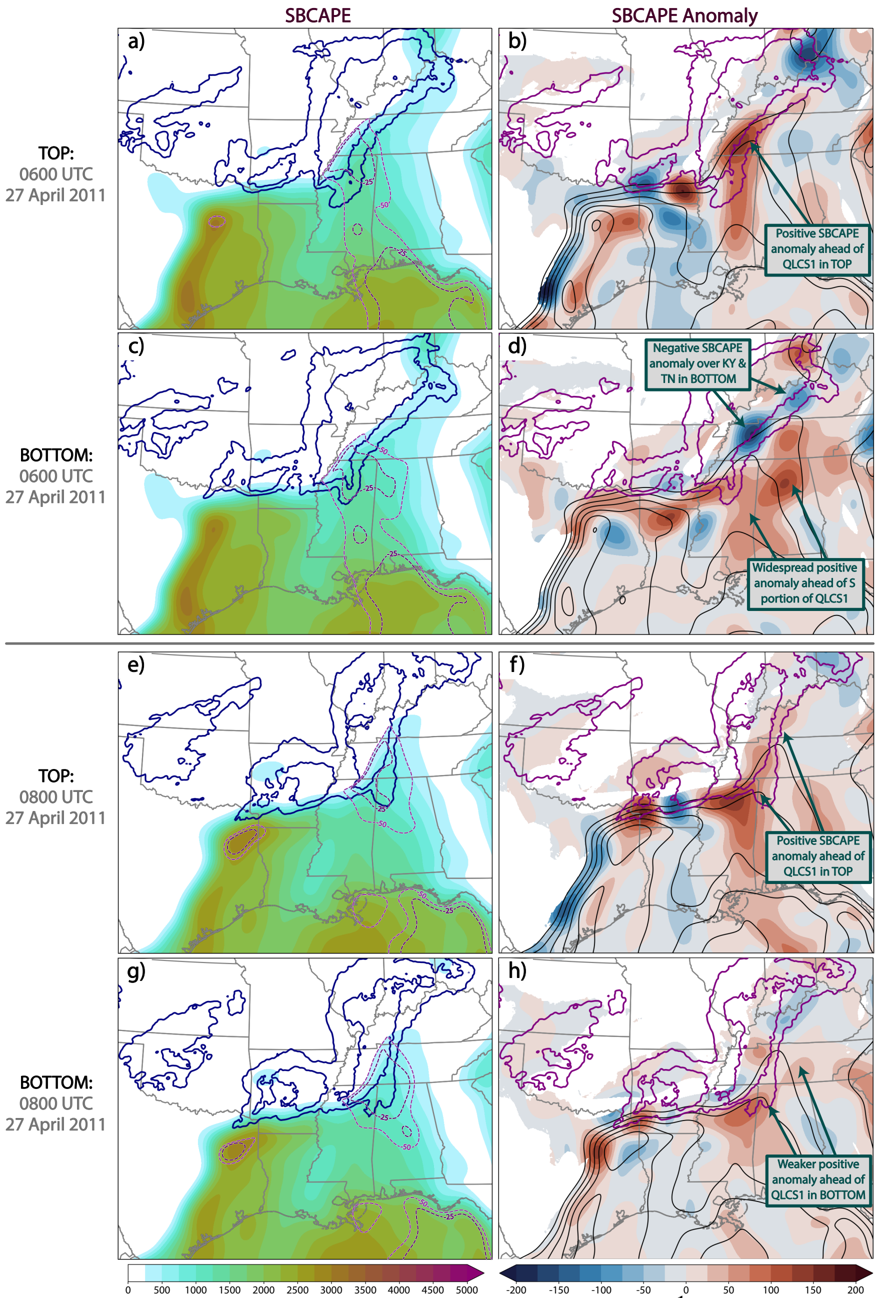

Figure 85: *Subset mean fields of (left) SBCAPE (shaded; J kg^{-1}), SBCIN where SBCAPE $\geq$ 250 J kg^{-1} (dashed dark purple contour = -25 J kg^{-1}; dashed light purple contour = -50 J kg^{-1}), and composite radar reflectivity (navy contours 20 dBZ $\geq$ 20 dBZ), and (right) SBCAPE anomaly (shaded; J kg^{-1}), SBCAPE (black contours; every 500 J kg^{-1} $\geq$ 500 J kg^{-1}), and composite radar reflectivity (purple contours; every 20 dBZ $\geq$ 20 dBZ) for (a),(b) TOP and (c),(d) BOTTOM at 0600 UTC 27 April, and (e),(f) TOP and (g),(h) BOTTOM at 0800 UTC 27 April 2011. All environmental fields were low-pass filtered with a 200-km cutoff wavelength.*

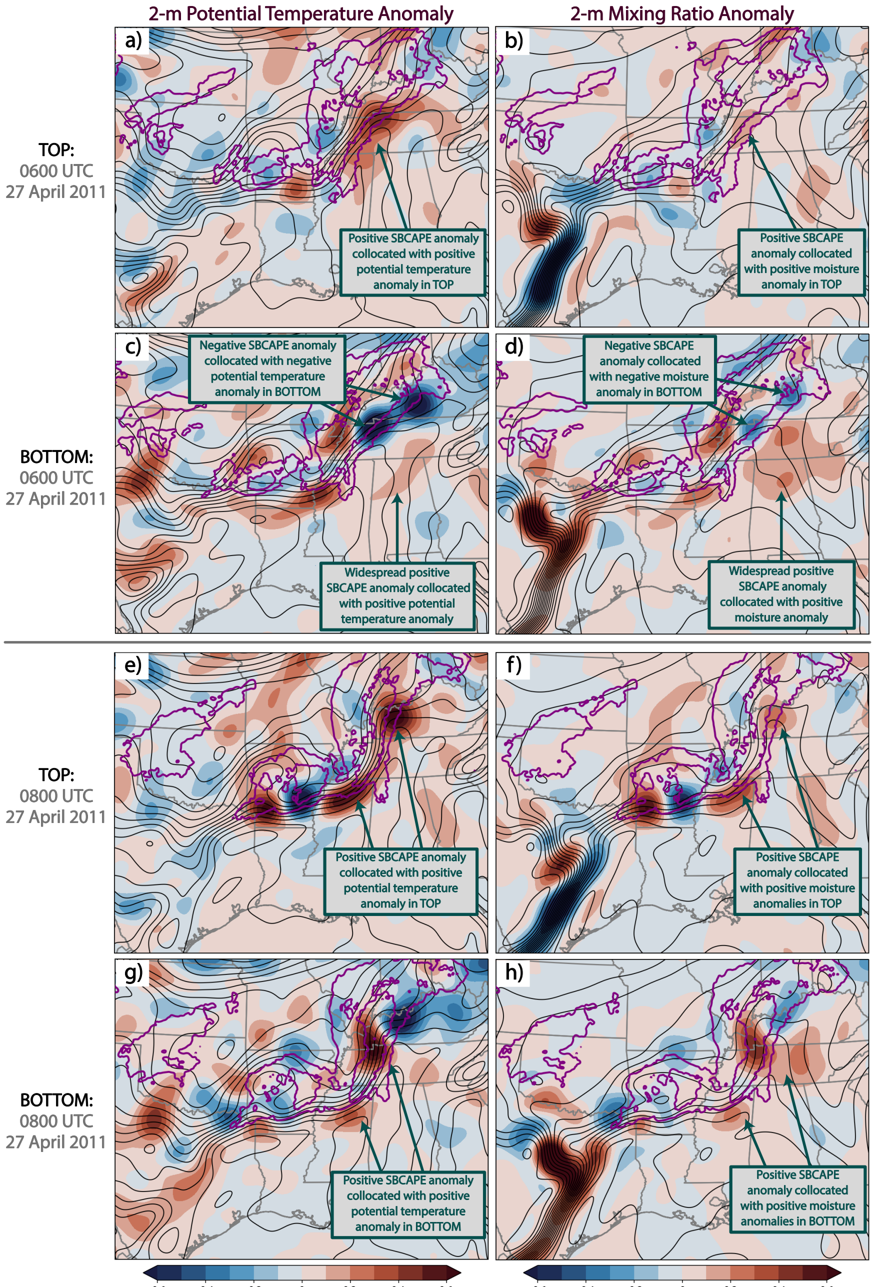

Figure 86: *Subset mean fields of (left) 2-m potential temperature anomaly (shaded; K), 2-m potential temperature (black contours; every 1 K), and composite radar reflectivity (purple contours every 20 dBZ ≥ 20 dBZ), and (right) 2-m mixing ratio anomaly (shaded; g kg^{-1}), 2-m mixing ratio (black contours; every 1 g kg^{-1}), and composite radar reflectivity (purple contours every 20 dBZ ≥ 20 dBZ) for (a),(b) TOP and (c),(d) BOTTOM at 0600 UTC 27 April, and (e),(f) TOP and (g),(h) BOTTOM at 0800 UTC 27 April 2011. All environmental fields were low-pass filtered with a 200-km cutoff wavelength.*

a surface-based updraft; e.g., Davies-Jones et al., 2001) but note that the trends in MUCAPE and MUCIN are similar. At 27/0600Z, the inflow environment over Tennessee and Mississippi in both subsets was characterized by SBCAPE values of 1000–1250+ J kg^{-1} and SBCIN values $\geq$ -50 J kg^{-1} (Figs. 85a,c), which supported surface-based convection within the southern portion of QLCS1. Farther to the north over Kentucky, SBCAPE values of 250–750 J kg^{-1} coincided with appreciable ($\leq$ -100 J kg^{-1}) SBCIN and presumably precluded the development of any persistent surface-based updrafts in this region. Thus, the northern portion of QLCS1 was likely predominately elevated and sustained by MUCAPE values > 750 J kg^{-1} that were accompanied by minimal (> -50 J kg^{-1}) MUCIN (not shown). However, higher values of SBCAPE extended farther northward in the TOP subset, and a coherent SBCAPE anomaly with values of 75–150 J kg^{-1} was situated over western Tennessee immediately ahead of QLCS1 (Fig. 85b). Accordingly, the portion of QLCS1 that remained predominantly surface-based was likely more extensive in the TOP subset at this time, and Figs. 86a,b indicate that this difference partly resulted from warmer (θ' = 0.2–0.5 K) and moister (q_v' = 0.1–0.2 g kg^{-1}) near-surface air. In contrast, the region of high SBCAPE and low SBCIN values extended farther to the east in the BOTTOM subset, and a widespread positive SBCAPE anomaly with values > 50 J kg^{-1} spanned from southern Mississippi into Middle Tennessee—largely in association with a positive surface moisture anomaly (Figs. 85d and 86c,d). We note that these CAPE and CIN anomalies were also influenced by potential temperature anomalies aloft (not shown).

Overall, SBCAPE values throughout the inflow environment had decreased by 27/0800Z, with the corridor of highest SBCAPE adjacent to the southern portion of QLCS1 comprising values $\leq$ 1000 J kg^{-1} (Figs. 85e,g). Compared to 2 h earlier, differences in the poleward extent of high SBCAPE values ahead of QLCS1 had largely diminished between the two subsets, although a positive SBCAPE anomaly > 50 J kg^{-1} persisted from Mississippi into Kentucky in the TOP subset and was primarily associated with large positive θ' and q_v' values (Figs. 85f and 86e,f). However, a positive SBCAPE anomaly—albeit smaller in magnitude—also extended from Mississippi into Middle Tennessee in the BOTTOM subset (Fig. 85h). More discernible differences between the two subsets were evident in the SBCIN fields (Figs. 85e,g), with the immediate inflow environment over northeastern Mississippi, northern Alabama, and Middle Tennessee exhibiting lower SBCIN values in the BOTTOM subset (i.e., ≥ -25 J kg^{-1} owing to a negative SBCIN anomaly of 10–20 J kg^{-1}) than in the TOP subset (i.e., ≥ -50 J kg^{-1} owing to a positive SBCIN anomaly of 10 J kg^{-1}; not shown).

Assessment of QLCS1 severity. It was previously hypothesized in Chapters 3 and 4 that the environmental modifications produced by QLCS1 would ultimately enhance its severity, thus acting as an upscale feedback effect. While it was relatively straightforward to deduce the environmental differences between the two subsets, there is considerably more ambiguity inherent in evaluating or quantifying the severity of convection within the simulations. Some reasons for this ambiguity include the inability of convection-permitting simulations with a horizontal grid spacing $\Delta x \sim 3$ km to properly resolve the physical processes responsible for the production of severe hazards (e.g., Bryan et al., 2003; Potvin and Flora, 2015), warranting the reliance on explicitly predicted diagnostic quantities that serve as "surrogates" for the occurrence of severe weather (e.g., Kain et al., 2008, 2010; Sobash et al., 2011); dependence on the choice in parameter used as a surrogate for a given hazard or combination of hazards (e.g., Sobash et al., 2016a, 2019, 2020); and uncertainly about what thresholds are appropriate to apply to these parameters (e.g., Clark et al., 2012; Milne, 2016; Sobash and Kain, 2017; Sobash et al., 2019, 2020).

Owing to the anomalously tornadic nature of QLCS1 and the formation of multiple long-lived mesovortices embedded within the observed system (e.g., Knupp et al., 2014), we sought (1) a quantity that would account for both the presence of widespread and strong updraft rotation within the simulations. Furthermore, QLCS1 produced numerous severe wind reports—primarily overnight throughout the Southeast (Figs. 1b,c)—warranting the use of (2) a parameter that would assess the strength of near-surface winds within the individual ensemble members. From the diagnostic quantities that were available in the WRF output files, we chose to evaluate the severity of QLCS1 based upon the hourly grid-point maximum (1) updraft helicity and (2) 10-m wind speed fields, which provide invaluable information about convective-scale processes that occur on timescales much shorter than the ensemble forecasts were output (i.e., every hour; Kain et al., 2010).

Updraft helicity (UH) is a widely used diagnostic designed for assessing updraft rotation within convection-permitting simulations (Kain et al., 2008). UH is computed by integrating the product of vertical velocity w and vertical vorticity ζ over a specified layer as

$$UH = \int_{z_0}^{z_1} w\zeta \, dz,$$

where z_0–z_1 is traditionally taken to be 2–5 km AGL such that UH provides a metric for midlevel updraft rotation (i.e., supercell mesocyclones). Midlevel UH has been successfully used to predict the generalized occurrence of severe hazards—including large hail, damaging winds, and/or tornadoes—associated with supercell thunderstorms (e.g., Sobash et al., 2011, 2016b), which are known to produce a disproportionate fraction of severe reports relative to other convective modes (e.g., Duda and Gallus, 2010). However, this quantity has been shown to overforecast the likelihood of tornadoes unless it is combined with environmental parameters that filter out mesocyclones associated with high-based and/or elevated convection, such as lifting condensation level (LCL) height and the ratio of SBCAPE to MUCAPE (e.g., Clark et al., 2012, 2013; Gallo et al., 2016). In lieu of this approach, recent studies have explored the utility of UH calculated over the lowest 1–3 km AGL (i.e., a proxy for low-level mesocyclone or mesovortex strength) for tornado prediction and found improved forecast skill over using 2–5-km UH, although midlevel UH remained more skillful at predicting the combined threat from all severe hazards produced by supercells and other intense convective systems (e.g., QLCSs; Sobash et al., 2016a, 2019). Unfortunately, only 2–5-km UH was included as a diagnostic in the WRF output files, precluding us from using hourly maximum low-level UH as a metric for the strength and intensity of low-level rotation within QLCS1 without rerunning the ensemble.

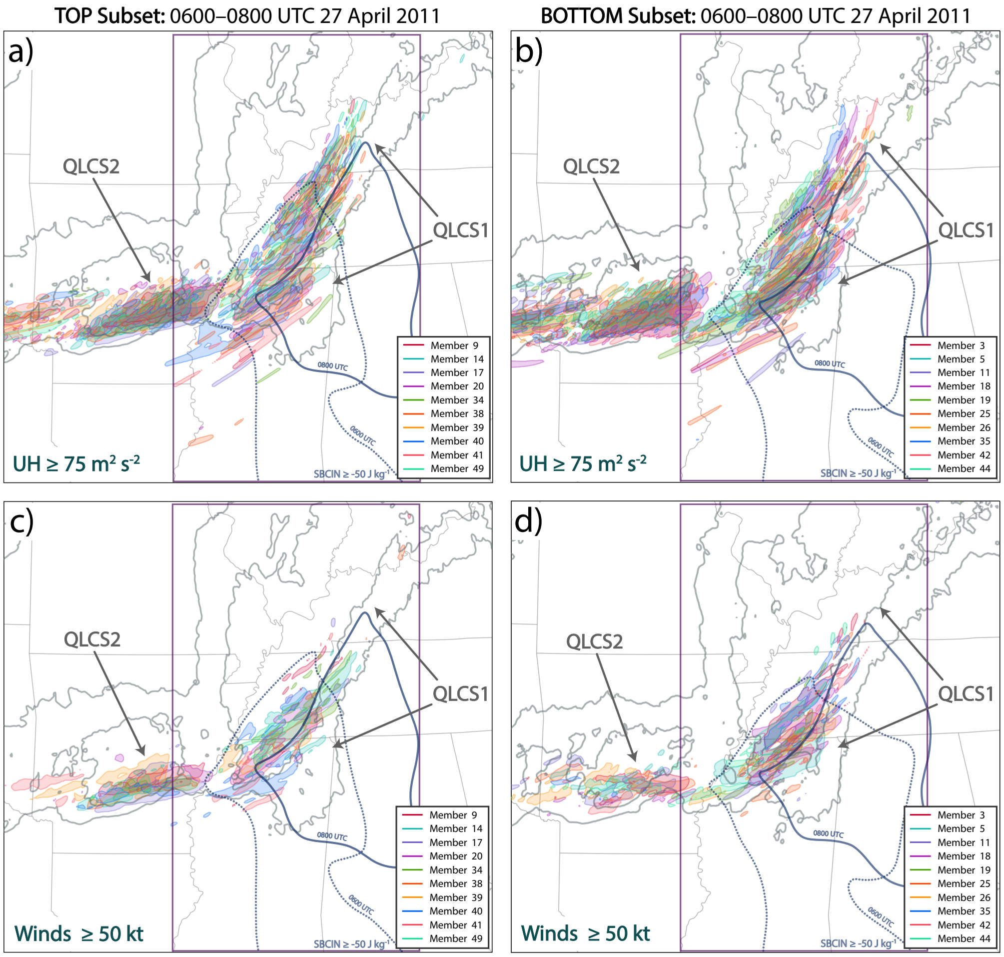

Figure 87: *2-h swaths of grid-point maximum (top) UH ≥ 75 m^2 s^{-2} and (bottom) 10-m wind speed ≥ 50 kt aggregated from 0600 UTC to 0800 UTC 27 April 2011 for all (a),(c) TOP and (b),(d) BOTTOM subset members. The mean composite radar reflectivity at 0700 UTC (gray contours every 20 dBZ ≥ 20 dBZ) is overlaid for each subset. Additionally, the region where SBCIN ≥ -50 J kg^{-1} is outlined in navy at 0600 UTC (dotted contour) and 0800 UTC (solid contour) for each subset. The purple box denotes the domain used to compute the values shown in Fig. 88.*

Although simulated UH has demonstrated success for the prediction of various convective hazards (including severe wind gusts), fewer studies have evaluated the performance of the hourly maximum 10-m wind speed diagnostic in depicting convectively driven high wind events (e.g., Hepper and Milne, 2016; Milne, 2016). As with UH, this quantity is computed at each model time step, and the maximum value attained at each horizontal grid point over the previous hour is included as a diagnostic field in the WRF output files. Although UH is known to be sensitive to the model configuration (particularly the horizontal grid spacing owing to the vertical vorticity component; e.g., Adlerman and Droegemeier, 2002; Sobash et al., 2019), the variables used to compute this parameter—namely, the 3D wind components u, v, and w—are solved directly on the model grid. In contrast, the 10-m wind speed is derived within the surface-layer parameterization scheme by extrapolating downward the wind components from the lowest model level (~26 m AGL in the simulations presented herein) using relationships from Monin-Obukhov similarity theory (e.g., Olson et al., 2021). Thus, these estimated wind speeds may be prone to large errors and highly sensitive to the model configuration due to the reliance on parameterization, further compounding any errors stemming from the inadequate resolution of convective-scale processes.

To evaluate the severity of each subset, both the hourly maximum 2–5-km UH (hereafter referred to as UH for simplicity) and 10-m wind speed fields were aggregated over the period from 27/0600Z–27/0800Z to produce swaths of 2-h maximum values for each grid point within a specified domain that encompassed QLCS1[5] (31.0°N, 91.5°W to 39.0°N, 86.5°W; shown in Fig. 87). Appropriate threshold values needed to be specified and applied to each aggregated parameter. For 10-m wind speed, a threshold of 50 kt (25.7 m s^{-1} or 58 mph) was chosen because this value corresponds to the National Weather Service's threshold for severe thunderstorm wind gusts. Sobash and Kain (2017) and Sobash et al. (2020) determined that the optimal thresholds for midlevel UH vary depending on the model configuration, region, season, and environmental characteristics. We chose to use a threshold of 75 m^2 s^{-2} for UH as several studies have demonstrated that this value produces good correspondence (bias ≈ 1) between simulated surrogate storm reports (a derived quantity based on hourly-maximum UH values; Sobash et al., 2011) and observed storm reports for forecasts generated with

[5]Note that UH and wind speed swaths associated with QLCS2 extended into the western portion of this domain. This was an undesirable but unavoidable consequence of the premature formation of this system and the fact that we wanted to maximize the swath areas associated with QLCS1 without moving the domain during this period. These swaths accompanying QLCS2 are not the focus of this discussion.

a 3-km horizontal grid spacing (e.g., Schwartz et al., 2015; Sobash et al., 2016b). This chosen threshold value corresponds to the 95.94^{th} percentile of all 2-h aggregated UH values computed over the specified domain during this period within the full 50-member ensemble. Because we are comparing forecasts of the same event generated by ensemble members with identical model configurations, we surmise that the choice in UH threshold is unlikely to make much of a difference so long as the chosen value is consistent with sufficiently strong midlevel rotation. A cursory look at analyses using other thresholds (e.g., 100 m^2 s^{-2}, 120 m^2 s^{-2}, the 99^{th} percentile of UH, etc.) support this (not shown).

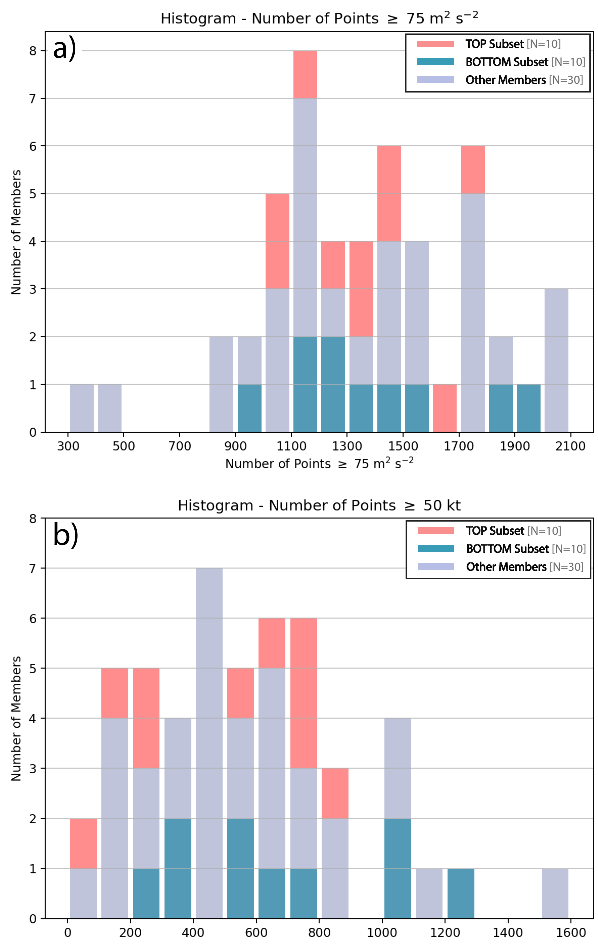

Figure 88: *Histograms showing the number of ensemble members as a function of the number of model grid points within the domain displayed in Fig. 87 where grid-point maximum (a) UH ≥ 75 m^2 s^{-2} and (b) 10-m wind speed ≥ 50 kt during the period from 0600 UTC to 0800 UTC 27 April 2011.*

Paintball plots depicting 2-h swaths of UH ≥ 75 m^2 s^{-2} for each of the 10 members within the TOP and BOTTOM subsets are shown in Figs. 87a,b. Upon inspection of these fields, it is immediately apparent that both subsets comprised members that collectively produced widespread UH swaths extending from northern Mississippi into northwestern Kentucky between 27/0600Z–27/0800Z. In both subsets, these large UH values were produced almost exclusively by the southern portion of QLCS1 as it included the strongest convection and was subjected to a more favorable thermodynamic inflow environment characterized by higher CAPE values and minimal CIN (Fig. 85). Furthermore, regions where SBCIN ≥ -50 J kg^{-1} at 27/0600Z and 27/0800Z are indicated on Fig. 87 and suggest that a sizeable fraction of these UH swaths was associated with convection that was presumably surface-based, increasing the likelihood that some of these areas of strong midlevel rotation embedded within QLCS1 were associated with tornadic circulations at low levels (e.g., Clark et al., 2013; Gallo et al., 2016; Sobash et al., 2016a). Note that strong midlevel rotation also developed during this period in association with QLCS2, which—while elevated—had an inflow environment characterized by ample MUCAPE (1500–3000 J kg^{-1}) that would have supported intense convective updrafts (not shown).

Although these spatial fields do not indicate that there were clearly discernible differences between the two subsets in either the intensity or coverage of midlevel rotation associated with QLCS1, we evaluated this quantitatively by plotting a histogram of the number of grid points within the specified domain where 2-h aggregated UH ≥ 75 m^2 s^{-2} for all 50 ensemble members (Fig. 88a). The histogram confirms that the two subsets did not differ substantially from one another or from the remaining 30 ensemble members in their depiction of midlevel rotation during the 27/0600Z–27/0800Z period. Indeed, the mean number of grid points where UH exceeded 75 m^2 s^{-2} was larger in the BOTTOM subset than in the TOP subset (1395.1 vs. 1352.9 points, respectively, compared to 1361.8 points in the full ensemble mean), and the three members with the greatest number of grid points were not included in either subset. Note that the two outliers containing fewer than

500 grid points corresponded to Members 32 and 50, which were omitted from the subset analysis owing to their deviant depictions of QLCS1 compared to the rest of the ensemble members.

A similar assessment was performed based on 2-h swaths of 10-m wind speed ≥ 50 kt, as shown for each of the 10 members within the TOP and BOTTOM subsets in Figs. 87c,d. The spatial distribution of severe wind swaths was comparable to that of UH, with members of both subsets consistently producing high winds with the southern portion of QLCS1. This was consistent with the convective morphology in the individual ensemble members, as this part of the QLCS was situated south of the primary mesolow and increasingly developed into one or more intense bowing segments throughout this period (Figs. 82e-h). Subtle differences in the region affected by severe winds were apparent between the two subsets, but these likely resulted primarily from slight differences in the location and orientation of QLCS1 rather than differences in the inflow environment.

A histogram of the number of grid points where 2-h aggregated 10-m wind speed ≥ 50 kt for the full ensemble is shown in Fig. 88b. Akin to the histogram of UH grid points, the distributions of the number of severe wind grid points for each subset are similar to each other and to the other 30 ensemble members during this time period. Moreover, the mean number of grid points where 10-m wind speed ≥ 50 kt was greater in the BOTTOM subset than in the TOP subset (683.8 vs. 522.9 points, respectively, compared to 574.4 points in the full ensemble mean), which—combined with the same result for the number of UH grid points—suggests that *the BOTTOM subset members were actually more severe than the TOP subset members between 27/0600Z–27/0800Z.*

To further explore this possibility and ensure that the ensemble members that produced the most widespread midlevel rotation were also the same members that produced the most widespread severe surface winds, a scatter plot of number of grid points where each threshold was exceeded is displayed in Fig. 89. Overall, there was a moderate positive linear relationship between the number of grid points surpassing the UH threshold and

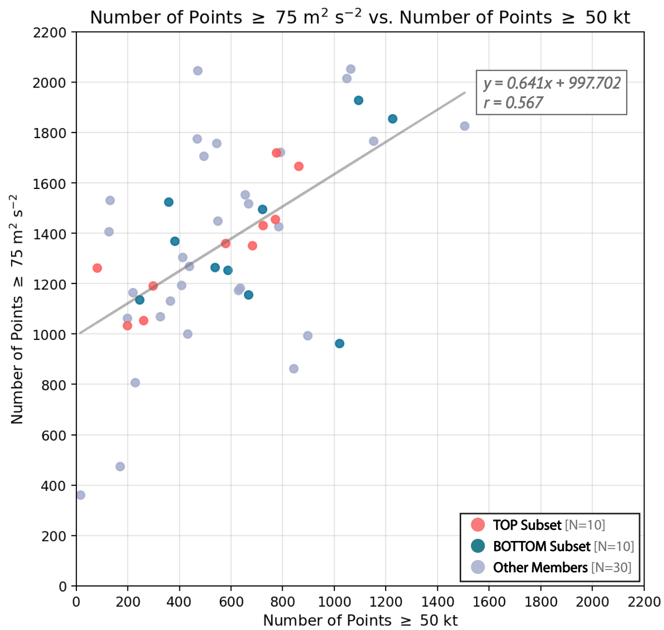

Figure 89: *Scatter plot of the number of grid points within the domain where UH ≥ 75 m^2 s^{-2} versus the number of grid points where 10-m wind speed ≥ 50 kt for all ensemble members during the period from 0600 UTC to 0800 UTC 27 April 2011. The least-squares linear regression line is shown in gray.*

the number of points exceeding the 10-m wind speed threshold, suggesting that members with more widespread midlevel rotation tended to produce more widespread severe surface winds. Furthermore, the number of grid points where maximum UH ≥ 75 m^2 s^{-2} was greater than the number of grid points where the maximum 10-m wind speed ≥ 50 kt in nearly all ensemble members (the sole exception being a member of the BOTTOM subset), with an average of 3.73 times as many UH grid points than severe wind grid points. Based on these two criteria combined, the most severe representation of QLCS1 was produced by Member 4 (1826 and 1505 grid points surpassing the UH and wind speed thresholds, respectively), which was included in neither subset, and 2/5 of the most severe members were part of the BOTTOM subset.

While these results indicate that the severity of QLCS1 in the two subsets was comparable—if not slightly greater on average in the BOTTOM subset—during the 27/0600Z–27/0800Z period, it is worth considering that the severity of convection may have peaked at different times in the TOP and BOTTOM subsets owing to differences (~1 h) in the timing of CI over eastern Oklahoma and Arkansas. Using maximum UH and 10-m wind speed values aggregated over other 2-h periods beginning at 27/0000Z and using a specified domain that retained the same dimensions but was adjusted for each period to remain centered on QLCS1 (not shown), it was discovered that the average number of grid points beyond each respective threshold was larger (~7–8% larger for UH and ~14–45% larger for wind speed) in the TOP subset from 27/0000Z–27/0400Z. During the 27/0400Z–27/0600Z period, the mean number of grid points with UH $\geq$ 75 m^2 s^{-2} remained ~9% greater in the TOP subset, whereas the mean number of grid points with severe surface winds became greater in the BOTTOM subset by ~22%. As we described above, the mean number of grid points beyond both thresholds in the BOTTOM subset had surpassed those in the TOP subset by the 27/0600Z–27/0800Z period. *Thus, QLCS1 was initially more severe in the TOP subset, but the difference in mean severity between the two subsets decreased and ultimately reversed sometime around 27/0600Z.* Evaluation of these successive periods also revealed temporal trends in each severe criterion that were consistent with the morphological evolution of QLCS1. In particular, the mean number of grid points exceeding the UH threshold decreased continuously from 27/0000Z–27/0800Z in both subsets, while the mean number of grid points with severe surface winds increased continuously over this same period. *This trend indicates that the dominant severe hazards produced by QLCS1 evolved with time in accordance with its changing convective organization and upscale growth.*

5.4 Summary and discussion

In this chapter, convection-permitting ensemble forecasts were used to (1) further examine how latent heat release associated with the two QLCSs promoted upscale environmental modifications, and (2) ultimately assess whether differences in the initial flow response following CI with QLCS1 had a discernible influence on its severity overnight.

First, two 50-member ensembles were generated using mean initial states from the GFS analysis and ERA5 reanalysis valid at 1800 UTC 26 April 2011. Output from these two ensembles—including simulated composite radar reflectivity from individual members and ensemble mean fields—were then compared with each other and to the observed radar reflectivity and RUC 1-h forecasts to determine which ensemble best depicted the outbreak evolution.

- All members of both ensembles simulated the initial development and upscale growth of QLCS1, secondary CI associated with QLCS2, and the formation of multiple quasi-discrete cells over the Southeast during the supercell outbreak. However, none of the members of either ensemble adequately captured the maintenance and upscale growth of pre-dryline convection into the prolific southernmost bowing segment with QLCS1 that produced numerous tornadoes overnight throughout the Southeast. Furthermore, neither ensemble correctly represented the initiation and morphological evolution of QLCS2, with the GFS ensemble producing CI prematurely and simulating the upscale growth into a strong bow echo, and the ERA5 ensemble developing convection slightly later but failing to organize it into a coherent system. Both ensembles subsequently depicted the formation of quasi-discrete convection over the warm sector in association with the afternoon supercell outbreak, although this convection developed farther east than was observed.

- Both ensembles adequately represented the rapid downstream formation of J_2 and the resultant LLJ intensification over the warm sector that immediately followed CI with QLCS1. Overall, the upper-level flow pattern became more amplified in the GFS ensemble, and QLCS1 accordingly underwent a faster meridional reorientation. Owing to the premature formation of QLCS2, J_4 developed too early in both ensembles, although it was initially much weaker in the ERA5 ensemble due to the absence of an organized convective system. This upper-level jet streak exhibited pulsed behavior in both ensembles and eventually reintensified, but peak wind speeds within J_4 were 30–40 kt weaker at the beginning of the supercell outbreak than in the corresponding RUC 1-h forecast valid at 27/1800Z. These differences in the evolution of J_4 were consequential for the timing and strength of supplemental isallobaric forcing ahead of SW_3 and thus further LLJ intensification over the warm sector prior to the afternoon supercell outbreak. Moreover, the influence of QLCS2 on the J_1 exit region and SW_3 was improperly represented by both ensembles, which had implications for the deep-layer shear profiles over the Southeast and—by reducing any potential stalling influence on SW_3—further enabled the positive bias in its forward motion.

- The GFS ensemble mean aligned better with the RUC 1-h forecasts and surface observations in its representation of the midlevel trough structure and its depiction of the surface lows at the beginning of the afternoon supercell outbreak. Therefore, this ensemble was chosen for use in all remaining analyses involving WRF output.

Following this selection, the ensemble mean and spread were examined for several fields throughout the lifecycle of QLCS1 and during the afternoon supercell outbreak to assess where considerable variability existed among the individual GFS ensemble members. The results from this assessment are summarized as follows.

- At both 250 hPa and 850 hPa, large standard deviations in the geopotential height and wind speed initially formed near the region of CI and propagated laterally outward through the environment over time. In the upper troposphere, enhanced ensemble spread developed downstream from QLCS1 and—in particular—along the northern and western flanks of J_2 as the unbalanced jet streak rapidly advanced poleward and the upper-level ridge became increasingly amplified over the Midwest. This enhanced spread primarily represented differences in the strength and northwestward extent of J_2 and the amplifying upper-level ridge among the individual members. At low levels, the largest standard deviation values became concentrated near the leading edge of QLCS1 and near the terminus of the LLJ after the system grew upscale. The increased spread within these regions likely reflected variations in the orientation of QLCS1 and in the isallobaric forcing for the intensification and poleward expansion of the

LLJ—all of which were ultimately tied to the differences in upper-level flow that developed within the ensemble.

- During the afternoon, the greatest spread in the surface fields reflected variability in the position of the effective warm front—which was strongly influenced by the preceding QLCSs—and the dryline—which was strongly influenced by PBL mixing and the downward penetration of the DCB. Furthermore, enhanced 2-m temperature standard deviation values developed over the warm sector and were primarily oriented along two distinct corridors that corresponded to enhanced cloud cover and weak simulated reflectivity within Bands 1-2 and Band 3. The mesoscale processes responsible for these warm sector bands are explored further in Chapter 6.

The enhanced ensemble spread that developed in the geopotential height and wind fields following CI with QLCS1 provided further support for our hypothesis that differences in the strength and spatial extent of convection that formed over eastern Oklahoma and Arkansas on 26 April would translate into coherent differences in the upscale flow response that began with the rapid genesis and poleward advancement of J_2. These resultant environmental differences were then postulated to yield differences in the morphological evolution and severity of QLCS1 several hours later, which was assessed from 27/0600Z–27/0800Z. To evaluate these hypotheses, two 10-member ensemble subsets were constructed by grouping the members with the strongest, most widespread convection and the weakest, least widespread convection during the 26/2100Z–27/0000Z period. Composites of these TOP and BOTTOM subsets were then compared with each other and to the ensemble mean to provide the following results.

- CI occurred earlier throughout Arkansas and eastern Oklahoma in the TOP subset and thus promoted a widespread region of stronger convection that was situated farther north by 27/0000Z. Consequently, the upper-level ridge became more amplified over the Midwest in the TOP subset, and J_2 developed sooner and extended farther downstream compared to either the ensemble mean or BOTTOM subset. These differences persisted with time and resulted in greater upper-level divergence that supported stronger isallobaric forcing for LLJ intensification over the warm sector and the faster upscale growth and meridional reorientation of QLCS1 in the TOP subset. Accordingly, the LLJ in the TOP subset had become more intense and extended farther poleward ahead of QLCS1 by 27/0600Z.

- In both subsets, the intensified LLJ supported strong low-level shear and high SRH values that were more than sufficient to support severe and/or tornadic convection by 27/0600Z. However, the shear and SRH anomaly fields exhibited a lot of mesoscale variability and were influenced by prominent mesolows that developed within QLCS1 in addition to the strengthened LLJ. Furthermore, the thermodynamic environment ahead of the southern portion of QLCS1 supported surface-based convection in both subsets, although higher SBCAPE values extended farther poleward in the TOP subset at 27/0600Z. However, the positive shear and SRH anomalies were generally displaced from the positive SBCAPE anomalies in both subsets, and the difference in the poleward extent of high SBCAPE values had largely diminished between the two subsets by 27/0800Z.

- The severity of QLCS1 was then evaluated for each ensemble member by calculating the number of grid points over a specified domain where the maximum midlevel UH ≥ 75 m^2 s^{-2} and 10-m wind speed ≥ 50 kt between 27/0600Z–27/0800Z. Members in both subsets collectively produced a widespread region of severe UH and surface wind swaths that predominantly developed within the surface-based portion of QLCS1. However, the subsets were comparable to each other and to the remaining 30 ensemble members in their depictions of strong midlevel rotation and severe surface winds. Moreover, the mean number of grid points exceeding each respective threshold was greater in the BOTTOM subset such that—on average—the BOTTOM subset members were more severe than the TOP subset members during this 2-h period.

- It was further considered that the severity of QLCS1 in the two subsets may have peaked at different times, motivating an examination of how the number of grid points surpassing each severe threshold evolved with time using 2-h intervals beginning at 27/0000Z. Convection was found to be more severe in the TOP subset than in the BOTTOM subset during the first few hours, but the difference in mean severity between the two subsets decreased with time and ultimately reversed around 27/0600Z. Furthermore, the mean number of grid points exceeding the UH threshold decreased continuously over time in both subsets, while the number of grid points surpassing the severe wind speed threshold concurrently increased—indicating that dominant severe hazards produced by QLCS1 evolved in accordance with its morphological evolution and upscale growth.

While the initial variations in CI ultimately did not yield an appreciable difference in QLCS1 severity several hours later (i.e., when tornado activity was ramping up with the observed system), we note that convection in *all ensemble members* produced dramatic upscale environmental modifications and existed within a shear-buoyancy parameter space known to support significant (EF2+) QLCS tornadoes (e.g., Thompson et al., 2012). Thus, the relatively small-magnitude anomalies found in the inflow environment of either subset were insufficient to "make or break" the severity of QLCS1 in this case. However, this might not hold true for other convective events—particularly those in more marginal and/or HSLC environments, wherein relatively minor changes to environmental conditions can lead to drastic differences in event outcomes (e.g., Cohen et al., 2015; Sherburn et al., 2016; King et al., 2017).

It is noteworthy that all ensemble members (including Members 32 and 50, although with differences compared to the other 48 members) ultimately produced a similar evolution in that the widespread development of convection rapidly distorted the waveguide to promote upper-level jetogenesis and large-scale flow amplification. Therefore, the ensemble demonstrated considerable skill at capturing this dramatic flow evolution when initialized with mean ICs that were valid $\leq$ 6 h prior to the main CI episode. While there were discernible variations in the initial strength and extent of convection over eastern Oklahoma and Arkansas, the overall spread within the ensemble during this period was limited (e.g., no members failed to produce convection altogether), which may not have been the case if the ensemble had been initialized earlier with longer forecast lead times (e.g., 12 or 24 h before CI). Exploring this possibility is beyond the scope of this study but may be worthy of future investigation due to the established loss in downstream predictability that often results from large convective systems interacting with the upper-level waveguide (e.g., Rodwell et al., 2013; Clarke et al., 2019; Baumgart et al., 2019).

Chapter 6

Mesoscale processes during the outbreak

6.1 Introduction

The preceding chapters emphasized the chronological evolution of this multiday outbreak and the upscale modifications produced by the two QLCSs. In this chapter, we use observations and convection-permitting simulations to further investigate some of the mesoscale processes that were highlighted in these previous chapters, with particular attention given to three primary aspects that were pertinent to the evolution of the afternoon supercell outbreak. These interrelated topics include:

1. *The mesoscale evolution of the cold front aloft and the dynamical significance of its interaction with the prefrontal moist layer.*

2. *The mesoscale processes governing rapid destabilization and the formation of a moist absolutely unstable layer over the Southeast prior to the supercell outbreak.*

3. *The mesoscale disturbances responsible for the development of multiple warm sector cloud bands during the afternoon supercell outbreak.*

6.2 Development of the CFA and prefrontal bore

6.2.1 Background and observations

Formation and early evolution of the prefrontal bore. As we previously discussed in Chapter 3, a CFA developed over Texas during the early morning as the Pacific cold front moved downslope in the lee of the Rockies and encountered low-level air masses with greater potential densities. The CFA passage was noted to induce a surface wind shift and sustained hydrostatic pressure rise at several observing sites despite the absence of any change in surface potential temperature. From the surface pressure tendency equation,

$$\frac{\partial p_s}{dt} = -\rho_s g \int_{z_s}^{z_t} \left[-\vec{v} \cdot \nabla_p \ \ln T_v + \frac{R_d}{g} \left(\frac{g}{c_p} + \frac{\partial T_v}{\partial z} \right) \frac{\omega}{p} + \frac{\dot{Q}}{c_p T} \right] dz \,, \tag{6.1}$$

where p is pressure, ρ is density, z is geopotential height, T_v is virtual temperature, T is temperature, $\vec{v}$ is the horizontal wind vector, ω is the vertical velocity in isobaric coordinates, R_d is the dry air gas constant, c_p is the specific heat capacity at constant pressure, $\dot{Q}$ is the diabatic heating rate, the subscripts s and t represent the surface and a level in the upper atmosphere, respectively, and pressure changes at z_t are assumed to be negligible (e.g., Kong, 2006; Knippertz and Fink, 2008), we can understand this observed pressure increase as the response to net column-integrated cold advection, which became progressively deeper with time at a given observing site following the frontal passage. However, an abrupt increase in surface pressure was also observed at several locations prior to the passage of the CFA (as was deduced by analyzing several supplemental datasets, including the RUC and HRRRx model fields and wind profiler observations, and by the onset of a more gradual but sustained surface pressure rise) and—as we demonstrate below—was related predominantly to ascent of stable low-level air within a prefrontal bore. Meteograms of 1-min ASOS observations that captured the abrupt pressure jump accompanying the bore passage and subsequent gradual pressure rise following the CFA passage are shown in Fig. 90.

The development and progression of this bore—which was associated with low-level cloud development along most of its length and evolved with time into a stunning amplitude-ordered train of solitary waves, or soliton (e.g., Christie et al., 1978, 1979; Christie, 1989; Rottman and Einaudi, 1993; Koch et al., 2008a,b; Chasteen et al., 2019)—was evident in the GOES-13 longwave infrared (IR) satellite imagery shown in Fig. 91. Figure 92 provides a zoomed-in depiction of the IR satellite imagery overlaid with conventional surface observations during the period of bore development. The disturbance was first detected in surface observations over central Texas at approximately 27/0300Z and—although it was

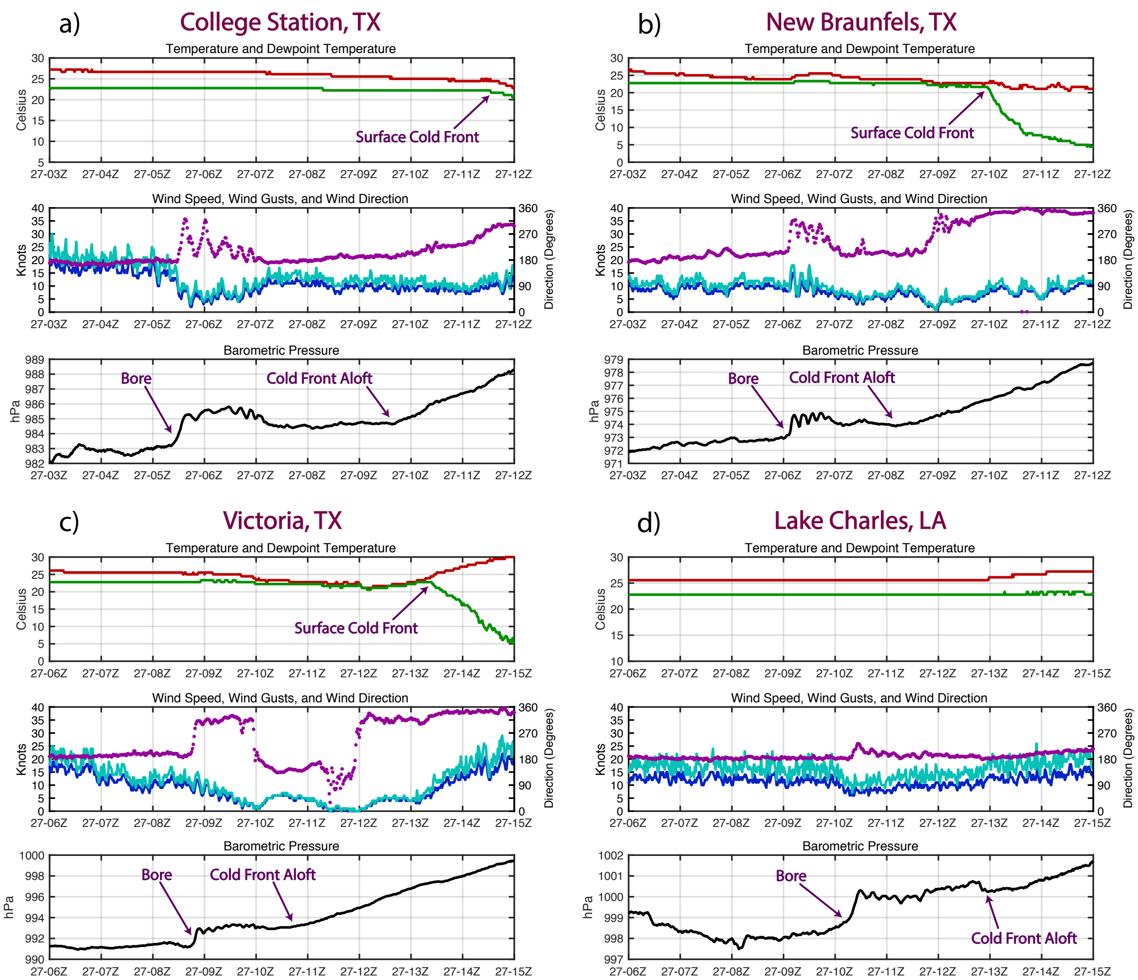

Figure 90: *Meteograms of 1-min ASOS observations from (a) College Station, TX, (b) New Braunfels, TX, (c) Victoria, TX, and (d) Lake Charles, LA, showing the passage of the bore and CFA. The fields displayed are the same as in Fig. 30.*

initially located near ongoing convection within the southern portion of QLCS1—extended west-southwestward well beyond where either convective outflow or the polar air mass over North Texas could have feasibly triggered its formation. Furthermore, the bore developed more than 250 km ahead of the surface Pacific cold front, which remained located over the high terrain of the southern Texas Panhandle at 27/0400Z. However, surface winds atop the Edwards Plateau (annotated in Fig. 92a) and ahead of the Pacific cold front had shifted to northwesterly and strengthened by this time, and observing sites immediately south of the plateau (e.g., Hondo and San Antonio, TX) had detected a bore passage by ~27/0600Z. Water vapor satellite imagery overlaid with 800-hPa wind speeds from the RUC

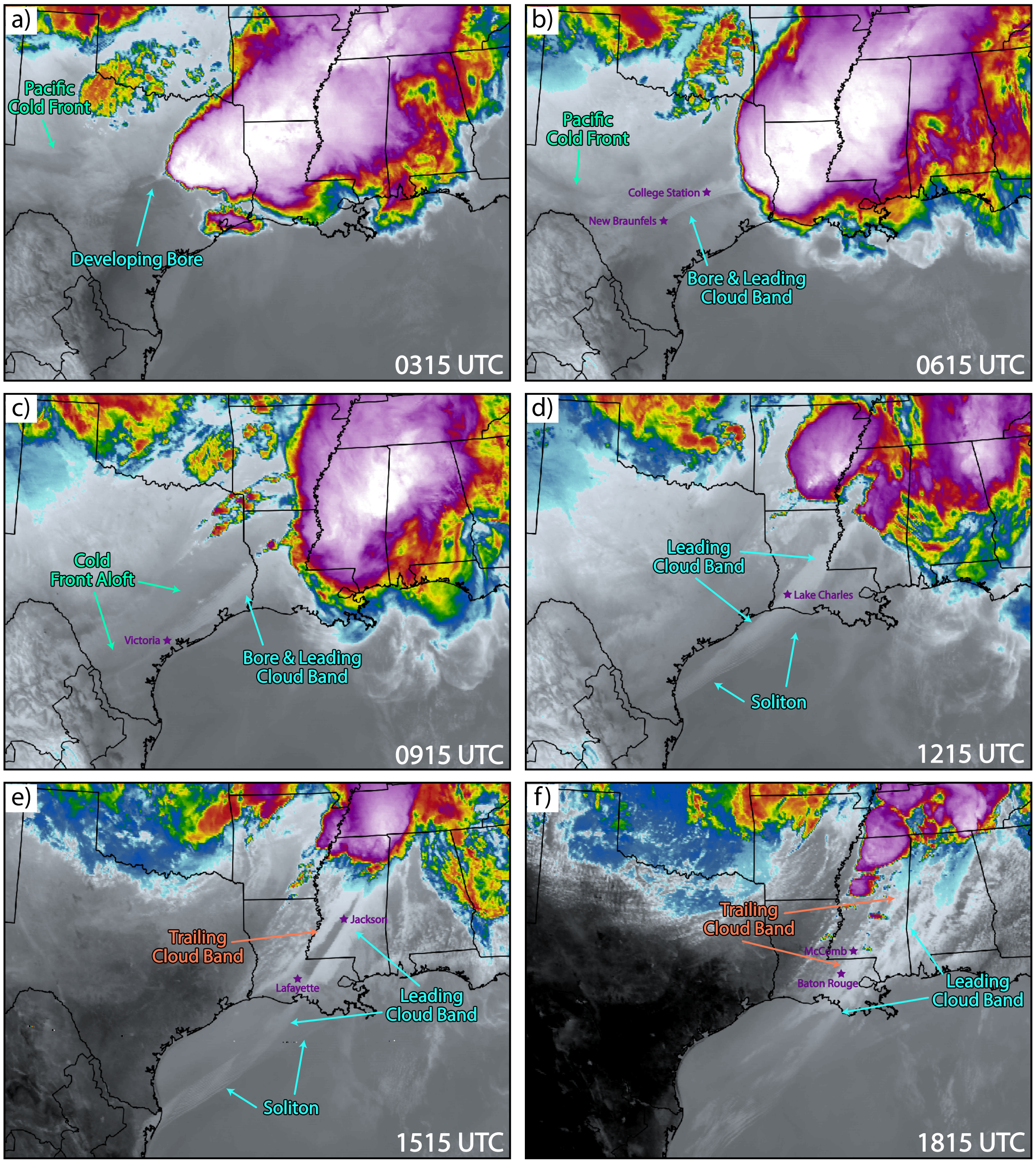

Figure 91: *GOES-13 IR satellite imagery at (a) 0315 UTC, (b) 0615 UTC, (c) 0915 UTC, (d) 1215 UTC, (e) 1515 UTC, and (f) 1815 UTC 27 April 2011 showing the prefrontal bore and distinct cloud bands that develop within the warm sector. The ASOS sites presented in Figs. 90 and 96 are denoted by the purple markers.*

1-h forecast valid at 27/0400Z indicates that a region of strong midlevel subsidence and an accompanying low-level momentum surge had developed over West Texas and was distinct from that associated with the Pacific cold front over the Texas Panhandle (Fig. 93). *Thus, we surmise that the impulse accompanying this momentum surge as it flowed downslope off*

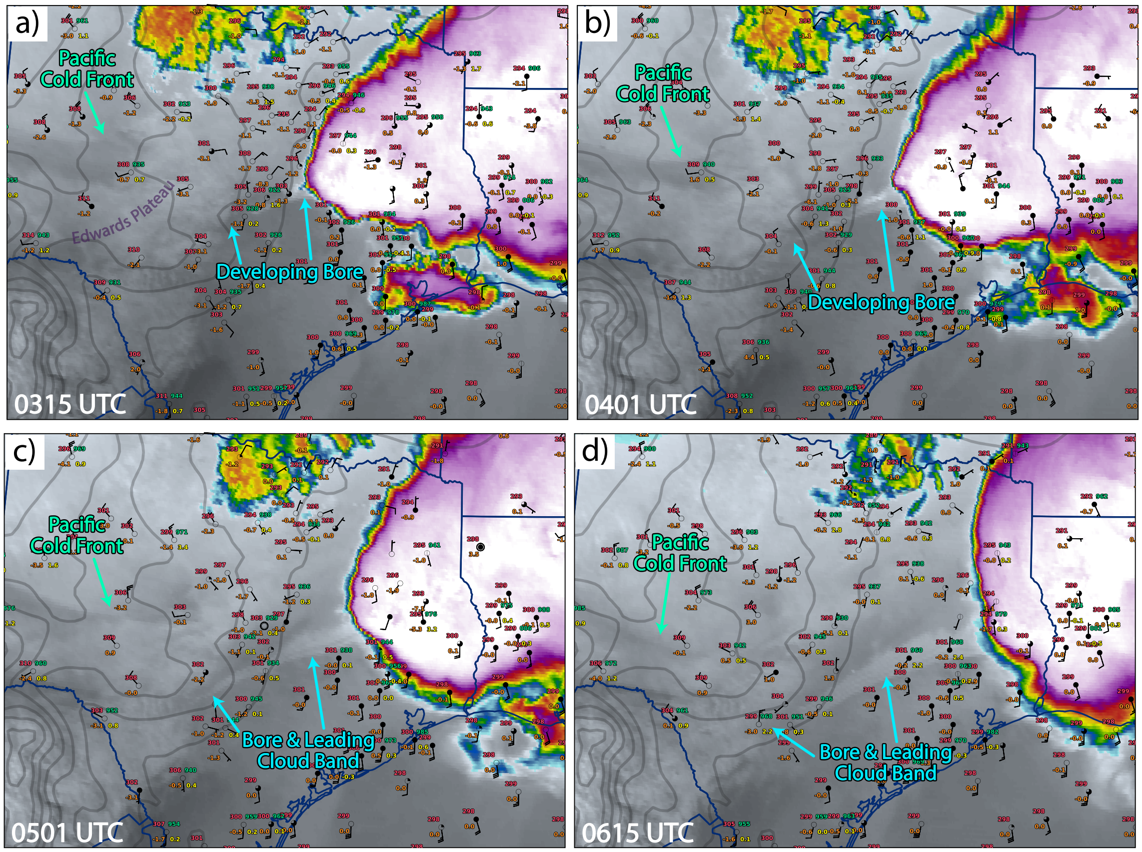

Figure 92: *GOES-13 IR satellite imagery overlaid with conventional surface observations (valid at the top of the corresponding hour) at (a) 0315 UTC, (b) 0401 UTC, (c) 0501 UTC, and (d) 0615 UTC 27 April 2011. On the station plots, the top left is potential temperature (red; K), bottom left is 1-h potential temperature change (orange; K), top right is sea level pressure (green; tenths of hPa with leading digit(s) omitted), and bottom right is 1-h sea level pressure change (yellow; hPa). The gray contours represent terrain height every 200 m ≥ 200 m from the RUC model.*

the Edwards Plateau and encountered the stable low-level moist layer may have triggered a bore in this region. However, the Pacific cold front quickly advanced southward overnight behind the bore (Fig. 92), and the postfrontal sounding released at 27/1103Z from Del Rio, TX, depicted incredibly dry air throughout the lower troposphere and a layer of backing winds (and implied CAA) that extended up to ~600 hPa (Fig. 95a).

The bore remained associated with low-level clouds as it propagated into the Gulf of Mexico and Southeast during the early morning, enabling its movement to be tracked via satellite. However, it evidently exhibited a heterogeneous structure, with a sharpening

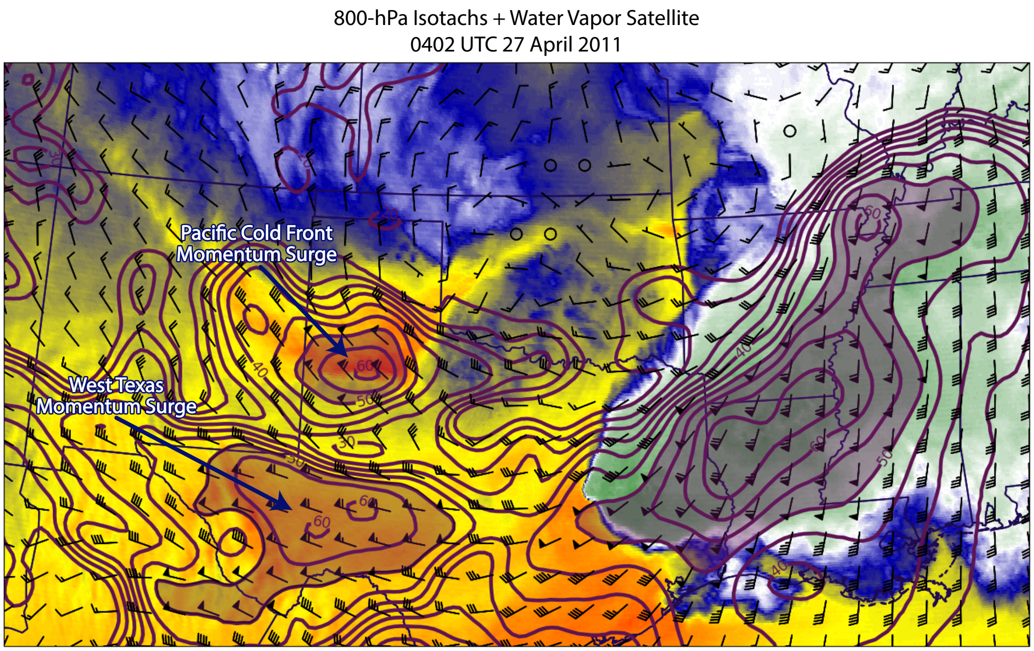

Figure 93: *GOES-13 water vapor satellite imagery from 0402 UTC 27 April overlaid with 800-hPa wind speed (contours every 5 kt ≥ 20 kt; shading ≥ 50 kt) and horizontal winds (barbs; kt) from the corresponding RUC 1-h forecast valid at 0400 UTC 27 April 2011.*

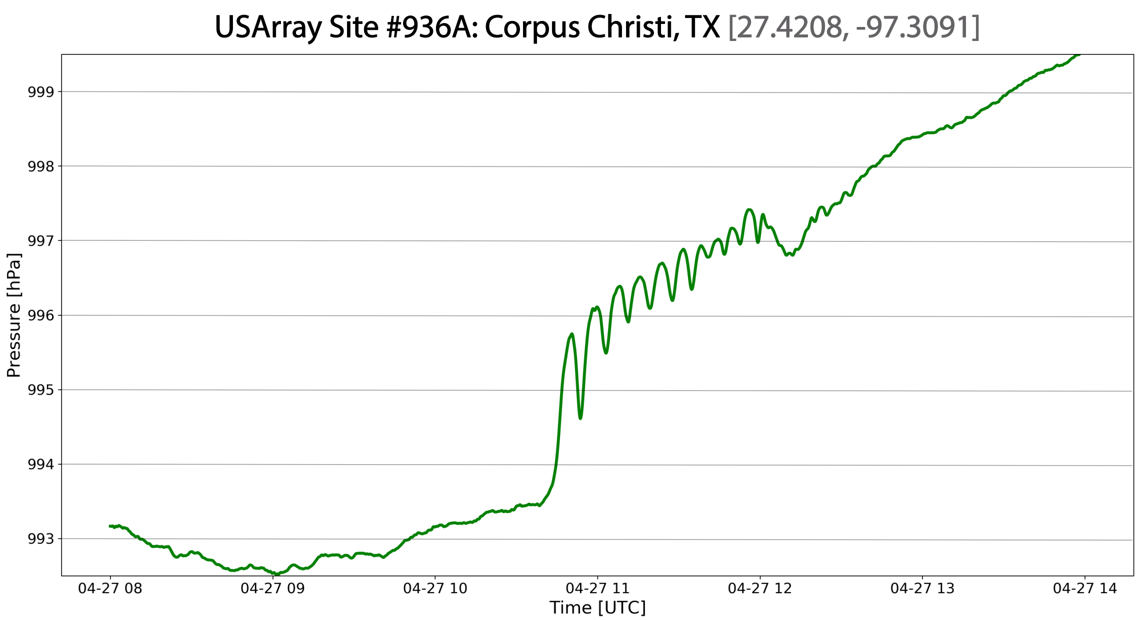

Figure 94: *Time series of surface pressure observations from the USArray Transportable Array site in Corpus Christi, TX, showing the passage of the bore and soliton at approximately 1045 UTC on 27 April 2011.*

mesoscale cloud band (denoted "leading cloud band" in Figs. 91c-e) located over Louisiana and Mississippi, which transitioned into a soliton structure with multiple short-wavelength cloud bands farther toward the southwest. The disturbance passed over numerous surface observing sites, including the ASOS sites shown in Fig. 90 and the USArray Transportable Array site #936A located in Corpus Christi, TX, which measured an initial pressure jump > 2 hPa at ~27/1045Z and 11 individual wave crests within the soliton (Fig. 94). The soliton over the Gulf of Mexico was studied by Lutzak (2013), who determined that its propagation speed c_{bore} = 18 m s^{-1} and that it comprised individual solitary waves with a horizontal wavelength λ = 7.3 km. A sounding was released from Corpus Christi at 27/1113Z just behind the bore and exhibited a shallow MAUL—reflective of the low-level cloud band—that was topped by a strong inversion between ~950–900 hPa (Fig. 95b). This inversion was even stronger in the Brownsville, TX, sounding (~18 K increase in θ over 900 m) and was based at the surface as the bore remained upstream from this location (not shown).

Formation and evolution of mesoscale cloud bands over the Southeast. Although the soliton was certainly interesting, the portion of the disturbance that moved over the Southeast during the morning as a sharpening mesoscale cloud band will be the primary focus of the remaining discussion as it was most relevant to the afternoon supercell outbreak. The potential significance of this feature—and a secondary mesoscale cloud band that had formed by 27/1500Z (i.e., the "trailing cloud band" in Fig. 91e)—was noted by SPC forecasters during the event, who stated the following in Mesoscale Discussion #620 issued at 27/1545Z:

> VISIBLE SATELLITE/SURFACE OBSERVATIONAL TRENDS IMPLY RELATIVELY QUICK AIRMASS RECOVERY/DESTABILIZATION IS OCCURRING FROM LA INTO MS/AL THROUGH MID/LATE MORNING. THIS IS THE CASE NOT ONLY FOR IN THE VICINITY OF EARLY MORNING

WEST-EAST OUTFLOW ACROSS MS/AL...WHERE SURFACE TEMPERATURES/DEWPOINTS HAVE EACH INCREASED 8-12F OVER THE PAST 2 HR...*BUT ALSO IN THE WAKE OF AN APPARENT WAVE-LIKE FEATURE SPREADING EASTWARD CROSS CENTRAL PORTIONS OF MS/LA AS A CU FIELD OTHERWISE CONTINUES TO INCREASE/ MATURE ACROSS NORTHEAST LA.*

The role of these disturbances in this noted rapid destabilization is described further in Section 6.3.

Surface observations and IR satellite imagery indicate that the leading cloud band was undeniably collocated with the bore during its early evolution over Texas, when the passage of the cloud band coincided with a rapid increase in surface pressure and accompanying response in low-level winds (cf. Figs. 90a-c and 91b-c). This spatial correspondence remained valid as the cloud band moved into southwestern Louisiana, with the ASOS site in Lake Charles measuring an abrupt rise in surface pressure shortly after 27/1000Z that was accompanied by veering and slowing of 10-m winds and persisted until nearly 27/1200Z (Fig. 90d). The Lake Charles site remained situated beneath the leading cloud band during this period (Fig. 91d), and the sounding released from Lake Charles at 27/1103Z implied the presence of strong mesoscale ascent with a deep saturated layer spanning ~925–800 hPa—the top portion of which exhibited the character of a MAUL (Fig. 95c). However, the identity of this cloud band became elusive during the morning as it sharpened and acquired a different orientation from the low-level wave train over Louisiana and Mississippi and thus appeared to become its own distinct entity. The separation between the cloud band and wave train was apparent off the coast of Louisiana in Figs. 91d-e, and the ASOS site in Lafayette, LA, measured a ~1-hPa pressure rise associated with the bore passage that preceded the arrival of the leading cloud band by approximately 1.5 hours (Fig. 96a). The bore remained upstream from Slidell at 27/1104Z such that the sounding in Fig. 95d provided a depiction of the environment through which it propagated during the morning.

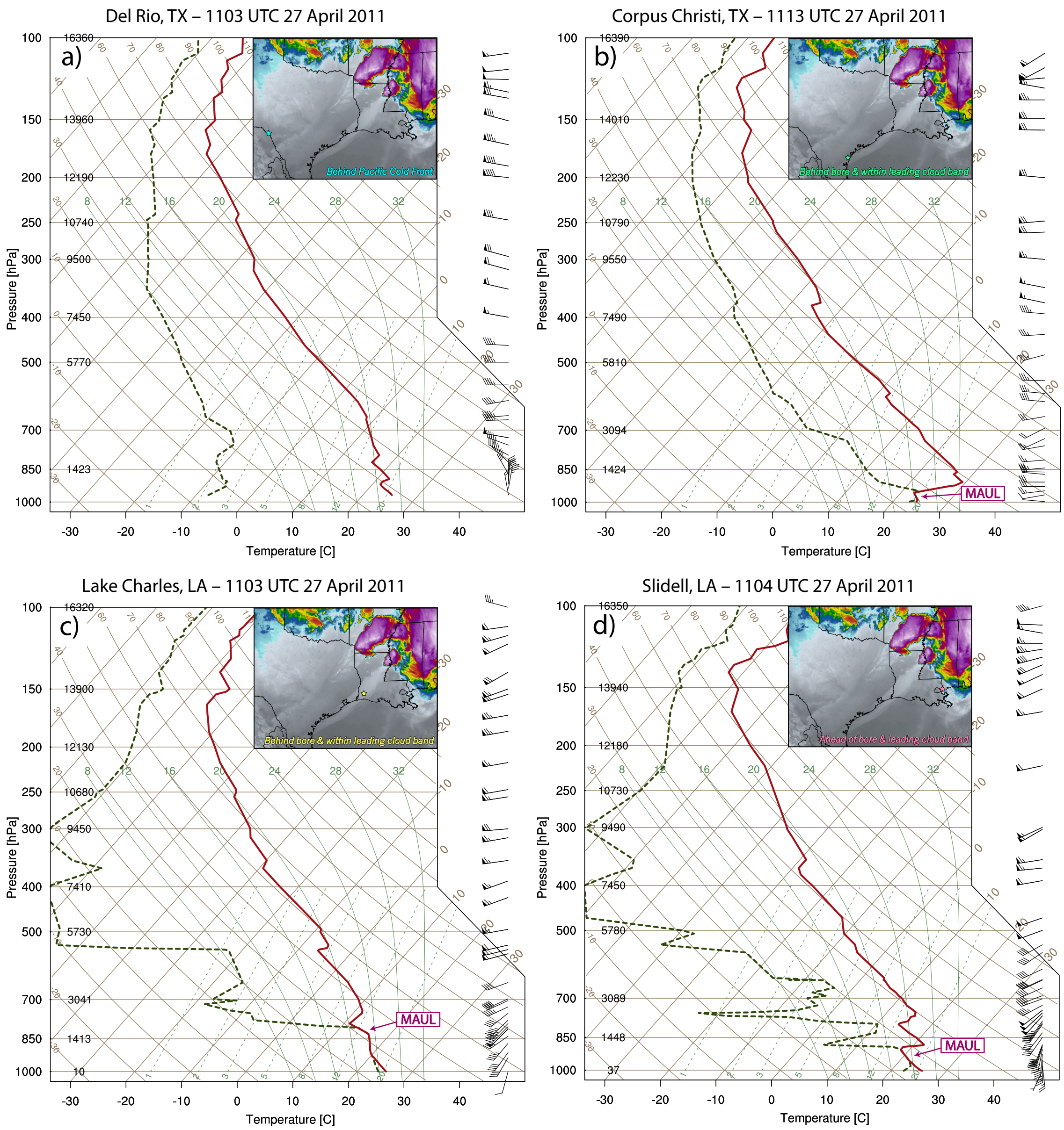

Figure 95: *Observed soundings valid at 1200 UTC 27 April from (a) Del Rio, TX, (b) Corpus Christi, TX, (c) Lake Charles, LA, and (d) Slidell, LA. The sounding release times are listed in each panel, and the sounding locations are denoted on the IR satellite insets.*

This sounding lacked a surface-based inversion and instead depicted a shallow unsaturated PBL that was overlaid by a ~50-hPa deep MAUL. However, two strong elevated inversions were present below ~750 hPa, which would have both permitted gravity wave propagation

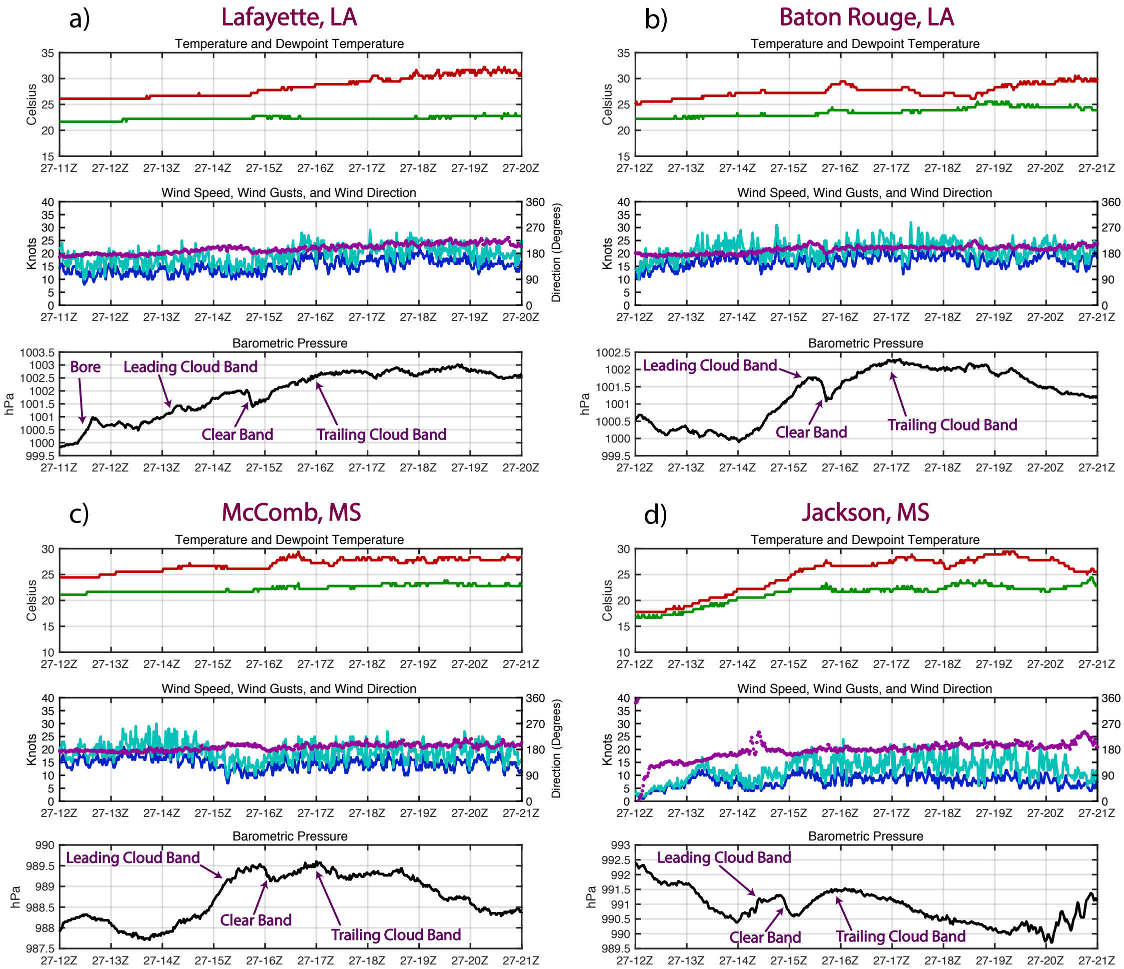

Figure 96: *Meteograms of 1-min ASOS observations from (a) Lafayette, LA, (b) Baton Rouge, LA, (c) McComb, MS, and (d) Jackson, MS, showing the passage of the two distinct cloud bands. The fields displayed are the same as in Fig. 30.*

(i.e., the vertical wavenumber m is real, yielding propagating wave solutions via the Taylor-Goldstein equation). Furthermore, these inversions—particularly the lower of the two—were topped by layers with weak static stability, yielding conditions favorable for wave trapping (e.g., Lindzen and Tung, 1976).

The cloud field over the warm sector became increasingly complex throughout the morning and early afternoon. At 27/1215Z, the leading cloud band can be seen in the IR satellite imagery extending southwestward from the Louisiana-Mississippi border into the Gulf of Mexico, while a secondary region of low-level cloud cover was developing behind this band over northwestern Louisiana (Fig. 91d). In Chapter 3, we described how this

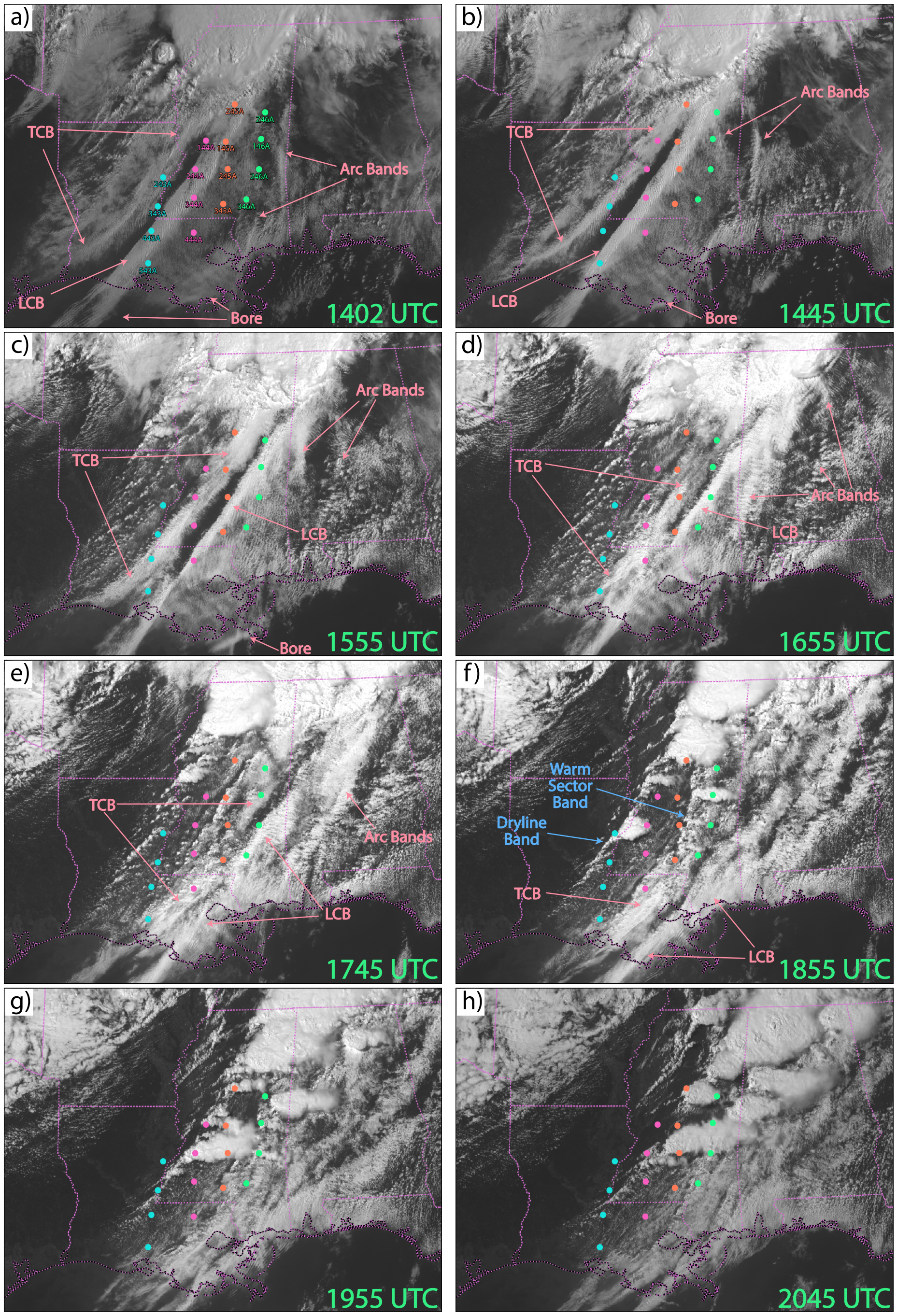

Figure 97: *GOES-13 visible satellite imagery at (a) 1402 UTC, (b) 1445 UTC, (c) 1555 UTC, (d) 1655 UTC, (e) 1745 UTC, (f) 1855 UTC, (g) 1955 UTC, and (h) 2045 UTC 27 April 2011 depicting the complex cloud field over the Southeast prior to and during the beginning of the afternoon supercell outbreak. Key cloud features are identified, including the leading cloud band (LCB) and trailing cloud band (TCB). The USArray sites presented in Figs. 98 and 99 are shown with the colored markers.*

stratocumulus layer progressively broke up into several low-level cumulus bands throughout the morning as it was overrun by dry air behind the CFA and subjected to deepening PBL mixing. This evolution had become apparent by 27/1515Z, and the leading cloud band—which had sharpened considerably over the Southeast during the previous 3 h—was followed by a distinct trailing cloud band that extended from QLCS2 into far southwestern Louisiana and immediately preceded a wedge of broken low-level clouds and a deepening cumulus field (Fig. 91e). The two mesoscale cloud bands were separated by a sharp corridor of clearing and were evidently moving into an environment that was actively destabilizing in the wake of QLCS1. By 27/1815Z, numerous banded structures spanning a range of spatial scales had developed within the deepening cumulus field over the Southeast, and the two once-distinct mesoscale cloud bands had evolved such that they were nearly imperceptible without carefully tracking their locations over time (Fig. 91f). By all appearances, the leading and trailing cloud bands described herein differed from the dryline and warm sector CI bands that were emphasized in Chapter 3.

The dramatic evolution of the low-level cloud field in the hours prior to the afternoon supercell outbreak is now examined further using GOES-13 visible satellite imagery, which became available shortly after 27/1300Z and provided a higher-resolution depiction of these complex cloud structures. Between 27/1400Z–27/1600Z, both the leading and trailing cloud bands (denoted LCB and TCB, respectively, in Fig. 97) were evident as distinct entities that extended southwestward from QLCS2 and sharpened as they contracted in scale over time (Figs. 97a-c). Furthermore, the tops of both mesoscale cloud bands comprised numerous fine-scale banded structures that ranged in orientation from approximately NW-SE to N-S and were thus at a large angle to their parent bands. Although more difficult to discern in the IR satellite imagery owing to its slightly coarser resolution, embedded banded structures that were largely transverse to the leading cloud band had developed by 27/0600Z and extended along the length of the disturbance as it moved into the Gulf of Mexico (Figs. 91b-f). Over the Southeast, these structures were most apparent during the early morning before the PBL had considerably deepened and were oriented approximately orthogonal to the shear vector near the top of the cloud layer (cf. Figs. 95c and 97a), suggesting that they were likely the manifestation of Kelvin-Helmholtz (KH) instability (e.g., Browning, 1971) rather than—perhaps—a type of horizontal convective roll (HCR) disturbance that formed within a sheared unstable layer aloft or within the growing PBL prior to being lifted atop the band (e.g., Weckwerth et al., 1997).

Ahead of the two mesoscale cloud bands, multiple banded disturbances became evident in the cloud field throughout the morning (labeled "arc bands" in Fig. 97) and—at least initially—had a predominantly meridional orientation and eastward direction of motion (Figs. 97a-c). These disturbances had a spacing of several tens of km and differed from the HCRs that developed in the deepening PBL during the morning (e.g., along the Gulf Coast in Fig. 97c). By late morning, several of these arc bands had either emanated from or evolved out of the leading and trailing cloud bands such that a mesoscale region of agitated cumulus extended from the Lower Mississippi Valley into central Alabama by 27/1745Z, rendering both of the initial bands increasingly indiscernible (Figs. 97c-e). By 27/1855Z, several mesoscale bands of agitated cumulus that were largely parallel to one another and oriented from SW-NE were evident throughout the warm sector, while CI was actively occurring over Mississippi along the dryline band and warm sector band described in Chapter 3—the latter of which was largely indistinguishable in the cloud field just 1 h earlier (Fig. 97f). With limited exceptions (e.g., the Cullman, AL, supercell that seemingly stemmed from the leading cloud band; not shown), these other numerous mesoscale cloud bands were associated with attempted but failed CI, which can be discerned from the weak cellular reflectivity echoes situated along the cloud bands at 27/1800Z in Fig. 3h.

Surface observations accompanying the passage of the mesoscale cloud bands. Overall, the satellite evolution demonstrates that highly complex interactions between multiple disturbances with different orientations, directions of motion, and spatial scales were occurring throughout the warm sector prior to the afternoon supercell outbreak. Truly characterizing

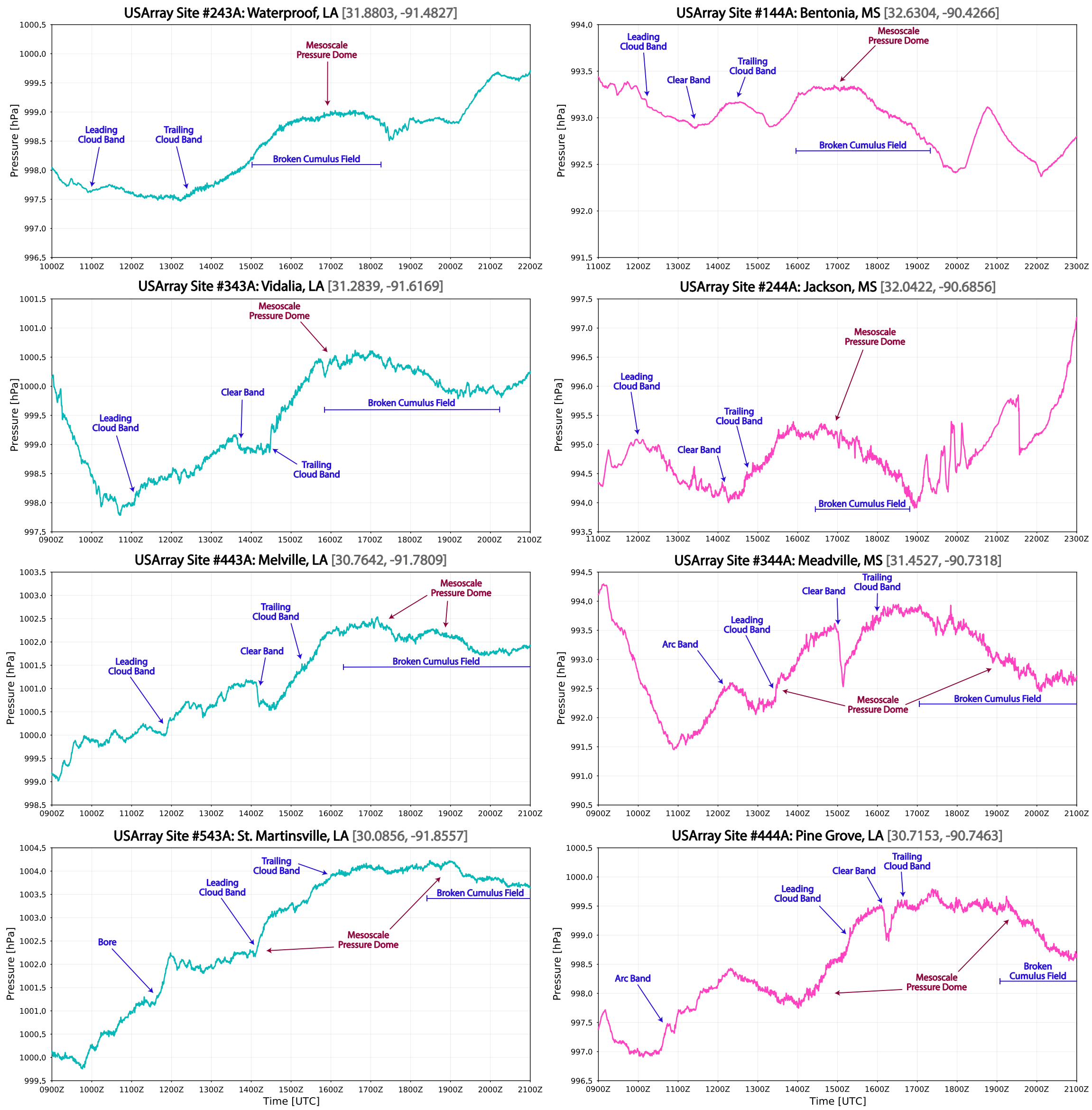

Figure 98: *Time series of surface pressure observations on 27 April 2011 from several USArray Transportable Array sites located over eastern Louisiana and western Mississippi (shown with the cyan and pink markers in Fig. 97).*

these disturbances and how their interactions led to CI is frankly impossible without a dense network of observations (including PBL profilers), which did not exist over this region. Fortunately, we are afforded the benefit of a mesoscale network of high-resolution surface pressure observations over much of the Southeast due to the USArray Transportable Array, which—when paired with 1-min ASOS and other observations (e.g., radar) from across the region—provides a gold mine of data that could be used to glean insight into the nature of these disturbances and how they evolved.

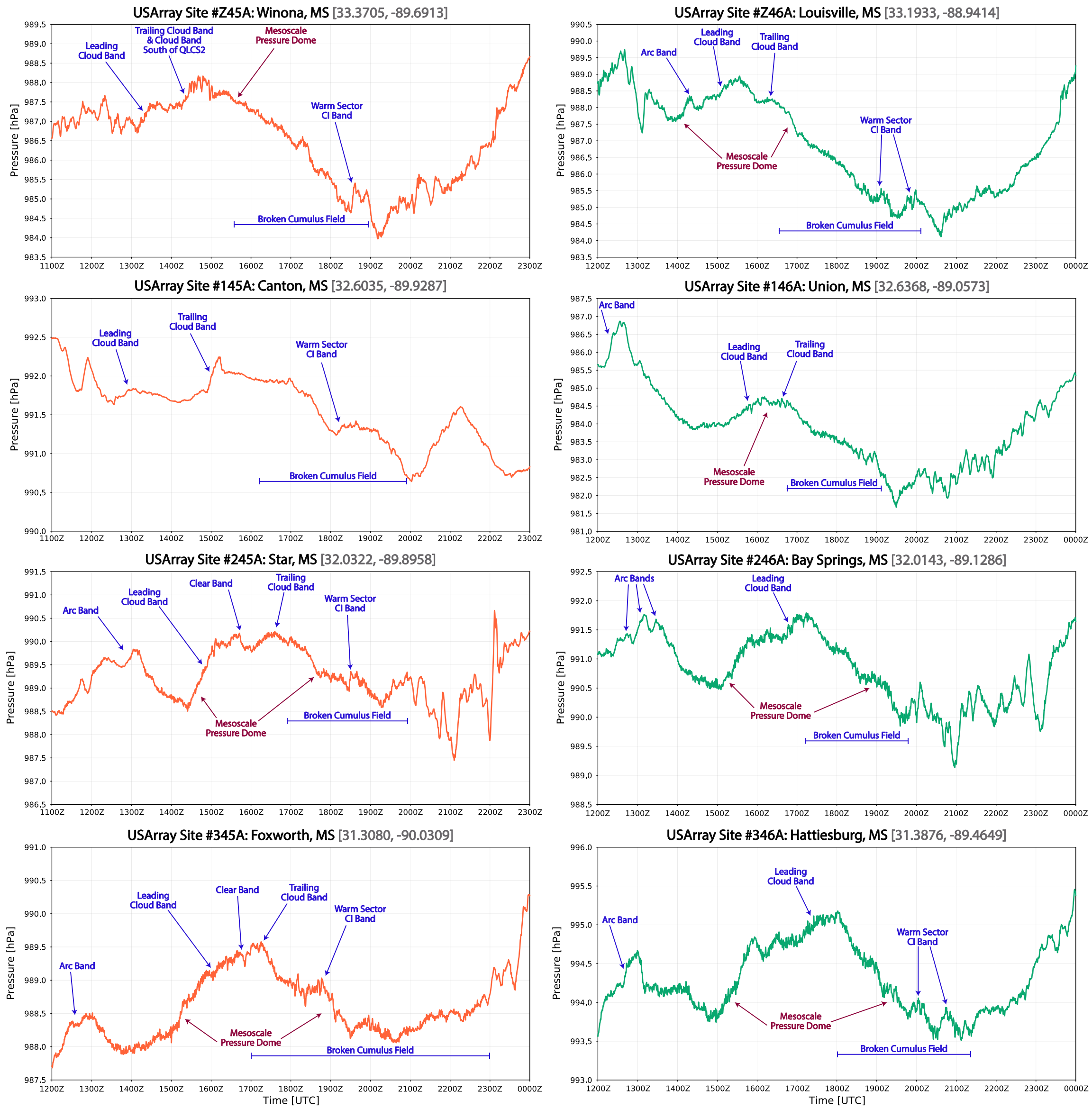

__Figure 99:__ As in Fig. 98 but for several sites located over central and eastern Mississippi (shown with the orange and green markers in Fig. 97).

Herein we only scratch the surface of this analysis and attempt to use observations from several ASOS and USArray sites located throughout Louisiana and Mississippi to identify signatures associated with the passage of coherent disturbances in the cloud field (as could be determined from satellite when not obscured by anvil cirrus). The ASOS locations described are shown in Figs. 91e-f and include Lafayette, LA, Baton Rouge, LA, McComb, MS, and Jackson, MS (Fig. 96). The USArray sites examined are denoted in Fig. 97 and are divided into four groups (each shown with a different colored marker) that correspond to similar longitudes (Figs. 98 and 99). The passage of several major disturbances within the warm sector are annotated on the pressure traces and include the bore, leading cloud band, trailing cloud band, clear band (i.e., the band of clearing between the leading and trailing cloud bands), arc bands, and warm sector CI band. However, note that there were numerous pressure perturbations observed at these locations for which we do not provide an identification or explanation herein due to a lack of time (e.g., the pressure ridges observed at ~27/2100Z by the USArray sites #144A, #244A, and #145A in Bentonia, Jackson, and Canton, MS, respectively). Overall, the complexity of the pressure traces presented in this analysis attests to the incredible variability and abundance of mesoscale disturbances present over the Southeast prior to the supercell outbreak. Some prominent signatures identified in the surface observations are summarized below.

- Several of the USArray sites detected an appreciable pressure rise with the passage of the arc band seen over eastern Mississippi and western Alabama in Figs. 97a-b. These increases were not sustained and were followed by a sharp pressure decrease at some locations (e.g., the USArray sites #146A and #346A in Union and Hattiesburg, MS, respectively), yielding a pressure signature that might be reflective of a solitary wave of elevation.

- A coherent pressure increase that unambiguously accompanied the bore passage but was displaced ahead of the leading cloud band was observed by the ASOS site in Lafayette (as was mentioned above) and by the USArray site #543A in St. Martinsville, LA.

- At many of the ASOS and USArray sites considered herein, a distinct pressure increase was either observed when the leading cloud band passed over the site (e.g., the USArray sites #343A and #443A in Vidalia and Melville, LA, respectively) or began within the hour or so prior to its passage. At some locations (e.g., the ASOS site in Jackson, MS, and USArray site #244A, which was situated ~65 km southwest of the Jackson ASOS site), the leading cloud band coincided with a coherent mesoscale pressure ridge, and wind perturbations were observed to accompany its passage at all four ASOS sites. The pressure rise associated with the leading cloud band was most apparent at sites located in the southwestern portion of the region considered (i.e., sites in southern Louisiana and southwestern Mississippi) but was absent or incredibly weak at some of the northern sites (e.g., the USArray sites #243A in Waterproof, LA, and #144A in Bentonia, MS).

- At most locations, a pressure increase > 1 hPa was observed that persisted for several hours (denoted a "mesoscale pressure dome" on the USArray pressure traces as it corresponded to a dome of lifted air and deeper moisture, which is discussed in the following section) and was either preceded by a distinct pressure rise that accompanied the leading cloud band passage (e.g., at the Jackson, MS, sites), initiated as the pressure increased in conjunction with or shortly before the leading cloud band passage (e.g., at the ASOS sites in Baton Rouge, LA, and McComb, MS, and the USArray sites #344A and #444A in Meadville, MS, and Pine Grove, LA, respectively), or began ~2 h prior to the leading cloud band passage but encompassed the period during which it passed (e.g., at the USArray sites #246A and #346A in Bay Springs and Hattiesburg, MS, respectively). At these latter sites, the initial pressure increase observed at ~27/1500Z likely accompanied the passage of an arc band that progressed into the warm sector ahead of the leading cloud band and led to sustained deepening of the low-level moist layer.

- The band of clearing that developed between the leading and trailing cloud bands and notably sharpened between 27/1400Z–27/1600Z (Figs. 97a-c) was accompanied by a pressure decrease at several locations. This pressure decrease occurred abruptly along the backside of the leading cloud band (e.g., at the USArray sites #443A in Melville, LA, and #245A in Star, MS) and had a signature that was consistent with a solitary wave of depression (e.g., the pressure and wind observations from all four ASOS sites and the high-amplitude pressure trough evident in the USArray observations from #344A and #444A in Meadville, MS, and Pine Grove, LA, respectively).

- Sites that detected a pressure drop with the band of clearing subsequently measured a pressure increase that was associated with the approaching trailing cloud band (e.g., at the ASOS site in Baton Rouge, LA, and the USArray sites #343A and #245A in Vidalia, LA, and Star, MS, respectively). At several locations, the trailing cloud band coincided with the apex of the mesoscale pressure dome (e.g., the ASOS sites in McComb and Jackson, MS, and the USArray sites #345A and #Z46A in Foxworth and Louisville, MS, respectively), and its passage was followed by a steady pressure fall that accompanied the region of broken clouds and deepening cumulus field that developed behind the trailing cloud band (labeled "broken cumulus field" on the USArray pressure traces). As we show later in this chapter, this steady pressure decrease likely reflected the dome-like nature of the deepened moist layer ahead of the CFA and subsidence warming that was occurring behind the trailing cloud band and CFA.

- Finally, pressure perturbations accompanying the warm sector CI band were observed at several of the USArray sites located in Mississippi (particularly the orange and green sites shown in Fig. 97). These perturbations manifested as relatively short period, transient pressure rises that occurred within the region of broken cumulus clouds and accompanying gradual pressure falls (e.g., at the USArray sites #245A, #246A, and #346A in Star, Foxworth, and Hattiesburg, MS, respectively). Whether these small-scale pressure perturbations were a reflection of mesoscale disturbances that directly promoted CI ahead of the CFA over Mississippi is unknown.

6.2.2 Analysis with HRRRx and GFS ensemble forecasts

We now investigate the formation and evolution of the bore over Texas and the prefrontal disturbances over the Southeast using fields derived from the 27/0000Z initialization of the HRRRx and the GFS ensemble described in Chapter 5. The HRRRx fields are presented herein for two primary reasons: (1) the HRRRx forecasts were made available in 2019 and permitted us to successfully examine and draw insight into these key mesoscale features for the first time, as their identities and evolutions were previously difficult or impossible to ascertain from the coarser-resolution RUC fields alone; and (2) there is considerable agreement between the HRRRx and GFS ensemble in their depictions of these disturbances, which provides confidence that they are adequately representing the most essential physical processes. We begin by discussing the 27/0000Z HRRRx forecasts, which were limiting owing to their short duration relative to the time span over which these disturbances evolved. Thus, the preliminary findings obtained from the HRRRx fields will then be expanded upon by analyzing the GFS ensemble forecasts.

CFA and prefrontal bore in the HRRRx. Shown in Fig. 100 is the equivalent potential temperature field at the surface, 900 hPa, and 800 hPa from the HRRRx forecast valid at 27/1300Z. At this time, high-θ_e surface air extended inland into southeastern Texas and much of the Southeast, while a notable cyclonic wind shift can be seen spanning from the southern tip of Texas into southwestern Mississippi within the moist air mass with no accompanying gradient in θ_e (Fig. 100a). However, a cyclonic wind shift was also apparent over this region at 900 and 800 hPa and coincided with a band of enhanced θ_e values (indicative of ascent transporting high-θ_e air upward) situated immediately ahead of low-θ_e air that had advanced over the warm sector behind the CFA (Figs. 100b-c).

Two vertical cross sections were taken across this wind shift band at 27/1300Z and are displayed in Fig. 101. Cross Section #1, which extended southeastward from near Abilene, TX, into the Gulf of Mexico, depicted a remarkable elevated intrusion of low-θ_e air that

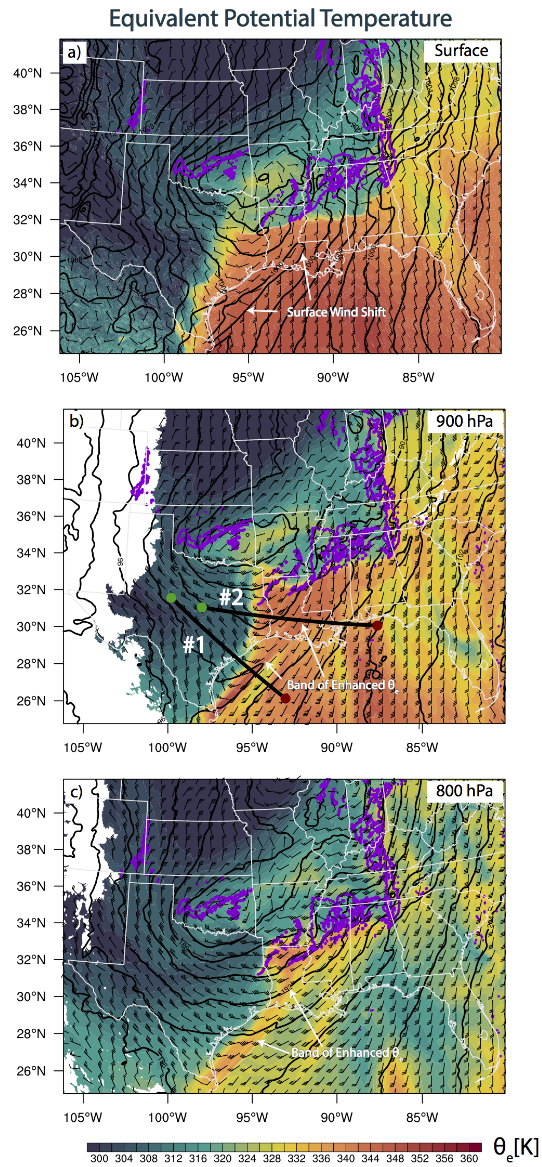

Figure 100: *Equivalent potential temperature (shaded; K) shown at 1300 UTC 27 April for (a) the surface, (b) 900 hPa, and (c) 800 hPa from the 0000 UTC initialization of the HRRRx. Sea level pressure (contours; hPa) and 10-m winds (barbs; kt) are shown in (a), and (b,c) geopotential height (contours; dam) and horizontal winds (barbs; kt) at 900 hPa and 800 hPa are shown in (b) and (c), respectively.*

had overrun the moist low-level air mass and was preceded by a high-amplitude bore (Fig. 101a). Examining how fields along this cross-section path evolved with time indicates that the bore developed as subsiding low-θ_e air moved downslope and encountered the stable moist layer in the lee of the Edwards Plateau (not shown). This disturbance had become

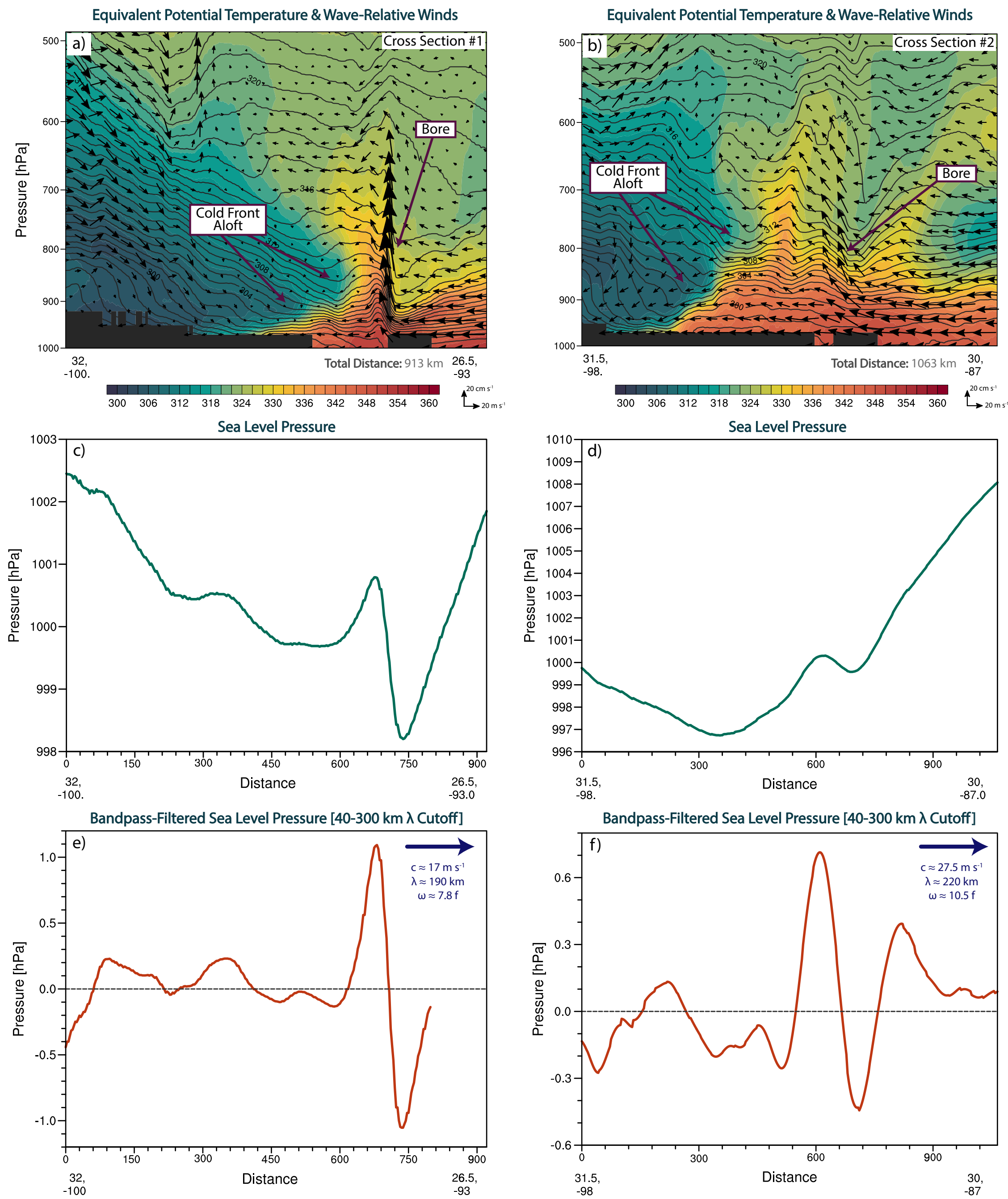

Figure 101: *Vertical cross-sections of equivalent potential temperature (shaded; K), potential temperature (contours; K), and wave-relative winds (vectors) at 1300 UTC 27 April from the 0000 UTC initialization of the HRRRx are shown in panels (a) and (b). Sea level pressure and corresponding bandpass-filtered sea level pressure along the cross-sections are shown in panels (c),(d) and (e),(f), respectively. Both cross-section paths are depicted in Fig. 100b.*

prominent by 27/1000Z and continued to amplify with time as the subsiding postfrontal airstream plowed forward into the moist air mass. By 27/1300Z, the disturbance appeared to take on the character of a mesoscale solitary wave of elevation that was preceded by a wave of depression (e.g., Christie et al., 1978; Rottman and Einaudi, 1993), with a combined wavelength of approximately 190 km and a propagation speed of 17 m s^{-1} (Figs. 100c,e)—in good agreement with the 18 m s^{-1} observed propagation speed noted by Lutzak (2013). Based on the θ_e contours alone, the intense updraft accompanying the wave of elevation appeared capable of lofting air situated near the top of the inversion layer by as much as 200 hPa. However, no deep convection developed along the Gulf Coast in association with this disturbance.

In contrast, Cross Section #2 extended east-southeastward from near Abilene, TX, to just off the Gulf Coast near Pensacola, FL, and intersected the cyclonic wind shift band over Louisiana, where it was much more subtle. This cross section also provided clear evidence of a CFA, which had overrun the moist layer over eastern Texas and western Louisiana and was immediately preceded by a band of increased midlevel θ_e values that was located within a broader mesoscale dome of deepened moisture (Fig. 100b). At the leading edge of this dome was a region of enhanced low-level convergence topped by a deep layer of mesoscale ascent, which promoted a sustained rise in the height of an elevated inversion layer and was situated roughly 100 km ahead of the CFA. Compared to Cross Section #1, the prefrontal moist layer was deeper over Louisiana and topped by a weaker inversion. However, the disturbance in this region also resembled a bore, which developed within the elevated inversion and led to a sustained expansion of the underlying moist layer ahead of the CFA. In both cross sections, the bore-relative winds within the moist layer notably decreased upon traversing the bore, while the bore-relative flow aloft increased—consistent with the flow response described by Klemp et al. (1997).

Comparison between the HRRRx and GFS ensemble. Unfortunately, the influence of this disturbance on the environmental conditions over the Southeast prior to the afternoon

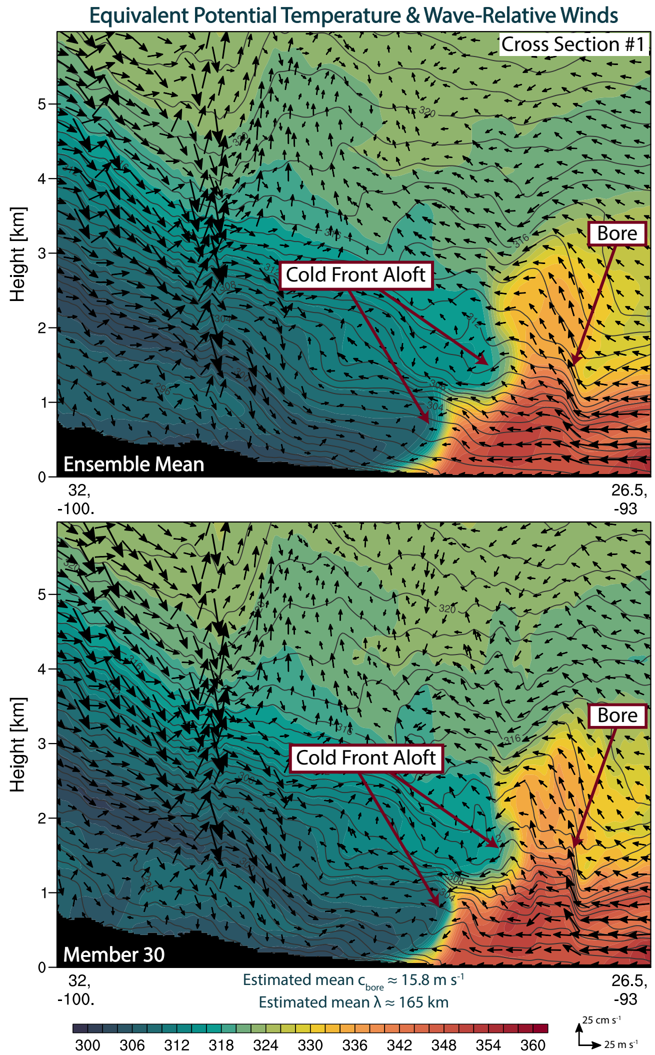

Figure 102: *As in Fig. 101a, but for (top) the GFS ensemble mean and (bottom) Member 30 at 1300 UTC 27 April 2011. The contours in these figures represent virtual potential temperature (K) in lieu of potential temperature. The cross section path is shown in Fig. 103.*

supercell outbreak cannot be fully ascertained using the HRRRx as the forecast terminated at 27/1500Z. Thus, all subsequent analysis of this disturbance over the Southeast will rely upon the GFS ensemble. However, before we begin this discussion, we first compare the structure of the bore over the Gulf of Mexico in Cross Section #1 from the HRRRx to that represented by the GFS ensemble mean and Member 30 at 27/1300Z. As can be seen in Fig. 102, the GFS ensemble produced a bore ahead of the CFA in a similar manner to that depicted by the HRRRx, but differences were evident in the structure of the disturbance.

Specifically, the bore in the GFS ensemble had a lower amplitude and exhibited a slower propagation speed, whereas the disturbance in the HRRRx developed more of a solitary wave structure. Furthermore, the distance between the CFA and leading edge of the bore was greater in the GFS ensemble such that the bore left a broader region of deepened moisture (~90 km) in its wake. These differences were likely due to both differences in mechanical forcing by the CFA and differences in the prefrontal environmental conditions—i.e., the Froude number within the stable moist layer, defined as

$$\mathrm{Fr} = \frac{U_{env} - C_{front}}{\sqrt{g \frac{\Delta\theta_v}{\overline{\theta_v}} h_0}}, \tag{6.2}$$

where $U_{env} - C_{front}$ represents the front-relative flow within the stable layer, $\Delta\theta_v$ is the change in virtual potential temperature with height over the stable layer, $\overline{\theta_v}$ is the mean virtual potential temperature within the stable layer, and h_0 is the depth of the stable layer (e.g., Koch et al., 1991). Notably, the inversion ahead of the bore was both stronger and somewhat shallower in the HRRRx, which—in addition to its higher amplitude—would support its faster propagation speed (e.g., Baines, 1984; Rottman and Simpson, 1989; Klemp et al., 1997). Despite the faster propagation speed in the HRRRx, we note that the bore was actually located farther to the southeast along the cross section in the GFS ensemble. This apparent discrepancy resulted from differences in the motion of the front, which was faster in the GFS ensemble and led to the front encountering the moist layer approximately 1 h earlier. However, an amplifying bore formed sooner in the HRRRx—presumably due to differences in the Froude number resulting from both the more favorable environmental conditions and the slower front motion, which would make it easier for the flow ahead of the front to become subcritical. Additionally, the structure of the bore and CFA were remarkably similar between the GFS ensemble mean and Member 30, with a slightly smoother disturbance evident in the ensemble mean. This suggests that the individual members consistently produced this disturbance ahead of the CFA over South Texas such that its formation and evolution were highly predictable. Due to this consistency, we will use the GFS ensemble mean in all subsequent analyses of the bore for simplicity.

Formation of the CFA and prefrontal bore. We now describe the formation of the CFA and prefrontal bore in the GFS ensemble. In the previous section, we conjectured that the low-level momentum surge that developed over West Texas and flowed downslope off the Edwards Plateau in advance of the Pacific cold front contributed to the development of the bore in this region. To explore this possibility, Figs. 103 and 104 show wind speed and virtual potential temperature advection every 3 h between 27/0200Z–27/1100Z at 500 m and 1000 m AGL, respectively. These fields further support the existence of the West Texas momentum surge, which can be seen comprising 50–70-kt wind speeds as it rapidly advanced southeastward along the Rio Grande and downslope during the nighttime. Furthermore, CAA was occurring within this momentum surge although it was located ahead of the main Pacific cold front and characterized by overall higher θ_v values (~310–314 K), yielding the arrival of low-level CAA along the Texas Gulf Coast by 27/0800Z (Figs. 103f and 104f). By 27/1100Z, the leading edges of CAA attending the momentum surge and main Pacific cold front were largely indistinct over eastern Texas at the two heights shown herein such that we have labeled this boundary as the Pacific cold front for simplicity. However, the characteristically higher θ_v values within the preceding momentum surge increases the likelihood that it was able to ascend atop the moist layer such that elevated CAA had moved farther into the warm sector than was apparent at or below 1000 m.

The temporal evolution of fields along Cross Section #1 is shown from 27/0500Z–27/1100Z in Fig. 105; recall that the fields at 27/1300Z were previously displayed in Fig. 102. At 27/0500Z, the cross section intersected the Pacific cold front, which was rapidly advancing downslope over the southern Texas Panhandle and was preceded by a strong frontal updraft, and the dryline, which marked the leading edge of a ≤1 km deep moist layer that was topped by a strong capping inversion (Fig. 105a). Moreover, this cross

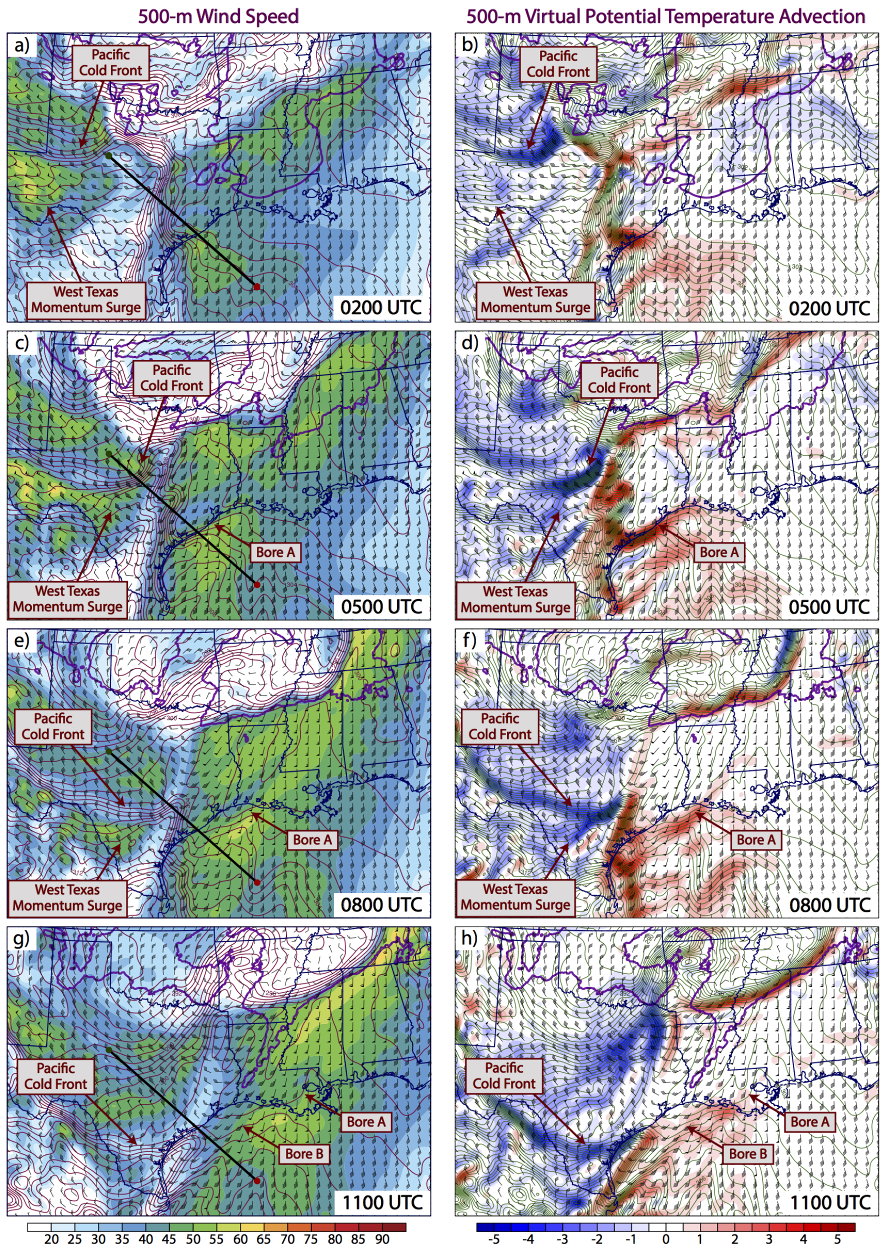

Figure 103: *GFS ensemble mean depiction of (left) 500-m horizontal wind speed (shaded; kt), 500-m virtual potential temperature (magenta contours; every 1 K), 500-m horizontal winds (barbs; kt), and simulated composite reflectivity = 0 dBZ (purple contours), and (right) 500-m virtual potential temperature advection (shaded; K h^{-1}), 500-m virtual potential temperature (green contours; every 0.5 K), 500-m horizontal winds (barbs; kt), and simulated composite reflectivity = 0 dBZ (purple contours) for (a),(b) 0200 UTC, (c),(d) 0500 UTC, (e),(f) 0800 UTC, and (g),(h) 1100 UTC 27 April 2011. All environmental fields were low-pass filtered with a cutoff wavelength of 100 km. The path for Cross Section #1 is shown in the left column.*

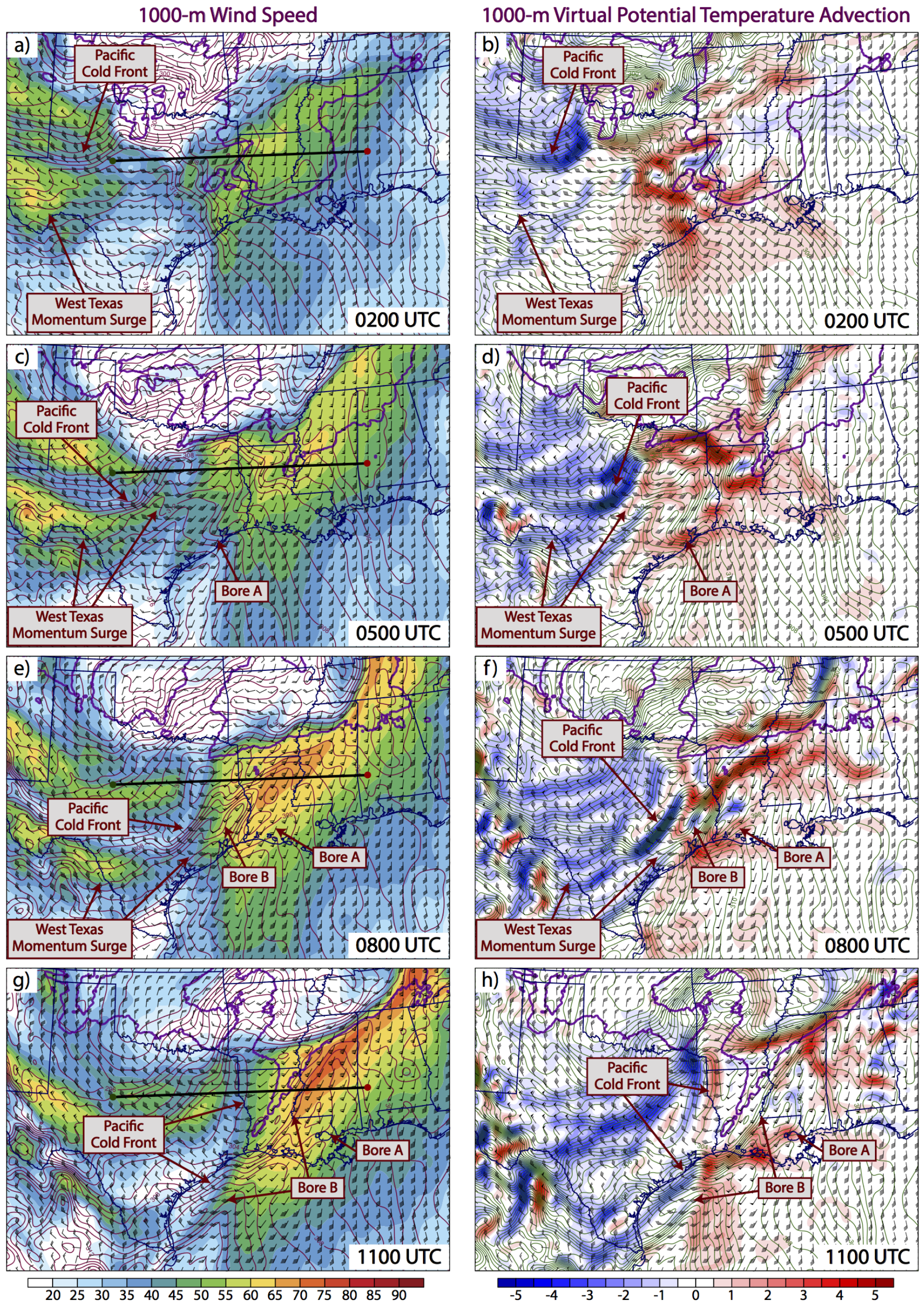

Figure 104: *As in Fig. 103, but for 1000 m. The path for Cross Section #3 is shown in the left column.*

section extended through a portion of the West Texas momentum surge, which had already encountered the dryline and had begun to advance atop the moist layer by this time (Fig. 105b). The leading edge of the momentum surge was identifiable as a region of enhanced 1-h potential temperature decrease (i.e., 1–2 K) that preceded an elevated nose of increased

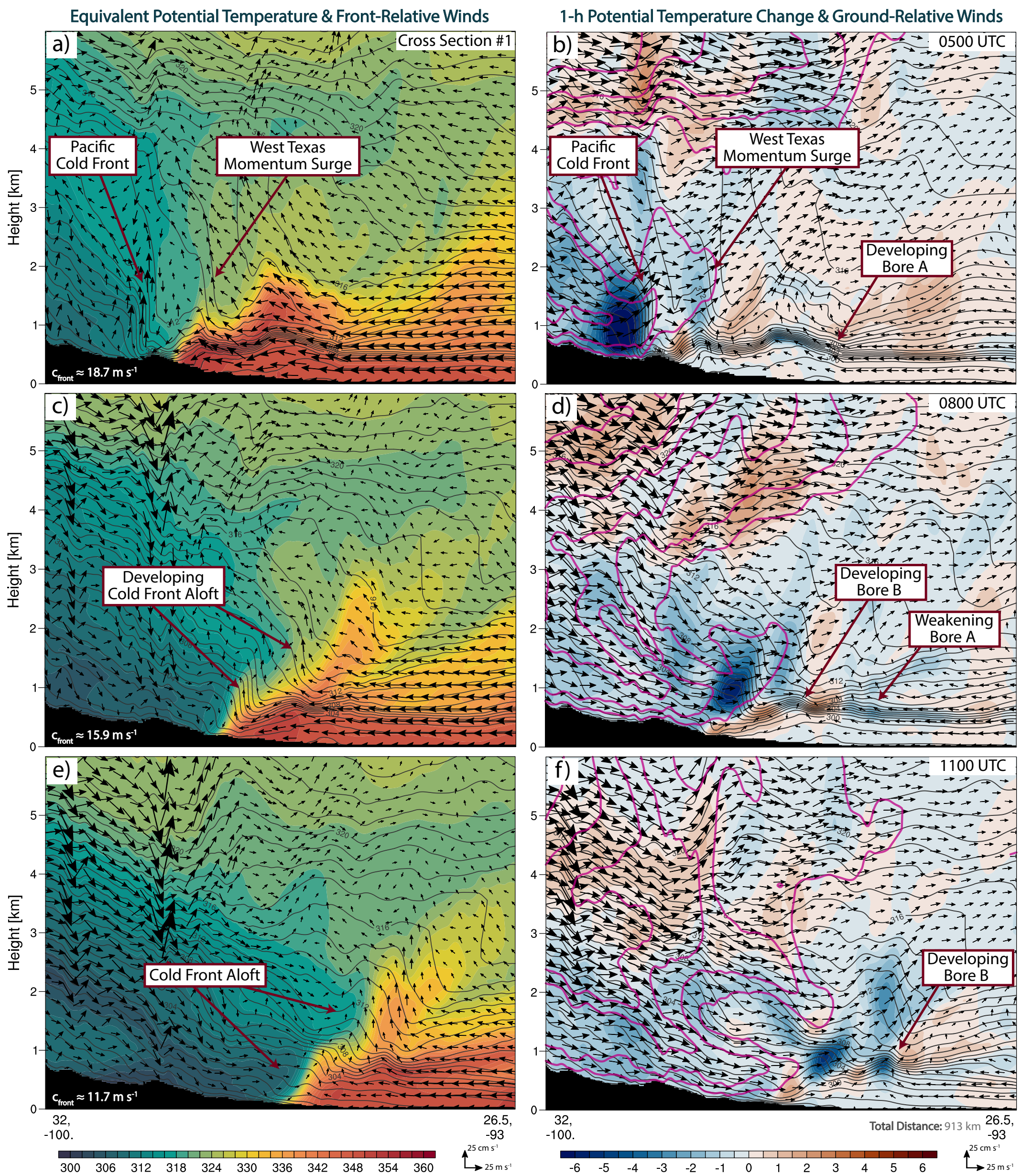

Figure 105: *Vertical cross sections along Cross Section Path #1 of (left) equivalent potential temperature (shaded; K), virtual potential temperature (gray contours; K), and front-relative winds (vectors) and (right) 1-h potential temperature change (shaded; K), potential temperature (gray contours; K), ground-relative winds in the cross-section plane (vectors), and horizontal wind speed in the cross-section plane (magenta contours; every 5 m s*$^{-1}$ $\geq$ *15 m s*$^{-1}$*, where positive values are defined as winds moving from left to right) from the GFS ensemble mean at (a),(b) 0500 UTC, (c),(d) 0800 UTC, and (e),(f) 1100 UTC 27 April 2011.*

wind speeds ($\geq$ 15 m s^{-1} in the cross-section plane). Farther toward the northwest, the main Pacific cold front had produced 1-h θ decreases in excess of 6 K h^{-1} and was followed by a 1–2-km deep layer wherein cross-section relative wind speeds > 20 m s^{-1}—greater than the estimated frontal motion and suggestive of a density current character (e.g., Smith and Reeder, 1988; Simpson, 1997; Koch and Clark, 1999). Although the main Pacific cold front remained upstream from the moist layer, a mesoscale disturbance was evident within the inversion layer along the Texas Gulf Coast and had the character of a developing bore. This bore also formed over the region in the HRRRx forecasts and was distinct from and eventually overtaken by the high-amplitude disturbance described previously at 27/1300Z (not shown). We will henceforth distinguish the bores apparent at 27/0500Z and 27/1300Z by labeling them "Bore A" and "Bore B", respectively. The signatures associated with these two disturbances were tracked through time and annotated on the figures herein, although we note that their structures varied spatially and evolved such that they did not always exhibit clear properties of a bore.

The Pacific cold front had merged with the dryline by 27/0800Z, yielding a region of upward motion and lofted moisture just ahead of the surface front, which was preceded by a CFA with a low-θ_e nose centered between 1–2.5 km MSL (Figs. 105c-d). The subsiding postfrontal air mass continued to advance southeastward along the cross-section as the low-level moist layer was gradually displaced. By 27/1100Z, a dual-nose structure to the CFA had become evident, with a lower branch that was sustained by strong downslope flow of notably low-θ_e air and existed largely in the same layer as the prefrontal moist layer, and an upper branch that comprised actively subsiding air that protruded more than 150 km ahead of the low-level cold front at ~1–2.5 km MSL and interacted primarily with the top portion of the moist layer (Figs. 105e-f). A coherent region of 1-h cooling was evident within the capping inversion ahead of the upper branch at this time and signified the developing prefrontal Bore B that became prominent by 27/1300Z in Fig. 102; meanwhile, this disturbance was preceded by a region of cooling within the inversion layer at 27/0800Z that was associated with Bore A, which appeared to be weakening overall along this cross section as it moved into southern Louisiana. The dual-branch CFA structure was well-established at this time, and these two branches collectively acted to push downward and forward into the stable moist layer as they continuously descended along the terrain slope and within the DCB over South Texas.

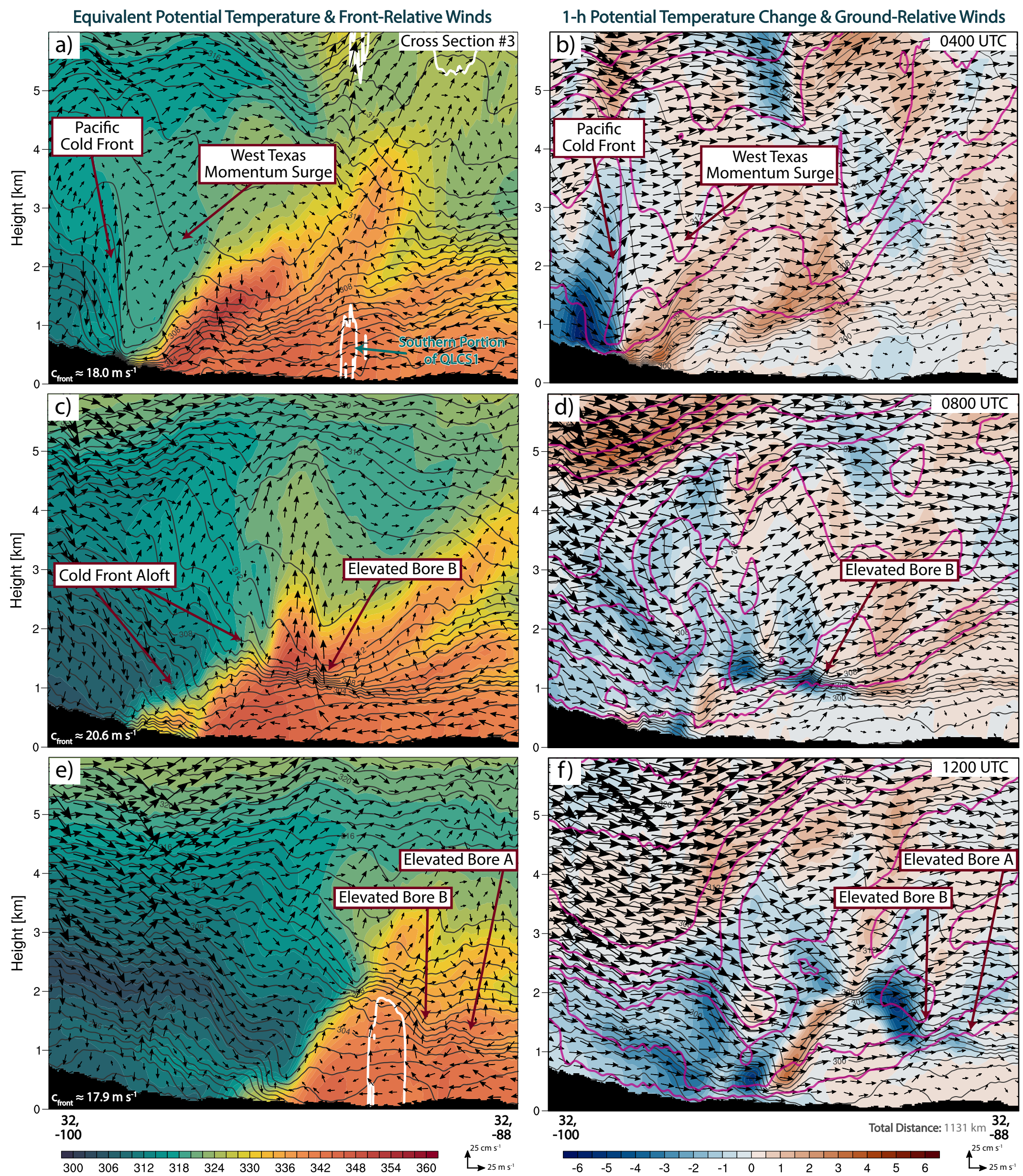

Figure 106: *As in Fig. 105 but for Cross Section Path #3 at (a),(b) 0400 UTC, (c),(d) 0800 UTC, and (e),(f) 1200 UTC 27 April 2011. The white contours in the left column represent ensemble mean composite reflectivity = 0 dBZ. The cross section path is shown in Fig. 104.*

The movement of the CFA into the Southeast and the development of the elevated bore apparent in Cross Section #2 from the HRRRx are now investigated using the GFS ensemble. We opted to use a slightly different cross section for this analysis as we wanted to fully capture the evolution of the Pacific cold front as it moved eastward over Texas and influenced the environment over the Southeast prior to the supercell outbreak. This path of this cross section—hereafter Cross Section # 3—is displayed in Fig. 104, and the leftmost point is the same as in Cross Section #1. Figure 106 depicts the evolution of fields along this cross section between 27/0400Z–27/1200Z. At 27/0400Z, the Pacific cold front was evident at the leading edge of a region of pronounced 1-h cooling that was rapidly moving downslope into north-central Texas and was accompanied by a distinct thermally direct frontal circulation (Figs. 106a-b). Relatively low-θ_e air from within the West Texas momentum surge can also be seen preceding the Pacific cold front and had begun to move atop the low-level moist layer by this time. Compared to Cross Section #1, the moist layer was noticeably deeper over this region and was topped by a weaker inversion. However, mesoscale subsidence and midlevel warming were occurring over eastern Texas and Louisiana behind QLCS1 and had acted to notably strengthen the capping inversion over the region by 27/0800Z (Figs. 106c-d).

A CFA had begun to develop along the cross section by 27/0600Z and had moved into eastern Texas by 27/0800Z, promoting strong low-level convergence, mesoscale ascent, and a net deepening of the prefrontal moist layer that extended *more than 150 km ahead of the front itself.* The isentropes near the top of the moist layer progressively steepened as the CFA advanced into the Southeast, ultimately yielding an abrupt jump in the isentropic surfaces that produced rapid adiabatic cooling and thus substantial weakening of the capping inversion and preceded a mesoscale dome of permanently deepened moisture—what we will term the "mesoscale moisture dome" (Figs. 106e-f). The passage of this jump—which we have deemed to be an elevated bore (i.e., Bore B) as it resided within the capping inversion, produced an abrupt and persistent increase in the height of the isentropes, and led to a sustained adjustment of the winds within the underlying deepened moist layer—promoted a 1-h increase in simulated sea level pressure > 1 hPa at locations along this cross section between 27/1100Z–27/1200Z (not shown). The resultant dome of lifted air behind the elevated bore and ahead of the CFA corresponded to the mesoscale pressure dome that was observed by the ASOS and USArray sites over the Southeast and described in the previous section. Furthermore, a mesoscale cloud band (evidenced by the 0 dBZ simulated reflectivity contour on Fig. 106e) had formed within the moisture dome by 27/1200Z and corresponded to the warm sector reflectivity bands annotated on Figs. 62a,c in Chapter 5. A second disturbance was also evident in the capping inversion ahead of Bore B at 27/1200Z and was related to Bore A, which had moved into Mississippi by this time.

It is worth emphasizing is that the bore generation in this case does not appear to be readily explainable by the classic development of partially blocked flow that results from the intrusion of a surface-based density current into a low-level stable layer (e.g., Rottman and Simpson, 1989), which has been studied extensively within the context of cold fronts (e.g., Koch and Clark, 1999; Hartung et al., 2010), thunderstorm outflow boundaries (e.g., Koch et al., 1991, 2008a,b; Chasteen et al., 2019; Grasmick et al., 2018; Haghi et al., 2019), and other mesoscale baroclinic zones (e.g., Clarke et al., 1981; Goler and Reeder, 2004). Perhaps the CFA behaves as an intrusive density current (or intrusion; e.g., Ungarish, 2009; Bluestein et al., 2017; Hitchcock and Schumacher, 2020); or the sheer depth of the descending postfrontal air mass leads to complete blocking of the flow as it encounters the moist layer (e.g., Houghton and Kasahara, 1968; Rottman and Simpson, 1989); or the scenario evolves similarly to a dam-break, wherein a deep layer of relatively dense fluid is released into a channel containing a shallower layer of comparably dense fluid (e.g., Klemp et al., 1997). *In any case, the bore—specifically Bore B—undoubtedly stemmed from a high-amplitude disturbance to the prefrontal moist layer that was produced by the CFA.*

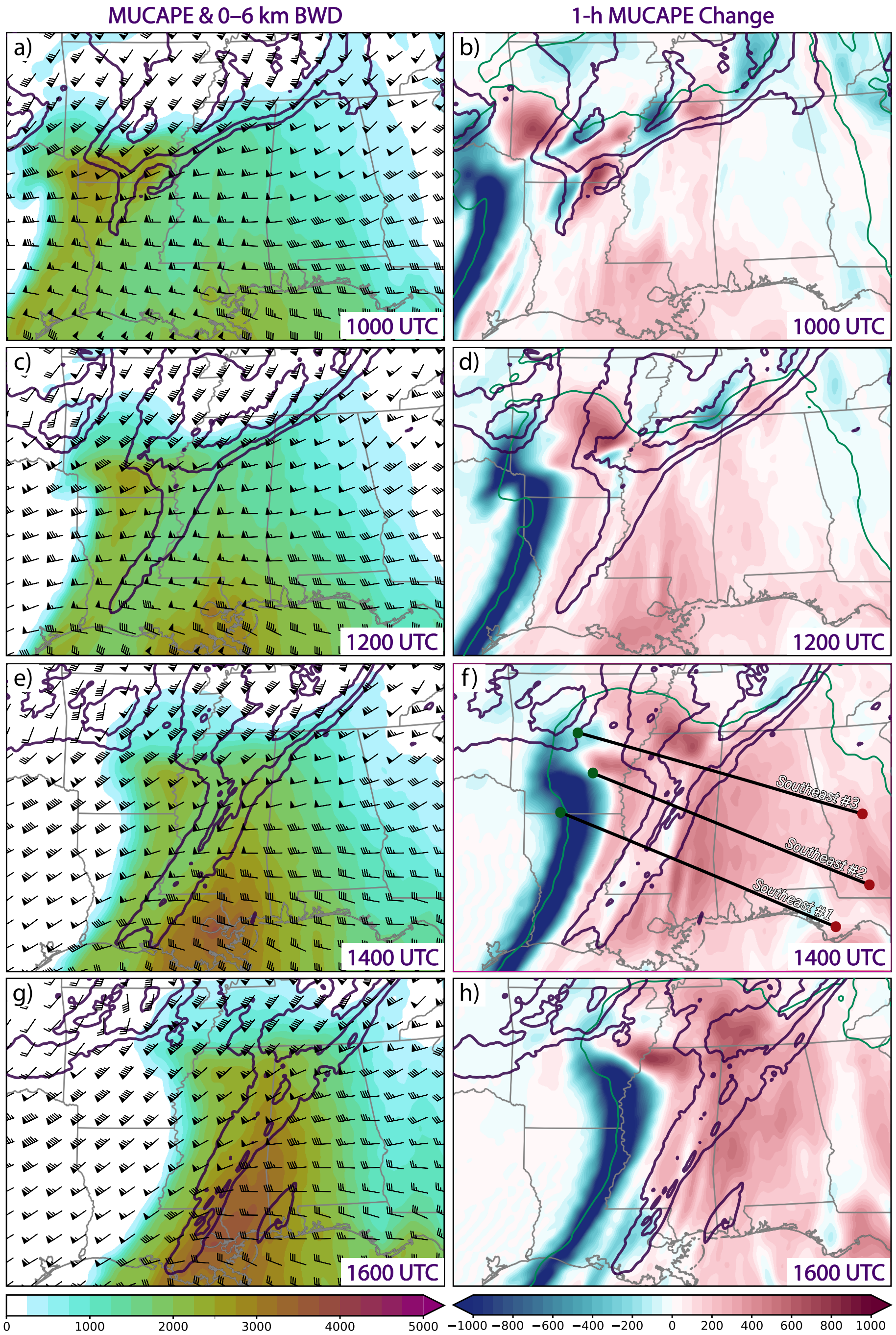

Figure 107: *Depiction of (left) MUCAPE (shaded; J kg^{-1}) and (right) 1-h MUCAPE change (shaded; J kg^{-1}) from the GFS ensemble mean valid at (a),(b) 1000 UTC, (c),(d) 1200 UTC, (e),(f) 1400 UTC, and (g),(h) 1600 UTC 27 April 2011. The 0–6-km BWD (barbs; kt) is overlaid in the left column, and simulated mean reflectivity (purple contours; every 20 dBZ ≥ 0 dBZ) and MUCAPE = 250 J kg^{-1} (green contour) are shown on all panels. Environmental fields were low pass filtered with a 40 km cutoff wavelength.*

6.3 Mesoscale destabilization over the Southeast

In this section, we investigate the processes that led to mesoscale destabilization over the Southeast prior to the afternoon supercell outbreak, which began with CI occurring at ~27/1700Z in the GFS ensemble members. In particular, we describe how the thermodynamic environment within the ensemble was modified by the passage of the prefrontal bores and how this related to the complex evolution of the low-level cloud field described in Section 6.2.1 and the formation of the MAUL and MAUL* that were apparent in the operational soundings released from Slidell, LA, and Birmingham, AL, respectively, just after 27/1730Z (see Fig. 33 in Chapter 3.3.3).

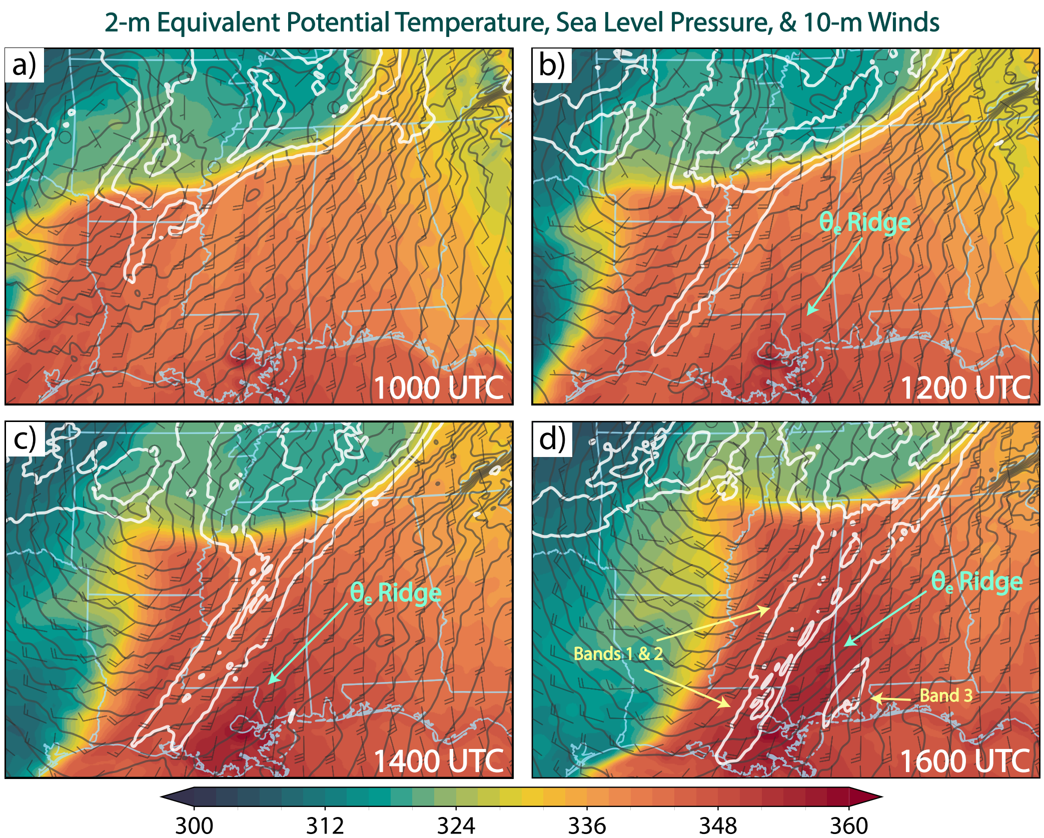

Figure 108: *Surface equivalent potential temperature (shaded; K), sea level pressure (gray contours; every 1 hPa), and 10-m winds (barbs; kt) at (a) 1000 UTC, (b) 1200 UTC, (c) 1400 UTC, and (d) 1600 UTC 27 April 2011. Environmental fields were low-pass filtered with a 40 km cutoff wavelength.*

Evolution of CAPE and CIN over the Southeast. We begin by describing how the MUCAPE and MUCIN fields (which were generally analogous to MLCAPE and MLCIN throughout the warm sector; see the footnote in Chapter 4.5.4 about how these fields were computed by wrf_python) evolved throughout the mesoscale environment during the period leading up to the supercell outbreak. Figure 107 depicts MUCAPE and its corresponding 1-h tendency field over the Southeast from 27/1000Z–27/1600Z. At 27/1000Z, MUCAPE values > 1000 J kg^{-1} extended throughout the warm sector from eastern Texas into central Alabama and were greatest (> 2000 J kg^{-1}) to the west of the mesoscale cloud band that could be seen developing over Louisiana to the south of QLCS2 (Fig. 107a). A secondary region of enhanced MUCAPE values (> 1500 J kg^{-1}) extended from southern Louisiana into southern Alabama and coincided with 1-h MUCAPE increases of ~100–300 J kg^{-1} (Fig. 107b). By 27/1200Z, MUCAPE > 1500 J kg^{-1} was evident throughout much of Mississippi, while values in excess of 2000 J kg^{-1} had developed over southeastern Louisiana and much of southern Mississippi (Fig. 107c). Such values were supported by appreciable MUCAPE increases (i.e., +200–450 J kg^{-1} between 27/1100Z–27/1200Z), with 1-h MUCAPE changes > 100 J kg^{-1} extending eastward into central Alabama (Fig. 107d). The MUCAPE increases that occurred during this period were largely due to increases in near-surface θ_e values (cf. Figs. 107a-d and 108a-b), which occurred prior to any appreciable influence from insolation (sunrise over the region occurred between ~27/1100Z–27/1130Z) and thus resulted predominantly from strong low-level advection. Note that the low-level thermodynamic environment over the Southeast in the GFS ensemble differed considerably from the observed environment owing to the previously described errors in the southern extent of QLCS1, which resulted in the absence of a cold pool over most of Mississippi and Alabama (evidenced by the lower 2-m potential temperature values present in the RUC analysis at 27/1200Z in Fig. 17e) and thus reduced low-level stability over a much more expansive warm sector.

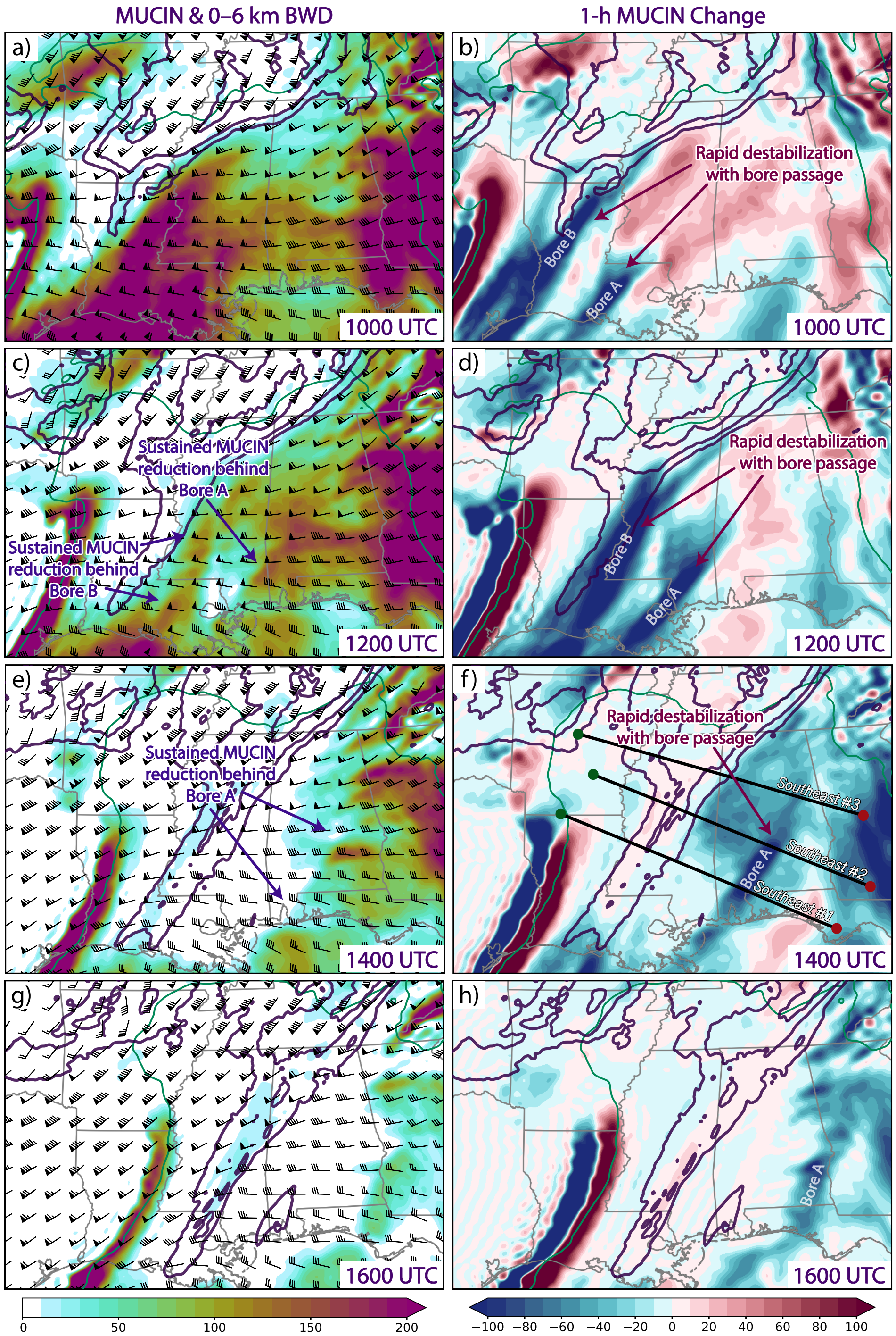

Figure 109: *As in Fig. 107, but for (left) MUCIN (shaded; J kg^{-1}) and (right) 1-h MUCIN change (shaded; J kg^{-1}). Note that the MUCIN values here are specified as positive (i.e., the magnitude of MUCIN) such that a positive change in MUCIN corresponds to increased inhibition and vice versa.*

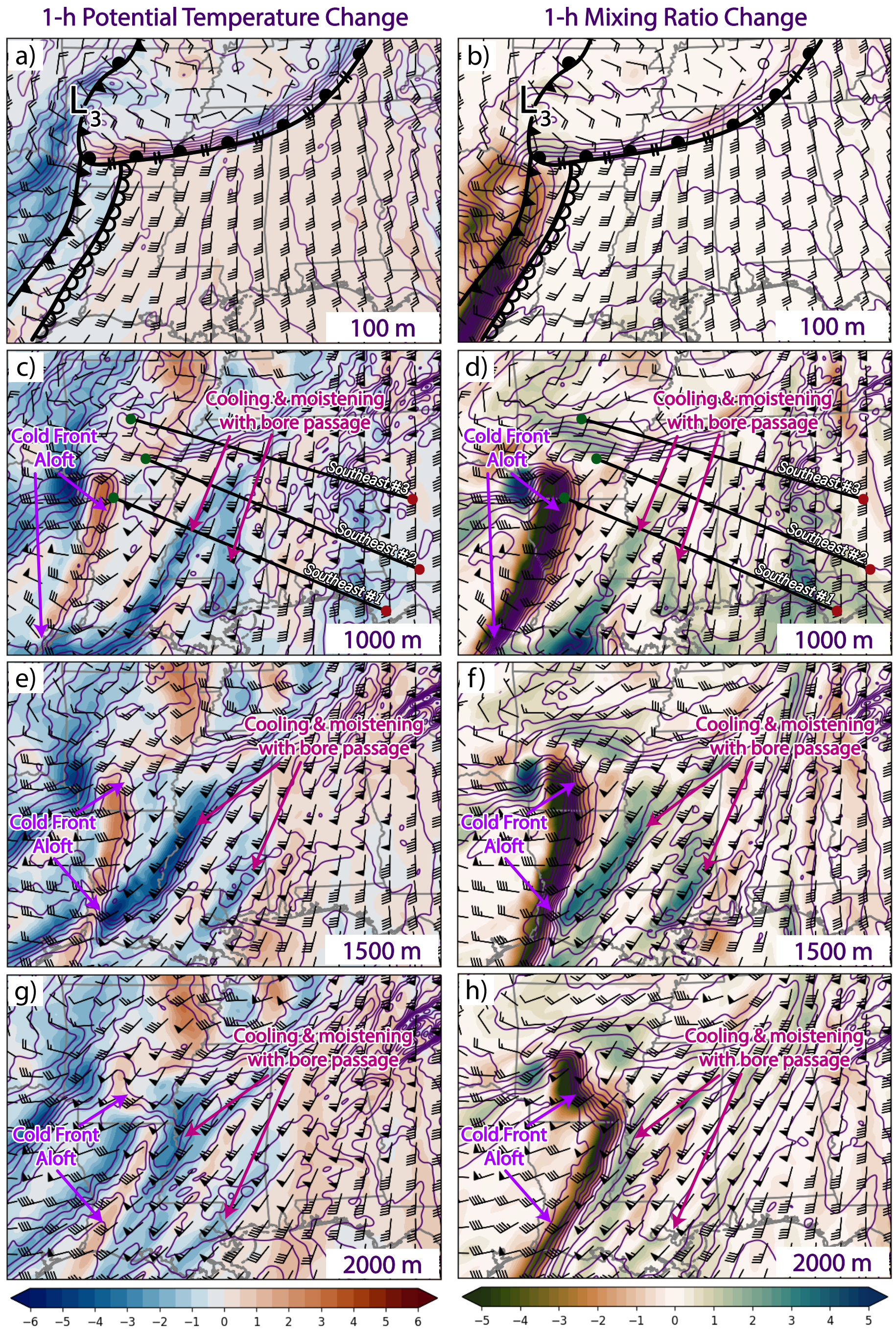

Figure 110: *Depiction of (left) 1-h potential temperature change (shaded; K), potential temperature (purple contours; every 1 K), and horizontal winds (barbs; kt) and (right) 1-h mixing ratio change (shaded; g kg^{-1}), mixing ratio (purple contours; g kg^{-1}), and horizontal winds (barbs; kt) at approximately (a),(b) 100 m, (c),(d) 1000 m, (e),(f) 1500 m, and (g),(h) 2000 m AGL from the GFS ensemble mean valid at 1200 UTC 27 April 2011. Fields were low-pass filtered with a 40 km cutoff wavelength.*

In contrast, the MUCIN and 1-h MUCIN change fields during the 27/1000Z–27/1200Z period exhibited much greater mesoscale variability and were poorly reflected by the near-surface θ_e distribution (Figs. 109a-d). At 27/1000Z, the environment ahead of the developing mesoscale cloud band over eastern Louisiana and western Mississippi was characterized by widespread MUCIN magnitudes > 200 J kg^{-1} (Fig. 109a) owing to the presence of a strong capping inversion between ~900–800 hPa (not shown). This capped environment was trailed to the west by a wedge-shaped region of considerably reduced MUCIN, with magnitudes < 20 J kg^{-1} located throughout northwestern Louisiana in the vicinity of the developing mesoscale cloud band. The sharp MUCIN gradient that extended throughout central Louisiana at the leading edge of this wedge-shaped region coincided with a distinct band comprising 1-h MUCIN decreases > 100 J kg^{-1} and was associated with Bore B (Fig. 109b). A secondary band of appreciable 1-h MUCIN decreases preceded Bore B and was related to the passage of Bore A over southeastern Louisiana. By 27/1200Z, both of these disturbances had moved eastward and promoted persistent reductions in MUCIN in their wakes (Figs. 109c-d). In particular, the movement of Bore A over southern Mississippi and southeastern Louisiana had promoted sustained lifting that weakened the overlying capping inversion (due to adiabatic cooling aloft) and deepened the low-level moist layer (through the upward transport of moisture). This effect—which was reflected in the 1-h potential temperature and mixing ratio change fields at various heights AGL in Fig. 110—acted in tandem with the near-surface θ_e increases from advection to support net destabilization over much of Mississippi and southeastern Louisiana. Bore A was then followed by the passage of Bore B, which promoted further cooling aloft and deepening of the moist layer to yield minimal MUCIN values in the vicinity of the mesoscale cloud band. *Thus, the two bores were responsible for producing rapid mesoscale destabilization over the warm sector ahead of the CFA, which was situated to the rear of the mesoscale cloud band.*

This notable destabilization effect produced by the two bores over the Southeast largely occurred prior to any appreciable destabilizing influence from surface heating (e.g., the

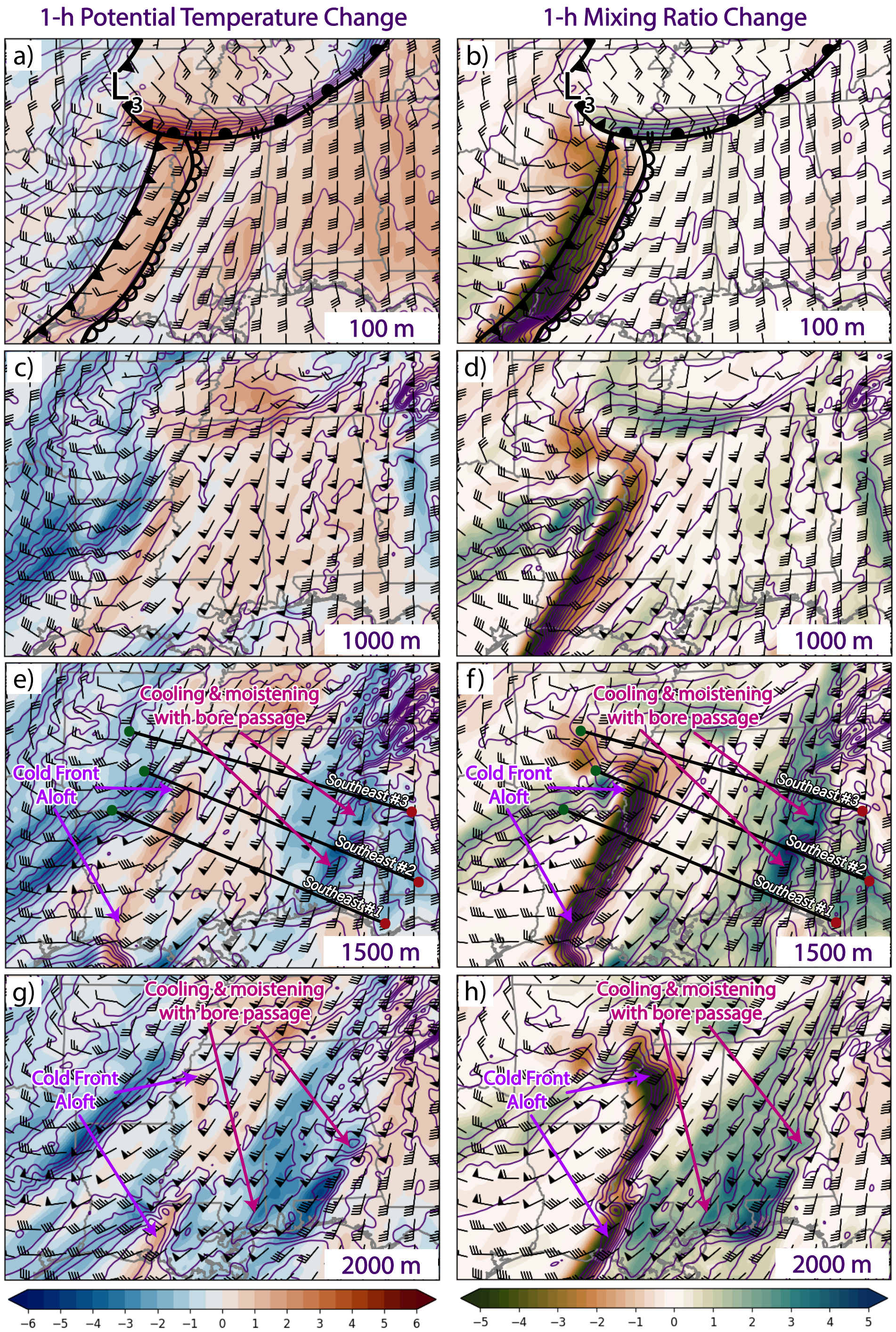

Figure 111: *As in Fig. 110 but for 1500 UTC 27 April 2011.*

1-h θ change between 27/1100Z–27/1200Z at 100 m AGL was < 0.5 K throughout the region; Fig. 110a). Consequently, the near-surface θ_e increases that subsequently resulted from surface heating further increased MUCAPE values during the daytime while further diminishing any MUCIN that remained in the wake of the two bores. By 27/1400Z, MUCAPE values > 1500 J kg^{-1} extended into central Alabama where 1-h MUCAPE increases were ~200–300 J kg^{-1} (Figs. 107e,f), while a region characterized by MUCAPE = 2000–3500 J kg^{-1} and 1-h MUCAPE increases of ~350–550 J kg^{-1} was collocated with a strengthening surface θ_e ridge ahead of the mesoscale cloud band over eastern Mississippi and southeastern Louisiana (Fig. 108c). MUCAPE values > 2000 J kg^{-1} extended as far north as the Alabama-Tennessee border ahead of the mesoscale cloud band by 27/1600Z (Figs. 107g,h), while MUCAPE > 3000 J kg^{-1} spanned from the Louisiana coast into western Alabama within a corridor of limited cloud cover—and thus enhanced near-surface θ_e values (Fig. 108d)—that was situated between the mesoscale cloud band and Band 3 (see Fig. **??** in Chapter 5). The 100-m potential temperature and 1-h potential temperature change fields shown at 27/1500Z in Fig. 111a suggest that this expanding low-level θ_e ridge and accompanying region of maximum MUCAPE likely resulted from a combination of large-scale confluence, differential surface heating, and an inland trajectory over Louisiana that maximized fetch over land and thus favored enhanced sensible heating due to the unique coastal geometry of this region.

Meanwhile, MUCIN values throughout the Southeast continued to decrease abruptly in response to adiabatic cooling within the lower- to mid-troposphere that accompanied the passage of the bores, thus enabling any remaining MUCIN to become almost entirely eroded after just a couple hours of surface heating. Specifically, MUCIN values within the environment ahead of the mesoscale cloud band had already decreased to < 10 J kg^{-1} by 27/1400Z, and this region of diminished MUCIN continued to spread eastward through Alabama during the morning behind Bore A (Figs. 109e-h). The 1-h potential temperature and mixing ratio change fields from 27/1400Z–27/1500Z are depicted in Fig. 111 and indicate that elevated cooling and moistening had developed over a broad region behind Bore A and ahead of the mesoscale cloud band. *This signature—which was most pronounced between ~1.5–2.5 km AGL—reflected the net destabilization and sustained deepening of* *the low-level moist layer that occurred throughout the mesoscale environment ahead of the CFA prior to the afternoon supercell outbreak.*

Further examination of mesoscale destabilization and MAUL formation over the warm sector. The environmental modifications that arose over the Southeast in association with the two bores—specifically their significance for rapidly destabilizing the mesoscale environment and for the development of a deep MAUL over the warm sector—are now described further using vertical cross sections and model soundings from the GFS ensemble mean. Three approximately parallel cross sections that extended across the Southeast in a NW-SE orientation are discussed herein, the paths for which are overlaid on Figs. 107 and 109–111. The temporal evolution of thermodynamic fields along these paths, including vertical profiles of equivalent potential temperature and 1-h potential temperature change, is shown from 27/1300Z–27/1700Z for Southeast #1 and Southeast #2 (the two southernmost cross sections) and from 27/1500Z–27/1900Z for Southeast #3. Unlike on the cross sections presented earlier in this chapter, the white contours overlaid onto the θ_e fields in the cross sections described in this section (e.g., in Fig. 112) represent regions where relative humidity (RH) exceeded 90%, 92.5%, 95%, and 97.5%. Analyzed together with the vertical profile of θ_e—which indicates the presence of potential instability where $\frac{\partial \theta_e}{\partial z} < 0$—the RH distribution enables an assessment of regions that may exhibit the character of a MAUL (or MAUL*, if not entirely saturated) without explicitly examining the saturation equivalent potential temperature field (Bryan and Fritsch, 2000). In other words, regions where potential instability exists (i.e., essentially everywhere throughout the low-level moist layer on the cross sections presented in this section) may become statically unstable if they attain saturation.

The formation of MAULs has most traditionally been attributed to layer lifting and slablike ascent that occurs as potentially unstable air is forced upward by a convectively generated cold pool (e.g., Kain and Fritsch, 1998; Bryan and Fritsch, 2000; Bryan et al., 2007). Bryan et al. (2007) describe how MAULs can breakdown via convective overturning

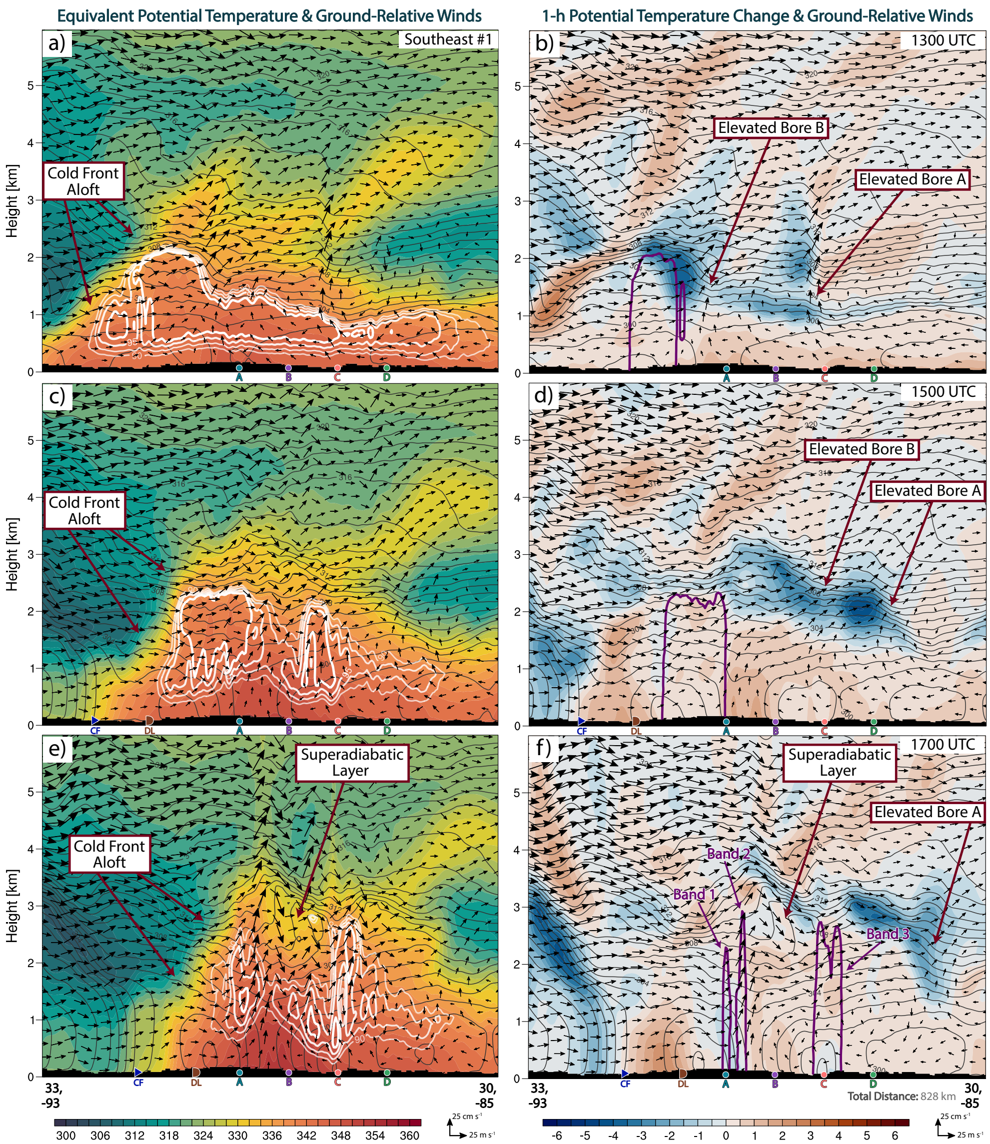

Figure 112: *Vertical cross sections along path Southeast #1 of (left) equivalent potential temperature (shaded; K), virtual potential temperature (gray contours; K), relative humidity (white contours; every 2.5% ≥ 90%), and ground-relative winds in the cross-section plane (vectors), and (right) 1-h potential temperature change (shaded; K), potential temperature (gray contours; K), composite reflectivity = 0 dBZ (purple contours), and ground-relative winds in the cross-section plane (vectors) from the GFS ensemble mean at (a),(b) 1300 UTC, (c),(d) 1500 UTC, and (e),(f) 1700 UTC 27 April 2011. The surface cold front and dryline locations are indicated by CF and DL, respectively. The locations of the soundings shown in Fig. 113 are denoted with the appropriate letters. Environmental fields in the right column were low-pass filtered with a cutoff wavelength of 40 km. The cross section path is shown in Fig. 109f.*

into quasi-horizontal rolls that are aligned with the shear vector in the unstable layer and are somewhat analogous to the HCRs that develop within the convective PBL. More recently, several studies have used both observations and numerical simulations to document elevated CI events that resulted from the formation of MAULs (e.g., Trier et al., 2017; Gebauer et al., 2018; Zhang et al., 2019). In these elevated CI cases, the MAULs developed in response to persistent mesoscale ascent and/or differential thermal and moisture advection. Because MAULs have been noted to lack any CIN by definition (e.g., Trier et al., 2017), the development of a MAUL in such cases is therefore presumed to be sufficient for CI. However, as we will show in this section, this assumption does not hold if the MAUL is topped by a strong midlevel inversion, which precludes (or at least delays) the formation of deep convection. *In other words, the convective overturning will be confined to the MAUL unless the resultant updrafts can penetrate through the overlying inversion layer.*

Figure 112 depicts how the mesoscale environment evolved along Southeast #1—which intercepted both the primary band of developing supercells over southern Mississippi (i.e., Bands 1 and 2 described in Chapter 5) and the preceding band of attempted CI in southern Alabama (i.e., Band 3 described in Chapter 5)—during the period leading up to CI at ~27/1700Z. At 27/1300Z, the CFA was evident within the northwestern portion of the cross section and overlaid a sloping layer of high-θ_e air that signified the low-level moist layer and became progressively shallower farther behind the front (Figs. 112a,b). The CFA was immediately preceded by the mesoscale moisture dome, wherein potential instability coincided with RH values $\geq$ 97% above the PBL and the mesoscale cloud band had developed, affirming that the layer had indeed reached saturation. Similar to Fig. 106 that was described in the previous section, the leading edge of the moisture dome was characterized by an abrupt jump in the isentropic surfaces that corresponded to appreciable adiabatic cooling in the lower to middle troposphere associated with the passage of Bore B. Furthermore, Bore A was apparent farther to the southeast ahead of Bore B, and its passage was also responsible for a net upward displacement in the height of the capping inversion and sustained deepening of the low-level moist layer. Therefore, the low-level moist layer and overlying inversion were initially lifted by the passage of Bore A, which produced a net destabilization effect through adiabatic cooling aloft and yielded a mesoscale region of deeper moisture with increased RH values (i.e., RH > 97%). Additional destabilization subsequently occurred with the passage of Bore B, which provided further cooling aloft, lifting of the capping inversion, and deepening of the underlying potentially unstable moist layer that was either saturated or nearly saturated.

The destabilization effects accompanying the passage of these mesoscale disturbances can also be gleaned from spatial variations in the model soundings shown in Fig. 113, wherein the 27/1300Z profiles at four locations along the cross section path are depicted by the lightest colors in each panel. At this time, Points C and D were situated ahead of both Bore A and Bore B and thus represented the environmental conditions before any significant destabilization had occurred. These soundings were characterized by a shallow moist PBL that was topped by a dual-inversion structure between ~925–750 hPa and accompanying warm, dry air. Consequently, both soundings exhibited large values of MUCIN that would have precluded the formation of convection absent any notable mesoscale ascent and destabilization. In contrast, Points A and B were both located behind Bore A but ahead of Bore B and exhibited deeper low-level moisture, relatively shallow saturated layers above ~900 hPa that had the character of MAULs, weaker overlying capping inversions, and reduced values of MUCIN. MUCAPE values were also greater at these two points compared to Points C and D.

Progressing through time to 27/1500Z, it is apparent that the low-level moist layer had deepened throughout the mesoscale environment ahead of the CFA (including ahead of Bore A), while the overlying inversion layer had been further lifted (Figs. 112c,d). Moreover, the PBL had deepened appreciably in response to surface heating, which had also increased values of near-surface θ_e and thus the degree of potential instability within the deepened moist layer (and throughout the troposphere in general). Presumably, the MAUL that had developed above the PBL at Points A and B by 27/1300Z would have persisted in the presence of sustained mesoscale forcing ahead of the CFA such that these near-surface θ_e increases would have invigorated the MAUL, yielding stronger convective overturning that further deepened the moist layer and weakened the overlying capping inversion. However, the broad region of low-level RH > 97% that was located behind Bore A at 27/1300Z had broken down into two primary bands in the ensemble mean by this time: one that remained situated immediately ahead of the CFA and coincided with the mesoscale cloud

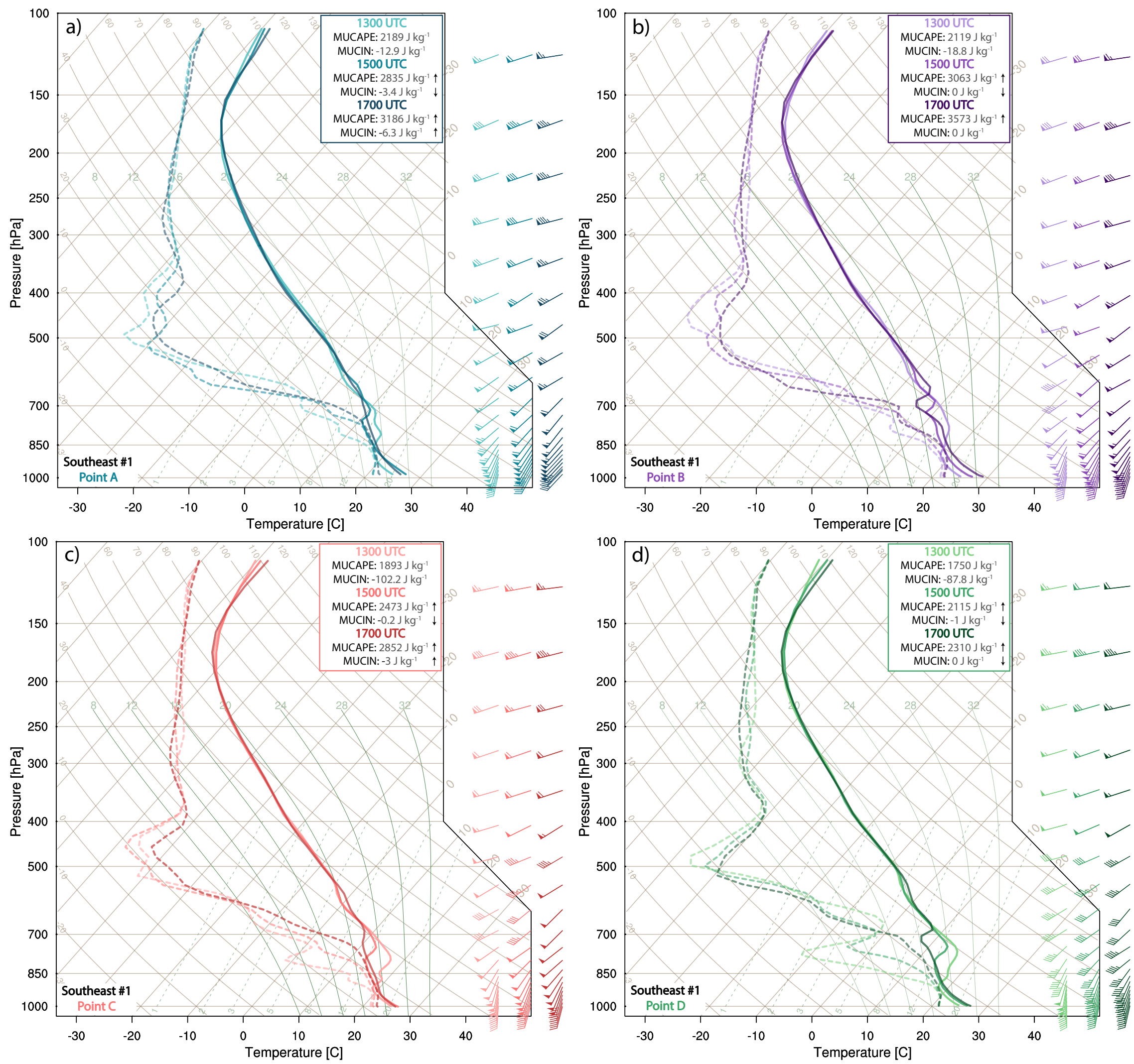

Figure 113: *Overlays of model soundings from four locations along Southeast #1 (labeled in Fig. 112) at (lightest colored lines) 1300 UTC, (medium colored lines) 1500 UTC, and (darkest colored lines) 1700 UTC 27 April 2011.*

band (which ultimately evolved into the reflectivity Bands 1 and 2), and a second that was located between Points B and C and was associated with Band 3. The character of the elevated bores had also changed during this 2-h period, although strong cooling signatures associated with these disturbances remained evident in the lower to middle troposphere throughout the destabilizing warm sector.

Conditions ahead of the CFA had become even more complex by 27/1700Z, with the two primary bands of enhanced RH values persisting but evolving into three distinct bands of simulated reflectivity that were located near Points A and C (Figs. 112e,f). The mesoscale corridor that separated Bands 1 and 2 from Band 3 coincided with the near-surface θ_e ridge, which was now topped by an elevated superadiabatic layer that had developed between ~2–3 km and comprised strong subsidence that depressed the depth of the low-level moist layer. Note that this elevated unstable layer was not a transient feature, and its persistence in the 50-member ensemble mean suggests that it developed due to processes that were consistently predicted by the individual members. Overall, its development ahead of Bands 1 and 2, the structure of the isentropes both within this layer and above it, and the strong vertical velocities that accompanied this disturbance lead us to hypothesize that it may have arisen due to processes analogous to a breaking mountain wave (e.g., Durran, 1990), wherein the "mountain" is really the obstacle that results from an updraft penetrating into a sheared and stratified layer aloft (e.g., Kuettner et al., 1987; O'Neill et al., 2021).

Additionally, the elevated cooling signature that accompanied the abrupt jump in the isentropes with Bore A remained coherent within the environment to the southeast of Band 3 at 27/1700Z and coincided with a θ_e gradient between ~1.5–3 km—signifying the leading edge of the deepened moist layer aloft—that had considerably sharpened over the previous 2 hours. Somewhat reminiscent of how Bore B initially formed ahead of the CFA several hours earlier, *we postulate that substantial lifting of the capped moist layer over a confined mesoscale region acted to tilt the isentropes and θ_e surfaces such that a high-amplitude discontinuity ultimately developed, yielding a disturbance that propagated through the* *warm sector as an elevated bore.* It was perhaps this mesoscale tilting and discontinuity effect that led to a prominent arc band emerging ahead of the leading cloud band during the late morning (as we described in the previous section) and the surface pressure increases that were observed to accompany its passage over southeastern Mississippi. We revisit this possibility later in this section.

The temporal evolution of the model soundings at the four points along Southeast #1 demonstrate further how the thermodynamic environment changed from 27/1300Z–27/1700Z (Fig. 113). After 27/1300Z, the elevated cooling signatures with the two bores continued to move southeastward along the cross section, altering the soundings with their respective passages over the four sites. By 27/1500Z, Bore A had moved over Points C and D, but Bore B remained upstream from these two locations. At Point C, the PBL had warmed and slightly moistened over the previous 2 hours, and the overlying capping inversion had been lifted (Fig. 113c). Moistening was evident in the sounding below ~600 hPa, and a MAUL* now extended upward from the PBL top to the base of the inversion at ~800 hPa. As a result of these modifications, values of MUCIN had decreased by 102 J kg^{-1} over a 2-h period behind Bore A. Similar modifications occurred at Point D, which depicted PBL warming, moistening below ~700 hPa, lifting of the capping inversion, and 2-h decreases in MUCIN of 86.8 J kg^{-1} (Fig. 113d). Meanwhile, Bore B had moved over Points A and B by 27/1500Z and produced further lifting, weakening of the capping inversion, and lofting of low-level moisture (Figs. 113a,b). The sounding at Point A—located immediately ahead of the mesoscale cloud band—now depicted a warmer PBL with an overlying MAUL* that extended up to the base of the inversion at ~775 hPa. Although strong mesoscale ascent had lifted the capping inversion and promoted net moistening below ~650 hPa at Point B, the profile between ~850–750 hPa (i.e., below the inversion) remained unsaturated and corresponded to the developing superadiabatic layer that had formed aloft within the mesoscale corridor separating Bands 1 and 2 from Band 3 by 27/1700Z. Values of MUCIN had decreased by 27/1500Z at both Points A and B in response to cooling aloft in the wake of Bore B and concurrent PBL warming and/or moistening. However, the decreases observed at these two sites were minimal compared to those observed at Points C and D, suggesting that *Bore A was the primary mesoscale disturbance responsible for destabilizing the environment along Southeast #1 during the morning.*

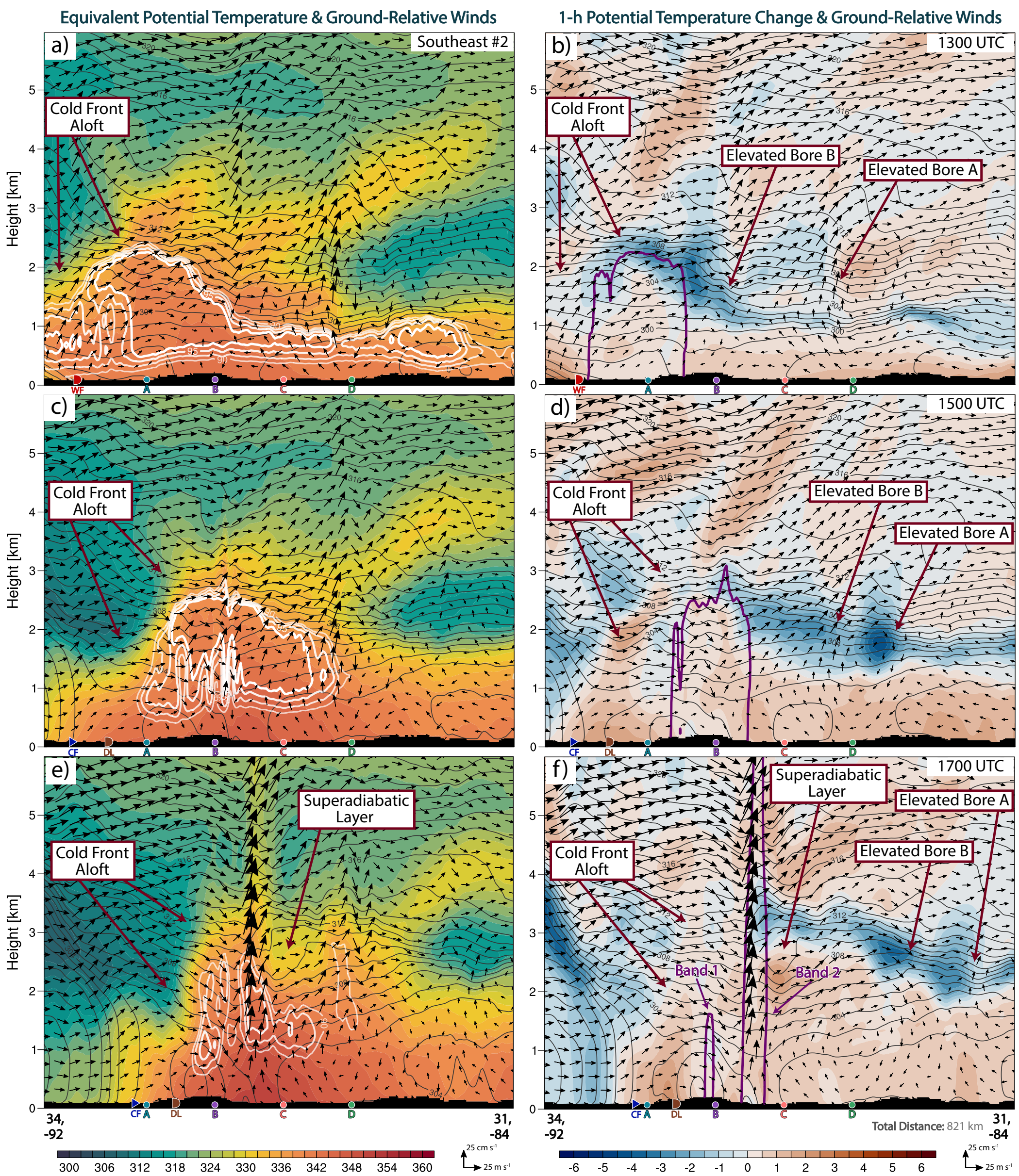

Figure 114: *As in Fig. 112 but for Southeast #2. The effective warm front is indicated by WF at 1300 UTC. The locations of the soundings shown in Fig. 115 are denoted with the appropriate letters. The cross section path is shown in Fig. 109f.*

At all four points, further lifting of the inversion layer and cooling within the lower to middle troposphere had occurred by 27/1700Z, with the greatest modifications apparent at Points C and D (Fig. 113). By this time, Point A was directly ahead of the CFA, and its thermodynamic profile was generally representative of the environment in which the band of supercells was developing over southern Mississippi (Fig. 113a). Specifically, the capping inversion had nearly entirely diminished following the warm sector destabilization that occurred behind the two bores and further lifting that was provided ahead of the CFA, and a MAUL* extended from the top of the PBL to ~750 hPa. At Point B, an unsaturated superadiabatic layer was evident atop the moist layer and below 700 hPa, and the environment below ~750 hPa had notably warmed over the previous 2 h—likely in response to surface heating and both subsidence and entrainment effects occurring within and at the base of the elevated statically unstable layer (Fig. 113b). Points C and D were situated behind the sharpened discontinuity that we previously conjectured to develop in response to sustained mesoscale ascent and tilting effects, and appreciable cooling had occurred within the lower to middle troposphere over the previous 2 hours at these locations (Figs. 113c,d). Furthermore, moistening had occurred over a deep layer at both locations—particularly at Point C, which was located near Band 3 and exhibited a MAUL* from ~950–750 hPa and increased moisture up to at least 600 hPa. At Point D, moistening was evident below ~700 hPa, and a MAUL* extended upward from the PBL top, although the environment between ~850–700 hPa was characterized by lower RH than at some of the other locations. Additionally, the lapse rates near the top of the MAUL* and below the inversion layer were trending toward dry adiabatic, and the cross section at 27/1700Z suggests that an elevated dry adiabatic to superadiabatic layer with accompanying subsidence may have been forming ahead of Band 3 in at least some of the ensemble members—further suggestive that this signature may have resulted from some sort of obstacle effect produced by a convective updraft (Figs. 112e,f).

Vertical cross sections along Southeast #2—which extended through central Mississippi—are displayed in Fig. 114 and depict an overall similar environmental evolution as what occurred along Southeast #1. Specifically, mesoscale destabilization and a net deepening of the low-level moist layer occurred ahead of the CFA and was largely due to the passages of Bores A and B and the onset of surface heating. At 27/1300Z, Point A was situated within the mesoscale moisture dome immediately ahead of the CFA, and the sounding from this location exhibited a MAUL that extended from the top of a shallow, moist PBL at ~925 hPa to the base of an inversion at ~775 hPa (Fig. 115a). The CFA had passed over Point A by 27/1500Z, yielding net drying above ~925 hPa and cooling between ~875–775 hPa. Further drying had occurred throughout the lower to middle troposphere by 27/1700Z as both the CFA and dryline had passed over Point A. Moreover, considerable cooling between ~800–650 hPa led to the removal of the elevated inversion by this time, while appreciable warming that had co-occurred throughout the deepened post-dryline PBL yielded much steeper lapse rates throughout the lower to middle troposphere. Despite this, MUCAPE at this location had decreased to 830 J kg^{-1} by 27/1700Z.

Point B was located behind Bore A and near the leading edge of Bore B at 27/1300Z and had thus experienced some destabilization via mesoscale ascent by this time. The sounding from this location exhibited a shallow MAUL* above the PBL that was topped by a dual-inversion structure between ~850–700 hPa (Fig. 115b). By 27/1500Z, Point B was situated within the mesoscale cloud band and had experienced lifting that promoted cooling and moistening between ~850–700 hPa and concurrent warming beneath 850 hPa. Lapse rates throughout the lower to middle troposphere had further steepened by 27/1700Z, but the profile was generally similar to that 2 h earlier as Point B remained located within the deepened moist layer ahead of the CFA.

Although Point C was situated behind Bore A at 27/1300Z (Figs. 114a,b), large values of MUCIN (-77.9 J kg^{-1}) remained at this location in association with a dual-inversion structure and accompanying warm air between ~900–700 hPa (Fig. 115c). However, these

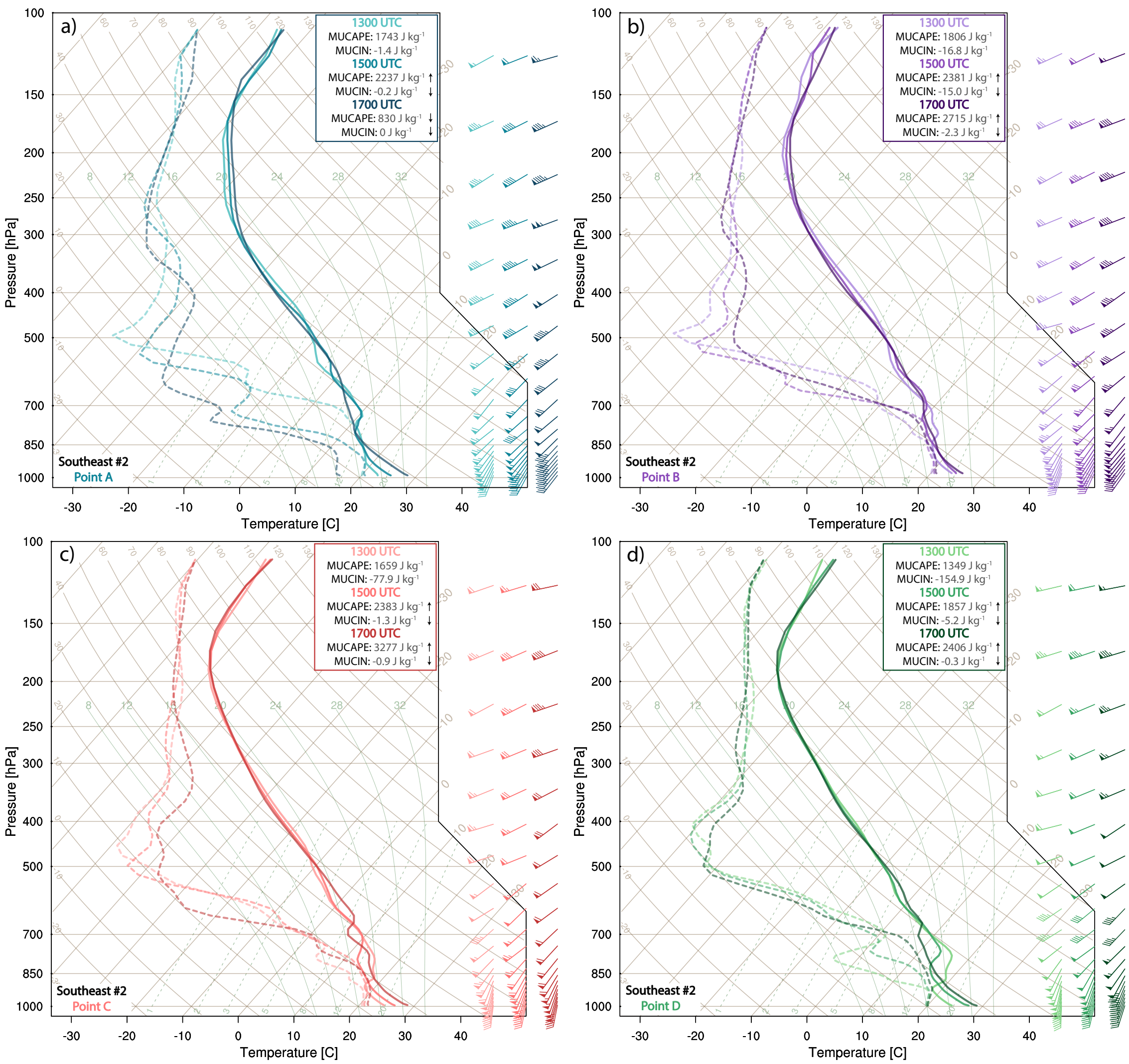

Figure 115: *As in Fig. 113 but for four locations along Southeast #2 (labeled in Fig 114).*

inversions were noticeably weaker than at Point D, which was situated ahead of Bore A and thus had not experienced any mesoscale ascent or destabilization from its passage (Fig. 115d). Accordingly, the MUCIN at Point D was -154.9 J kg^{-1} and—due to the similar PBL temperature and moisture profiles at Points C and D—suggests that the passage of Bore A approximately halved the inhibition along Southeast #2 by producing cooling within the lower to middle troposphere. Bore B had moved over Point C by 27/1500Z (Figs. 114c,d), and the sounding depicted a warmer and moister PBL that was topped by a MAUL* between ~925–800 hPa (Fig. 115c). Moreover, cooling and moistening had occurred between ~900–700 hPa over the past 2 hours, yielding a net decrease in MUCIN

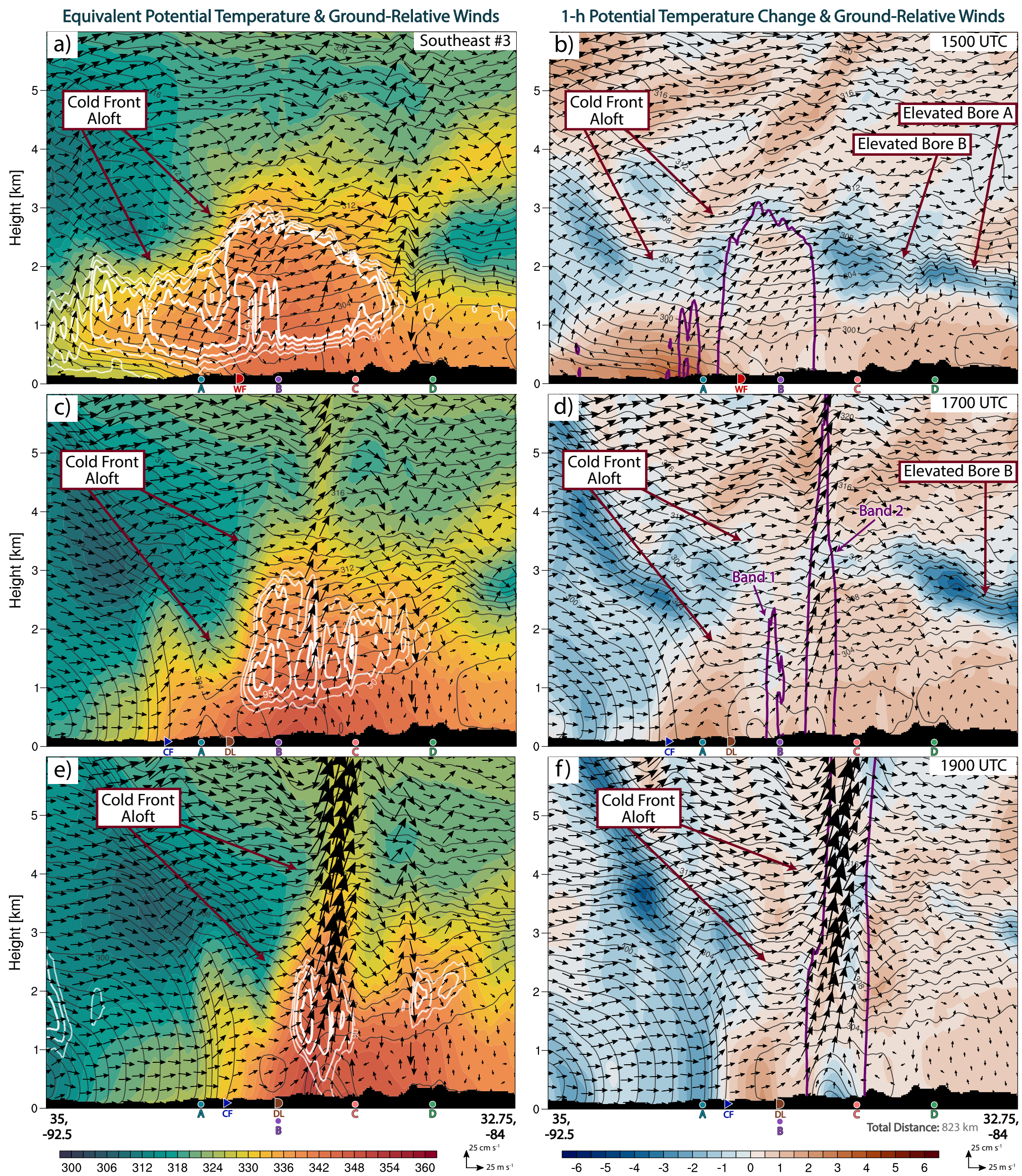

Figure 116: *As in Fig. 114 but for Southeast #3 at (a),(b) 1500 UTC, (c),(d) 1700 UTC, and (e),(f) 1900 UTC 27 April 2011. The locations of the soundings shown in Fig. 117 are denoted with the appropriate letters. The cross section path is shown in Fig. 109f.*

of 76.6 J kg^{-1}. Warming and moistening continued throughout the PBL at Point C, while the inversion layer had further lifted by 27/1700Z. Point C was located just ahead of Band 2 at this time (Figs. 114e,f), and an elevated dry adiabatic to superadiabatic layer had formed near the top of the moist layer at this location—similar to what had occurred along Southeast

#1. Meanwhile, Bore A had passed over Point D by 27/1500Z and promoted cooling and moistening between ~925–700 hPa (Fig. 115d). Acting together with PBL warming, the MUCIN at this location had decreased by 149.7 J kg^{-1} over the previous 2 hours. Further destabilization had occurred by 27/1700Z owing to the passage of Bore B and continued low-level warming, yielding a deep MAUL* that extended from the top of the PBL to ~700 hPa and a much weaker capping inversion.

Finally, the cross sections for Southeast #3 are shown in Fig. 116 from 27/1500Z–27/1900Z. This period was chosen for this path because (1) the path intersected the southern portion of QLCS2 at 27/1300Z and (2) the profiles at 27/1900Z provide a depiction of conditions over northern Mississippi and Alabama after CI. However, these cross sections and their corresponding soundings (Fig. 117) also provide an opportunity to highlight how the thermodynamic conditions changed across various boundaries. The profile at Point D in Southeast #3 evolved most similarly to the profiles previously emphasized along the other two paths, so we will begin by describing its evolution. At 27/1500Z, this location was situated behind Bore A but ahead of Bore B (Figs. 116a,b), and the sounding depicted a capping inversion and accompanying dry layer between ~800–775 hPa (Fig. 117d). Bore B had passed over this location by 27/1700Z (Figs. 116c,d), promoting mesoscale ascent that weakened the capping inversion and produced moistening below 700 hPa. Moreover, the profile beneath ~800 hPa had warmed during the previous 2 hours. This trend continued during the daytime, and the profile below ~700 hPa had further warmed and moistened by 27/1900Z, while the midlevel inversion had been further lifted.

The primary episodes of mesoscale ascent that promoted cooling aloft and deepened the moist layer had occurred at Points B and C prior to 27/1500Z, yielding MAUL*s above the PBL and little to no midlevel remnants of the preexisting capping inversion (Figs. 117b,c). Point C remained within the moisture dome ahead of the CFA throughout the 4-h period discussed herein and was located near the leading edge of Band 2 by 27/1900Z (Figs. 116e,f). In contrast, Point B was located within the rear portion of the moisture dome at

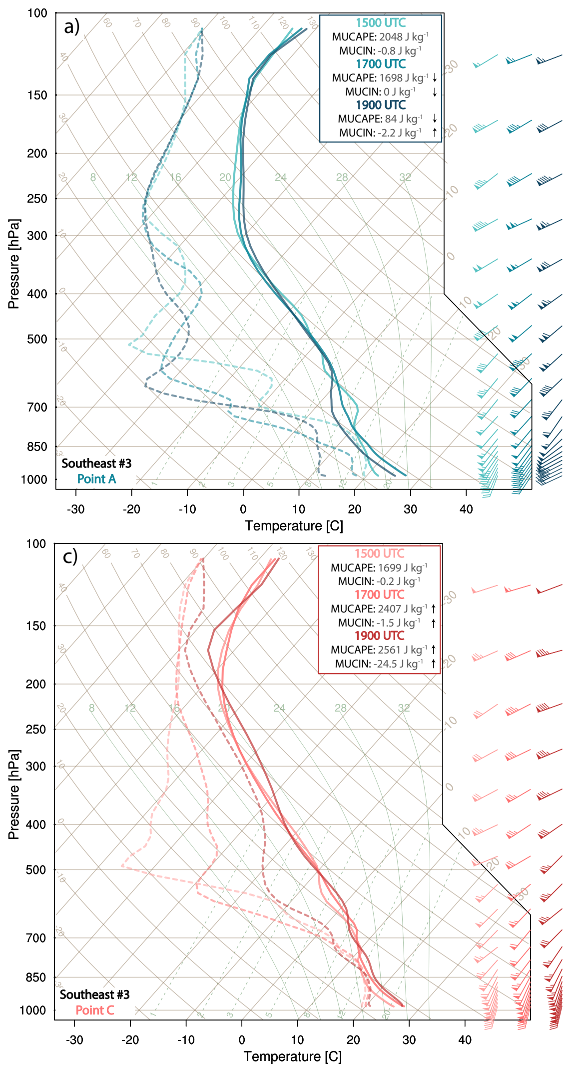

Figure 117: *As in Fig. 113 but for four locations along Southeast #3 (labeled in Fig 116) at (lightest colored lines) 1500 UTC, (medium colored lines) 1700 UTC, and (darkest colored lines) 1900 UTC 27 April 2011.*

27/1700Z and exhibited a MAUL* that extended above the PBL to ~750 hPa. Additionally, drying had occurred between ~800–600 hPa over the previous 2 hours—likely due to the entrainment of dry air into the low-level moist layer that was occurring near the CFA. By 27/1900Z, Point B was located near the dryline and beneath a region of elevated subsidence behind the CFA such that net warming and drying had occurred below ~575 hPa.

The environment at Point A had the most interesting evolution as it was located behind the effective warm front and CFA at 27/1500Z (Figs. 116a,b), behind the dryline and

CFA at 27/1700Z (Figs. 116c,d), and behind the surface cold front and CFA at 27/1900Z (Figs. 116c,d). At 27/1500Z, the sounding from Point A depicted a cool, moist PBL that was overlaid by a MAUL* between ~925–800 hPa (Fig. 117a). Moreover, vertical cross sections from this time indicate that the CFA extended past this location above the nearly saturated low-level moist layer. By 27/1700Z, warming had occurred below ~800 hPa following the passage of the dryline, while cooling had occurred between ~800–600 hPa in the wake of the CFA—collectively steepening the lapse rates throughout the lower to middle troposphere. Together, the passage of both of these boundaries had also produced net drying below ~550 hPa. However, MUCAPE of nearly 1700 J kg^{-1} persisted in the environment at this time. The surface cold front had passed over Point A by 27/1900Z and produced significant cooling beneath ~600 hPa. Further drying below ~800 hPa had also occurred following the passage of the cold front, yielding little remaining MUCAPE.

Discussion and comparison with the observed soundings. The preceding analysis demonstrated that the generation and propagation of elevated disturbances ahead of the CFA contributed to rapid mesoscale destabilization of the warm sector over the Southeast prior to the supercell outbreak. This destabilization occurred primarily due to abrupt reductions in temperature and stability within the lower to middle troposphere (i.e., substantial weakening and erosion of the capping inversion) and concurrent deepening of the moist layer, which was augmented by low-level θ_e advection and surface heating. Moreover, a deep layer that exhibited the character of a MAUL (or MAUL* if not fully saturated) developed over the top of the unsaturated PBL. While we distinguished between the PBL and the MAUL in the previous discussion, we postulate that these two layers were intimately linked such that turbulent motions that developed within the convective PBL during the daytime were likely part of deep overturning circulations that spanned the depth of both layers—hereafter the PBL*. Consequently, the depth of the PBL* (including the portion that resembled a MAUL*) continued to grow throughout the daytime in response to surface heating. Assuming this evolution held true, then we would expect that HCR-type circulations similar to those described by Bryan et al. (2007) may have developed throughout this deep layer in the presence of strong vertical wind shear and contributed to some of the banded structures observed in the cloud field prior to the supercell outbreak.

Indeed, embedded longitudinal roll structures were apparent within the mesoscale cloud band in the simulated reflectivity fields from the individual ensemble members—primarily between 27/1300Z–27/1600Z. These structures are displayed in Fig. 118 for Members 24 and 30 at 27/1500Z and 27/1600Z. Vertical cross sections through these bands (zoomed in along the path of Southeast #1) demonstrate that the upward branches of these roll circulations acted to loft higher-θ_e air upward, while the downward branches transported lower-θ_e air downward—similar to the structures seen in Fig. 2 of Bryan et al. (2007). Prior to CI, the vertical motions attending these circulations spanned from just above the surface to ~3 km, which was much deeper than one would expect with HCRs that were confined to the depth of the unsaturated convective PBL. Furthermore, the horizontal spacing of the bands that formed in the ensemble members generally ranged from ~20–30 km, which was much larger than the 3-km average band spacing noted by Bryan et al. (2007) and the typical spacing of HCRs that develop within the PBL (e.g., Banghoff et al., 2020). By 27/1600Z, deepening convective updrafts had developed in both members, suggesting that *CI occurred where these circulations were able to overcome the weakened but remnant midlevel capping inversion.*

Some characteristics of the model soundings presented along the cross sections in this section resembled those in the observed soundings released over the Southeast just after 27/1730Z. Figure 119 shows the thermodynamic profiles below 500 hPa from these soundings (the full profiles were presented in Fig. 33). As we described in Chapter 3, the Slidell, LA, and Birmingham, AL, soundings exhibited the character of a MAUL and MAUL*, respectively, above the unsaturated PBL—both of which were overlaid by capping inversions that acted to suppress deep convective development. However, note that a superadiabatic layer had developed atop the MAUL* and beneath the capping inversion in

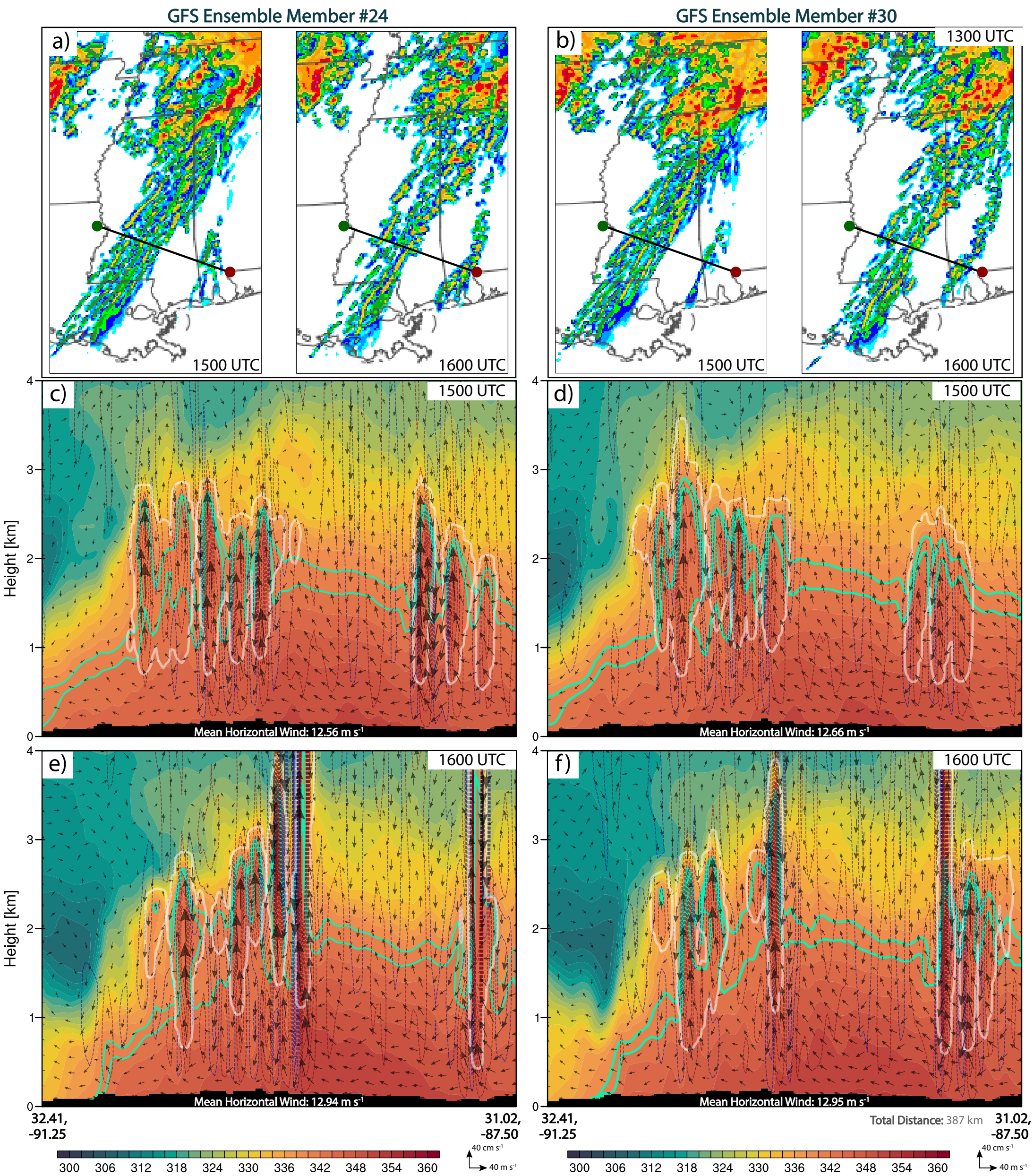

__Figure 118:__ Simulated composite radar reflectivity at 1500 UTC and 1600 UTC 27 April 2011 from (a) Member 24 and (b) Member 30. Zoomed-in cross sections along Southeast #1 of equivalent potential temperature (shaded; K), equivalent potential temperature between 340–342 K (green contour), upward vertical velocity (dashed red contours; every 20 cm s^{-1} $\geq$ 10 cm s^{-1}), downward vertical velocity (dashed blue contours; every 20 cm s^{-1} $\leq$ -10 cm s^{-1}), cloud water mixing ratio = 0.01 g kg^{-1} (white contour), and 2D wind vectors where the mean horizontal wind in the cross-section plane has been removed (vectors) at (c),(d) 1500 UTC and (e),(f) 1600 UTC April 27 for (left) Member 24 and (right) Member 30. The cross-section paths are shown in the top panels.

the Birmingham sounding, yielding a profile that was reminiscent of the model soundings from Point B along Southeast #1 at 27/1500Z and 27/1700Z, from Point D along Southeast #1 at 27/1700Z, and from Point C along Southeast #2 at 27/1700Z (Figs. 113b,d and 115c). Recall that all of the model soundings with an elevated superadiabatic layer were located immediately ahead of the developing precipitation bands. Of the model soundings presented in this section, the Slidell sounding was most similar to the sounding from Point A along Southeast #1 at 27/1300Z, which had a relatively shallow MAUL above the PBL that was overlaid by a dual-inversion structure (Fig. 113a). This model sounding had previously experienced mesoscale lifting with the passage of Bore A but remained upstream from Bore B and the dome of deepest low-level moisture at 27/1300Z. None of the model soundings shown herein had a striking resemblance to the sounding released from Jackson, MS, which had steep lapse rates throughout the lower to middle troposphere (reflective of prior mesoscale ascent) but retained multiple inversions between ~900–600 hPa and remained unsaturated. Perhaps the most similar profile was from Point C along Southeast #2 at 27/1700Z, which also bore some resemblance to the Birmingham sounding (Fig. 115c).

The observed sounding release locations are overlaid with visible satellite imagery at 27/1732Z, 27/1740Z, and 27/1745Z in Figs. 119e-g to aid in the interpretation of various signatures seen within the lower to middle troposphere. Assuming a mean sounding ascension rate of $\sim$300 m min^{-1}, which is based on standard values used within the National Weather Service for routine sounding observations[1], we estimated that the Slidell sounding reached the 850 hPa and 700 hPa levels at ~27/1740Z and 27/1745Z, respectively, while the Birmingham sounding reached the 850 hPa and 700 hPa levels at ~27/1738Z and 27/1744Z, respectively. Thus, the MAUL observed by the Slidell sounding was likely associated with the leading cloud band, whereas the MAUL* observed by the Birmingham sounding was likely related to an arc band that emerged ahead of the leading cloud band (cf. Figs. 97e and 119e-g) and was previously postulated to correspond to the elevated discontinuity that

[1]The NWS Rawinsonde Observations Manual is available at `https://www.nws.noaa.gov/directives/sym/pd01014001curr.pdf`.

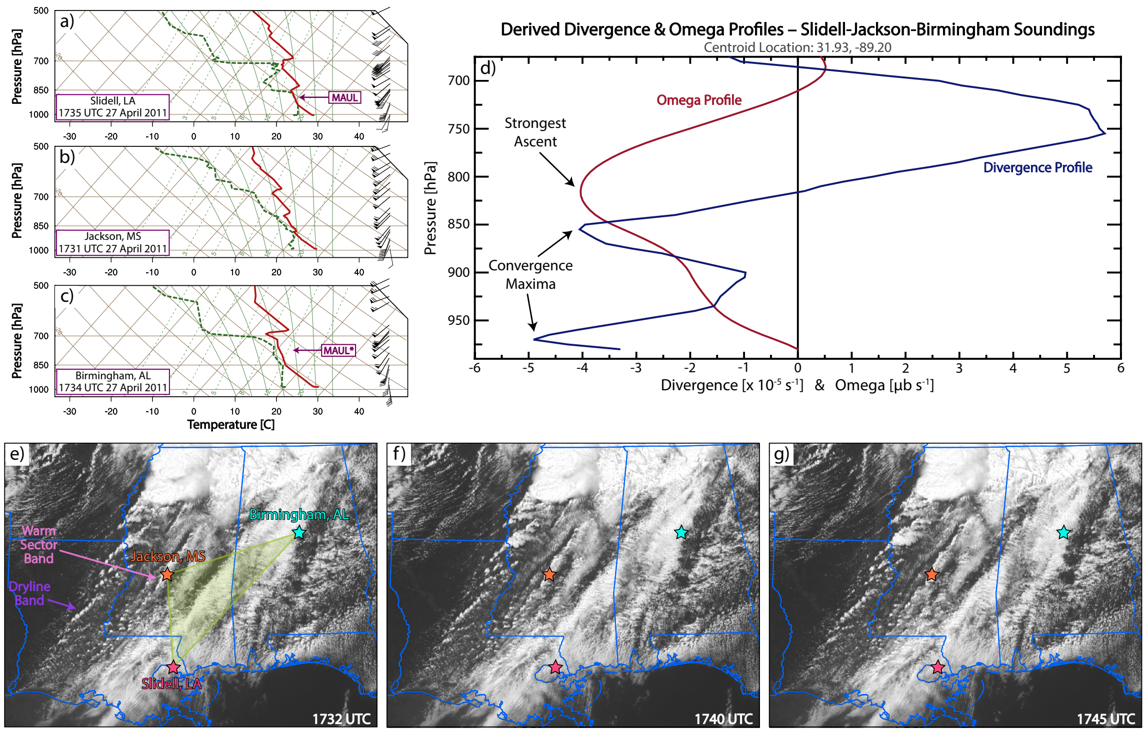

Figure 119: *The lowest 500 hPa of the operational soundings presented in Fig. 33 from (a) Slidell, LA, at 1735 UTC, (b) Jackson, MS, at 1731 UTC, and (c) Birmingham, AL, at 1734 UTC 27 April 2011. The vertical profile of the average horizontal divergence ($\times\ 10^{-5}\ s^{-1}$) and omega ($\mu b\ s^{-1}$) calculated over the triangular region bounded by the three soundings is displayed in (d). GOES-13 visible satellite imagery is shown at (e) 1732 UTC, (f) 1740 UTC, and (g) 1745 UTC is shown with the sounding locations annotated.*

developed at the front edge of the deepened moist layer in the simulations. Moreover, the Birmingham sounding was released immediately ahead of this arc band, and the agreement between signatures seen in this observed sounding and several of the ensemble mean soundings from locations just ahead of the developing precipitation bands suggests that similar processes occurring ahead of the arc band may have contributed to the elevated superadiabatic layer observed above the MAUL* and beneath the midlevel inversion.

Kinematically derived vertical profiles of ω and divergence that represent average quantities over the triangular area bounded by the three observed sounding locations are shown at 5-hPa intervals from the lowest common observed pressure level (i.e., 980 hPa) to 675 hPa in Fig. 119d. For a detailed description of the procedure used to compute these profiles, we refer the reader to Trier et al. (2017, p. 2925–2926). These profiles indicate that average convergence was occurring below ~825 hPa with two maxima centered at approximately 975 hPa (100–200 m AGL within the PBL) and 850 hPa. Coupled with maximum divergence within the ~775–725 hPa layer, this profile yielded average upward vertical motion below 700 hPa (i.e., below the prominent midlevel capping inversion), with $\omega < -3\ \mu\text{b s}^{-1}$ (or -10.8 hPa h^{-1}) occurring between ~860–760 hPa. These estimated values of upward motion (average w of roughly 3 cm s^{-1}) were much less than what would be required to produce the dramatic thermodynamic modifications and destabilization seen in the model soundings and were accordingly much less than the vertical velocities associated with the bore passages in the ensemble mean. Thus, we surmise that the bulk of the destabilization had already occurred at all three sounding locations such that the ascent estimated from the observed soundings reflected the continued gradual growth of the previously deepened moist layer that occurred throughout the daytime.

6.4 Summary and discussion

In this final chapter, we used observations and convection-permitting simulations to further investigate the evolution of the CFA and the dynamical consequences of its interaction with the prefrontal moist layer as they pertained to mesoscale destabilization of the warm sector prior to the afternoon supercell outbreak. Moreover, we examined the character of the mesoscale cloud bands that developed over the Southeast and related these bands to signatures seen in the surface observations, GFS ensemble forecasts, and observed soundings. The primary findings of this investigation are summarized below.

- Observations and forecasts from both the HRRRx and GFS ensemble demonstrated that a bore and low-level cloud band initially developed in the stable moist layer over Texas due to a mechanical impulse that accompanied the downslope movement of a low-level momentum surge. This momentum surge stemmed from a region of strong midlevel subsidence over West Texas that was distinct from that associated with the primary Pacific cold front but still provided low-level CAA. Vertical cross sections extending from the southern Texas Panhandle into the Gulf of Mexico suggest that this initial disturbance (Bore A) evolved separately from a second high-amplitude disturbance (Bore B) that subsequently formed as the actively subsiding low-θ_e airstream behind the Pacific cold front plowed forward into the moist air mass and ultimately evolved into a CFA.

- Satellite imagery showed that the prefrontal disturbance and accompanying mesoscale cloud band acquired a heterogeneous structure during the morning, with the segment that moved into Louisiana and Mississippi evolving into the sharp leading cloud band, and the portion that moved into the Gulf of Mexico evolving into a long-lived soliton. Soundings from the Texas Gulf Coast indicated the presence of a strong surface-based inversion atop an incredibly shallow moist layer, whereas the sounding from Slidell, LA, showed elevated inversion layers that were situated above a deeper—and, at this particular location, absolutely unstable—moist layer. These regional thermodynamic differences were also evident in the HRRRx and GFS ensemble forecasts, which both developed an elevated prefrontal bore within the capping inversion as the CFA advanced toward the Southeast. However, over both the Gulf of Mexico and the Southeast, the bore passage was associated with an abrupt jump in the isentropic surfaces that yielded dramatic adiabatic cooling in the lower- to mid-troposphere and promoted sustained deepening of the low-level moist layer that extended well into the warm sector ahead of the CFA.

- The trailing cloud band developed over Louisiana during the morning and immediately preceded a wedge of broken low-level clouds and a deepening cumulus field. This coherent mesoscale band was located behind the leading cloud band, and the two were separated by a sharp band of clearing. Surface observations throughout the Southeast indicated that a pressure increase either coincided with or preceded the passage of the leading cloud band, and the ASOS sites presented herein observed that a mesoscale pressure ridge concurrent with wind perturbations accompanied this band. An abrupt pressure drop and wind shift were observed along the backside of the leading cloud band and indicate that the band of clearing had the character of a solitary wave of depression. The pressure subsequently rose following the passage of this clear band in association with the approaching trailing cloud band. The perturbations associated with these individual disturbances occurred as part of (or were superposed onto) a longer-duration pressure increase $>$ 1 hPa that persisted for several hours and corresponded to the mesoscale dome of of lifted air and deepened low-level moisture that developed behind Bore B and ahead of the CFA in the GFS ensemble. The trailing cloud band largely coincided with the apex of this observed mesoscale pressure dome and thus the corridor of greatest lifting, and its passage was followed by a gradual surface pressure decrease that coincided with the broken cumulus field.

- Processes leading to rapid destabilization over the Southeast and the formation of the MAUL evident in the observed soundings just prior to the afternoon supercell outbreak were assessed using the GFS ensemble mean. The sequential passages of Bore A and Bore B promoted considerable adiabatic cooling within the lower- to mid-troposphere, lifting and weakening of the capping inversion, and deepening of the low-level moist layer that collectively produced abrupt and significant reductions to CIN values over the Southeast. These reductions largely occurred prior to any destabilizing influence from surface heating such that any remaining CIN was almost entirely eroded in the couple of hours after sunrise, yielding a preconditioned minimally capped environment over much of the region. The dramatic thermodynamic modifications that accompanied the bore passages were commensurate with those documented to occur in HSLC environments by King et al. (2017) and shown in Fig. 7, suggesting that these prefrontal disturbances may contribute to rapid mesoscale destabilization during other severe events in the Southeast. This conjecture is further supported by the knowledge that a prefrontal bore was also present during a VORTEX-SE case in 2017, as was documented by Chasteen et al. (2020).

- The deepened moist layer that developed over the warm sector—primarily that within the mesoscale moisture dome behind Bore B—exhibited the character of a MAUL (or MAUL*) that extended from the top of the unsaturated PBL to the base of the overlying capping inversion. As expected, the PBL deepened appreciably after sunrise in response to surface heating. However, this evolution was accompanied by further deepening of the moist layer throughout the mesoscale environment (including ahead of Bore A) and further lifting and weakening of the midlevel capping inversion. We postulated that this occurred as surface heating increased the degree of potential instability throughout the lower troposphere, which consequently invigorated the MAUL and promoted stronger convective overturning that further deepened the moist layer and weakened the overlying capping inversion. Accordingly, we surmised that the turbulent convective motions expected to develop in the PBL during the daytime actually manifested as deep overturning circulations that spanned the combined depths of the unsaturated PBL and overlying MAUL (or MAUL*) such that these two layers behaved as one PBL* that grew over time in response to sensible heating.

- Because this daytime PBL* growth was most pronounced in the mesoscale region that had already experienced lifting by the bore(s), tilting effects ensued along its periphery such that the isentropes and θ_e surfaces notably steepened and ultimately became a high-amplitude discontinuity that then proceeded to move through the warm sector as an elevated bore. This evolution was posed as an explanation for the prominent arc band that was observed to emerge ahead of the leading cloud band during the late morning and led to a surface pressure rise and the eastward expansion of the agitated cumulus field over the warm sector.

- Previous studies have generally treated the formation of a MAUL as a sufficient condition for CI because these layers possess no CIN by definition. Although MAULs of varying depths were present over the Southeast in both the observed soundings and in the GFS ensemble, the widespread formation of deep convection was precluded by the persistence of an overlying inversion. *In other words, a widespread region comprising mesoscale bands of agitated cumulus developed over the warm sector during the daytime, but the circulations attending most of these cloud bands were constrained by the remnant capping inversion such that they did not promote CI.* We used vertical cross sections from individual GFS ensemble members to examine the character and evolution of the circulations that developed within the deepened moist PBL*. These analyses supported our previous conjectures by demonstrating that deep convective overturning occurred throughout the PBL* and was accomplished by longitudinal rolls that formed in the presence of strong vertical wind shear and extended from just above the surface to ~3 km, where their upward branches generally became overwhelmed by negative buoyancy within the overlying inversion. However, CI eventually occurred where the upward branches of these mesoscale circulations were successfully able to penetrate through the weakened midlevel inversion. The longitudinal rolls that formed in the simulated PBL* were at least somewhat analogous to traditional HCRs that develop within the PBL, although they exhibited a horizontal spacing of ~20–30 km—much larger than the typical spacing of HCRs and the HCR-type longitudinal circulations that were documented to form within a MAUL by Bryan et al. (2007).

Chapter 7

Conclusions

In this dissertation, we provided a comprehensive multiscale investigation of the prolific tornado outbreak that occurred on 26–27 April 2011. In a historical sense, this outbreak was noteworthy for several reasons, including the sheer number of tornadoes—many of which were significant and/or long-track—that developed from three successive convective episodes and the anomalously high mortality rate that resulted although the potential for a high-end severe event over the Southeast on the afternoon of 27 April was well forecast and warning lead times during this event were longer than the national average. The devastating outcomes from this outbreak and the long-established fact that tornadoes in the Southeast produce a disproportionately greater number of fatalities than those in other parts of the country ultimately motivated the Congressional mandate that established support for NOAA's VORTEX-SE program in 2015.

The research presented herein aimed to unravel this incredibly complex multiepisode outbreak by providing answers to the following questions:

1. *What mesoscale processes contributed to the initiation, organization, and morphological evolution of the three tornadic convective systems that impacted the Southeast on 27 April 2011?* **[Q1]**

2. *How did the environmental characteristics evolve throughout the outbreak to support three successive convective episodes that each exhibited a different severity and modality?* **[Q2]**

3. *How was the environment modified by latent processes occurring within the first two convective systems and how did these upscale environmental modifications contribute to the severity of this prolific multiepisode tornadic outbreak?* **[Q3]**

4. *How are the relevant multiscale processes and upscale feedbacks arising from convection depicted within a convection-permitting ensemble?* **[Q4]**

These questions were answered through a series of comprehensive and detailed analyses that were described in Chapters 3–6. The early stages of this research sought answers to **Q1** and **Q2** by examining conventional observations in combination with a series of 1-h forecasts from the operational RUC model. Although these early analyses provided numerous ideas and insights about how this outbreak evolved, it simultaneously revealed just how complex this case was owing to the prevalence of scale-interactions and interconnected processes that are inherent during multiepisode convective events. Thus, we quickly recognized that **Q1** and **Q2** could not be answered without factoring in the apparent significance of upscale environmental modifications, which then led us to propose **Q3**.

The bulk of the time spent conducting this research ultimately centered on answering **Q2** and **Q3**, with insights also gleaned into **Q1** throughout this extensive process. This work involved conducting the WRF simulations with and without latent heat release in 2019, which—in combination with the RUC 1-h forecasts—largely enabled us to answer **Q3**. We also received access to several Experimental HRRR forecasts of this event in 2019, which proved to be invaluable as these forecasts shed light about several mesoscale processes that were difficult to decipher from the RUC fields alone. These processes included the formation and evolution of the CFA and the prefrontal bores over Texas, which then allowed us to derive insights into the formation and evolution of both QLCS2 and the numerous warm sector cloud bands that eventually became the prolific afternoon supercell outbreak. Although the HRRRx forecasts had limitations, which we discussed in Chapters 2 and 6, they significantly helped to refine our conceptual understanding of this complex event and provided guidance about how to best structure our analyses using other data sources. The results from this extensive investigation formed the basis of Chapters 3 and 4 and their accompanying publications, Chasteen and Koch (2021a) and Chasteen and Koch (2021b), respectively.

Finally, the dramatic upscale environmental modifications that we uncovered in Chapter 4 and the complex assortment of mesoscale processes that were presumably occurring throughout the warm sector prior to the supercell outbreak helped to motivate the need for convection-permitting ensemble forecasts, which were generated in early 2021. This led to the formulation of **Q4**, which sought to further understand the importance of these scale-interactive processes by assessing how their representations varied among the individual ensemble members and then determining how these different representations ultimately influenced the forecasts at subsequent times. The ensemble was also used to provide additional support for the results we found in Chapter 4 and to further answer **Q3** by allowing us to explicitly evaluate whether simulated differences in the upscale flow modifications produced by QLCS1 led to differences in the system's severity. These results were presented in Chapter 5. Additionally, the ensemble forecasts were used to thoroughly investigate the evolution of the CFA and how it interacted with the low-level moist layer to generate prefrontal bores and ultimately promote CI over the warm sector during the supercell outbreak. The results from this examination—in combination with the analyses presented in Chapter 3—completed our investigation of **Q1** and were presented in Chapter 6.

Numerous discoveries were made throughout this comprehensive investigation that ranged in significance from perplexing nuances to incredibly consequential multiscale process interactions. The primary takeaways are summarized as follows.

- This extended tornado outbreak unfolded ahead of a slowly moving longwave trough that amplified with time over the Rocky Mountains in association with the equatorward movement of an anomalously strong upper-level jet streak that developed during a multiday anticyclonic Rossby wave breaking event over the Pacific Ocean. The highly amplified synoptic pattern enabled the trough base to persist over the south-central U.S. for multiple consecutive days, supporting—through favorable positioning with respect to the regional topography—the formation of a lee trough and dryline over the SGP and the continued replenishment of potential instability through sustained differential advection of low-level warm, moist air from the Gulf of Mexico and an overlying EML plume that was transported off the elevated terrain. Episodic convective development occurred throughout this multiday period as a sequence of disturbances embedded within the broader upper-level jet moved into the lee of the Rockies, including three prominent shortwave troughs. This general synoptic evolution was consistent with the findings of several past studies that have identified dynamical linkages between extreme weather events and upstream Rossby wave breaking episodes owing to the latter's role in establishing a highly amplified flow pattern (e.g., Bosart et al., 2017; Wirth et al., 2018; Moore et al., 2019).

- Dramatic and lasting upscale flow modifications resulted from the interaction between QLCS1 and the midlatitude waveguide. Notably, the formation of convection over eastern Oklahoma and Arkansas during the evening of 26 April led to pronounced alterations to the large-scale flow pattern through promoting an unbalanced upper-level jet streak that rapidly strengthened and surged poleward over the Midwest. This progression resulted from the widespread development of deep convection (and thus latent heat release) adjacent to preexisting upper-level PV and geopotential height gradients that both had a substantial meridional component due to the prior evolution of SW_1. As a result, strong convective outflow winds abruptly sharpened the background PV gradient through advection and—because they were directed down the height gradient—continued to accelerate as they moved downstream in accordance with dynamical flow imbalance. Consequently, considerable upper-level divergence developed within the entrance region of this highly unbalanced jet streak, which contributed to the upscale growth of QLCS1 as it quickly surged poleward. This evolution was accompanied by the amplification of the upper-level ridge over the Midwest, a reduction in the wavelength of the large-scale flow pattern, and a strong isallobaric response that rapidly intensified the LLJ throughout the warm sector. Accordingly, the low-level vertical wind shear abruptly strengthened within QLCS1's inflow environment, yielding shear vectors that were oriented largely parallel to the system and thus ample streamwise vorticity and high SRH. These notable flow modifications were postulated to have enhanced the severity of QLCS1 by providing more favorable kinematic conditions for the production of severe convective hazards (e.g., damaging winds and tornadoes) and persisted throughout the remainder of the outbreak—an upscale feedback effect.

- Additionally, the formation and upscale growth of QLCS1 was accompanied by the amplification of SW_2, development of a secondary tropopause fold, and cyclogenesis along the quasi-stationary front over the Midwest—none of which occurred in the absence of latent heating and were therefore a direct consequence of the upscale modifications produced by this system. These modifications were also sustained throughout the rest of the outbreak such that (1) the height perturbations accompanying L_2 and its associated trough supported more veered low-level flow over the warm sector, and (2) the amplification of SW_2 reduced the large-scale flow curvature downstream from the upper-level trough and helped to establish strong southwesterly midlevel flow over the Southeast during the supercell outbreak.

- The environment quickly destabilized in the wake of QLCS1 owing to the movement of SW_3 into the SGP, allowing QLCS2 to develop ahead of the CFA and near the LLJ terminus atop the QLCS1 cold pool. QLCS2 was predominantly elevated and was therefore comparably less severe than the other two convective episodes. However, this system induced a meso-α-scale region of upper-level height rises and midlevel warming that increased the mesoscale flow curvature and baroclinity ahead of SW_3. QLCS2 was also responsible for triggering an unbalanced upper-level jet streak that rapidly intensified downstream from the warm sector and for splitting the approaching jet exit region into two branches—the southern of which contributed to the strong deep-layer shear during the supercell outbreak. Furthermore, this evolution yielded an isallobaric response that further strengthened the LLJ ahead of SW_3 and established a regional maxima in low-level wind speed over northern Mississippi and Alabama during the afternoon. QLCS2 also contributed to the maintenance of a pronounced cold pool and associated effective warm front, which delimited the northern extent of the region of greatest tornado potential during the afternoon and influenced the overall structure and evolution of L_3.

- The supercell outbreak unfolded as SW_3 and its attendant deep tropopause fold moved into the Lower Mississippi Valley. Although this final and most severe convective episode was associated with a coupled upper-level jet configuration, it was neither associated with a highly diffluent shortwave trough nor rapid surface cyclogenesis, and the strong LLJ present over the Southeast at its onset largely originated from the accumulated flow intensification that followed the development of QLCS1 and QLCS2. The unique overlap of notably large buoyancy, highly favorable vertical shear profiles, and the mesoscale organization of numerous supercells that primarily developed along two bands (i.e., ahead of the dryline and CFA) and remained largely discrete for several hours as they traversed the warm sector contributed to the prolific nature of the afternoon supercell outbreak.

- Although the two preceding QLCSs moved through the Southeast during the morning and left a widespread region of convective outflow (particularly QLCS1), the environment quickly destabilized in response to PBL heating, strong differential advection ahead of SW_3, and mesoscale ascent ahead of the CFA to yield anomalously high CAPE values throughout the warm sector by the beginning of the supercell outbreak. Furthermore, the GFS ensemble demonstrated that sustained deepening of the low-level moist layer concurrent with dramatic cooling in the lower to middle troposphere occurred as two elevated bores moved through the Southeast ahead of the CFA. These elevated disturbances were responsible for substantially weakening the capping inversion and thus promoting rapid reductions in CIN throughout the mesoscale environment. Furthermore, the deepened moist layer behind the bores and ahead of the CFA acquired the character of a MAUL (or MAUL* if it was not entirely saturated) that was situated above the PBL and beneath the weakened midlevel inversion. The simulations demonstrated that the unsaturated PBL and overlying MAUL* behaved as one PBL* that continued to grow in response to daytime sensible heating and comprised deep overturning circulations that were analogous to HCRs but exhibited a spacing of ~20–30 km. CI occurred over the warm sector ahead of the CFA where the upward branches of these longitudinal roll circulations were able to successfully penetrate through the weakened capping inversion.

- We sought to understand the process evolution that established strong vertical wind shear and elongated hodographs with ample low-level curvature and large SRH over the warm sector at the beginning of the supercell outbreak. Spatial plots of storm-relative hodographs indicated that the notably high SRH values were attributable to a combination of large streamwise vorticity and strong storm-relative winds in the lower troposphere that resulted from ~45–55-kt estimated storm motions oriented at a large angle to the LLJ. Furthermore, the deep-layer shear vectors were oriented favorably for the formation and sustenance of discrete supercells ahead of both the dryline and warm sector CI bands. Strong low-level shear and ample hodograph curvature were found to develop over the Southeast well before strong deep-layer shear, and this evolution was attributed to the accumulated LLJ intensification that began immediately after QLCS1 formed on the previous evening and was augmented following the development of QLCS2 ahead of SW_3. In contrast, deep-layer shear strengthened throughout the morning as the approaching midlevel jet exit region was split into two branches around QLCS2, yielding a southwesterly branch that was adjacent to the system's southern flank over the Southeast. We further investigated the shear characteristics by partitioning the hodographs from four locations over the Southeast into their geostrophic and ageostrophic counterparts. The geostrophic hodographs exhibited strong southwesterly flow but overall weak vertical wind shear that alone would not have supported a prolific tornado outbreak. In contrast, the highly curved hodographs and strength of the vertical wind shear throughout the lower to middle troposphere were almost entirely governed by the ageostrophic wind profile, which veered considerably with height and resulted from a combination of frictional effects, flow curvature, and strong accelerations within the LLJ entrance region. Thus, this analysis revealed that strong ageostrophic motions were absolutely essential for establishing the highly favorable shear profiles present over the warm sector during the afternoon supercell outbreak.

Ultimately, this doctoral research and the broader VORTEX-SE program through which it was supported were motivated by the need for improved physical understanding and forecasts of tornado outbreaks in the Southeast, which are generally plagued by poor mesoscale predictability and frequently occur during prolonged periods of convection. Herein we demonstrated that the two QLCSs provided a complex array of upscale environmental modifications prior to the prolific supercell tornado outbreak on the afternoon of 27 April 2011. The dramatic modifications produced by QLCS1 persisted throughout the remainder of the outbreak and were hypothesized to have enhanced both its own severity and contributed to the severity and evolution of the subsequent convective episodes. Although the ensemble subset analysis in Chapter 5 showed that initial variations in the coverage and intensity of convection with QLCS1 promoted differences in the upscale flow response that translated to differences in the system's severity during its early evolution, no clear relationship could be established as pronounced upscale flow modifications ultimately occurred in all members of both subsets. Additionally, both ensembles failed to sustain the southernmost bowing segment of QLCS1, which was the portion of the system responsible for producing numerous tornadoes throughout the Southeast overnight. Perhaps as a consequence of the errors with this part of the system or perhaps due to other errors, neither ensemble correctly depicted the development, intensity, and morphological evolution of QLCS2. The limited predictability of this system extended to other forecast models, such as the HRRRx (not shown herein), was noted to be a major source of uncertainty for forecasters in real-time, and had considerable implications for the subsequent evolution of the supercell outbreak owing to its role in modifying the mesoscale environment over the Southeast. These implications manifested in the GFS ensemble forecasts in several ways, including: the warm sector extended too far poleward during the afternoon following the poor depictions of the southernmost bowing segment and QLCS2; the downstream formation of J_4 was improperly represented, which consequently affected not only the strength of the LLJ, but also the period over which it intensified and thus its degree of ageostrophy over the warm sector during the afternoon; the system's interactions with the midlevel jet exit region and SW_3 were considerably downplayed, which affected the deep-layer shear profiles over the Southeast and likely further enabled the positive bias in the forward motion of SW_3. Unfortunately, such errors within the simulations preclude us from fully understanding how the upscale influences of QLCS1 and QLCS2 affected the outcome of the afternoon supercell outbreak.

The overall findings of this multiscale investigation lend support to Trapp (2014)'s hypothesis that convective feedbacks may contribute to the tendency for tornado outbreaks to occur following multiday periods of severe weather. To our knowledge, the significance of upscale feedbacks in multiepisode severe outbreaks had not been previously evaluated although such events are notoriously challenging for operational forecasters. We hope that greater attention is drawn to this matter—especially within the forecasting and numerical modeling communities—as simulated environmental modifications are expected to be highly sensitive to the timing and location of CI, the extent and strength of convection, the specific representation of latent processes (i.e., model configuration), and the degree to which the convection interacts with the greater baroclinic environment. Owing to the significance of highly nonlinear processes involving unbalanced dynamics, small errors in the representation of moist processes have the potential to grow rapidly such that they quickly become incredibly consequential for the subsequent forecast evolution.

Bibliography

Adams-Selin, R. D. and R. H. Johnson, 2013: Examination of gravity waves associated with the 13 March 2003 bow echo. *Mon. Wea. Rev.*, **141 (11)**, 3735–3756.

Adlerman, E. J. and K. K. Droegemeier, 2002: The sensitivity of numerically simulated cyclic mesocyclogenesis to variations in model physical and computational parameters. *Mon. Wea. Rev.*, **130 (11)**, 2671–2691.

Agee, E., C. Church, C. Morris, and J. Snow, 1975: Some synoptic aspects and dynamic features of vortices associated with the tornado outbreak of 3 April 1974. *Mon. Wea. Rev.*, **103 (4)**, 318–333.

Alexander, C. R., et al., 2012: High-Resolution Rapid Refresh (HRRR) forecast evaluation of tornado events in April and May of 2011. *Special Symposium on the Tornado Disasters of 2011, 92nd Amer. Meteor. Soc. Annual Meeting, New Orleans, LA* [Available online at `https://ams.confex.com/ams/92Annual/webprogram/Paper200906.html`].

Anderson, J., T. Hoar, K. Raeder, H. Liu, N. Collins, R. Torn, and A. Avellano, 2009: The data assimilation research testbed: A community facility. *Bull. Amer. Meteor. Soc.*, **90 (9)**, 1283–1296.

Anderson, J. L., 2001: An ensemble adjustment Kalman filter for data assimilation. *Mon. Wea. Rev.*, **129 (12)**, 2884–2903.

Anderson-Frey, A. K. and H. Brooks, 2019: Tornado fatalities: An environmental perspective. *Wea. Forecasting*, **34 (6)**, 1999–2015.

Anderson-Frey, A. K., Y. P. Richardson, A. R. Dean, R. L. Thompson, and B. T. Smith, 2019: Characteristics of tornado events and warnings in the southeastern United States. *Wea. Forecasting*, **34 (4)**, 1017–1034.

Anthes, R. A., Y.-H. Kuo, S. G. Benjamin, and Y.-F. Li, 1982: The evolution of the mesoscale environment of severe local storms: Preliminary modeling results. *Mon. Wea. Rev.*, **110 (9)**, 1187–1213.

Antonescu, B., G. Vaughan, and D. M. Schultz, 2013: A five-year radar-based climatology of tropopause folds and deep convection over Wales, United Kingdom. *Mon. Wea. Rev.*, **141 (5)**, 1693–1707.

Archambault, H. M., L. F. Bosart, D. Keyser, and J. M. Cordeira, 2013: A climatological analysis of the extratropical flow response to recurving western North Pacific tropical cyclones. *Mon. Wea. Rev.*, **141 (7)**, 2325–2346.

Archambault, H. M., D. Keyser, L. F. Bosart, C. A. Davis, and J. M. Cordeira, 2015: A composite perspective of the extratropical flow response to recurving western North Pacific tropical cyclones. *Mon. Wea. Rev.*, **143 (4)**, 1122–1141.

Ashley, W. S., 2007: Spatial and temporal analysis of tornado fatalities in the United States: 1880–2005. *Wea. Forecasting*, **22 (6)**, 1214–1228.

Ashley, W. S., A. M. Haberlie, and J. Strohm, 2019: A climatology of quasi-linear convective systems and their hazards in the United States. *Wea. Forecasting*, **34 (6)**, 1605–1631.

Ashley, W. S., A. J. Krmenec, and R. Schwantes, 2008: Vulnerability due to nocturnal tornadoes. *Wea. Forecasting*, **23 (5)**, 795–807.

Atallah, E. H. and L. F. Bosart, 2003: The extratropical transition and precipitation distribution of Hurricane Floyd (1999). *Mon. Wea. Rev.*, **131 (6)**, 1063–1081.

Baines, P. G., 1984: A unified description of two-layer flow over topography. *J. Fluid Mech.*, **146**, 127–167.

Banacos, P. C. and H. B. Bluestein, 2004: Hodograph variability within analytically modeled, synoptic-scale, baroclinic systems. *Mon. Wea. Rev.*, **132 (6)**, 1448–1461.

Banghoff, J. R., J. D. Sorber, D. J. Stensrud, G. S. Young, and M. R. Kumjian, 2020: A 10-year warm-season climatology of horizontal convective rolls and cellular convection in Central Oklahoma. *Mon. Wea. Rev.*, **148 (1)**, 21–42.

Barker, D., et al., 2012: The weather research and forecasting model's community variational/ensemble data assimilation system: WRFDA. *Bull. Amer. Meteor. Soc.*, **93 (6)**, 831–843.

Bartels, D. L. and R. A. Maddox, 1991: Midlevel cyclonic vortices generated by mesoscale convective systems. *Mon. Wea. Rev.*, **119 (1)**, 104–118.

Baumgart, M., P. Ghinassi, V. Wirth, T. Selz, G. C. Craig, and M. Riemer, 2019: Quantitative view on the processes governing the upscale error growth up to the planetary scale using a stochastic convection scheme. *Mon. Wea. Rev.*, **147 (5)**, 1713–1731.

Baumgart, M. and M. Riemer, 2019: Processes governing the amplification of ensemble spread in a medium-range forecast with large forecast uncertainty. *Quart. J. Roy. Meteor. Soc.*, **145 (724)**, 3252–3270.

Bednarczyk, C. N. and B. C. Ancell, 2015: Ensemble sensitivity analysis applied to a southern plains convective event. *Mon. Wea. Rev.*, **143 (1)**, 230–249.

Benjamin, S. G., G. A. Grell, J. M. Brown, T. G. Smirnova, and R. Bleck, 2004a: Mesoscale weather prediction with the RUC hybrid isentropic–terrain-following coordinate model. *Mon. Wea. Rev.*, **132 (2)**, 473–494.

Benjamin, S. G., B. D. Jamison, W. R. Moninger, S. R. Sahm, B. E. Schwartz, and T. W. Schlatter, 2010: Relative short-range forecast impact from aircraft, profiler, radiosonde, VAD, GPS-PW, METAR, and mesonet observations via the RUC hourly assimilation cycle. *Mon. Wea. Rev.*, **138 (4)**, 1319–1343.

Benjamin, S. G., et al., 2004b: An hourly assimilation–forecast cycle: The RUC. *Mon. Wea. Rev.*, **132 (2)**, 495–518.

Benjamin, S. G., et al., 2016: A North American hourly assimilation and model forecast cycle: The Rapid Refresh. *Mon. Wea. Rev.*, **144 (4)**, 1669–1694.

Berman, J. D., R. D. Torn, G. S. Romine, and M. L. Weisman, 2017: Sensitivity of northern Great Plains convection forecasts to upstream and downstream forecast errors. *Mon. Wea. Rev.*, **145 (6)**, 2141–2163.

Biddle, M. D., R. P. Brown, C. A. Doswell III, and D. R. Legates, 2020: Regional differences in the human toll from tornadoes: A new look at an old idea. *Wea. Climate Soc.*, **12 (4)**, 815–825.

Bluestein, H. B., 1993: *Synoptic-dynamic meteorology in midlatitudes. Volume II. Observations and theory of weather systems*. Oxford University Press, 594 pp pp.

Bluestein, H. B. and M. L. Weisman, 2000: The interaction of numerically simulated supercells initiated along lines. *Mon. Wea. Rev.*, **128 (9)**, 3128–3149.

Bluestein, H. B., Z. B. Wienhoff, D. D. Turner, D. W. Reif, J. C. Snyder, K. J. Thiem, and J. B. Houser, 2017: A comparison of the finescale structures of a prefrontal wind-shift line and a strong cold front in the Southern Plains of the United States. *Mon. Wea. Rev.*, **145 (8)**, 3307–3330.

Blumberg, W. G., K. T. Halbert, T. A. Supinie, P. T. Marsh, R. L. Thompson, and J. A. Hart, 2017: SHARPpy: An open-source sounding analysis toolkit for the atmospheric sciences. *Bull. Amer. Meteor. Soc.*, **98 (8)**, 1625–1636.

Blumen, W., 1972: Geostrophic adjustment. *Rev. Geophys.*, **10 (2)**, 485–528.

Bosart, L. F., B. J. Moore, J. M. Cordeira, and H. M. Archambault, 2017: Interactions of North Pacific tropical, midlatitude, and polar disturbances resulting in linked extreme weather events over North America in October 2007. *Mon. Wea. Rev.*, **145 (4)**, 1245–1273.

Bretherton, C. S. and P. K. Smolarkiewicz, 1989: Gravity waves, compensating subsidence and detrainment around cumulus clouds. *J. Atmos. Sci.*, **46 (6)**, 740–759.

Brock, F. V., K. C. Crawford, R. L. Elliott, G. W. Cuperus, S. J. Stadler, H. L. Johnson, and M. D. Eilts, 1995: The Oklahoma Mesonet: a technical overview. *J. Atmos. Oceanic Technol.*, **12 (1)**, 5–19.

Brooks, H. E., C. A. Doswell, and M. P. Kay, 2003: Climatological estimates of local daily tornado probability for the United States. *Wea. Forecasting*, **18 (4)**, 626–640.

Brooks, H. E. and R. B. Wilhelmson, 1993: Hodograph curvature and updraft intensity in numerically modeled supercells. *J. Atmos. Sci.*, **50 (12)**, 1824–1833.

Brotzge, J. and W. Donner, 2013: The tornado warning process: A review of current research, challenges, and opportunities. *Bull. Amer. Meteor. Soc.*, **94 (11)**, 1715–1733.

Brown, M. C., C. J. Nowotarski, A. R. Dean, B. T. Smith, R. L. Thompson, and J. M. Peters, 2021: The early evening transition in southeastern U.S. tornado environments. *Wea. Forecasting*, **36 (4)**, 1431—-1452.

Browning, K., 1971: Structure of the atmosphere in the vicinity of large-amplitude Kelvin-Helmholtz billows. *Quart. J. Roy. Meteor. Soc.*, **97 (413)**, 283–299.

Browning, K., 1997: The dry intrusion perspective of extra-tropical cyclone development. *Meteor. Appl.*, **4 (4)**, 317–324.

Browning, K., 2005: Observational synthesis of mesoscale structures within an explosively developing cyclone. *Quart. J. Roy. Meteor. Soc.*, **131 (606)**, 603–623.

Browning, K., S. Clough, C. Davitt, N. Roberts, T. Hewson, and P. Healey, 1995: Observations of the mesoscale sub-structure in the cold air of a developing frontal cyclone. *Quart. J. Roy. Meteor. Soc.*, **121 (526)**, 1229–1254.

Browning, K. and G. Monk, 1982: A simple model for the synoptic analysis of cold fronts. *Quart. J. Roy. Meteor. Soc.*, **108 (456)**, 435–452.

Browning, K. and N. Roberts, 1994: Structure of a frontal cyclone. *Quarterly Journal of the Royal Meteorological Society*, **120 (520)**, 1535–1557.

Browning, K. A., 1986: Conceptual models of precipitation systems. *Wea. Forecasting*, **1 (1)**, 23–41.

Bryan, G. H. and J. M. Fritsch, 2000: Moist absolute instability: The sixth static stability state. *Bull. Amer. Meteor. Soc.*, **81 (6)**, 1207–1230.

Bryan, G. H., R. Rotunno, and J. M. Fritsch, 2007: Roll circulations in the convective region of a simulated squall line. *J. Atmos. Sci.*, **64 (4)**, 1249–1266.

Bryan, G. H., J. C. Wyngaard, and J. M. Fritsch, 2003: Resolution requirements for the simulation of deep moist convection. *Mon. Wea. Rev.*, **131 (10)**, 2394–2416.

Bunkers, M. J., M. R. Hjelmfelt, and P. L. Smith, 2006: An observational examination of long-lived supercells. Part I: Characteristics, evolution, and demise. *Wea. Forecasting*, **21 (5)**, 673–688.

Bunkers, M. J., B. A. Klimowski, J. W. Zeitler, R. L. Thompson, and M. L. Weisman, 2000: Predicting supercell motion using a new hodograph technique. *Wea. Forecasting*, **15 (1)**, 61–79.

Businger, S., W. H. Bauman III, and G. F. Watson, 1991: The development of the Piedmont front and associated outbreak of severe weather on 13 March 1986. *Mon. Wea. Rev.*, **119 (9)**, 2224–2251.

Cahn, A., 1945: An investigation of the free oscillations of a simple current system. *J. Meteor.*, **2 (2)**, 113–119.

Carlson, T., S. Benjamin, G. Forbes, and Y. Li, 1983: Elevated mixed layers in the regional severe storm environment: Conceptual model and case studies. *Mon. Wea. Rev.*, **111 (7)**, 1453–1474.

Carlson, T. N., 1980: Airflow through midlatitude cyclones and the comma cloud pattern. *Mon. Wea. Rev.*, **108 (10)**, 1498–1509.

Carr, F. H., P. L. Spencer, C. A. , and J. D. Powell, 1995: A comparison of two objective analysis techniques for profiler time-height data. *Mon. Wea. Rev.*, **123 (7)**, 2165–2180.

Castle, J. A., J. D. Locatellli, J. E. Martin, and P. V. Hobbs, 1996: Structure and evolution of winter cyclones in the central United States and their effects on the distribution of precipitation. Part IV: The evolution of a drytrough on 8–9 March 1992. *Mon. Wea. Rev.*, **124 (7)**, 1591–1595.

Charney, J., 1955: The use of the primitive equations of motion in numerical prediction. *Tellus*, **7 (1)**, 22–26.

Chasteen, M. B., T. J. Galarneau, M. J. Krocak, and Z. A. B. Zibton, 2020: Environmental nuances and convective morphology during the 30 April 2017 tornado outbreak in the southeastern United States. *100^{th} Amer. Meteor. Soc. Annual Meeting, Boston, MA*, AMS.

Chasteen, M. B. and S. E. Koch, 2021a: Multiscale aspects of the 26–27 April 2011 tornado outbreak. Part I: Outbreak chronology and environmental evolution. *Mon. Wea. Rev.*, in press.

Chasteen, M. B. and S. E. Koch, 2021b: Multiscale aspects of the 26–27 April 2011 tornado outbreak. Part II: Environmental modifications and upscale feedbacks arising from latent processes. *Mon. Wea. Rev.*, in press.

Chasteen, M. B., S. E. Koch, and D. B. Parsons, 2019: Multiscale processes enabling the longevity and daytime persistence of a nocturnal mesoscale convective system. *Mon. Wea. Rev.*, **147 (2)**, 733–761.

Chiu, C. H., A. H. Schnall, C. E. Mertzlufft, R. S. Noe, A. F. Wolkin, J. Spears, M. Casey-Lockyer, and S. J. Vagi, 2013: Mortality from a tornado outbreak, Alabama, April 27, 2011. *Am J Public Health*, **103 (8)**, e52–e58.

Christenson, C. E. and J. Martin, 2012: The large-scale environment associated with the 25–28 April 2011 severe weather outbreak. Preprints, *16th Annual Severe Storms and Doppler Radar Conf.*, Des Moines, IA, National Weather Association.

Christenson, C. E., J. E. Martin, and Z. J. Handlos, 2017: A synoptic climatology of Northern Hemisphere, cold season polar and subtropical jet superposition events. *J. Climate*, **30 (18)**, 7231–7246.

Christie, D., K. Muirhead, and A. Hales, 1978: On solitary waves in the atmosphere. *J. Atmos. Sci.*, **35 (5)**, 805–825.

Christie, D., K. Muirhead, and A. Hales, 1979: Intrusive density flows in the lower troposphere: A source of atmospheric solitons. *J. Geophys. Res.*, **84 (C8)**, 4959–4970.

Christie, D. R., 1989: Long nonlinear waves in the lower atmosphere. *J. Atmos. Sci.*, **46 (11)**, 1462–1491.

Clark, A. J., J. Gao, P. T. Marsh, T. Smith, J. S. Kain, J. Correia Jr, M. Xue, and F. Kong, 2013: Tornado pathlength forecasts from 2010 to 2011 using ensemble updraft helicity. *Wea. Forecasting*, **28 (2)**, 387–407.

Clark, A. J., J. S. Kain, P. T. Marsh, J. Correia Jr, M. Xue, and F. Kong, 2012: Forecasting tornado pathlengths using a three-dimensional object identification algorithm applied to convection-allowing forecasts. *Wea. Forecasting*, **27 (5)**, 1090–1113.

Clarke, R., R. Smith, and D. Reid, 1981: The morning glory of the Gulf of Carpentaria: An atmospheric undular bore. *Mon. Wea. Rev.*, **109 (8)**, 1726–1750.

Clarke, S. J., S. L. Gray, and N. M. Roberts, 2019: Downstream influence of mesoscale convective systems. Part 2: Influence on ensemble forecast skill and spread. *Quart. J. Roy. Meteor. Soc.*, **145 (724)**, 2953–2972.

Coffer, B. E., M. D. Parker, R. L. Thompson, B. T. Smith, and R. E. Jewell, 2019: Using near-ground storm relative helicity in supercell tornado forecasting. *Wea. Forecasting*, **34 (5)**, 1417–1435.

Cohen, A. E., S. M. Cavallo, M. C. Coniglio, and H. E. Brooks, 2015: A review of planetary boundary layer parameterization schemes and their sensitivity in simulating southeastern US cold season severe weather environments. *Wea. Forecasting*, **30 (3)**, 591–612.

Cohen, A. E., S. M. Cavallo, M. C. Coniglio, H. E. Brooks, and I. L. Jirak, 2017: Evaluation of multiple planetary boundary layer parameterization schemes in southeast US cold season severe thunderstorm environments. *Wea. Forecasting*, **32 (5)**, 1857–1884.

Colle, B. A. and C. F. Mass, 1995: The structure and evolution of cold surges east of the Rocky Mountains. *Mon. Wea. Rev.*, **123 (9)**, 2577–2610.

Corfidi, S. F., S. J. Weiss, J. S. Kain, S. J. Corfidi, R. M. Rabin, and J. J. Levit, 2010: Revisiting the 3–4 April 1974 super outbreak of tornadoes. *Wea. Forecasting*, **25 (2)**, 465–510.

Cotton, W. R., M.-S. Lin, R. L. McAnelly, and C. J. Tremback, 1989: A composite model of mesoscale convective complexes. *Mon. Wea. Rev.*, **117 (4)**, 765–783.

Danielsen, E., 1974: The relationship between severe weather, major dust storms and rapid cyclogenesis. NCAR, 215–241 pp.

Danielsen, E. F., 1964: Project springfield report. Tech. rep., Defense Atomic Support Agency, Washington D. C. 20301, DASA 1517 (NTIS # AD - 607980), 97 pp.

Danielsen, E. F., 1968: Stratospheric-tropospheric exchange based on radioactivity, ozone and potential vorticity. *J. Atmos. Sci.*, **25 (3)**, 502–518.

Davies-Jones, R., 1984: Streamwise vorticity: The origin of updraft rotation in supercell storms. *J. Atmos. Sci.*, **41 (20)**, 2991–3006.

Davies-Jones, R., 1990: Test of helicity as a forecast parameter. Preprints, *16th Conf. on Severe Local Storms*, Kananaskis Park, AB, Canada.

Davies-Jones, R., R. J. Trapp, and H. B. Bluestein, 2001: Tornadoes and tornadic storms. *Severe Convective Storms, Meteor. Monogr.*, No. 50, Amer. Meteor. Soc., 167–221.

Davis, C. A., 1992: Piecewise potential vorticity inversion. *J. Atmos. Sci.*, **49 (16)**, 1397–1411.

Davis, C. A. and K. A. Emanuel, 1991: Potential vorticity diagnostics of cyclogenesis. *Mon. Wea. Rev.*, **119 (8)**, 1929–1953.

Davis, C. A. and M. L. Weisman, 1994: Balanced dynamics of mesoscale vortices produced in simulated convective systems. *J. Atmos. Sci.*, **51 (14)**, 2005–2030.

de Groot-Hedlin, C. D., M. A. Hedlin, and K. T. Walker, 2014: Detection of gravity waves across the USArray: A case study. *Earth and Planetary Science Letters*, **402**, 346–352.

Dean, A. and R. Schneider, 2008: Forecast challenges at the NWS Storm Prediction Center. Preprints, *24th Conf. on Severe Local Storms*, Charleston SC, Amer. Meteor. Soc.

Dial, G. L., J. P. Racy, and R. L. Thompson, 2010: Short-term convective mode evolution along synoptic boundaries. *Wea. Forecasting*, **25 (5)**, 1430–1446.

Dickinson, M. J., L. F. Bosart, W. E. Bracken, G. J. Hakim, D. M. Schultz, M. A. Bedrick, and K. R. Tyle, 1997: The March 1993 superstorm cyclogenesis: Incipient phase synoptic- and convective-scale flow interaction and model performance. *Mon. Wea. Rev.*, **125 (12)**, 3041–3072.

Doswell, C., R. Edwards, R. Thompson, J. Hart, and K. Crosbie, 2006: A simple and flexible method for ranking severe weather events. *Wea. Forecasting*, **21 (6)**, 939–951.

Doswell, C. A., 1991: A review for forecasters on the application of hodographs to forecasting severe thunderstorms. *Natl. Weather Dig.*, **16 (1)**, 2–16.

Doswell, C. A. and L. F. Bosart, 2001: Extratropical synoptic-scale processes and severe convection. *Severe Convective Storms*, Springer, 27–69.

Duchon, C. E., 1979: Lanczos filtering in one and two dimensions. *J. Appl. Meteor.*, **18 (8)**, 1016–1022.

Duda, J. D. and W. A. Gallus, 2010: Spring and summer midwestern severe weather reports in supercells compared to other morphologies. *Wea. Forecasting*, **25 (1)**, 190–206.

Duell, R. S. and M. S. Van Den Broeke, 2016: Climatology, synoptic conditions, and misanalyses of Mississippi river valley drylines. *Mon. Wea. Rev.*, **144 (3)**, 927–943.

Durran, D. R., 1990: Mountain waves and downslope winds. *Atmospheric processes over complex terrain*, Springer, 59–81.

Ecklund, W. L., D. A. Carter, and B. B. Balsley, 1988: A UHF wind profiler for the boundary layer: Brief description and initial results. *J. Atmos. Oceanic Technol.*, **5 (3)**, 432–441.

Ek, M., K. Mitchell, Y. Lin, E. Rogers, P. Grunmann, V. Koren, G. Gayno, and J. Tarpley, 2003: Implementation of Noah land surface model advances in the National Centers for Environmental Prediction operational mesoscale Eta model. *Journal of Geophysical Research: Atmospheres*, **108 (D22)**.

Ellis, K. N., D. Burow, K. N. Gassert, L. R. Mason, and M. S. Porter, 2020: Forecaster perceptions and climatological analysis of the influence of convective mode on tornado climatology and warning success. *Ann. Amer. Assoc. Geogr.*, **110 (4)**, 1075–1094.

Emanuel, K. A., 1979: Inertial instability and mesoscale convective systems. Part I: Linear theory of inertial instability in rotating viscous fluids. *J. Atmos. Sci.*, **36 (12)**, 2425–2449.

Ertel, H., 1942: Ein neuer hydrodynamischer wirbelsatz. *Met. Z.*, **59**, 277–281.

Flournoy, M. D. and M. C. Coniglio, 2019: Origins of vorticity in a simulated tornadic mesovortex observed during PECAN on 6 July 2015. *Mon. Wea. Rev.*, **147 (1)**, 107–134.

Fritsch, J. and R. Maddox, 1981: Convectively driven mesoscale weather systems aloft. Part I: Observations. *J. Appl. Meteor.*, **20 (1)**, 9–19.

Fritsch, J., J. Murphy, and J. Kain, 1994: Warm core vortex amplification over land. *J. Atmos. Sci.*, **51 (13)**, 1780–1807.

Fuhrmann, C. M., C. E. Konrad, M. M. Kovach, J. T. McLeod, W. G. Schmitz, and P. G. Dixon, 2014: Ranking of tornado outbreaks across the United States and their climatological characteristics. *Wea. Forecasting*, **29 (3)**, 684–701.

Fujita, T. T., D. L. Bradbury, and C. Van Thullenar, 1970: Palm Sunday tornadoes of April 11, 1965. *Mon. Wea. Rev.*, **98 (1)**, 29–69.

Gallo, B. T., A. J. Clark, and S. R. Dembek, 2016: Forecasting tornadoes using convection-permitting ensembles. *Wea. Forecasting*, **31 (1)**, 273–295.

Galway, J. G. and A. Pearson, 1981: Winter tornado outbreaks. *Mon. Wea. Rev.*, **109 (5)**, 1072–1080.

Garner, J., 2012: Environments of significant tornadoes occurring within the warm sector versus those occurring along surface baroclinic boundaries. *Electronic J. Severe Storms Meteor.*, **7 (5)**.

Gebauer, J. G., A. Shapiro, E. Fedorovich, and P. Klein, 2018: Convection initiation caused by heterogeneous low-level jets over the Great Plains. *Mon. Wea. Rev.*, **146 (8)**, 2615–2637.

Gold, D. A. and J. W. Nielsen-Gammon, 2008: Potential vorticity diagnosis of the severe convective regime. Part IV: Comparison with modeling simulations of the Moore tornado outbreak. *Mon. Wea. Rev.*, **136 (5)**, 1612–1629.

Goler, R. A. and M. J. Reeder, 2004: The generation of the morning glory. *J. Atmos. Sci.*, **61 (12)**, 1360–1376.

Grams, C. M. and H. M. Archambault, 2016: The key role of diabatic outflow in amplifying the midlatitude flow: A representative case study of weather systems surrounding western North Pacific extratropical transition. *Mon. Wea. Rev.*, **144 (10)**, 3847–3869.

Grams, C. M., S. C. Jones, C. A. Davis, P. A. Harr, and M. Weissmann, 2013: The impact of Typhoon Jangmi (2008) on the midlatitude flow. Part I: Upper-level ridgebuilding and modification of the jet. *Quart. J. Roy. Meteor. Soc.*, **139 (677)**, 2148–2164.

Grams, J. S., R. L. Thompson, D. V. Snively, J. A. Prentice, G. M. Hodges, and L. J. Reames, 2012: A climatology and comparison of parameters for significant tornado events in the United States. *Wea. Forecasting*, **27 (1)**, 106–123.

Grasmick, C., B. Geerts, D. D. Turner, Z. Wang, and T. Weckwerth, 2018: The relation between nocturnal MCS evolution and its outflow boundaries in the stable boundary layer: An observational study of the 15 July 2015 MCS in PECAN. *Mon. Wea. Rev.*, **146 (10)**, 3203–3226.

Grell, G. A. and D. Devenyi, 2002: A generalized approach to parameterizing convection combining ensemble and data assimilation techniques. *Geophys. Res. Lett.*, **29 (14)**, 38–1.

Griffiths, M., A. J. Thorpe, and K. A. Browning, 2000: Convective destabilization by a tropopause fold diagnosed using potential-vorticity inversion. *Quart. J. Roy. Meteor. Soc.*, **126 (562)**, 125–144.

Guyer, J. L. and A. R. Dean, 2010: Tornadoes within weak CAPE environments across the continental United States. Preprints, *25th Conf. on Severe Local Storms*, Denver, CO, Amer. Meteor. Soc.

Guyer, J. L., D. A. Imy, and A. Kis, 2006: Cool season significant (F2-F5) tornadoes in the Gulf Coast states. Preprints, *23rd Conf. on Severe Local Storms*, St. Louis, MO, Amer. Meteor. Soc.

Haghi, K. R., et al., 2019: Bore-ing into nocturnal convection. *Bull. Amer. Meteor. Soc.*, **100 (6)**, 1103–1121.

Hamill, T. M., R. S. Schneider, H. E. Brooks, G. S. Forbes, H. B. Bluestein, M. Steinberg, D. Meléndez, and R. M. Dole, 2005: The May 2003 extended tornado outbreak. *Bull. Amer. Meteor. Soc.*, **86 (4)**, 531–542.

Hanley, K., D. Kirshbaum, N. Roberts, and G. Leoncini, 2013: Sensitivities of a squall line over central Europe in a convective-scale ensemble. *Mon. Wea. Rev.*, **141 (1)**, 112–133.

Hartung, D. C., J. A. Otkin, J. E. Martin, and D. D. Turner, 2010: The life cycle of an undular bore and its interaction with a shallow, intense cold front. *Mon. Wea. Rev.*, **138 (3)**, 886–908.

Hepper, J. I. L., R. M. and J. M. Milne, 2016: Assessing the skill of convection-allowing ensemble forecasts of severe MCS winds from the SSEO. Preprints, *28th Conf. on Severe Local Storms*, Portland, OR, Amer. Meteor. Soc., 16B.2, `https://ams.confex.com/ams/28SLS/webprogram/Paper300\,134.html`.

Hersbach, H., et al., 2020: The era5 global reanalysis. *Quart. J. Roy. Meteor. Soc.*, **146 (730)**, 1999–2049.

Hill, A. J., C. C. Weiss, and B. C. Ancell, 2016: Ensemble sensitivity analysis for mesoscale forecasts of dryline convection initiation. *Mon. Wea. Rev.*, **144 (11)**, 4161–4182.

Hitchcock, S. M. and R. S. Schumacher, 2020: Analysis of back-building convection in simulations with a strong low-level stable layer. *Mon. Wea. Rev.*, **148 (9)**, 3773–3797.

Hobbs, P. V., J. D. Locatelli, and J. E. Martin, 1990: Cold fronts aloft and the forecasting of precipitation and severe weather east of the Rocky Mountains. *Wea. Forecasting*, **5 (4)**, 613–626.

Hobbs, P. V., J. D. Locatelli, and J. E. Martin, 1996: A new conceptual model for cyclones generated in the lee of the Rocky Mountains. *Bull. Amer. Meteor. Soc.*, **77 (6)**, 1169–1178.

Hoch, J. and P. Markowski, 2005: A climatology of springtime dryline position in the US Great Plains region. *J. Climate*, **18 (12)**, 2132–2137.

Holzman, B., 1936: Synoptic determination and forecasting significance of cold fronts aloft. *Mon. Wea. Rev.*, **64 (12)**, 400–414.

Homeyer, C. R. and K. P. Bowman, 2013: Rossby wave breaking and transport between the tropics and extratropics above the subtropical jet. *J. Atmos. Sci.*, **70 (2)**, 607–626.

Hoskins, B. J., 1975: The geostrophic momentum approximation and the semi-geostrophic equations. *J. Atmos. Sci.*, **32 (2)**, 233–242.

Houghton, D. D. and A. Kasahara, 1968: Nonlinear shallow fluid flow over an isolated ridge. *Commun. Pure Appl. Math*, **21 (1)**, 1–23.

Houze, R. A., 1989: Observed structure of mesoscale convective systems and implications for large-scale heating. *Quart. J. Roy. Meteor. Soc.*, **115 (487)**, 425–461.

Houze, R. A., 2018: 100 years of research on mesoscale convective systems. *Meteor. Monogr.*, **59**, 17–1.

Hoxit, L. R. and C. F. Chappell, 1975: Tornado outbreak of April 3-4, 1974: Synoptic analysis. NOAA Tech. Rep. ERL 338-APCL 37, 48pp.

Iacono, M. J., J. S. Delamere, E. J. Mlawer, M. W. Shephard, S. A. Clough, and W. D. Collins, 2008: Radiative forcing by long-lived greenhouse gases: Calculations with the AER radiative transfer models. *Journal of Geophysical Research: Atmospheres*, **113 (D13)**.

Jacques, A. A., J. D. Horel, E. T. Crosman, and F. L. Vernon, 2017: Tracking mesoscale pressure perturbations using the USArray transportable array. *Mon. Wea. Rev.*, **145 (8)**, 3119–3142.

Jensen, M. P., et al., 2016: The midlatitude continental convective clouds experiment (MC3E). *Bull. Amer. Meteor. Soc.*, **97 (9)**, 1667–1686.

Johns, R. H., 1993: Meteorological conditions associated with bow echo development in convective storms. *Wea. Forecasting*, **8 (2)**, 294–299.

Johnson, R. H. and P. J. Hamilton, 1988: The relationship of surface pressure features to the precipitation and airflow structure of an intense midlatitude squall line. *Mon. Wea. Rev.*, **116 (7)**, 1444–1473.

Kain, J. S., S. R. Dembek, S. J. Weiss, J. L. Case, J. J. Levit, and R. A. Sobash, 2010: Extracting unique information from high-resolution forecast models: Monitoring selected fields and phenomena every time step. *Wea. Forecasting*, **25 (5)**, 1536–1542.

Kain, J. S. and J. M. Fritsch, 1998: Multiscale convective overturning in mesoscale convective systems: Reconciling observations, simulations, and theory. *Mon. Wea. Rev.*, **126 (8)**, 2254–2273.

Kain, J. S., et al., 2008: Some practical considerations regarding horizontal resolution in the first generation of operational convection-allowing NWP. *Wea. Forecasting*, **23 (5)**, 931–952.

Kaplan, M. L., Y.-L. Lin, D. W. Hamilton, and R. A. Rozumalski, 1998: The numerical simulation of an unbalanced jetlet and its role in the Palm Sunday 1994 tornado outbreak in Alabama and Georgia. *Mon. Wea. Rev.*, **126 (8)**, 2133–2165.

Kelnosky, R. T., G. J. Tripoli, and J. E. Martin, 2018: Subtropical/polar jet influence on Plains and Southeast tornado outbreaks. *Nat. Hazards*, **93 (1)**, 373–392.

Keyser, D. and M. Shapiro, 1986: A review of the structure and dynamics of upper-level frontal zones. *Mon. Wea. Rev.*, **114 (2)**, 452–499.

Keyser, D. A. and D. R. Johnson, 1984: Effects of diabatic heating on the ageostrophic circulation of an upper tropospheric jet streak. *Mon. Wea. Rev.*, **112 (9)**, 1709–1724.

King, J. R., M. D. Parker, K. D. Sherburn, and G. M. Lackmann, 2017: Rapid evolution of cool season, low-cape severe thunderstorm environments. *Wea. Forecasting*, **32 (2)**, 763–779.

Kis, A. K. and J. M. Straka, 2010: Nocturnal tornado climatology. *Wea. Forecasting*, **25 (2)**, 545–561.

Klemp, J. B., R. Rotunno, and W. C. Skamarock, 1997: On the propagation of internal bores. *J. Fluid Mech.*, **331**, 81–106.

Knippertz, P. and A. H. Fink, 2008: Dry-season precipitation in tropical West Africa and its relation to forcing from the extratropics. *Mon. Wea. Rev.*, **136 (9)**, 3579–3596.

Knupp, K. R., et al., 2014: Meteorological overview of the devastating 27 April 2011 tornado outbreak. *Bull. Amer. Meteor. Soc.*, **95 (7)**, 1041–1062.

Koch, S. E., 2001: Real-time detection of split fronts using mesoscale models and WSR-88D radar products. *Wea. Forecasting*, **16 (1)**, 35–55.

Koch, S. E. and W. L. Clark, 1999: A nonclassical cold front observed during COPS-91: Frontal structure and the process of severe storm initiation. *J. Atmos. Sci.*, **56 (16)**, 2862–2890.

Koch, S. E., M. DesJardins, and P. J. Kocin, 1983: An interactive Barnes objective map analysis scheme for use with satellite and conventional data. *J. Climate Appl. Meteor.*, **22 (9)**, 1487–1503.

Koch, S. E. and P. B. Dorian, 1988: A mesoscale gravity wave event observed during CCOPE. Part III: Wave environment and probable source mechanisms. *Mon. Wea. Rev.*, **116 (12)**, 2570–2592.

Koch, S. E., P. B. Dorian, R. Ferrare, S. Melfi, W. C. Skillman, and D. Whiteman, 1991: Structure of an internal bore and dissipating gravity current as revealed by Raman lidar. *Mon. Wea. Rev.*, **119 (4)**, 857–887.

Koch, S. E., W. Feltz, F. Fabry, M. Pagowski, B. Geerts, K. M. Bedka, D. O. Miller, and J. W. Wilson, 2008a: Turbulent mixing processes in atmospheric bores and solitary waves deduced from profiling systems and numerical simulation. *Mon. Wea. Rev.*, **136 (4)**, 1373–1400.

Koch, S. E., C. Flamant, J. W. Wilson, B. M. Gentry, and B. D. Jamison, 2008b: An atmospheric soliton observed with Doppler radar, differential absorption lidar, and a molecular Doppler lidar. *J. Atmos. Oceanic Technol.*, **25 (8)**, 1267–1287.

Koch, S. E., R. E. Golus, and P. B. Dorian, 1988: A mesoscale gravity wave event observed during CCOPE. Part II: Interactions between mesoscale convective systems and the antecedent waves. *Mon. Wea. Rev.*, **116 (12)**, 2545–2569.

Koch, S. E., D. Hamilton, D. Kramer, and A. Langmaid, 1998: Mesoscale dynamics in the Palm Sunday tornado outbreak. *Mon. Wea. Rev.*, **126 (8)**, 2031–2060.

Koch, S. E. and J. McCarthy, 1982: The evolution of an Oklahoma dryline. Part II: Boundary-layer forcing of mesoconvective systems. *J. Atmos. Sci.*, **39 (2)**, 237–257.

Kocin, P. J., L. W. Uccellini, and R. A. Petersen, 1986: Rapid evolution of a jet streak circulation in a pre-convective environment. *Meteor. Atmos. Phys.*, **35 (3)**, 103–138.

Kong, K.-Y., 2006: Understanding the genesis of Hurricane Vince through the surface pressure tendency equation. Preprints,, 27th Conf. on Hurricanes and Tropical Meteorology, Monterey, CA, Amer. Meteor. Soc.[Available online at `http://ams.confex.com/ams/pdfpapers/108938.pdf.`], Vol. 6.

Kuettner, J. P., P. A. Hildebrand, and T. L. Clark, 1987: Convection waves: Observations of gravity wave systems over convectively active boundary layers. *Quart. J. Roy. Meteor. Soc.*, **113 (476)**, 445–467.

Kuo, Y.-H., M. Shapiro, and E. G. Donall, 1991: The interaction between baroclinic and diabatic processes in a numerical simulation of a rapidly intensifying extratropical marine cyclone. *Mon. Wea. Rev.*, **119 (2)**, 368–384.

Lackmann, G. M., 2002: Cold-frontal potential vorticity maxima, the low-level jet, and moisture transport in extratropical cyclones. *Mon. Wea. Rev.*, **130 (1)**, 59–74.

Lane, T. P. and M. J. Reeder, 2001: Convectively generated gravity waves and their effect on the cloud environment. *J. Atmos. Sci.*, **58 (16)**, 2427–2440.

Lee, B. D., B. F. Jewett, and R. B. Wilhelmson, 2006: The 19 April 1996 Illinois tornado outbreak. Part I: Cell evolution and supercell isolation. *Wea. Forecasting*, **21 (4)**, 433–448.

Lee, B. D. and R. B. Wilhelmson, 1997: The numerical simulation of non-supercell tornadogenesis. Part I: Initiation and evolution of pretornadic misocyclone circulations along a dry outflow boundary. *J. Atmos. Sci.*, **54 (1)**, 32–60.

Lichtblau, S., 1936: Upper-air cold fronts in North America. *Mon. Wea. Rev.*, **64**, 414–425.

Lindzen, R. and K. Tung, 1976: Banded convective activity and ducted gravity waves. *Mon. Wea. Rev.*, **104 (12)**, 1602–1617.

Liu, C. and M. W. Moncrieff, 2004: Effects of convectively generated gravity waves and rotation on the organization of convection. *J. Atmos. Sci.*, **61 (17)**, 2218–2227.

Lloyd, J., 1942: The development and trajectories of tornadoes. *Mon. Wea. Rev.*, **70 (4)**, 65–75.

Locatelli, J. D., J. E. Martin, J. A. Castle, and P. V. Hobbs, 1995: Structure and evolution of winter cyclones in the central United States and their effects on the distribution of precipitation. Part III: The development of a squall line associated with weak cold frontogenesis aloft. *Mon. Wea. Rev.*, **123 (9)**, 2641–2662.

Locatelli, J. D., R. D. Schwartz, M. T. Stoelinga, and P. V. Hobbs, 2002a: Norwegian-type and cold front aloft–type cyclones east of the Rocky Mountains. *Wea. Forecasting*, **17 (1)**, 66–82.

Locatelli, J. D., M. T. Stoelinga, and P. V. Hobbs, 2002b: A new look at the super outbreak of tornadoes on 3–4 April 1974. *Mon. Wea. Rev.*, **130 (6)**, 1633–1651.

Locatelli, J. D., M. T. Stoelinga, R. D. Schwartz, and P. V. Hobbs, 1997: Surface convergence induced by cold fronts aloft and prefrontal surges. *Mon. Wea. Rev.*, **125 (11)**, 2808–2820.

Lutzak, P. A., 2013: A proposal for analyzing and forecasting lower-atmospheric undular bores in the western Gulf of Mexico region. *Wea. Forecasting*, **28 (1)**, 55–76.

Maddox, R., D. Perkey, and J. Fritsch, 1981: Evolution of upper tropospheric features during the development of a mesoscale convective complex. *J. Atmos. Sci.*, **38 (8)**, 1664–1674.

Maddox, R. A., 1980: Mesoscale convective complexes. *Bull. Amer. Meteor. Soc.*, **61 (11)**, 1374–1387.

Maddox, R. A. and C. A. Doswell, 1982: An examination of jet stream configurations, 500 mb vorticity advection and low-level thermal advection patterns during extended periods of intense convection. *Mon. Wea. Rev.*, **110 (3)**, 184–197.

Maddox, R. A., M. S. Gilmore, C. A. Doswell III, R. H. Johns, C. A. Crisp, D. W. Burgess, J. A. Hart, and S. F. Piltz, 2013: Meteorological analyses of the Tri-State tornado event of March 1925. *Electronic J. Severe Storms Meteor.*, **8 (1)**.

Maddox, R. A., L. R. Hoxit, and C. F. Chappell, 1980: A study of tornadic thunderstorm interactions with thermal boundaries. *Mon. Wea. Rev.*, **108 (3)**, 322–336.

Markowski, P., C. Hannon, J. Frame, E. Lancaster, A. Pietrycha, R. Edwards, and R. L. Thompson, 2003: Characteristics of vertical wind profiles near supercells obtained from the Rapid Update Cycle. *Wea. Forecasting*, **18 (6)**, 1262–1272.

Markowski, P. and Y. Richardson, 2006: On the classification of vertical wind shear as directional shear versus speed shear. *Wea. Forecasting*, **21 (2)**, 242–247.

Markowski, P. and Y. Richardson, 2011: *Mesoscale meteorology in midlatitudes*. Wiley-Blackwell, 424 pp.

Martin, J. E., J. D. Locatelli, P. V. Hobbs, P.-Y. Wang, and J. A. Castle, 1995: Structure and evolution of winter cyclones in the central United States and their effects on the distribution of precipitation. Part I: A synoptic-scale rainband associated with a dryline and lee trough. *Mon. Wea. Rev.*, **123 (2)**, 241–264.

McCarthy, J. and S. E. Koch, 1982: The evolution of an Oklahoma dryline. Part I: A meso-and subsynoptic-scale analysis. *J. Atmos. Sci.*, **39 (2)**, 225–236.

McCaul, E. W. and M. L. Weisman, 2001: The sensitivity of simulated supercell structure and intensity to variations in the shapes of environmental buoyancy and shear profiles. *Mon. Wea. Rev.*, **129 (4)**, 664–687.

Melhauser, C. and F. Zhang, 2012: Practical and intrinsic predictability of severe and convective weather at the mesoscales. *J. Atmos. Sci.*, **69 (11)**, 3350–3371.

Miller, D. A. and F. Sanders, 1980: Mesoscale conditions for the severe convection of 3 April 1974 in the east-central United States. *J. Atmos. Sci.*, **37 (5)**, 1041–1055.

Milne, J., 2016: Verification of 10-Meter Wind Forecasts from NSSL-WRF in Predicting Severe Wind-Producing MCSs. M.S. thesis, School of Meteorology, University of Oklahoma, 77pp.

Molina, M. J. and J. T. Allen, 2019: On the moisture origins of tornadic thunderstorms. *J. Climate*, **32 (14)**, 4321–4346.

Moore, B. J., D. Keyser, and L. F. Bosart, 2019: Linkages between extreme precipitation events in the central and eastern United States and Rossby wave breaking. *Mon. Wea. Rev.*, **147 (9)**, 3327–3349.

Morgan, M. C. and J. W. Nielsen-Gammon, 1998: Using tropopause maps to diagnose midlatitude weather systems. *Mon. Wea. Rev.*, **126 (10)**, 2555–2579.

Nakanishi, M. and H. Niino, 2006: An improved Mellor-Yamada level-3 model: Its numerical stability and application to a regional prediction of advection fog. *Boundary-Layer Meteorology*, **119 (2)**, 397–407.

Nakanishi, M. and H. Niino, 2009: Development of an improved turbulence closure model for the atmospheric boundary layer. *Journal of the Meteorological Society of Japan. Ser. II*, **87 (5)**, 895–912.

Neiman, P. J., F. M. Ralph, M. Shapiro, B. Smull, and D. Johnson, 1998: An observational study of fronts and frontal mergers over the continental United States. *Mon. Wea. Rev.*, **126 (10)**, 2521–2554.

Neiman, P. J. and R. M. Wakimoto, 1999: The interaction of a Pacific cold front with shallow air masses east of the Rocky Mountains. *Mon. Wea. Rev.*, **127 (9)**, 2102–2127.

Nicholls, M. E., R. A. Pielke, and W. R. Cotton, 1991: Thermally forced gravity waves in an atmosphere at rest. *J. Atmos. Sci.*, **48 (16)**, 1869–1884.

Ninomiya, K., 1971: Mesoscale modification of synoptic situations from thunderstorm development as revealed by ATS III and aerological data. *J. Appl. Meteor.*, **10 (6)**, 1103–1121.

NOAA, 2011: State of the Climate, Tornadoes: Annual 2011. [Available online at https://www.ncdc.noaa.gov/sotc/tornadoes/201113.].

NOAA, 2017: On This Day: 2011 Tornado Super Outbreak. [Available online at www.ncei.noaa.gov/news/2011-tornado-super-outbreak.].

Nolen, R. H., 1959: A radar pattern associated with tornadoes. *Bull. Amer. Meteor. Soc.*, **40 (6)**, 277–279.

Novak, D. R., B. A. Colle, and A. R. Aiyyer, 2010: Evolution of mesoscale precipitation band environments within the comma head of northeast U.S. cyclones. *Mon. Wea. Rev.*, **138 (6)**, 2354–2374.

Olson, J. B., T. Smirnova, J. S. Kenyon, D. D. Turner, J. M. Brown, W. Zheng, and B. W. Green, 2021: A description of the MYNN surface-layer scheme. *NOAA Technical Memorandum OAR GSL-67,* 26 pp. [Available online at https://repository.library.noaa.gov/view/noaa/30605].

Olsson, P. Q. and W. R. Cotton, 1997: Balanced and unbalanced circulations in a primitive equation simulation of a midlatitude MCC. Part II: Analysis of balance. *J. Atmos. Sci.*, **54 (4)**, 479–497.

Ortega, K., T. Smith, J. Zhang, C. Langston, Y. Qi, S. Stevens, and J. Tate, 2012: The multi-year reanalysis of remotely sensed storms (MYRORSS) project. *26th Conf. on Severe Local Storms, Nashville, TN, Amer. Meteor. Soc.,* [Available online at https://ams.confex.com/ams/26SLS/webprogram/Handout/Paper211413/p4_74_ortegaetal_myrorss.pdf.

O'Neill, M. E., L. Orf, G. M. Heymsfield, and K. Halbert, 2021: Hydraulic jump dynamics above supercell thunderstorms. *Science*, **373 (6560)**, 1248–1251.

Parker, M. D., 2017: How much does "backing aloft" actually impact a supercell? *Wea. Forecasting*, **32 (5)**, 1937–1957.

Parsons, D. B., M. A. Shapiro, and E. Miller, 2000: The mesoscale structure of a nocturnal dryline and of a frontal–dryline merger. *Mon. Wea. Rev.*, **128 (11)**, 3824–3838.

Phoenix, D. B., C. R. Homeyer, M. C. Barth, and S. B. Trier, 2019: Mechanisms responsible for stratosphere-to-troposphere transport around a mesoscale convective system anvil. *J. Geophys. Res.*

Plougonven, R. and F. Zhang, 2014: Internal gravity waves from atmospheric jets and fronts. *Rev. Geophys.*, **52 (1)**, 33–76.

Posselt, D. J. and J. E. Martin, 2004: The effect of latent heat release on the evolution of a warm occluded thermal structure. *Mon. Wea. Rev.*, **132 (2)**, 578–599.

Potvin, C. K. and M. L. Flora, 2015: Sensitivity of idealized supercell simulations to horizontal grid spacing: Implications for Warn-on-Forecast. *Mon. Wea. Rev.*, **143 (8)**, 2998–3024.

Powers, J. G., et al., 2017: The weather research and forecasting model: Overview, system efforts, and future directions. *Bull. Amer. Meteor. Soc.*, **98 (8)**, 1717–1737.

Pyle, M. E., D. Keyser, and L. F. Bosart, 2004: A diagnostic study of jet streaks: Kinematic signatures and relationship to coherent tropopause disturbances. *Mon. Wea. Rev.*, **132 (1)**, 297–319.

Ralph, F. M., P. J. Neiman, D. W. Van de Kamp, and D. Law, 1995: Using spectral moment data from NOAA's 404-MHz radar wind profilers to observe precipitation. *Bull. Amer. Meteor. Soc.*, **76 (10)**, 1717–1740.

Rasmussen, E., 2015: VORTEX-Southeast program overview. *National Severe Storms Laboratory Rep*, **36**.

Rasmussen, E. N., 2003: Refined supercell and tornado forecast parameters. *Wea. Forecasting*, **18 (3)**, 530–535.

Rasmussen, E. N. and D. O. Blanchard, 1998: A baseline climatology of sounding-derived supercell and tornado forecast parameters. *Wea. Forecasting*, **13 (4)**, 1148–1164.

Raymond, D., 1992: Nonlinear balance and potential-vorticity thinking at large rossby number. *Quart. J. Roy. Meteor. Soc.*, **118 (507)**, 987–1015.

Raymond, D. and H. Jiang, 1990: A theory for long-lived mesoscale convective systems. *J. Atmos. Sci.*, **47 (24)**, 3067–3077.

Riemer, M., S. C. Jones, and C. A. Davis, 2008: The impact of extratropical transition on the downstream flow: An idealized modelling study with a straight jet. *Quart. J. Roy. Meteor. Soc.*, **134 (630)**, 69–91.

Rodwell, M. J., et al., 2013: Characteristics of occasional poor medium-range weather forecasts for Europe. *Bull. Amer. Meteor. Soc.*, **94 (9)**, 1393–1405.

Roebber, P. J., D. M. Schultz, and R. Romero, 2002: Synoptic regulation of the 3 May 1999 tornado outbreak. *Wea. Forecasting*, **17 (3)**, 399–429.

Rogers, J. W., B. A. Hagenhoff, A. E. Cohen, R. L. Thompson, B. T. Smith, and E. E. Carpenter, 2017: Lower Mississippi River Valley quasi-linear convective system tornado environments and radar signatures. *J. Operational Meteor.*, **5 (4)**.

Rossby, C.-G., 1938: On the mutual adjustment of pressure and velocity distributions in certain simple current systems, II. *J. mar. Res*, **1 (3)**, 239–263.

Rottman, J. W. and F. Einaudi, 1993: Solitary waves in the atmosphere. *J. Atmos. Sci.*, **50 (14)**, 2116–2136.

Rottman, J. W. and J. E. Simpson, 1989: The formation of internal bores in the atmosphere: A laboratory model. *Quart. J. Roy. Meteor. Soc.*, **115 (488)**, 941–963.

Rotunno, R. and J. Klemp, 1985: On the rotation and propagation of simulated supercell thunderstorms. *J. Atmos. Sci.*, **42 (3)**, 271–292.

Rotunno, R. and J. B. Klemp, 1982: The influence of the shear-induced pressure gradient on thunderstorm motion. *Mon. Wea. Rev.*, **110 (2)**, 136–151.

Rotunno, R., J. B. Klemp, and M. L. Weisman, 1988: A theory for strong, long-lived squall lines. *J. Atmos. Sci.*, **45 (3)**, 463–485.

Rotunno, R., W. C. Skamarock, and C. Snyder, 1994: An analysis of frontogenesis in numerical simulations of baroclinic waves. *J. Atmos. Sci.*, **51 (23)**, 3373–3398.

Rowe, S. M. and M. H. Hitchman, 2015: On the role of inertial instability in stratosphere–troposphere exchange near midlatitude cyclones. *J. Atmos. Sci.*, **72 (5)**, 2131–2151.

Rowe, S. M. and M. H. Hitchman, 2016: On the relationship between inertial instability, poleward momentum surges, and jet intensifications near midlatitude cyclones. *J. Atmos. Sci.*, **73 (6)**, 2299–2315.

Ruppert, J. H. and L. F. Bosart, 2014: A case study of the interaction of a mesoscale gravity wave with a mesoscale convective system. *Mon. Wea. Rev.*, **142 (4)**, 1403–1429.

Saide, P., et al., 2015: Central American biomass burning smoke can increase tornado severity in the US. *Geophys. Res. Lett.*, **42 (3)**, 956–965.

Sanders, S., T. Adams, and E. Joseph, 2020: Severe weather forecasts and public perceptions: An Analysis of the 2011 Super Outbreak in Tuscaloosa, Alabama. *Wea. Climate Soc.*, **12 (3)**, 473–485.

Schaefer, J. T., 1974: The life cycle of the dryline. *J. Appl. Meteor.*, **13 (4)**, 444–449.

Schmit, T. J., P. Griffith, M. M. Gunshor, J. M. Daniels, S. J. Goodman, and W. J. Lebair, 2017: A closer look at the ABI on the GOES-R series. *Bull. Amer. Meteor. Soc.*, **98 (4)**, 681–698.

Schultz, D. M., 2005: A review of cold fronts with prefrontal troughs and wind shifts. *Mon. Wea. Rev.*, **133 (8)**, 2449–2472.

Schultz, D. M. and C. A. Doswell, 1999: Conceptual models of upper-level frontogenesis in south-westerly and north-westerly flow. *Quart. J. Roy. Meteor. Soc.*, **125 (559)**, 2535–2562.

Schultz, D. M., D. Keyser, and L. F. Bosart, 1998: The effect of large-scale flow on low-level frontal structure and evolution in midlatitude cyclones. *Mon. Wea. Rev.*, **126 (7)**, 1767–1791.

Schultz, D. M. and P. N. Schumacher, 1999: The use and misuse of conditional symmetric instability. *Mon. Wea. Rev.*, **127 (12)**, 2709–2732.

Schultz, D. M., C. C. Weiss, and P. M. Hoffman, 2007: The synoptic regulation of dryline intensity. *Mon. Wea. Rev.*, **135 (5)**, 1699–1709.

Schultz, D. M., et al., 2019: Extratropical cyclones: a century of research on meteorology's centerpiece. *Meteor. Monogr.*, **59**, 16–1.

Schumacher, R. S., 2011: Ensemble-based analysis of factors leading to the development of a multiday warm-season heavy rain event. *Mon. Wea. Rev.*, **139 (9)**, 3016–3035.

Schwartz, C. S., G. S. Romine, R. A. Sobash, K. R. Fossell, and M. L. Weisman, 2019: NCAR's real-time convection-allowing ensemble project. *Bull. Amer. Meteor. Soc.*, **100 (2)**, 321–343.

Schwartz, C. S., G. S. Romine, M. L. Weisman, R. A. Sobash, K. R. Fossell, K. W. Manning, and S. B. Trier, 2015: A real-time convection-allowing ensemble prediction system initialized by mesoscale ensemble Kalman filter analyses. *Wea. Forecasting*, **30 (5)**, 1158–1181.

Schwartz, C. S., M. Wong, G. S. Romine, R. A. Sobash, and K. R. Fossell, 2020: Initial conditions for convection-allowing ensembles over the conterminous United States. *Mon. Wea. Rev.*, **148 (7)**, 2645–2669.

Shapiro, M. A. and D. Keyser, 1990: Fronts, jet streams and the tropopause. *Extratropical cyclones: The Erik Palmén Memorial Volume*, C. W. Newton and E. O. Holopainen, Eds., Amer. Meteor. Soc., 167–191.

Sherburn, K. D. and M. D. Parker, 2014: Climatology and ingredients of significant severe convection in high-shear, low-CAPE environments. *Wea. Forecasting*, **29 (4)**, 854–877.

Sherburn, K. D., M. D. Parker, J. R. King, and G. M. Lackmann, 2016: Composite environments of severe and nonsevere high-shear, low-CAPE convective events. *Wea. Forecasting*, **31 (6)**, 1899–1927.

Sherrer, A. T., 2014: Observational analysis of the interaction between a baroclinic boundary and supercell storms on 27 April 2011. M.S. thesis, Department of Atmospheric and Earth Science, University of Alabama– Huntsville, 139pp.

Simmons, K. M. and D. Sutter, 2012: The 2011 tornadoes and the future of tornado research. *Bull. Amer. Meteor. Soc.*, **93 (7)**, 959–961.

Simpson, J. E., 1997: *Gravity currents: In the environment and the laboratory*. Cambridge University Press, 244 pp.

Sims, J. H. and D. D. Baumann, 1972: The tornado threat: Coping styles of the North and South. *Science*, **176 (4042)**, 1386–1392.

Skamarock, W., J. Klemp, J. Dudhia, D. Gill, M. Barker, W. Wang, and J. Powers, 2008: A Description of the Advanced Research WRF Version 3: NCAR Technical Note. *National Center for Atmospheric Research*.

Smith, B. T., R. L. Thompson, J. S. Grams, C. Broyles, and H. E. Brooks, 2012: Convective modes for significant severe thunderstorms in the contiguous United States. Part I: Storm classification and climatology. *Wea. Forecasting*, **27 (5)**, 1114–1135.

Smith, R. K. and M. J. Reeder, 1988: On the movement and low-level structure of cold fronts. *Mon. Wea. Rev.*, **116 (10)**, 1927–1944.

Sobash, R. A. and J. S. Kain, 2017: Seasonal variations in severe weather forecast skill in an experimental convection-allowing model. *Wea. Forecasting*, **32 (5)**, 1885–1902.

Sobash, R. A., J. S. Kain, D. R. Bright, A. R. Dean, M. C. Coniglio, and S. J. Weiss, 2011: Probabilistic forecast guidance for severe thunderstorms based on the identification of extreme phenomena in convection-allowing model forecasts. *Wea. Forecasting*, **26 (5)**, 714–728.

Sobash, R. A., G. S. Romine, and C. S. Schwartz, 2020: A comparison of neural-network and surrogate-severe probabilistic convective hazard guidance derived from a convection-allowing model. *Wea. Forecasting*, **35 (5)**, 1981–2000.

Sobash, R. A., G. S. Romine, C. S. Schwartz, D. J. Gagne, and M. L. Weisman, 2016a: Explicit forecasts of low-level rotation from convection-allowing models for next-day tornado prediction. *Wea. Forecasting*, **31 (5)**, 1591–1614.

Sobash, R. A., C. S. Schwartz, G. S. Romine, K. R. Fossell, and M. L. Weisman, 2016b: Severe weather prediction using storm surrogates from an ensemble forecasting system. *Wea. Forecasting*, **31 (1)**, 255–271.

Sobash, R. A., C. S. Schwartz, G. S. Romine, and M. L. Weisman, 2019: Next-day prediction of tornadoes using convection-allowing models with 1-km horizontal grid spacing. *Wea. Forecasting*, **34 (4)**, 1117–1135.

Stein, A., R. R. Draxler, G. D. Rolph, B. J. Stunder, M. Cohen, and F. Ngan, 2015: NOAA's HYSPLIT atmospheric transport and dispersion modeling system. *Bull. Amer. Meteor. Soc.*, **96 (12)**, 2059–2077.

Steinfeld, D. and S. Pfahl, 2019: The role of latent heating in atmospheric blocking dynamics: a global climatology. **53 (9-10)**, 6159–6180.

Stensrud, D. J., 1996: Effects of persistent, midlatitude mesoscale regions of convection on the large-scale environment during the warm season. *J. Atmos. Sci.*, **53 (23)**, 3503–3527.

Stobie, J. G., F. Einaudi, and L. W. Uccellini, 1983: A case study of gravity waves–convective storms interaction: 9 May 1979. *J. Atmos. Sci.*, **40 (12)**, 2804–2830.

Stoelinga, M. T., 1996: A potential vorticity-based study of the role of diabatic heating and friction in a numerically simulated baroclinic cyclone. *Mon. Wea. Rev.*, **124 (5)**, 849–874.

Strader, S. M. and W. S. Ashley, 2018: Finescale assessment of mobile home tornado vulnerability in the central and southeast United States. *Wea. Climate Soc.*, **10 (4)**, 797–812.

Stumpf, G. J., R. H. Johnson, and B. F. Smull, 1991: The wake low in a midlatitude mesoscale convective system having complex convective organization. *Mon. Wea. Rev.*, **119 (1)**, 134–158.

Sutter, D. and K. M. Simmons, 2010: Tornado fatalities and mobile homes in the United States. **53 (1)**, 125–137.

Thompson, G., P. R. Field, R. M. Rasmussen, and W. D. Hall, 2008: Explicit forecasts of winter precipitation using an improved bulk microphysics scheme. Part II: Implementation of a new snow parameterization. *Mon. Wea. Rev.*, **136 (12)**, 5095–5115.

Thompson, G., R. M. Rasmussen, and K. Manning, 2004: Explicit forecasts of winter precipitation using an improved bulk microphysics scheme. Part I: Description and sensitivity analysis. *Mon. Wea. Rev.*, **132 (2)**, 519–542.

Thompson, R. L. and R. Edwards, 2000: An overview of environmental conditions and forecast implications of the 3 May 1999 tornado outbreak. *Wea. Forecasting*, **15 (6)**, 682–699.

Thompson, R. L., R. Edwards, J. A. Hart, K. L. Elmore, and P. Markowski, 2003: Close proximity soundings within supercell environments obtained from the Rapid Update Cycle. *Wea. Forecasting*, **18 (6)**, 1243–1261.

Thompson, R. L., B. T. Smith, A. R. Dean, and P. T. Marsh, 2013: Spatial distributions of tornadic near-storm environments by convective mode. *Electronic J. Severe Storms Meteor.*, **8 (5)**.

Thompson, R. L., B. T. Smith, J. S. Grams, A. R. Dean, and C. Broyles, 2012: Convective modes for significant severe thunderstorms in the contiguous United States. Part II: Supercell and QLCS tornado environments. *Wea. Forecasting*, **27 (5)**, 1136–1154.

Thorncroft, C., B. Hoskins, and M. McIntyre, 1993: Two paradigms of baroclinic-wave life-cycle behaviour. *Quart. J. Roy. Meteor. Soc.*, **119 (509)**, 17–55.

Torn, R. D. and G. J. Hakim, 2008: Ensemble-based sensitivity analysis. *Mon. Wea. Rev.*, **136 (2)**, 663–677.

Torn, R. D., G. J. Hakim, and C. Snyder, 2006: Boundary conditions for limited-area ensemble Kalman filters. *Mon. Wea. Rev.*, **134 (9)**, 2490–2502.

Torn, R. D. and G. S. Romine, 2015: Sensitivity of central Oklahoma convection forecasts to upstream potential vorticity anomalies during two strongly forced cases during MPEX. *Mon. Wea. Rev.*, **143 (10)**, 4064–4087.

Torn, R. D., G. S. Romine, and T. J. Galarneau, 2017: Sensitivity of dryline convection forecasts to upstream forecast errors for two weakly forced MPEX cases. *Mon. Wea. Rev.*, **145 (5)**, 1831–1852.

Trapp, R. J., 2014: On the significance of multiple consecutive days of tornado activity. *Mon. Wea. Rev.*, **142 (4)**, 1452–1459.

Trapp, R. J., S. A. Tessendorf, E. S. Godfrey, and H. E. Brooks, 2005: Tornadoes from squall lines and bow echoes. Part I: Climatological distribution. *Wea. Forecasting*, **20 (1)**, 23–34.

Trexler, C. M. and S. E. Koch, 2000: The life cycle of a mesoscale gravity wave as observed by a network of Doppler wind profilers. *Mon. Wea. Rev.*, **128 (7)**, 2423–2446.

Trier, S. B., G. S. Romine, D. A. Ahijevych, and R. A. Sobash, 2019: Lower-tropospheric influences on the timing and intensity of afternoon severe convection over modest terrain in a convection-allowing ensemble. *Wea. Forecasting*, **34 (6)**, 1633–1656.

Trier, S. B., G. S. Romine, D. A. Ahijevych, R. A. Sobash, and M. B. Chasteen, 2021: Relationship of convection initiation and subsequent storm strength to ensemble simulated environmental conditions during IOP3b of VORTEX Southeast 2017. *Mon. Wea. Rev.*, **149 (10)**, 3265–3287.

Trier, S. B., G. S. Romine, D. A. Ahijevych, R. J. Trapp, R. S. Schumacher, M. C. Coniglio, and D. J. Stensrud, 2015: Mesoscale thermodynamic influences on convection initiation near a surface dryline in a convection-permitting ensemble. *Mon. Wea. Rev.*, **143 (9)**, 3726–3753.

Trier, S. B., J. W. Wilson, D. A. Ahijevych, and R. A. Sobash, 2017: Mesoscale vertical motions near nocturnal convection initiation in PECAN. *Mon. Wea. Rev.*, **145 (8)**, 2919–2941.

Tytell, J., F. Vernon, M. Hedlin, C. de Groot Hedlin, J. Reyes, B. Busby, K. Hafner, and J. Eakins, 2016: The USArray Transportable Array as a platform for weather observation and research. *Bull. Amer. Meteor. Soc.*, **97 (4)**, 603–619.

Uccellini, L. W. and D. R. Johnson, 1979: The coupling of upper and lower tropospheric jet streaks and implications for the development of severe convective storms. *Mon. Wea. Rev.*, **107 (6)**, 682–703.

Uccellini, L. W. and S. E. Koch, 1987: The synoptic setting and possible energy sources for mesoscale wave disturbances. *Mon. Wea. Rev.*, **115 (3)**, 721–729.

Uccellini, L. W., P. J. Kocin, R. A. Petersen, C. H. Wash, and K. F. Brill, 1984: The Presidents' Day cyclone of 18–19 February 1979: Synoptic overview and analysis of the subtropical jet streak influencing the pre-cyclogenetic period. *Mon. Wea. Rev.*, **112 (1)**, 31–55.

Ungarish, M., 2009: *An introduction to gravity currents and intrusions*. CRC press, 489 pp.

Van Tuyl, A. H. and J. A. Young, 1982: Numerical simulation of nonlinear jet streak adjustment. *Mon. Wea. Rev.*, **110 (12)**, 2038–2054.

Weckwerth, T. M., J. W. Wilson, R. M. Wakimoto, and N. A. Crook, 1997: Horizontal convective rolls: Determining the environmental conditions supporting their existence and characteristics. *Mon. Wea. Rev.*, **125 (4)**, 505–526.

Weisman, M. L., 1993: The genesis of severe, long-lived bow echoes. *J. Atmos. Sci.*, **50 (4)**, 645–670.

Weisman, M. L. and J. B. Klemp, 1984: The structure and classification of numerically simulated convective storms in directionally varying wind shears. *Mon. Wea. Rev.*, **112 (12)**, 2479–2498.

Weisman, M. L. and R. Rotunno, 2000: The use of vertical wind shear versus helicity in interpreting supercell dynamics. *J. Atmos. Sci.*, **57 (9)**, 1452–1472.

Weisman, M. L. and R. J. Trapp, 2003: Low-level mesovortices within squall lines and bow echoes. Part I: Overview and dependence on environmental shear. *Mon. Wea. Rev.*, **131 (11)**, 2779–2803.

Weisman, M. L., et al., 2015: The mesoscale predictability experiment (MPEX). *Bull. Amer. Meteor. Soc.*, **96 (12)**, 2127–2149.

Wernli, H., S. Dirren, M. A. Liniger, and M. Zillig, 2002: Dynamical aspects of the life cycle of the winter storm 'Lothar'(24–26 December 1999). *Quart. J. Roy. Meteor. Soc.*, **128 (580)**, 405–429.

Wetzel, P. J., W. R. Cotton, and R. L. McAnelly, 1983: A long-lived mesoscale convective complex. Part II: Evolution and structure of the mature complex. *Mon. Wea. Rev.*, **111 (10)**, 1919–1937.

Wheatley, D. M. and R. J. Trapp, 2008: The effect of mesoscale heterogeneity on the genesis and structure of mesovortices within quasi-linear convective systems. *Mon. Wea. Rev.*, **136 (11)**, 4220–4241.

Whitaker, J. S. and C. A. Davis, 1994: Cyclogenesis in a saturated environment. *J. Atmos. Sci.*, **51 (6)**, 889–908.

Whitney, L. F., 1977: Relationship of the subtropical jet stream to severe local storms. *Mon. Wea. Rev.*, **105 (4)**, 398–412.

Winters, A. C., D. Keyser, L. F. Bosart, and J. E. Martin, 2020: Composite synoptic-scale environments conducive to North American polar–subtropical jet superposition events. *Mon. Wea. Rev.*, **148 (5)**, 1987–2008.

Winters, A. C. and J. E. Martin, 2016: Synoptic and mesoscale processes supporting vertical superposition of the polar and subtropical jets in two contrasting cases. *Quart. J. Roy. Meteor. Soc.*, **142 (695)**, 1133–1149.

Wirth, V., M. Riemer, E. K. Chang, and O. Martius, 2018: Rossby wave packets on the midlatitude waveguide—A review. *Mon. Wea. Rev.*, **146 (7)**, 1965–2001.

Wolf, B. J. and D. R. Johnson, 1995: The mesoscale forcing of a midlatitude upper-tropospheric jet streak by a simulated convective system. Part I: Mass circulation and ageostrophic processes. *Mon. Wea. Rev.*, **123 (4)**, 1059–1087.

Yussouf, N., D. C. Dowell, L. J. Wicker, K. H. Knopfmeier, and D. M. Wheatley, 2015: Storm-scale data assimilation and ensemble forecasts for the 27 April 2011 severe weather outbreak in Alabama. *Mon. Wea. Rev.*, **143 (8)**, 3044–3066.

Zack, J. W. and M. L. Kaplan, 1987: Numerical simulations of the subsynoptic features associated with the AVE-SESAME I case. Part I: The preconvective environment. *Mon. Wea. Rev.*, **115 (10)**, 2367–2394.

Zhang, C., Y. Wang, and K. Hamilton, 2011: Improved representation of boundary layer clouds over the southeast Pacific in ARW-WRF using a modified Tiedtke cumulus parameterization scheme. *Mon. Wea. Rev.*, **139 (11)**, 3489–3513.

Zhang, D.-L. and R. Harvey, 1995: Enhancement of extratropical cyclogenesis by a mesoscale convective system. *J. Atmos. Sci.*, **52 (8)**, 1107–1127.

Zhang, F., N. Bei, R. Rotunno, C. Snyder, and C. C. Epifanio, 2007: Mesoscale predictability of moist baroclinic waves: Convection-permitting experiments and multistage error growth dynamics. *J. Atmos. Sci.*, **64 (10)**, 3579–3594.

Zhang, F., C. A. Davis, M. L. Kaplan, and S. E. Koch, 2001: Wavelet analysis and the governing dynamics of a large-amplitude mesoscale gravity-wave event along the East Coast of the United States. *Quart. J. Roy. Meteor. Soc.*, **127 (577)**, 2209–2245.

Zhang, F., S. E. Koch, C. A. Davis, and M. L. Kaplan, 2000: A survey of unbalanced flow diagnostics and their application. *Adv. Atmos. Sci.*, **17 (2)**, 165–183.

Zhang, F., C. Snyder, and R. Rotunno, 2003: Effects of moist convection on mesoscale predictability. *J. Atmos. Sci.*, **60 (9)**, 1173–1185.

Zhang, M., Z. Meng, Y. Huang, and D. Wang, 2019: The mechanism and predictability of an elevated convection initiation event in a weak-lifting environment in central-eastern China. *Mon. Wea. Rev.*, **147 (5)**, 1823–1841.